HELICAL TRANSITION METAL COMPLEXES: SYNTHESIS, CHARACTERIZATION AND ASYMMETRIC EPOXIDATIONS

by

TINGTING LIU

B.E., Southwestern University of China, 1999
M.S., Lanzhou Institute of Chemical Physics, CAS, 2002

AN ABSTRACT OF A DISSERTATION

submitted in partial fulfillment of the requirements for the degree

DOCTOR OF PHILOSOPHY

Department of Chemistry
College of Arts and Sciences

KANSAS STATE UNIVERSITY
Manhattan, Kansas

2011

Abstract

A series of chiral titanium and manganese complexes with helix-directing salen ligands have been prepared, characterized and studied. Their structures displayed as a chiral helical motif as expected. And it was also found that all M(salen) units were exclusively *M*-helimeric in the solid state, except Ti(cyclohexyl-benz[a]anthryl) as *P*-helix. This may be due to the energy difference between *P* and *M* helice, which enables crystal packing forces to control and drive the molecular structure. This is also in agreement with the previous computational studies that the *M* configuration predominates in THF solution. All metal centers adopt a cis-β octahedral geometry except in Mn(binapthyl-phenanthryl-salen). Most of M(salen) complexes in this work afforded μ–oxo dinuclear helicates, instead of the expected monohelicate, except Mn(binapthyl-phenanthryl-salen), which is bridged by a third salen ligand.

The titanium salt affected the complex solution behavior. In the presence of Cl⁻, only mononuclear species was found by ESI-MS, while both di- and mononuclear species was found in MeOH in the presence of ⁻O^{i}Pr. The NMR spectra of Ti(salen) indicated one major species with cis-β geometry exist in most solution, which could be monomer or dimer, except Ti(binapthyl-salen). No counterions have been found in the solid state of Mn(salen) complexes in this work, but they affected the ligand decomposition in the solution in Mn(binapthyl-phenanthryl-salen).

The Mn(salen) complexes could effectively and enatioselectively catalyze the asymmetric epoxidation of somoe *trans*, *cis* and terminal olefin, and various oxidants were employed.

HELICAL TRANSITION METAL COMPLEXES: SYNTHESIS, CHARACTERIZATION AND ASYMMETRIC EPOXIDATIONS

by

TINGTING LIU

B.E., Southwestern University of China, 1999
M.S., Lanzhou Institute of Chemical Physics, CAS, 2002

A DISSERTATION

submitted in partial fulfillment of the requirements for the degree

DOCTOR OF PHILOSOPHY

Department of Chemistry
College of Arts and Sciences

KANSAS STATE UNIVERSITY
Manhattan, Kansas

2011

Approved by:

Major Professor
Christopher J. Levy

Copyright

TINGTING LIU

2011

Abstract

A series of chiral titanium and manganese complexes with helix-directing salen ligands have been prepared, characterized and studied. Their structures displayed as a chiral helical motif as expected. And it was also found that all M(salen) units were exclusively *M*-helimeric in the solid state, except Ti(cyclohexyl-benz[a]anthryl) as *P*-helix. This may be due to the energy difference between *P* and *M* helice, which enables crystal packing forces to control and drive the molecular structure. This is also in agreement with the previous computational studies that the *M* configuration predominates in THF solution. All metal centers adopt a cis-β octahedral geometry except in Mn(binapthyl-phenanthryl-salen). Most of M(salen) complexes in this work afforded μ–oxo dinuclear helicates, instead of the expected monohelicate, except Mn(binapthyl-phenanthryl-salen), which is bridged by a third salen ligand.

The titanium salt affected the complex solution behavior. In the presence of Cl⁻, only mononuclear species was found by ESI-MS, while both di- and mononuclear species was found in MeOH in the presence of ⁻O^{i}Pr. The NMR spectra of Ti(salen) indicated one major species with cis-β geometry exist in most solution, which could be monomer or dimer, except Ti(binapthyl-salen). No counterions have been found in the solid state of Mn(salen) complexes in this work, but they affected the ligand decomposition in the solution in Mn(binapthyl-phenanthryl-salen).

The Mn(salen) complexes could effectively and enatioselectively catalyze the asymmetric epoxidation of somoe *trans*, *cis* and terminal olefin, and various oxidants were employed.

Table of Contents

List of Figures

List of Tables

Acknowledgements

First of all, I would like to thank my advisor Dr. Christopher Levy for his help, advice, encouragement and support during my PhD years in his research group. I have learnd a lot from him. Thanks also go to my committee members Dr. Eric Maatta, Dr. Stefen Bossmann, Dr. John Tomich, and outside chair, Dr. Melinda Wilkerson. I would also like to express my gratitude to Dr. John Desper, Jim and everybody else in the chemistry department: labmates, professors, friends and staff.

Most importantly, I'd like to thank my family: husband, son and parents. Nothing would be possible without them. Their love, support and guidance has allowed me to not only go through the past few years, but also become a chemist in the future.

Dedication

To my husband, son and parents

Chapter 1 - Introduction

Cytochrome P450 is a large and diverse group of enzymes to catalyze the oxidation of organic substances in nature[1a]. The monooxygenase reaction is one of the most common reactions catalyzed by cytochrome P450. In such reactions, one oxygen atom of molecular oxygen is inserted into an organic substrate (RH) while the other oxygen atom is reduced to water (Eq 1).

$$RH \ + \ O_2 \ + \ 2H^+ + \ 2e^- \longrightarrow \ ROH \ + \ H_2O \tag{1}$$
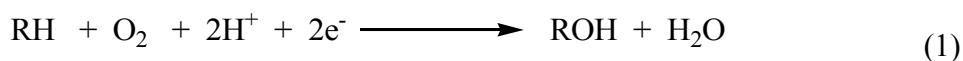
The active site of cytochrome P450 contains a heme, or iron-porphyrin center. Structurally related to the porphyrins, the metallosalen complexes have also shown various applicabilities for the oxidation. Historically, the interest in using Mn complexes as catalyst for the epoxidation of alkenes comes from biologically relevant oxidative Mn porphyrins.

1.1 Symmetric Salen ligands and metal-salen complexes

The first report of a reaction between an amine with an aldehyde by Schiff led to the establishment of a large class of ligands called Schiff bases.[1b] One of the most important classes of Schiff bases are the tetradentate salen (*N,N'*-bis(salicylaldehydro)ethylenediamine,), which are generally synthesized by condensation between a salicylaldehyde and a diamine in a 2:1 ratio (Figure 1.1). These ligands have two nitrogen and two oxygen donors, and are said to have a N_2O_2 donor set.
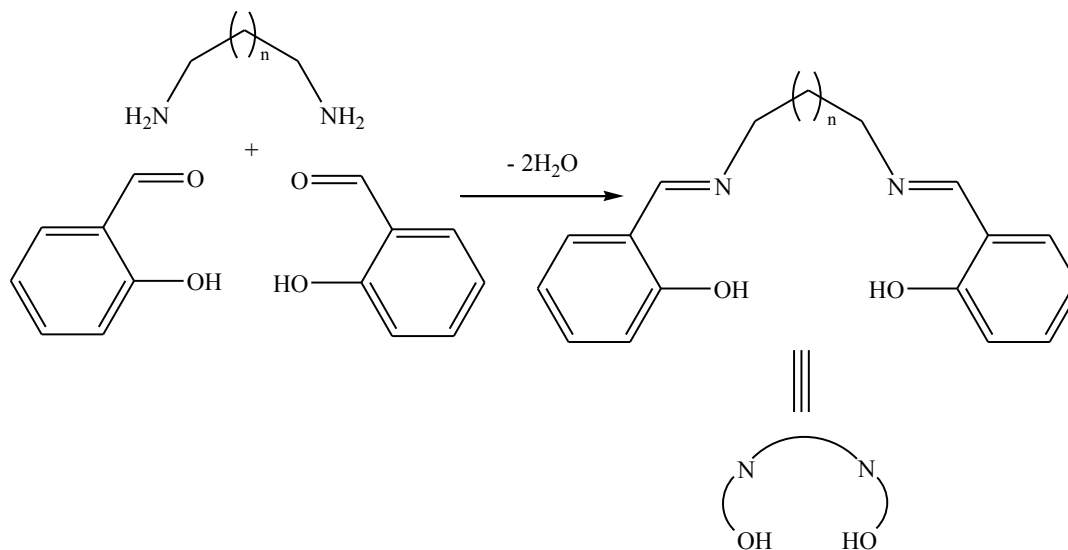
Figure 1.1 Synthesis of salen by condensation.

Since a variety of chiral and achiral salicylaldehydes and diamines are readily available, a wide variety of salen ligands can be produced through their combination. After deprotonation of two phenolic protons, these dianionic N_2O_2 compounds can easily form complexes with various metals. Metal-salen complexes often display octahedral geometry, and have two ancillary ligands. These complexes prove to be effective in various chemoselective catalytic reactions, such as epoxidation, cyclopropantion, and sulfoxidation.[2, 3, 4]

The configuration of metal-salen complexes directly correlates with chiral induction and catalytic performance in catalysis. The configuration can be finely tuned by the combination of diamine units, metal centers and the ancillary ligands. Since the diamine backbone has two sp^3 carbons, the metal-salen complexes normally have three possible configurations: *trans*, *cis*-α, and *cis*-β. In the *trans* isomer, the ancillary ligands position apically *trans* to each other and the N_2O_2 donors in the same plane. In the *cis*-α isomer, two ancillary ligands occupy two equatorial

positions while one equatorial and one apical positions in *cis*-β isomer. In addition, N_2O_2 donors are in non-planar in both cases (Figure 1.2).
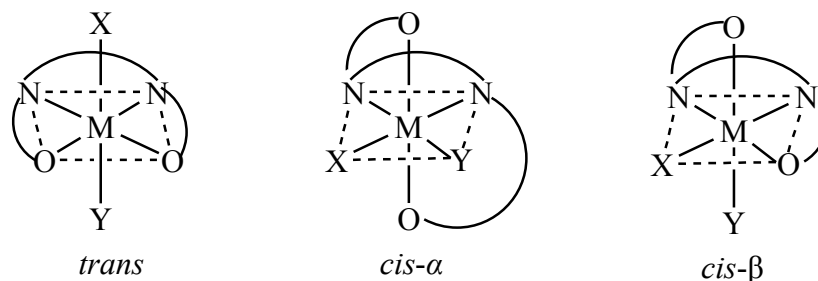
Figure 1.2 Synthesis of salen by condensation Possible configurations of octahedral metallosalen complexes. X and Y indicate ancillary ligand.

1.1.1 *trans*-metallosalen complexes

A *trans*-metallosalen complex can adopt stepped or umbrella conformations (examples using ethylenediamine as backbone, Figure 1.3) due to the free rotation of the diamine unit. The conformation of the five-membered chelating ring comprising the central metal and ethylenediamine can govern the complex conformation: the complex adopts a stepped conformation when the chelating ring shows a half-chair conformer, and an umbrella conformation when the ring bears an envelope conformer. Most of metallosalen complexes adopt a non-planar stepped conformation.[2,5]

Figure 1.3 Possible conformations of *trans*-metallosalen complexes. Left, step; right, umbrella.[2]

Both the chiral nature and the conformation of the metallosalen complex greatly influence the catalytic enantioselectivity. For flexible achiral ligands, there can be an equilibrium between two enantiomeric conformers in a stepped *trans*-metallosalen complex (Figure 1.4). If the salen ligand is chiral (chiral 8 and 8' carbons), then one enantiomer (A) is dominant, since the half-chair conformer allows both substituents at 8 and 8' postions to occupy stable quasi-equatorial position. If the salen ligand is achiral, then there could be two conditions: when a chiral donor ligand L is apically position, the enantiomeric conformers become diastereomeric, which makes the equilibrium shift to one side (A); if the apical ligand is achiral, two enantiomers equilibrate (A + B).
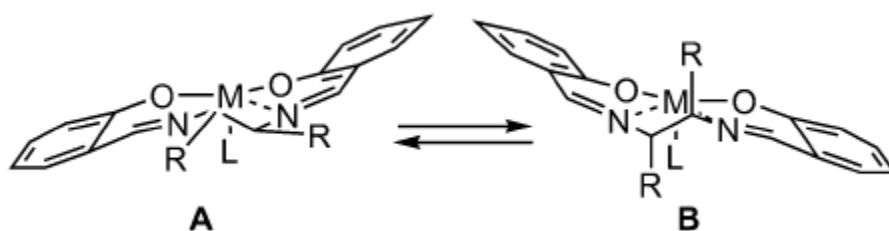
Figure 1.4 Equillibrium between two enantiomeric conformers.[2]

A wide variety of chiral *trans*-metallosalen, such as Co,[6] Mn,[7] Cr,[8] Ru,[9] Ti,[10] V,[11] and Cu[12] complexes have been developed so far.

1.1.2 *cis*-β-Metallosalen complexes

In the presence of a multidentate ligand, *cis*-β metallosalen complexes are more often formed than *trans*-metallosalens. Some metals, such as Ru and Zr, prefer to the adopt *cis*-β conformation even only monodentate ligands present. Some metallosalens also adopt a *cis*-β configuration when the salen ligands bear axially chiral diamines[13] such as binaphthyl

derivatives. A *trans*-metallosalen can transform into a *cis*-β one in the presence of a bidentate ligand (Figure 1.5).
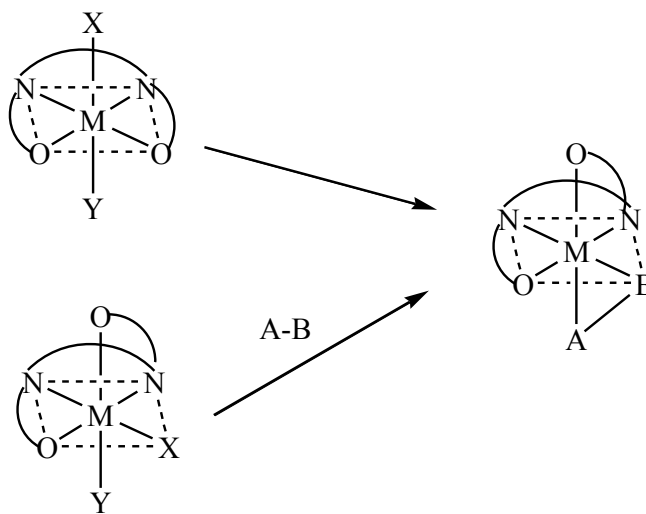
Figure 1.5 Transformation of a *trans*-metallosalen to a *cis*-β complex. A-B: bidentate reagent.

All *cis*-β configurations are chiral. A finely tuned *cis*-β metallosalen can generate a unique asymmetric reaction site for catalytic reactions, which may enhance asymmetric induction. The chiral *cis*-β metallosalens[2] show unique characters in the catalysis as compared to the *trans* analogous (Figure 1.6).
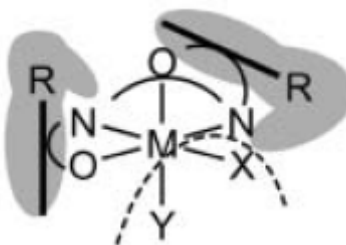
Figure 1.6 Unique reaction site for chiral *cis*-β metallosalens.[2]

The configuration of a metal-salen complex is generally determined by spectroscopy. X-ray diffraction is the most reliable method for its structure determination if a single crystal can be grown. The structure can also be determined by NMR in solution samples, but in some cases, the NMR spectra are not very informative due to the paramagnetism of metal centers and the associated broadening.

1.2 Helical complexes

Helical complexes are common molecules in nature. A helix is defined as a coiled shape, like a spring or spiral form. The helical compound can either be left handed (*M*) or right handed (*P*) up to their spiral direction. The most famous helical molecule in biology is double-stranded DNA helix. Nowadays, increasing attentions have been paid to the helical transition metal complexes[14, 15, 16] due to their potential as chiral catalysts. Furthermore, the study of self-assembly and helix formation can help in the understanding of supermolecular chemistry.[17, 18, 19, 20]

Helical complexes with one metal ion are called monohelices. These can be further classified as single, double and triple stranded molecules depending on the number of chelating ligands around the metal center (Figure 1.7). Helical compounds with two or more metal ions are named helicates. The common form of helicates includes double-stranded dinuclear helicates (Figure 1.7).
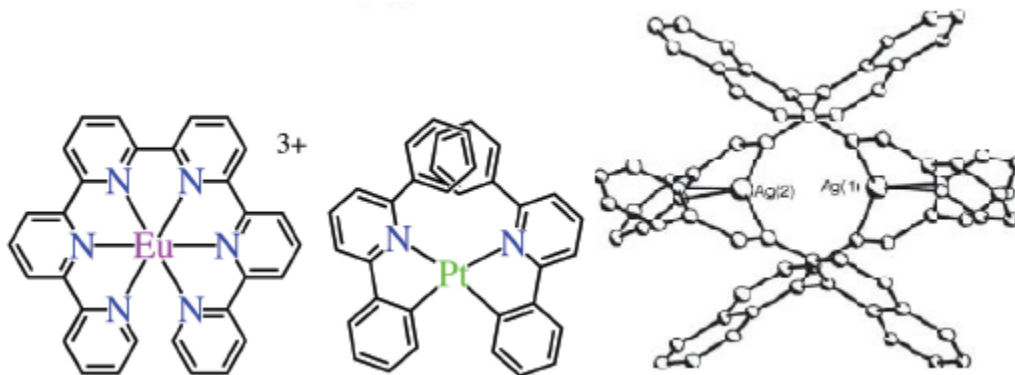
Figure 1.7 Examples of single, double-stranded monohelices and double-stranded helicates.[17,19,20]

In order to form monohelices, both the multidentate ligand nature (donor atoms, flexibility, chirality) and metal center (coordination preference, size, change, etc.) need to be considered. The donor groups of the ligand prefer being directed to the metal center, meanwhile binding atoms need to be arranged close enough to each other so that they can coordinate to the same metal. On the other side, different metal ions form different types of helices, even in the presence of same ligand.[14] In addition, metals that prefer a square planar (Cu^{II}) or octahedral (Fe^{II}) geometry are more likely to form monohelices.

1.3 Catalytic asymmetric epoxidation (AE) of olefins

Selective oxidation is a key technology for transforming petroleum and natural gas derived raw materials to a wide variety of bulky and fine chemicals. When the concept of sustainability[21] was introduced in the world in 1990s, attention has been focused on the developing greener and more efficient process, such as catalytic oxidation. The epoxidation of olefins is an important and useful oxidation reaction in organic synthesis. In this reaction, two C-O bonds are formed as well as up to two chiral centers in the case of asymmetric epoxidation (AE, Figure 1.8). Considerable

efforts are currently put into the development of new, improved catalytic AE processes for the synthesis of enantiopure epoxides at the industrial and labotary scales.
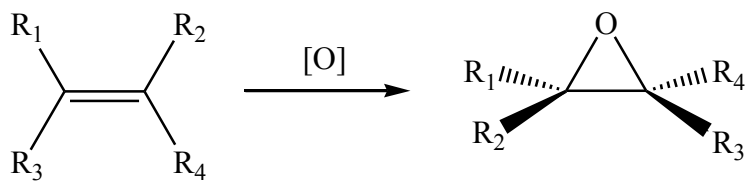
Figure 1.8 General scheme for asymmetric epoxidation. [O] indicates the oxidant.

1.3.1 Catalytic AE – A Green and Sustainable Process

Chemistry has a fundamental influence on our modern and daily life. It generates energy, provides medicine, modifies and stores food, protect crops and invent new materials. But the chemical industry has been traditionally considered as hazardous and polluting. It produces stoichiometric amounts of waste, and causes air and water pollution. Furthermore, traditional chemical industry has to face a big problem and challenge: sustainable development worldwide. According to UN report,[22] sustainability means "meeting the needs of the current generation without sacrificing the ability to meet the need of future generation". There are various ways to reach sustainable development, one of which is green chemistry. The concept of "green chemistry" was firstly introduced to the public in the 1990s, and has been promoted worldwide. It focuses on hazard/waste prevention, rather than treating or solving.

Catalysis is an important tool for green chemistry and sustainable development. Compared to traditional noncatalytic counterparts, catalytic processes proceed more efficiently and under milder conditions (energy-efficient), show more selectivity and activity (usage optimal in raw materials), and produce less waste with the catalyst recyclable. So a greater amount of efforts must be focused on the development of new, improved catalytic processes.

1.3.2 Epoxides

Epoxides are very important chemical intermediates due to their versatility. They can be easily converted to various products, as illustrated in Figure 1.9 using α-olefins as substrates. The long-chain primary alcohols can be produced by hydrogenation in the presence of a nickel catalyst, and the epoxides can be easily transformed to allyl alcohols over basic lithium phosphate, and to allyl aldehydes over aluminium phosphate, by rearrangement. They can also be converted to allylic alcohols with aluminum alkoxide catalysts.

$$
\begin{array}{c}
\overset{O}{\overset{\|}{RCH_2CCH_3}} \\
\uparrow [H^+] \\
\end{array}
$$

RCH=CHCH₂OH and/or RCHCH=CH₂ (OH) ← [Li₂HPO₄] — RH₂CHC△CH₂ — H₂/[Ni] → RC₃H₆OH ↓ [AlPO₄] → RCH₂H₂CHO
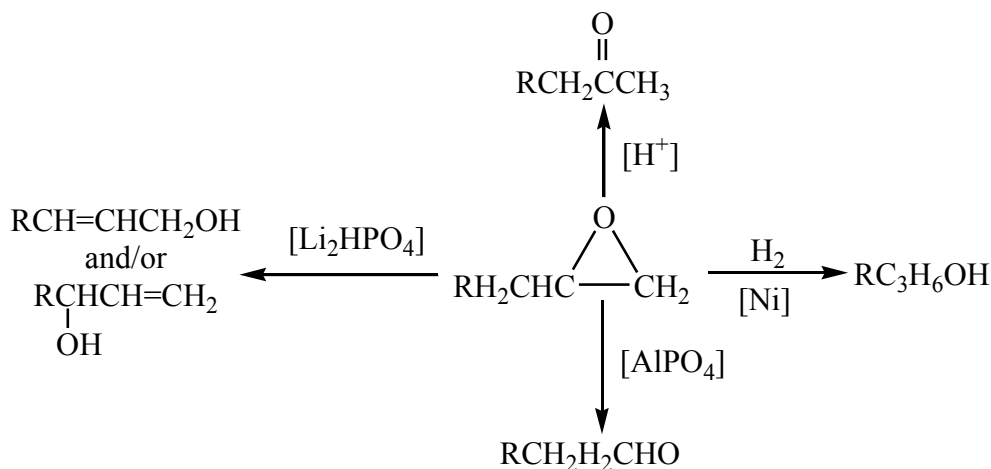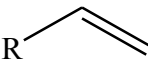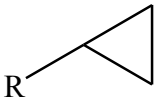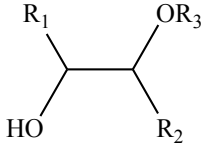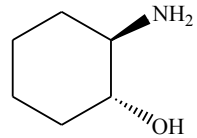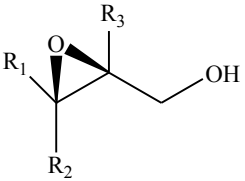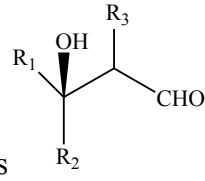
Figure 1.9 Versatile conversion of α–olefin epoxide.

The amount of epoxides utilized per year varies from millions of tons for commodity chemicals such as ethylene oxide (EO) and propylene oxides (PO), to a few grams for synthetic intermediates.[23, 24] Some of the most common and important epoxides and their usages are summarized in Table 1.1.

Table 1.1 Some common epoxides and their usage.

Starting olefins	epoxides	usage
Ethylene/propylene	Ethylene oxide/propylene oxide	Ethylene glycols, polyurethane polyols, propylene glycols
cyclohexene	Cyclohexene oxide	Polymer,
Allyl alcohols		Proprionates,α– hydroxyketones

Both ethylene oxide[23] (EO) and propylene oxide[23] (PO) are major commodity chemicals produced by epoxidation. They are widely applied in the production of ethylene glycos, polyurethane polyols, propylene glycols, and more of alcohols.

Terminal epoxides[23,24] can undergo ring-opening with alcohols to produce hydroxyethers. These hydroxyethers are lipid-soluble, non-sticky and compatible with human tissues, which make them useful in cosmetic and pharmaceutical industry.

Cyclohexene oxide[24] can act as monomer in polymerization with CO_2, and convert to enantiopure β–aminoalcohols and β–diimanes, which can be used as chirality-induced ligands and precursors for pharmaceuticals and agrochemicals.

Allyl epoxides produced by the Sharpless process[25] can be used to synthesize polypropionate structures by Lewis acid-induced rearrangement. They also can be converted to

α–hydroxyketones. These ketones are difficult to obtain by conventional methods, but are vital precursors in the synthesis of natural products, such as β–hydroxyl-α-amino acids.

Both the steric and electronic characteristics will affect the stability of epoxides. Cyclooctene epoxide is very stable because the steric hindrance of the ring will slow down the side reactions of the epoxide group, while cyclohexene epoxides are very reactive and the steric properties of cyclohexane ring favor the ring-opening reaction of the epoxide. Most of the terminal epoxides are stable to ring-opening, but styrene oxide is reactive, because the intermediate products are electronically stabilized by the aromatic ring.

1.3.3 Oxidants

The oxygen source is an important aspect of epoxidation. There are several oxidants available for transition-metal catalyzed AE (Table 1.2).

Alkyl hydroperoxides, such as *tert*-butyl hydroperoxide (TBHP) are widely applied in the Sharpless[25] system. TBHP is thermally stable, less sensitive in the presence of metal, and safer to handle as compared to other organic peracids. Furthermore, TBHP is unreactive with most organic compounds in contrast to peracids and H_2O_2, so it is particularly suitable for the epoxidation of acid-sensitive olefins and those having a functional group that reacts with a peracid.

Table 1.2 Oxidants used in transition-metal catalyzed epoxidation.[26]

Oxidant	Active oxygen content/wt%	Waste product
O_2	100	Nothing or H_2O
O_2/reductor	50	H_2O
H_2O_2	47	H_2O
NaOCl	21.6	NaCl
CH_3CO_3H	21.1	CH_3CO_2H
$^tBuOOH(TBHP)$	17.8	^tBuOH
$KHSO_5$	10.5	$KHSO_4$
BTSP	9	Hexamethyldisiloxane
PhIO	7.3	PhI

Both NaOCl and iodosylbenzene (PhIO) are good terminal oxidants in metalloporphyrin[27] and metal-salen[28] catalyst systems. NaOCl normally requires a very basic (pH: 11~12) environment, which limits its application. PhIO is insoluble in most organic solvents, so it is very hard to determine its exact concentration in the reaction phase. It also has very low active oxygen content (7.3%) and undesirable waste produced (PhI), so it is not a green oxidant.

Molecular oxygen (O_2) is the most ideal oxidant for the epoxidation due to its great availability, high active oxygen content and clean waste product. However, O_2 cannot be readily utilized in practice because of occurrence of an autooxidation radical pathway, leading to low/no selectivity of epoxides. Currently, only a few catalytic systems[29] can directly activate O_2, which limit its application in epoxidation.

Hydrogen peroxide is a very potent terminal oxidant and has been applied in some Ag, Mn-, Pt-, Re-complexes catalyzed AE[30] with good to reasonable selectivity. Its relatively high content of active oxygen and water as product make it a candidate in the Green AE process. In some Ti complex[30] catalyzed system, diluted aqueuous H_2O_2 has been used to achieve reasonable to good

results. In the Mn-salen[30] catalytic system, the problem is the catalyst deactivation in the presence of water. Anhydrous H_2O_2, either in the form of urea-H_2O_2 or triphenylphsphine-H_2O_2, have been applied to avoid this problem. The yield and selectivity are comparable to those using NaOCl, but the catalyst loading is much higher, and the produced waste, Ph_3PO, is an additional problem.

1.3.4 Successful transition metal complexes catalyzed AE examples

In 1979 Groves[27] published the first paper of olefin epoxidation catalyzed by the iron porphyrin Fe(TPP)Cl with PhIO as oxidant.

The Sharpless reaction[25] is so far the most successful example applied in industry for catalytic AE. Typically, allylic alcohols are epoxidized in the presence of a titanium tartrate catalyst and TBHP as the terminal oxidant. Molecular sieves need to be added in order to remove any water. All reagents are readily available and the system is easy to handle. The enantiomeric excess (*ee*) value can be achieved as high as >90% and the yield 70-90% with primary allylic alcohols as substrate and Ti-isopropoxide-diethyltartrate (DET) as the source for *in-situ* catalyst (Table 1.3). However, this kind of reaction is only appliable to allylic alcohols.

Table 1.3 Sharpless Ti-tartrate AE of allylic alcohols.

$$R_1\text{—}R_2 \quad \xrightarrow[\substack{\text{DET, CH}_2\text{Cl}_2,\ -20\ ^0\text{C} \\ \text{molecular seives}}]{\text{TBHP, Ti(O-}^i\text{Pr)}_4} \quad R_1\text{—}R_2$$

TBHP, Ti(O-^{i}Pr)$_4$

DET, CH$_2$Cl$_2$, -20 ^{0}C
molecular seives

70-90% yield
>90% *ee*
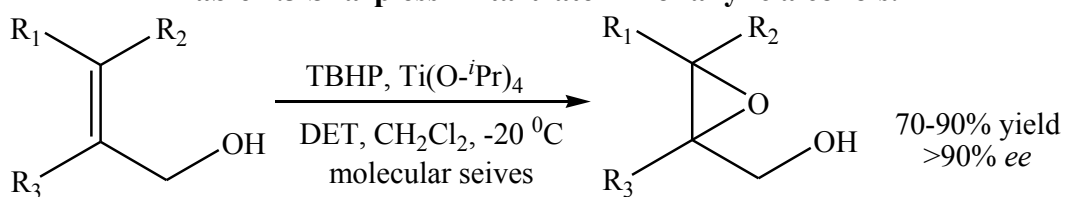
Substrate	Yield/%	*ee*/%
⌒⌒OH	65	90
⌒⌒⌒OH	70	96
Ph⌒⌒⌒OH	89	>98
⌒⌒OH	50	>95
⌒⌒⌒⌒OH	40	95

Catalytic loading: 5 mol%

Jacobsen-Kaksuki catalysts[28,31] are specialized for the epoxidation of unfuntionalized olefins, particularly for *cis*-disubstitued and trisubstituted alkenes. In 1990, Jacobsen and Kaksuki independently reported chiral Mn(III)-salen catalysts **1** and **2** for AE. Bleach or PhIO is normally used as the oxygen atom donor, but peracides, like *m*-chloroperbenzoic acid (*m*-CPBA) can also be used. The catalyst loading is as little as 0.5 mol% in these systems. By finely tuning the electronic and steric properties of the salen ligand, the *ee*% can reach >90% (Table 1.4).

Table 1.4 Jacobsen-Kaksuki AE of unfunctionalized olefins.

36-87% yield
30-98% *ee*
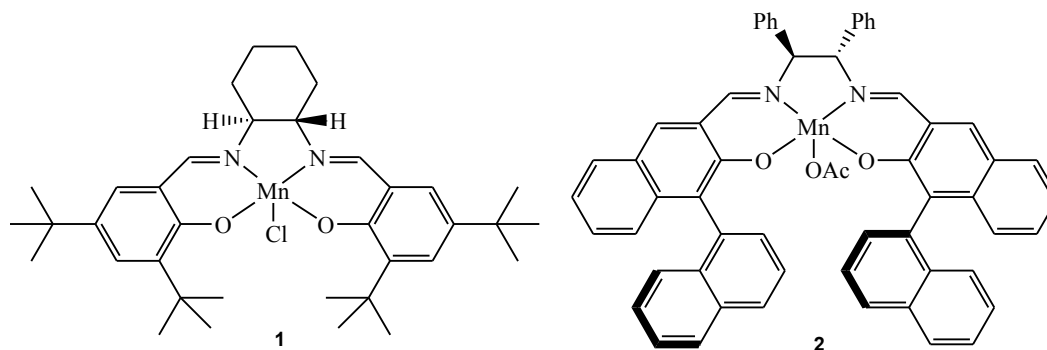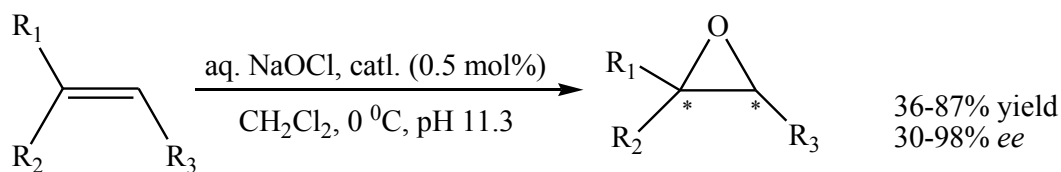
olefin	Method	Cata. Loading	Isolated yield	*ee*
Ph ⌒⌒	A	4 mol%	84%	92
(indene)	A	1 mol%	80%	88
(dihydronaphthalene)	A	4 mol%	67%	88
(2,2-dimethylchromene)	A	2 mol%	87%	98
(dioxolane spiro)	B	1.5 mol%	63%	94
Ph ⌒⌒ CO$_2$Et	B	8 mol%	67%	97

Method A: NaOCl, pH 11.3, CH$_2$Cl$_2$, 0 °C,
Method B: same as A, plus 0.2 eq. 4-phenylpyride-N-oxide.

In some cases, amine-*N* oxides[32] can act as axial ligands in the active species, which improves the selectivity. It is believed that the additives can prevent the homolysis of the O-O

bond and the subsequent destruction of the metal complex. One drawback of these Mn-salen catalysts is their oxidation under reaction condition, leading to low turnover numbers (40-200) and lack of recyclability.

Katsuki and coworkers[33] develop a robust Mn-salen catalyst **3**. A carboxylic acid group is attached to the diamine backbone. This new catalyst can convert 2, 2-dimethylchromene to the corresponding epoxide with 99% *ee* using PhIO as the oxidant. Turnover numbers were as high as 9200 after 6 hr reaction.
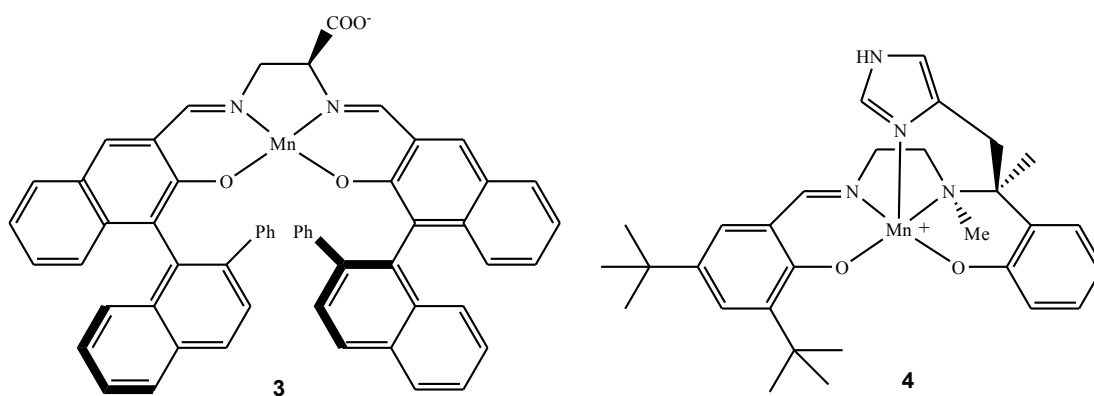
Considerable efforts have been devoted to the use of H_2O_2 in AE with Mn-salen complexes.[26] Promising results have been reported even though turnover numbers are typically low. The presence of an additive is essential for the catalytic activity. A chiral Mn catalyst **4,** with a dihydrosalen ligand functionalized by an imidazole group displays reasonable acitivity and moderate selectivity in the epoxidation of **1**, 2-dihydronaphthalene. In this system, the additive is not needed. Katsuki used Mn-salen with *N*-methylimidazole as the additive in the presence of a carboxylate salt, to obtain reasonable *ee* in the conversion of dihydronaphthalene to the corresponding epoxide. Improved results and shorter reaction times are achieved with maleic

anhydride and UHP (in situ prepared peroxycarboxylic acid from anhydride and anhydrous H_2O_2), as compared with aqueous H_2O_2 and carboxylate salt (Table 1.5).

Table 1.5 Epoxidation of olefins by Mn-salen complexes using H_2O_2 as oxidant.
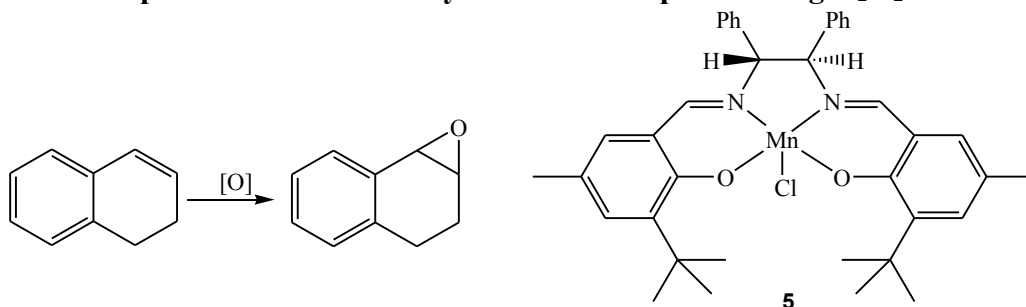
Cata.	Oxidant (equiv.)	Yield/%	*ee*/%
4	1 % H_2O_2 (10)	72	64
5	30% H_2O_2 (1.5)	74	69
5	Urea/ H_2O_2/maleic anhydride (1.5)	70	73

Katsuki[34] et al. developed a series of Ti complexes for AE with H_2O_2 as oxidant. These complexes form *in situ* from Ti tetraalkyloxide and salen, salan, and salalen ligands. Salan and salalen are fully reduced and half-reduced salen ligands, and show better epoxidation results than salen. In their AE system, excellent to reasonable yield and selectivity are achieved for terminal olefins with aqueous H_2O_2 as oxidant (Table 1.6). Ti(salan) catalysts need much higher loadings (5 mol%) and more H_2O_2 (1.5 eq.) as compared to Ti(salalan) counterparts (1 mol%, 1.05 eq.), but considering the simple synthesis of salan and *in situ* complexaiton, it is still a promising catalyst.

Table 1.6 Ti-complex catalyzed AE using aqueous H_2O_2.

di-μ-oxo Ti(salalen)-**6**   di-μ-oxo Ti(salan)-**7**
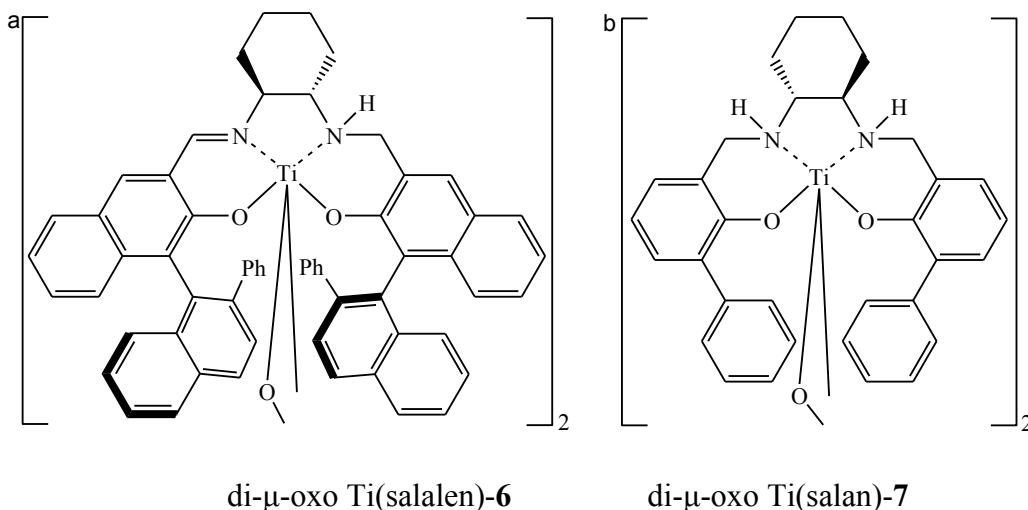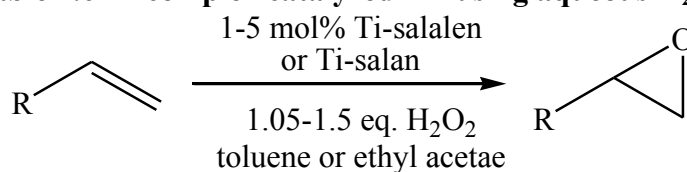
Olefins	Cata.	Loading	Eq. 30% aqueous H_2O_2	Yield	*ee*
Ph (allylbenzene)	**6**	1 mol%	1.05	90%	93%
	7	5 mol%	1.5	47%	82%
C_6H_{13} (olefin)	**6**	1 mol%	1.05	70%	82%
	7	5 mol%	1.5	25%	55%
(dihydronaphthalene)	**6**	1 mol%	1.05	99%	99%
	7	5 mol%	1.5	87%	96%

1.3.5 Mechanism of transition metal complexes-catalyzed AE

Great efforts have been focused on the study of the mechanism of AE, which plays a remarkable role not only in improving technology, but also in advancing fundamental understanding in the field of chemistry. In the following section, the mechanic studies about two AE systems are introduced.

1.3.5.1 Sharpless Ti-tartrate AE system

It is generally believed[35] that a Lewis acid mechanism occurs with high-valent early transition metal ions, such as Ti(IV), V(V), W(VI), Mo(VI) and Re(VI). The most commonly used oxidants are hydrogen peroxide or alkyl hydroperoxides in their epoxidation system. The peroxometal adduct (M-OOH or M-OOR) is first formed, and then the positively charged oxygen atom next to the metal center (called proximal oxygen) is transferred to the nucleophilic olefin in a concerted way (Figure 1.10). The metal center acts as a Lewis acid since it withdraws electrons from the O-O bond, to facilitate the O-O dissociation and proximal O activation for the further insertion into the olefin double bond. During the process, the oxidation state of the metal ion does not change. The more distant O (distal O) constitutes a good leaving group in the form of OH or OR. Active catalysts are those metals that are strong Lewis acids with vacant coordination sites but relatively weak oxidants (to avoid one electron oxidation of the peroxides) in their highest oxidation states.
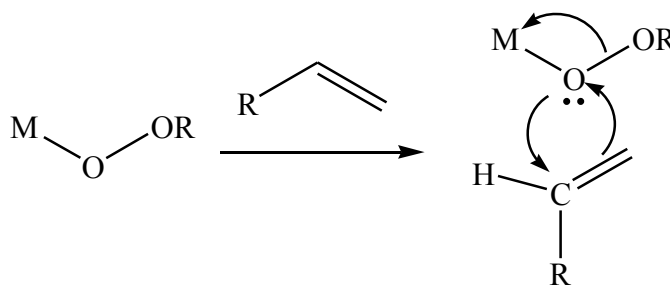
Figure 1.10 Lewis acid (peroxometal) mechanism of early TM catalyzed AE.

The Sharpless AE system is one of the most thoroughly investigated processes. From the rate determination and kinetics observation, it is proposed[36, 37] that the Ti(tartrate) complex is formed by removing two alkoxide ligands, and then the remaining two alkoxide ligands are exchanged by TBHP and the allyl alcohol. The order of displacement is not certain. The rate-

determing step is the oxygen transfer from the coordinated hydroperoxide to one enantioface of a coordinated allyl alcohol (Figure 1.11).

Ti(OR)$_4$ $\xrightarrow[]{\text{-2ROH}}$ [Ti(tartrate)(OR)$_2$] $\underset{\text{-2ROH}}{\overset{\text{TBHP, AOH}}{\rightleftarrows}}$ [Ti(tartrate)(OA)(OOtBu)]

+

tartrate

$\downarrow$ oxygen transfer

[Ti(tartrate)(OE)(OOtBu)]
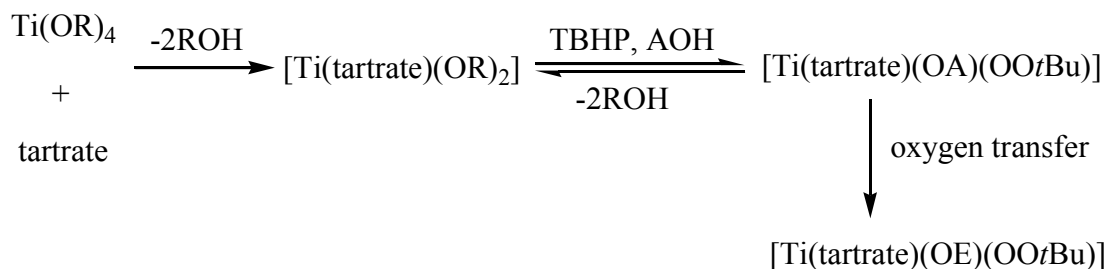
Figure 1.11 Ligand exchange in the Sharpless process.
AOH: allylic alcohol; OA: allylic alkoxide; OE: epoxy alkoxide

It has been found that allyl alcohols with electron-donating groups increase the reaction rate, while the substrates with electron-withdrawing groups decrease the rate, suggesting that the olefin substrate acts as a nucleophile. The stoichiometric study shows that more than one active Ti-tartrate species exist, but one 2: 2 titanium(IV) tartrate dimer species (Figure 1.12 a) is dominant based on the FTIR and NMR analysis. In this dimer, hydroperoxide is coordinated to Ti in η^2 bidentate mode (Figure 1.12, b), which indicates that TBHP is sterically more demanding than alkoxide. The DFT calculation agrees that the Ti-O-O is approaching the allyl C=C moiety in a spiro fashion. The ester groups prefer the equatorial site in stead of axial in the transition state, and they do not coordinate with the Ti center.
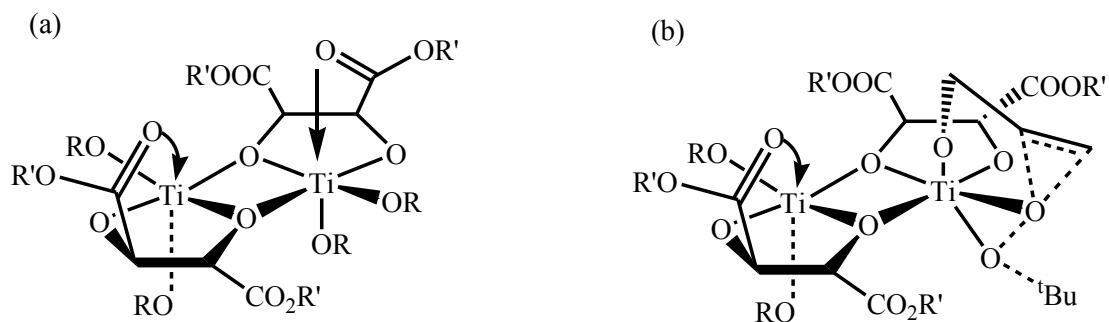
Figure 1.12 Structure of the active Ti-tartrate catalyst. (a) dominant [Ti(tartrate)$_2$(OR)$_2$]$_2$ dimer; and (b) coordinated with TBHP.

1.3.5.2 Jacobsen-Katsuki Mn-Salen catalysts

It is generally accepted[35] that a redox mechanism is involved in the late transition metal complex-catalyzed AE, such as Mn, Fe and Ru, which have multiple oxidation states. An O=M oxo species is initially formed with the oxidant, followed by oxygen atom transfer to an olefin by the active intermediate (Figure 1.13). This intermediate is still in question and could be a metallacycle, or a radical or cationic species. During the process, the oxidation state of metal ions increase by 2.
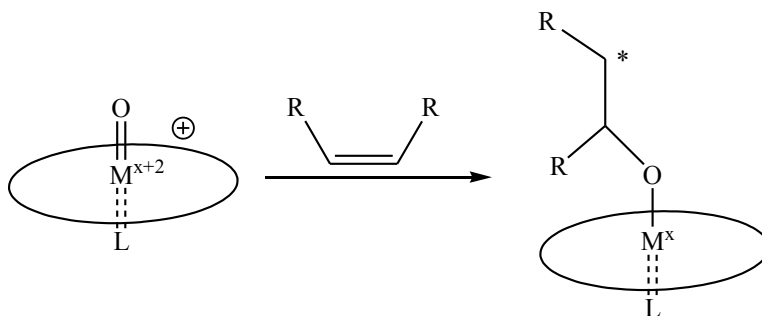
Figure 1.13 Redox mechanism of late transition metal catalyzed AE.

The mechanism of Jacobsen-Katsuki Mn-salen system has been a hot topic since it was firstly reported in 1990. It is all agreed that the active species, a O=Mn(V) oxo species, is first

formed, followed by adding the olefin. In contrast to the Sharpless AE process, the Mn-salen system does not require pre-coordination of the olefin to the metal center, hence unfunctional olefins can be efficiently and selectively oxidized.

It is found[38] that with various iodosylbenzene oxidants (PhIO, C_6H_5IO and MesIO) in Mn-salen AE system, the *cis/trans* ratio is dependent on the oxidant. It is suggested the oxidant is complexed with the Mn center, otherwise one single active species O=Mn(salen) would generate similar *cis/trans* ratio under this condition. It is also found[39] that the ligand counterions play a role in the determination of epoxide isomer: Mn-salen catalysts with ligating counterions such as Cl^- yield *trans* epoxide as the major products, while with nonligating counterions such as PF_6^- give *cis* epoxide as the major product in the epoxidation of *cis*-stilbene. The reason is thought to be the participation of different spin states of oxomanganese(V) salen intermediates and/or multiple active oxidants in oxygen transfer.

The electronic properties of the ligand directly correlate with the enantioselectivity in AE.[26,35] The complex bearing electron-donating group in salen ligand shows the highest *ee* values. It is proposed that the chiral selectivity is associated with the position of the transition state along the reaction coordinate. In the presence of electron-withdrawing group, a more reactive Mn oxo species is generated, which is added by an olefin in the early transition state and yield lower selectivity, while a less reactive oxo species is produced, which undergoes a late transition state and leads to higher selectivity. This is also clear evidence that the process reacts without substrate precoordination.

The steric character of the ligand[26,35] plays an important role in governing the trajectory of the side-on approaching of the olefin, and as a consequence the chiral induction, especially the substituents at the C_2 symmetric diimine bridge and bulky substituents at the 3,3'-positions. As

shown in Figure 1.14, in the presence of the non-planar five-membered chelating ring, comprising the ethylenediamine unit and the Mn(V)-ion, the olefin approaches the Mn center over the downwardly bent benzene ring of the salen ligand along one of the Mn-N bonds. Meanwhile the largest substituents of the alkenes is then pointing away from the 3,3'-substituents and this governs the stereochemical outcome of the reaction between the Mn(V)-oxo intermediate and the alkene.
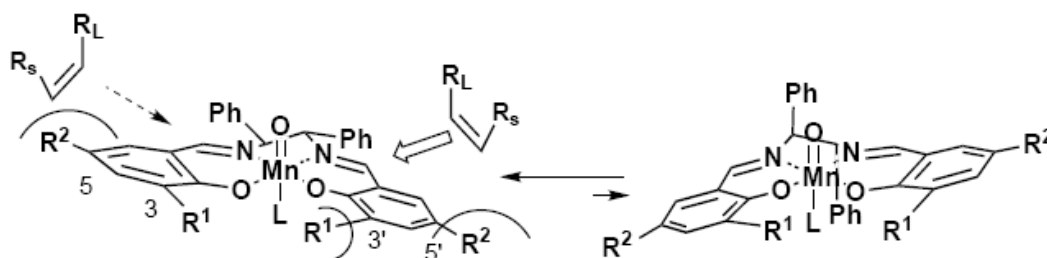
Figure 1.14 Model rationalizing the stereocontrol in Mn-salen epoxidation.[26]

1.4 Research Goals

Based on the information provided above, the following objectives are going to be reached.

Goal 1. To design and synthesize chiral transition metal complexes using chiral helix-directing salen ligands.The complexes will have helical structures and may possess greater activity in the AE of *trans*-alkenes. Both the metal center and its surrounding ligands in metal complexes are the crucial factor in the catalyst design.

A. Chiral helix-directing salen ligand

Salen ligands are widely used since they are easy to synthesize and handle, diverse in composition, and can be applied to a variety of reaction system. Both steric and electronic effects

need to be considered when designing the salen ligand. The steric factors include ligand size, flexibility and symmetry/chirality. The ligand size will not only determine the space around the metal center, but also influence the associate/dissociate equilibrium. Usually, the dissociation of the ligand transforms the metal complex to the active catalytic species. The ligand flexibility can determine the ligand geometry and the coordination state in the catalytic cycle. And the symmetry/chirality of ligand can influence the selectivity (both stereo and enantio) of product by governing the trajectories of incoming olefins. Considering overlapping between π orbital of substrate and d orbital of metal center of a helical complex, and easy access to the active center, the side-on approaching from e is the most feasible in metal (Figure 1.15).
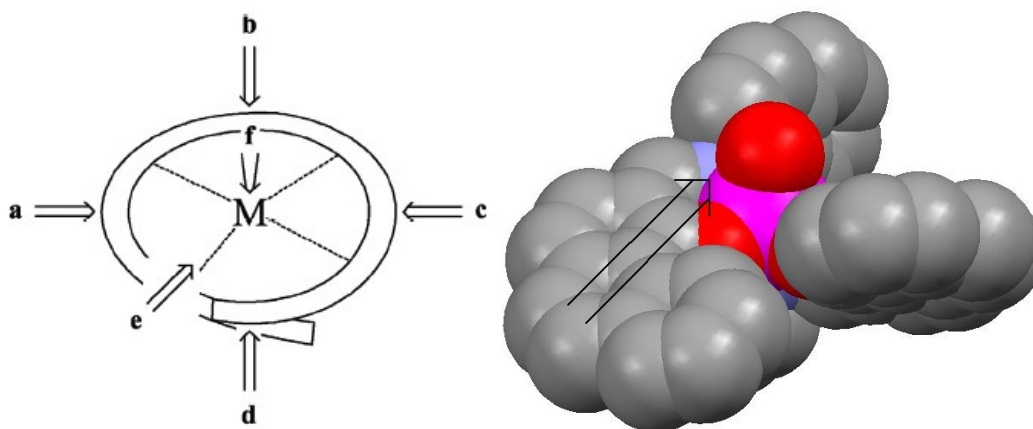
Figure 1.15 Possible trajectories for the approach of the substrate to the metal center of a helical complex[40] (left) and a O=Mn(salen) model, which is created using coordination of 12 (right).

Anionic phenoxide donors such as those incorporate within salen complexes are useful for the oxidation, since readily stable intermediates with high valence can be generated. The electronic character of the ligand is closely associated with the catalytic enantioselectivity in AE. It is found[26] that transition metal complexes bearing electron-donating group on the salen ligand

show higher *ee* values compared to that with electron-withdrawing substituentes. The reason is proposed to be the different reactivity of metal oxo intermediate generated during the reaction.

In our group, some novel chiral helix-directing salen ligands (Figure 1.16) have been already developed. The N_2O_2 donor set is suitable for complexation of a variety of transition metals in various pattens (Figure 1.17).[40,41,42] In addition, some transition metal salen complexes are found to be effective catalyst in AE.[2,8] Two distinct chiral diamine backbones (cyclohexyl and binaphthyl) will not only introduce the chirality, but also provide a highly twisted shape to the ligand, making helix formation possible after metallation. The chirality of the diamine bridge is assumed to be transmitted to the two salicylidene rings only upon formation of the putative species, leading to significant chiral distortion for effective stereochemical communication. Two extended fused phenyl rings are applied as sidearms (benz[a]anthryl and phenanthryl). They are rigid, planar and show low steric bulkiness so that they can wrap around one metal center. Furthermore, the extended sidearms will overlap after metallation, to help to lock the configuration, which will facilitate the selectivity in the reaction.

H₂S1

H₂S2

H₂S3

H₂S4
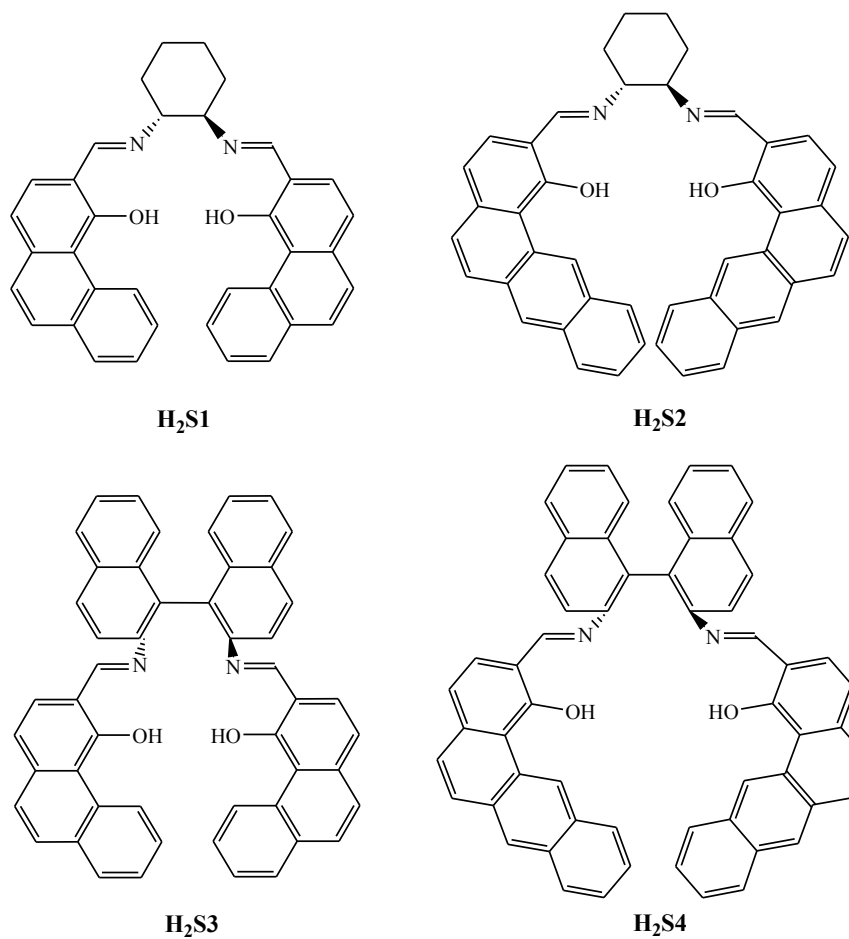
Figure 1.16 Schemic structures of chiral helix-directing salen ligands.
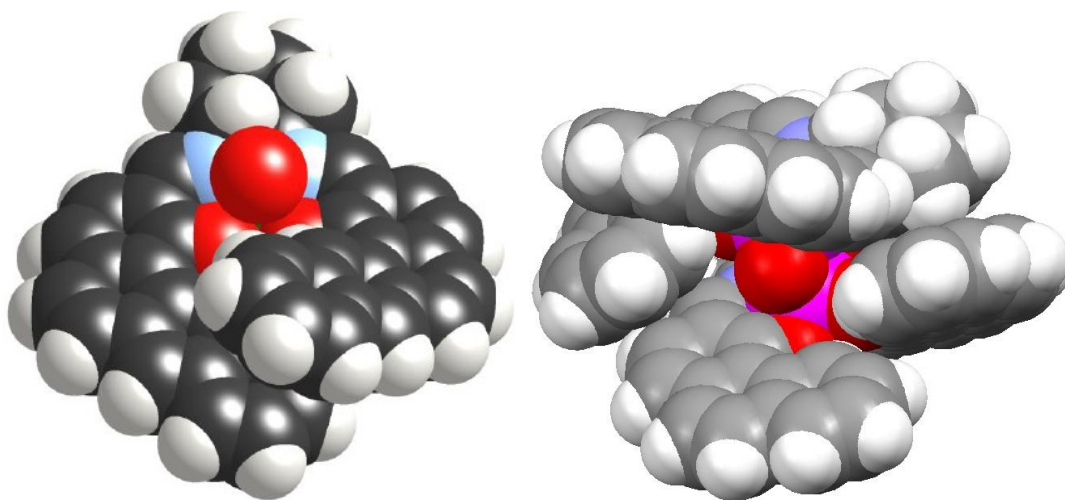
Figure 1.17 Examples of metal complexes chelated by our chiral helix-directing ligands. Left, O=V(S2); right, (μ-O)₂-[Mn(S1)]₂.

B.Transition metal centers

The metal ion is another key factor in catalysis. Manganese and titanium salen complexes have proved to be good catalyst in AE. However, all manganese complexes are paramagnetic and difficult to characterize by NMR. They are also air/moisture sensitive. Manganese generally prefers octahedral coordination, and Mn(III) complexes usually show a significant Jahn-Taller elongation. In this work, manganese(II) salts (MnCl$_2$, Mn(NO$_3$)$_2$ and Mn(OAc)$_2$) are chosen as the metal source in the complexation since they are easy to handle and readily oxidize to the 3+ state to produce catalyst precursors. And the anions from metal precursor may also participate in complexation when the metal has a 3+ or higher oxidation state in metal-salen complexes. Both the ligating ability and electronic features of counterions need to be considered in the catalytic design, since they may affect the activity and selectivity of reactive species during catalysis. Titanium is an early transition metal and d^0 nature of Ti(IV) makes it suitable for NMR characterization. In this thesis, two titanium(IV) salts are employed (TiCl$_4$ and Ti(O-^{i}Pr)$_4$) since they are readily available and easily react with ligand. The effect of anions will also be observed in the complexation and catalytic reactions. Since late and early transition metal complexes may carry out different mechanisms during AE, the choice of manganese (late TM) and titanium (early TM) may help us to better understand the distinct catalytic ways.

Goal 2. To examine the catalytic activity of helical complexes in asymmetric epoxidation.

As mentioned before, *trans*-olefin is a difficult target in AE due to the steric hinderance between the substrate and active species when the substrate is approaching the active species (Figure 1.18). To avoid this problem, the shape of active species must be deeply stepped. A helical shape provides this structure. In addition, the helix is a highly asymmetric shape, which

can help the chiral induction, and may increase the activity due to the unique shape of corresponding active species.
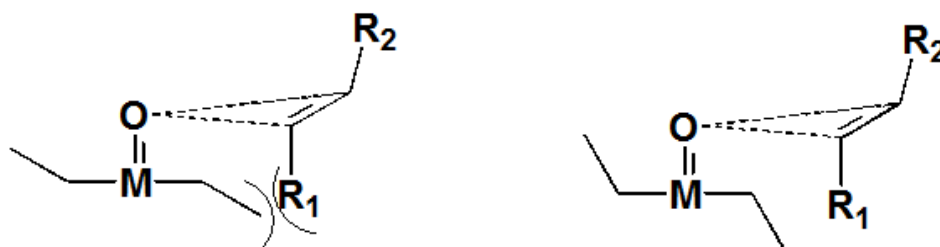
Figure 1.18 *trans*-alkene approaching the active species of Mn-salen catalyst.

Furthermore, the effects of metal precursor and various oxidants will also be tested, especially those green oxidants such as aqueous H_2O_2, as well as the optimization of reaction conditions.

Besides the AE reaction of *trans*-alkene, other substrates (*cis*- and unfunctoinalized alkene) and other oxidations may also be tried, to test the limitation of catalyst usage.

Goal 3. To facilitate the understanding of the mechanic process in catalysis.

The mechanism study involved in AE can not only improve the catalysis technology, but also advance the fundamental knowledge in the area of chemical and biological system. Computational chemistry is a good strategy in the study of mechanism. Some quantum calculations have already been done in our lab to predict the solution conformation of some zinc and iron salen complexes.[42] Based on the direct experimental observation, the DFT calculation (ADF) of simulated the CD spectra and confirmed the *P/M* assignment.
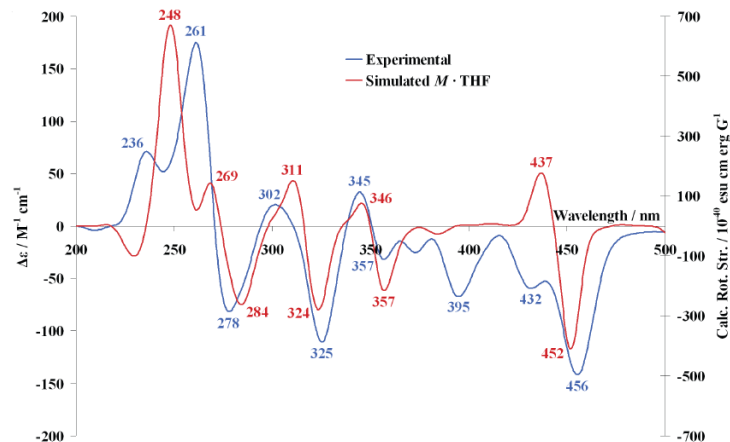
Figure 1.19 Simulated and experimental CD spectra of *M*-Zn(salen) complex.[42]

Such computation will predict/characterize the reaction intermediate (electronic configuration, geometries and spin state, etc), profile energies barriers between transition states, and explore individual steps in the catalytic cycle.

1.5 References

1. (a). Lewis, D. F. V. Guide to cytochromes P450: structure and function. Taylor&Francis, London, 2001 (b).Schiff, H. About some reactions of the aminde oximes. Justus Liebigs Annalen der Chemie 1902, 321, 357-371.

2. Katsuki, T. Unique asymmetric catalysis of cis-β metal complexes of salen and its related Schiff-base ligand. Chem. Soc. Rev. 2004, 33, 437-445.

3. Sheldon, R. A.; Kochi, J. K. Metal-catalyzed oxidations of organic compounds; Acedemic Press, London, 1981.

4. Rothenberg, G. Catalysis, Wiley-VCH, Weinheim, 2008.

5. Katsuki, T. Chiral metallosalen complexes: structure and catalyst tuning for asymmetric epoxidation and cyclopropanation. *Adv. Synth. Catal.* **2002**, 344, 131-147.

6. Tokunage, M., Larrow, J. F., Kakiuchi, F., Jacobsen, E. N. Asymmetric catalysis with water; efficient kinetic resolution of terminal epoxides by means of catalytic hydrolysis. *Science*, **1997**, 277, 936-938.

7. Katsuki, T. Catalytic asymmetric oxidation using optically active (salen)manganese(III) complexes as catalysts. *Coord. Chem. Rev.* **1995**, 140, 189-214.

8. Konsler, R. G., Karl, J., Jacobsen, E. N. Cooperative asymmetric catalytic with dimeric salen complexes. *J. Am. Chem. Soc.* **1998**, 120, 10780-10781.

9. Uchida, T., Irie, R., Katsuki, T. cis- and enantio-selective cyclopropanation with chiral (ON+)Ru-salen complexes as a catalyst. *Tetrahedron*, **2000**, 56, 3501-3509.

10. Belokon, Y. N., Green, B., Ikonnikov, N. S., North, M., Parsons, T., Tararov, V. I. Optimized catalysts for the asymmetric addition of trimethylsilyl cyanide to aldehydes and ketones. *Tetrahedron*, **2001**, 57, 771-779.

11. Belokon, Y. N., North, M.; Parsons, T. Vanadium-catalyzed asymmetric cyanohydrin synthesis. *Org, Lett.* **2000**, 2, 1617-1619.

12. Belokon, Y. N., North, M., Churkina, T. D.; Ikonnikov, N. S. Maleev, V. I. Chiral salen-metal complexes as novel catalyst for the asymmetric synthesis of α–amino acids under phase transfer catalysis conditions. *Tetrahedron*, **2001**, 57, 2491-2498.

13. Kight, P. D., Scott, P. Predetermination of chirality at octahedral centers with tetradentate ligands: prospects for enantioselective catalysis. *Coordin. Chem. Rev.* **2003**, 242, 125-143.

14. Lalehzari, A., Desper, J., Levy, C. J. Double-stranded monohelical complexes from an unsymmetrical chiral schiff-base ligand. *Inorg. Chem.* **2008**, 47, 1120-1126.

15. Garcia-Deibe, A. M., Sanmartin, M., Matalobos, J., Fondo, M., Vazquez, M., Bermejo, M. R. Conformational studies on complexes of a diimine containing a $(CH_2)_2$ spacer: crystal

structure of a double-stranded Zn(II) *meso*-helicate and an enantiopure Δ–Cu(II) monohelicate. *Inorg. Chimica Acta* **2004**, 357, 2561-2569.

16. Vazquez, M., Bermejo, M. R., Fondo, M., Garcia-Deibe, A. M., Sanmartin, J., Pedrido, R., Sorace, L., Gatteschi, D. Monohelical complexes of a novel asymmetric N_4 Schiff base: unfamiliar tetrahedral environments of manganese(II) and iron(II) helicates. *Eurp. J. Inorg, Chem.* **2003**, 1128-1135.

17. Constable, E. C., Chotalia, R., Tocher, T. A. The first example of a mono-helical complex of 2,2':6',2'':6'',2''':6''',2'''':6'''',2'''''-sexipyridine: preparation, crystal and molecular structure of bis(nitrato-*O,O*')(2,2':6',2'':6'',2''':6''',2'''':6'''',2'''''-sexipyridine)europium(III) nitrate. *J. Chem. Soc. Chem. Comm.* **1992**, 771-773.

18. Bell, T. W., Jousselin, H. Self-assembly of a double-helical complex of sodium. *Nature* **1994**, 367, 441-444.

19. Kawamoto, T., Kushi, Y. Synthesis and characterization of trinuclear metal complex showing helical chirality. *Chem. Lett.* **1992**, 2, 297-300.

20. Naskar, S., Naskar, S., Butcher, R. J., Chattopadhyay, S. K. Synthesis, X-ray crystal structures and spectroscopic properties of two Ni(III) complexes of pyridoxal Schiff's bases with diamines: importance of steric factor in stabilization of water helices in the lattices of metal complex. *Inorg. Chimi. Acta.* **2010**, 363, 404-411.

21. Anastas, P. T., Heine, L. G., Williamson, T. C. (Eds.) *Green Chemical Synthesis and Processes*, **2000**, American Society, Washington DC.

22. Rothenberg, G. *Catalysis*, **2008**, Wiley-VCH, Weinheim.

23. http://www.mrw.interscience.wiley.com/kirk/ Kirk-othmer Encyclopedia of Chemical Technology, John Wiley&Sons, New York, 2006.

24.   http://www.mrw.interscience.wiley.com/ueic   Ulmann's   Encyclopedia   of   Industrial

Chemistry, Verlag Chemie, Weinheim.

25. Katsuki, T., Sharpless, K. B. The first practical method for asymmetric epoxidation. *J. Am.*
     Chem. Soc. **1980**, 102, 5974-5976.

26. Bachvall, J. E. (Ed.) *Modern oxidation methods*, **2004**, Wiley-VCH, Weinheim

27. Grove, J. T., Nemo, T. E., Myers, R. S. Hydroxylation and epoxidation catalyzed by iron-
     porphine complexes. Oxygen transfer from iodosylbenzene. *J. Am. Chem. Soc.* **1979**, 101,
     1032-1033.

28. Zhang, W., Loebach, J. L., Wilson, S. R., Jacobsen, E. N. Enantioselective epoxidation of
     unfunctionalized olefins catalyzed by salen manganese complexes. *J. Am. Chem. Soc.* **1990**,
     112, 2801-2803.

29. Punniyamurthy, T., Velusamy, S., Iqbal, J. Recent advances in transition metal catalyzed
     oxidation of organic substrates with molecular oxygen. *Chem. Rev.* **2005**, 105, 2329-2363.

30. Grigoropoulou, G., Clark, J. H., Elings, J. A. Recent development on the epoxidation of
     alkenes using hydrogen peroxide as an oxidant. *Green Chem.* **2003**, 5, 1-7.

31. Irie, R., Noda, K., Ito, Y., Matsumoto, N., Katsuki, T. Catalytic asymmetric epoxidation of
     unfunctionalized olefins. *Tetrahedral Lett.* **1990**, 31, 7345-7348.

32. Berkessel, A., Frauenkron, M., Schwenkreis, T., Steinmetz, A., Baum, G., Fenske, D.
     Pentacoordinated manganese(III) dihydrosalen complexes as biomimetic oxidation catalyst.
     J. Mol. Catal. A: Chem. **1996**, 113, 321-342.

33. Ito, Y., Katsuki, T. What is the origin of highly asymmetric induction by a chiral
     (salen)manganese(III) complex? Design of a conformationally fixed complex and its

application to asymmetric epoxidation of 2,2-dimethylchromenes. *Tetrahedral Lett.* **1998**, 39, 43254328.

34. Sawade, Y., Matsumoto, K., Kondo, S., Watanabe, H., Ozawa, T., Suzuki, K., Saito, B., Katsuki, T. Titanium-salan-catalyzed asymmetric epoxidation with aqueous hydrogen peroxide as the oxidant. *Angew. Chem. Int. Ed.* **2006**, 45, 3478-3480.

35. Oyama, S. T. (Ed.) *Mechanisms in Homogeneous and Heterogeneous Epoxidation catalysis*, **2008**, Elsevier, Oxford, UK

36. Woodard, S. S., Finn, M. G., Sharpless, K. B. Mechanism of asymmetric epoxidation. 1. kinetics. *J. Am. Chem. Soc.* **1991**, 113, 106-113.

37. Finn, M. G., Sharpless, K. B. Mechanism of asymmetric epoxidation. 2. catalyst structure. *J. Am. Chem. Soc.* **1991**, 113, 113-126.

38. Collman, J. P., Zeng, L., Brauman, J. I. Donor ligand effect on the nature of the oxygenating species in MnIII(salen)-catalyzed epoxidation of olefins: experimental evidence for multiple active oxidants. *Inorg. Chem.* **2004**, 43, 2672-2679.

39. Adam, W., Roschmann, K. J., Saha-Moller, C. R., Seebach, D. *cis*-stilbene and (1α,2β,3α)-(2-ethenyl-3-methoxycyclopropyl)benzene as mechanistic probes in the MnIII(salen)-catalyzed epoxidation: influence of the oxygen source and the counterion on the diastereoselectivity of the competitive concerted and radical-type oxygen transfer. *J. Am. Chem. Soc.* **2002**, 124, 5068-5073.

40. Wiznycia, A. V., Desper, J., Levy, C. J. Iron(II) and zinc(II) monohelical binaphthyl-salen complexes with overlapping benz[a]anthryl sidearms. *Dalton Transactions* **2007**, 15, 1520-1527.

41. Wiznycia, A. V., Desper, J., Levy, C. J. Monohelical iron(II) and zine(II) complexes of a (1R,2R)-cyclohexyl salen ligand with benz[a]anthryl sidearms. *Inorg. Chem.* **2006**, 45, 10034-10036.

42. Wiznycia, A. V., Desper, J., Levy, C. J. Iron(II) and zinc(II) monohelical binaphthyl salen complexes. *Chem. Comm.* **2005**, 37, 4693-4695.

Chapter 2 - Synthesis, characterization and study of titanium(salen) complexes

2.1 Introduction

Titanium salen complexes are some of the most versatile Lewis acid catalysts, used in a wide range of reactions, such as ring-opening of epoxidations,[1] Diels-Alder reactions,[2] sulfoxidations,[3] addition of cyanides to aldehydes/ketones,[4] etc. These titanium salen complexes can be monometallic[5], homobimetallic[2,3] or heterobimetallic.[6] One reason for Ti(salen) complexes as potential catalysts is that the N_2O_2 donor groups of salen ligands can wrap around a Ti center to afford a variety of geometries.[3] Furthermore, use of chiral ligands can lead to the preferred formation of 'chiral-at-Ti' complexes. All these are of great potential interest for enantioselective catalysis. Currently, the mechanisms of these catalysts are uncertain and under debate, due to the lack of structural models for reasonable catalyst intermediates.

2.2 Synthesis of Ti(salen) complexes

The synthesis of Ti(salen) complexes is straightforward (Figure 2.1). Solutions of salen ligands (**S1-S4**) in anhydrous CH_2Cl_2 are metallated with equimolar $TiCl_4$ to afford the dark red crystalline complexes **1-4** [Ti(salen)Cl$_2$]. The yield is between 70-90%. No added base is needed to deprotonate the phenol groups. The unreacted ligands and $TiCl_4$ salt are washed away by hexane due to the low solubility of the complexes in hexane. The reactions are easily monitored by an immediate color change from bright yellow/orange to dark brown upon adding $TiCl_4$ to the ligand solution. The ^1H NMR spectra indicate that the products are of high purity.
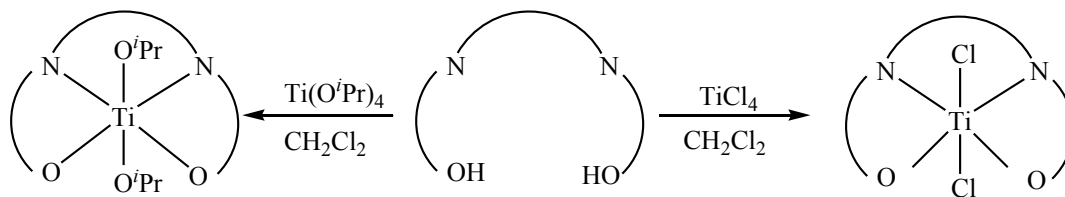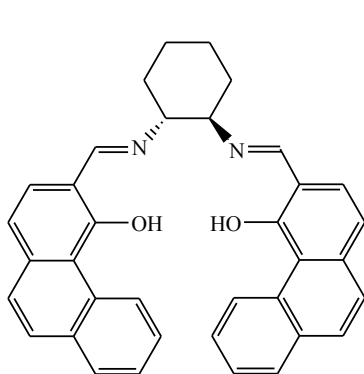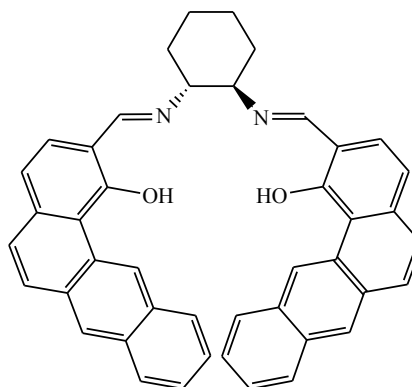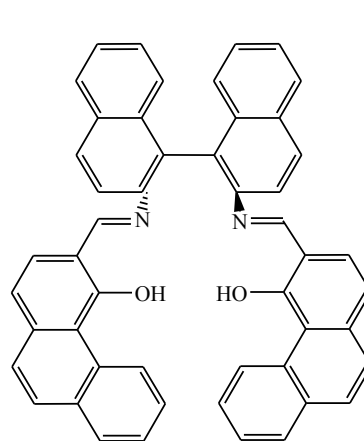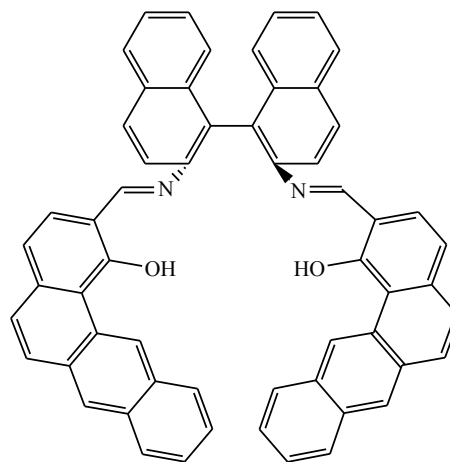
Figure 2.1 Synthesis of Ti(salen) complexes 1-8.

H₂S1: 3,3'-[(1*R*,2*R*)-1,2-cyclohexanediylbis(nitrilomethylidyne)]bis-4-phenanthrenol
H₂S2: 2,2'-[(1*R*,2*R*)-1,2-cyclohexanediylbis(nitrilomethylidyne)]bis(benz[a]anthracen-1-ol)
H₂S3; 3,3'-[(*R*)-[1,1'-binaphthalene]-2,2'-diylbis(nitrilomethylidyne)]bis-4-phenanthrenol
H₂S4: 2,2'-[(R)-[1,1'-binaphthalene]-2,2'-diylbis(nitrilomethylidyne)]bis(benz[a]anthracen-1-ol)

In a similar process complexes **5-8** [Ti(salen)(O^{i}Pr)$_2$] are synthesized by the dropwise addition of a solution of Ti(O^{i}Pr)$_4$ to an equimolar amount of salen ligand (**H$_2$S**) in CH$_2$Cl$_2$. The products are purified by decanting with diethyl ether and diethyl ether/hexane (1:1) mixture, in order to remove unreacted Ti(O^{i}Pr)$_4$ and ligands. The yield of greenish yellow powders is 65-82%.

These new complexes **1-8** were characterized by UV/vis, IR and NMR, as well as mass spectrometry and single crystal XRD. All these complexes are soluble in most organic solvents and are extremely sensitive to moisture; therefore inert conditions must be employed.

2.3 Electronic and infrared spectra
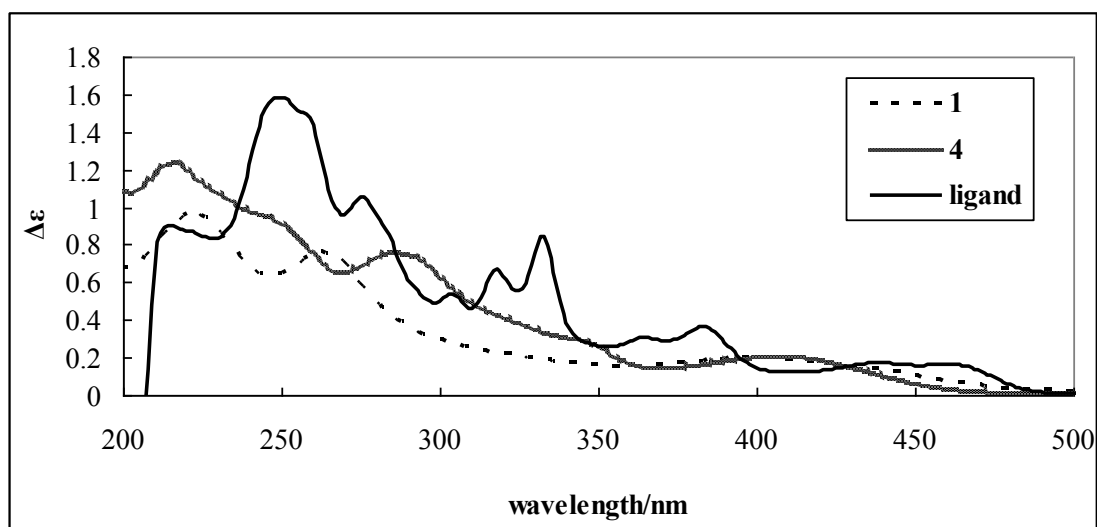
Figure 2.2 UV-vis spectrum of complex 1 (dashed), 5 (wavy) and free ligand H$_2$S1 (solid).

The UV-vis spectra of all complexes (**1-8**) in CH$_3$CN show a single band in the region of 410-390 nm, which is assigned to the π-π* charge transfer band and is in accordance with a $3d^04s^0$ electronic configuration since no *d-d* transition would occur.[7] One more band is observed

37

at 290-270 nm for salen-TiCl$_4$ and 310-300 nm for salen-Ti(O^{i}Pr)$_4$, which may be due to intraligand transitions.[7]

The characteristic IR bands of complex **1-8** are summarized in Table 2.1. Compared to the free ligands, the red shift in the position of v(C=N) in the corresponding complexes indicates the coordination of imine N to the Ti metal ion. Furthermore, the phenoxo v(C-O) bands are blue shifted in the corresponding complexes, which indicates the coordination of phenol O to the metal center (Figure 2.3.). In addition, the observation of a pair of bands around 740 and 620 cm$^-$^{1} indicates the presence of Ti-(μ-O)$_2$ groups in complexes **5-8** (Table 2.2). [7,8,9]
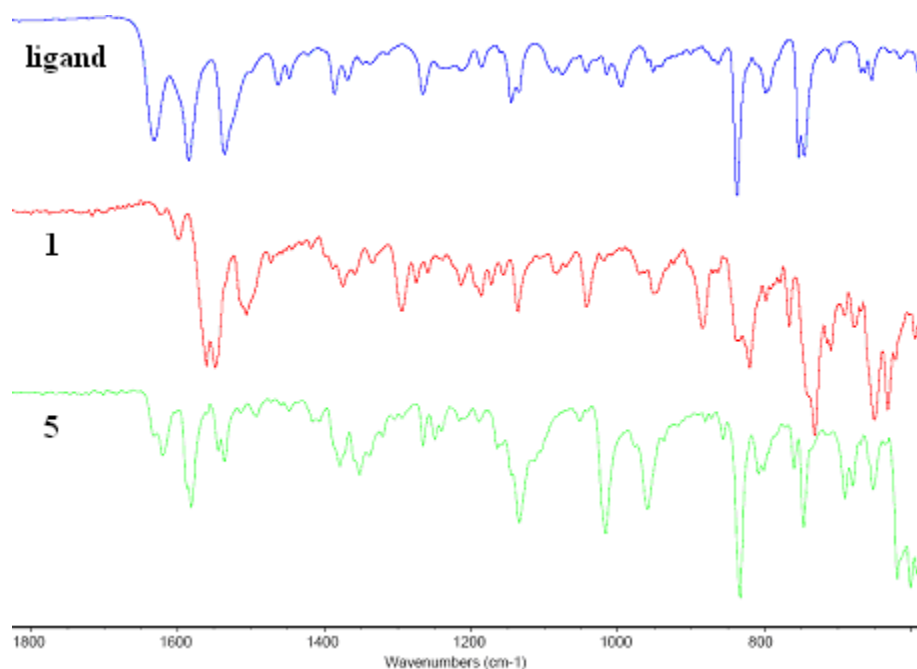
Figure 2.3 IR spectra of free ligand H$_2$S1 (blue), complexes 1 (red) and 5 (green).

The characteristic bands derived from the aromatic region in the salen ligand and in the complex are very complicated, and most are in the fingerprint region and very hard to assign. Thus, the spectra suggest that salen ligands have complexed to Ti by coordination through imine nitrogens

and phenoxy oxygens, and dioxo bridges may also form in complexes **5-8**. The spectral properties of complexes are also consistent with other six-coordinate Ti-salen complexes. [7,8,9]

Table 2.1 Characteristic IR bands for salens S1-S4 and Ti(salen) complexes 1-8.

compound	v(C=N)/cm^{-1}	v(C-O)/cm^{-1}
S1	1632	1265
1 [Ti(S1)Cl$_2$]	1600	1287
5 [Ti(S1)(O^{i}Pr)$_2$]	1623	1266
S2	1635	1262
2 [Ti(S2)Cl$_2$]	1628	1291
6 [Ti(S2)(O^{i}Pr)$_2$]	1616	1303
S3	1627	1295
3 [Ti(S3)Cl$_2$]	1619	1322
7 [Ti(S3)(O^{i}Pr)$_2$]	1607	1334
S4	1595	1302
4 [Ti(S4)Cl$_2$]	1596	1301
8 [Ti(S4)(O^{i}Pr)$_2$]	1564	1307

Table 2.2 IR bands for Ti-(μ-O)$_2$ vibration in complexes 5-8.

complex	**5**	**6**	**7**	**8**
v(Ti-(μ-O)$_2$)/cm^{-1}	744, 617	741, 630	741, 616	744, 628

2.4 Mass spectra analysis

The mass spectra of complexes (**1-8**) provided valuble information concerning their compositions and structures. The spectra are obtained from two different methods: low-resolution-ESI-MS in CH$_2$Cl$_2$ and high-resolution-ESI-MS in methanol. Structural information

can be provided from the mass peaks in the molecular ion cluster and from the isotope patterns which are matched to those calculated for particular chemical compositions.

2.4.1 Complexes 1-4, Ti(salen)Cl$_2$

The mass spectra of the Ti(salen)Cl$_2$ complexes **1-4** are highly sensitive to the methods used to ionize the sample. In CH$_2$Cl$_2$ solutions, the mass spectra clearly show the molecular ion peaks for the [Ti(salen)Cl]$^+$ species except for complex **1**. While the spectra recorded from HR-ESI-MS in MeOH solution show the high-intensity peaks corresponding to [Ti(salen)(OMe)]$^+$ species. These results agree with Katsuki's[10] and Belokon's[6] work on the method-dependence of the structure of Ti(salen) complexes. The bimetallic species [(salen)Ti(μ-O)(μ-OMe)Ti(salen)]$^+$ is also observed for complex **1** by HR-MS (*m/z* = 1183.3378, calc. 1183.3394, 1.4 ppm), while not in the complexes **2-4** since the masses for the dimeric species were beyond the measurement limits of the instrument. The mass spectra also illustrate the presence of fragments of free ligand below *m/z* = 550.
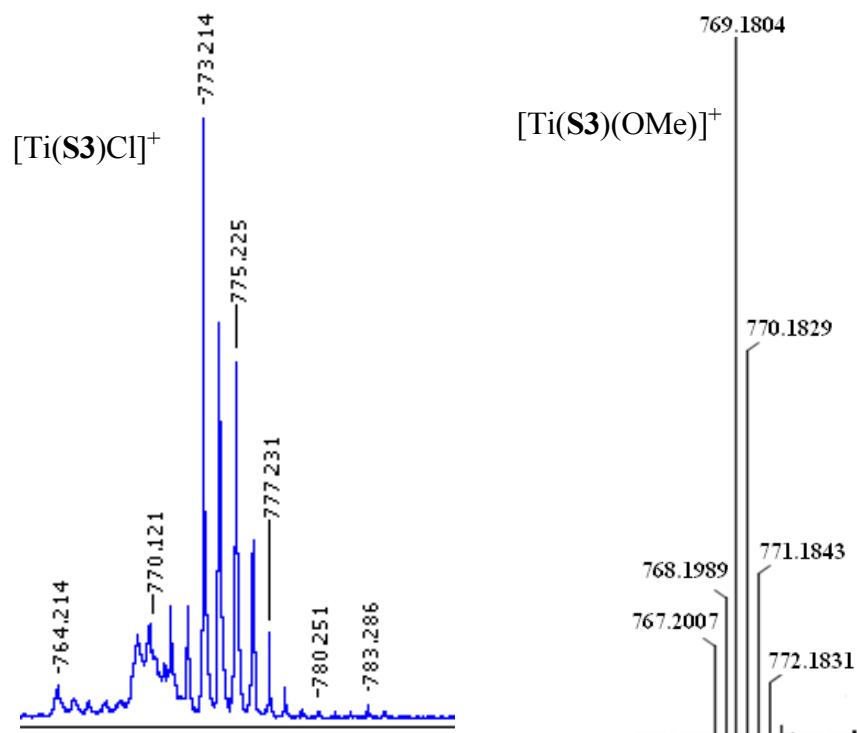
Figure 2.4 Isotopic patterns of [Ti(S3)Cl]$^+$ by LR-ESI-MS in CH$_2$Cl$_2$ (left) and [Ti(S3)(OMe)]$^+$ by HR-ESI-MS in MeOH (right) of complex 3.

Table 2.3 Common species detected in mass spectra of Ti(salen)Cl$_2$ complexes 1-4.

$$[Ti(salen)(OMe)]^+ \xleftarrow{MeOH} Ti(salen)Cl_2 \xrightarrow{CH_2Cl_2} [Ti(salen)Cl]^+$$

Ti(salen)Cl$_2$ complex	*m/z* of observed ion cluster	
	[Ti(salen)Cl]$^+$ species ionized from CH$_2$Cl$_2$	[(salen)Ti(OMe)]$^+$ species ionized from MeOH
1	---	599.1810, calc. 599.1814, 0.7 ppm
2	703	699.2112, calc. 699.2127, 2.1 ppm
3	773	769.1985, calc. 769.1971, 1.8 ppm
4	873	869.2278, calc. 869.2284, 0.7 ppm

2.4.2 Complexes 5-8 Ti(salen)(O^{i}Pr)$_2$

Ti(salen) complexes **5-8** synthesized from the Ti(O^{i}Pr)$_4$ precursor give good and distinct mass spectrometric results using both methods, but all these spectra are different from those of Ti(salen)Cl$_2$. In the CH$_2$Cl$_2$ sample, the signals indicate the presence of the mononuclear species [Ti(salen)(OH)]$^+$ and [Ti(salen)(O^{i}Pr)]$^+$. Besides these main peaks, those corresponding to the possible dimeric species are also visible, due to the high *m/z* value, but are not able to be assigned. The mass peaks below *m/z* = 500 clearly indicates the fragment of free ligands.
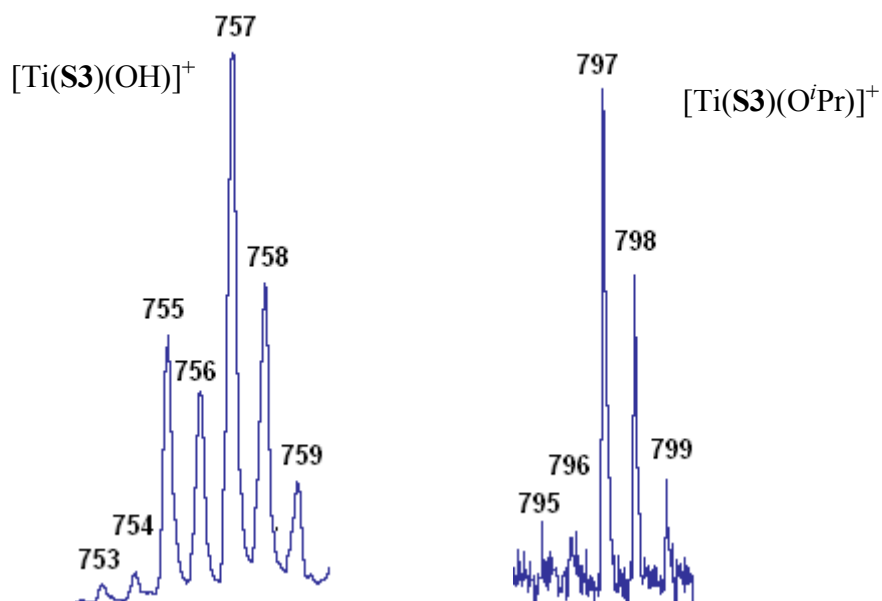
Figure 2.5 Isotopic patterns of [Ti(S3)(OH)]$^+$ and [Ti(S3)(O^{i}Pr)]$^+$ by LR-ESI-MS in CH$_2$Cl$_2$ (left) of complex 7.

In the spectra recorded from methanol solution (Figure 2.6), both methoxo mononuclear [Ti(salen)(OMe)]$^+$ and dimeric [(salen)Ti(μ-O)(μ-OMe)Ti(salen)]$^+$ species are clearly identified, suggesting that conversion of the di-μ-oxo complex to a monomeric Ti(salen) complex occurs smoothly in methanol. The relative intensities of these two species are comparable in complexes **5** and **6**, while the relative intensities of monomer are much higher than those of dimer in

complexes **7** and **8** (Table 2.4.). Comparison of the above data shows that in all titanium(salen) complexes, the methoxylated monotitanium species $[Ti(salen)(OMe)]^+$ is always the major species present when ionized in methanol, and the methoxy dimeric Ti species is also seen in the case of $Ti(salen)(O^iPr)_2$.
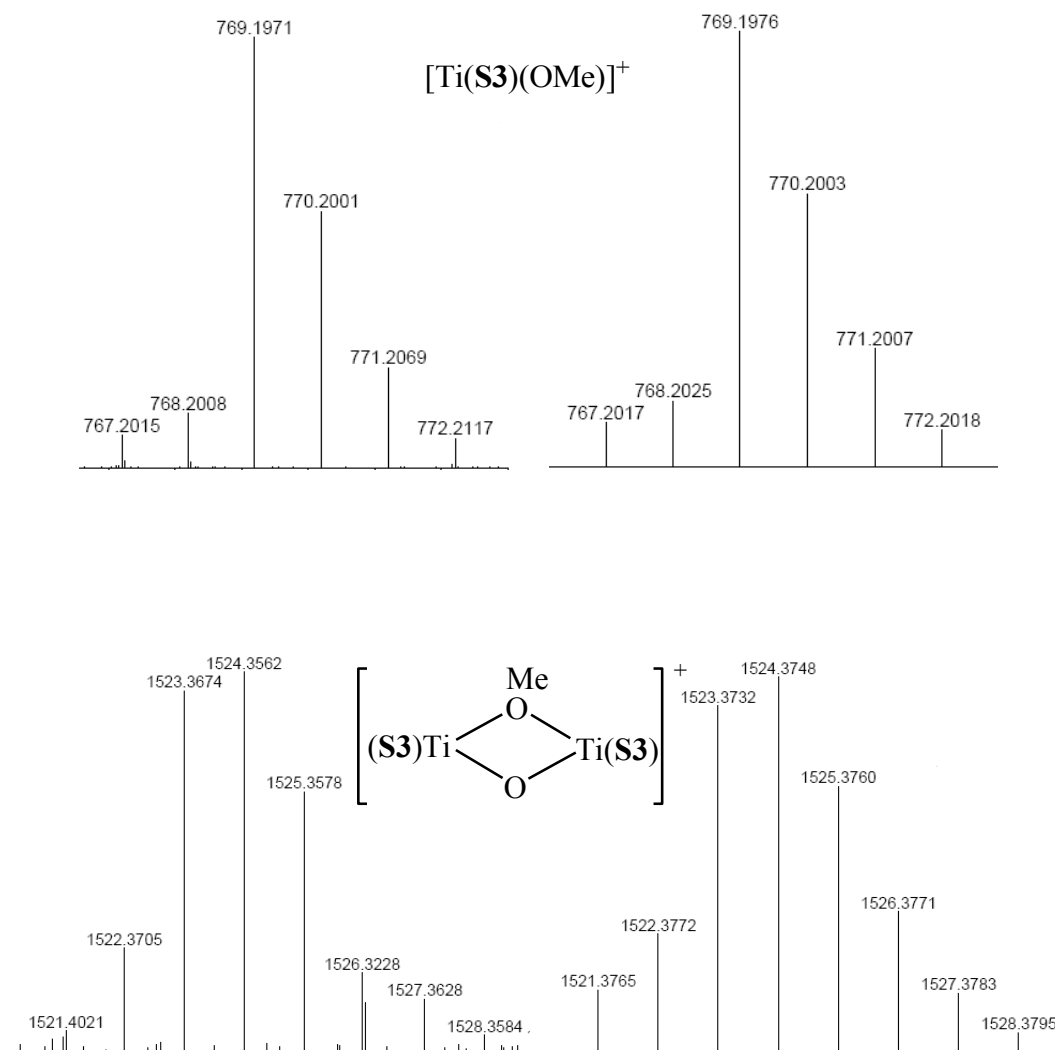
Figure 2.6 Experimental (left) and simulated (right) isotopic patterns of [Ti(S3)(OMe)]$^+$ and [(S3)Ti(μ-O)(μ-OMe)Ti(S3)]$^+$ by HR-ESI-MS in MeOH of complex 7.

This is consistent with Katsuki's work[10] on the solvent dependence of the structure of Ti(salen)O complex. Complexes **1-8** also exhibit the presence of molecular ions ([M-Cl/O^{i}Pr]$^+$, M indicates

Ti(salen)Cl$_2$ or Ti(salen)(O^{i}Pr)$_2$) in dichloromethane solution, indicating the CH$_2$Cl$_2$ solvent has no effect on the ionization.

Table 2.4 Common speices detected in the mass spectra of Ti(salen)(O^{i}Pr)$_2$ complexes.

$$\left[(salen)Ti \diagdown \begin{smallmatrix} Me \\ O \\ \\ O \end{smallmatrix} \diagup Ti(salen) \right]^+ , [Ti(salen)(OMe)]^+$$

$\uparrow$ MeOH

Ti(salen)(O^{i}Pr)$_2$

$\downarrow$ CH$_2$Cl$_2$

[Ti(salen)(OH)]$^+$, [Ti(salen)(O^{i}Pr)]$^+$
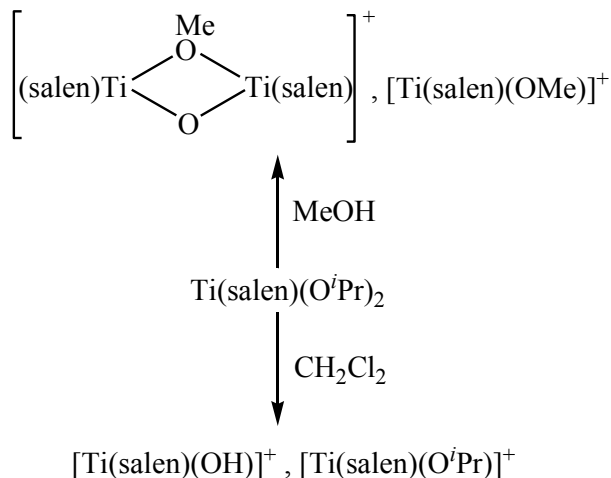
Ti(S)(O^{i}Pr)$_2$ Complex	*m/z* of observed ion clusters	
	[Ti(S)(OH)]$^+$, [Ti(S)(O^{i}Pr)]$^+$ ionized from CH$_2$Cl$_2$	[Ti(S)(OMe)]$^+$ and dimer ionized in MeOH
5	585, 627	599.1804 (calc. 599.1814, 1.7 ppm), 1183.3368 (calc. 1183.3394, 2.2 ppm)
6	685, 727	699.2104 (calc. 699.2127, 3.3 ppm), 1383.3951 (calc. 1383.4020, 5.0 ppm)
7	755, 797	769.1971 (calc. 769.1971, 0.0 ppm), 1523.3674, (calc.1523.3707, 2.2 ppm)
8	855, 897	869.2292 (calc. 869.2284, 0.9 ppm), 1723.4363 (calc. 1723.4333, 5.6 ppm)

2.4.3 Doubly charged polymeric species derived from complexes coordinated with ligands bearing the cyclohexyl backbone

Besides those signals for singly charged species, more than one doubly charged polymeric species are observed in complexes **1**, **2**, **5** and **6** by HR-MS (Figure 2.7, Table 2.5). No evidence for the formation of such species is detected in complexes **3**, **4**, **7** and **8**, since none of the isotope peaks occurred at half-integer spacing.

The three polymeric species from complex **1** are identical to those seen for complex **5**, while the only species from complex **2** is also the same as one of the three from **6**. In these doubly charged polymers, tri-titanium species are the most abundant in all cases. The quatra-titanium oligomers are the least abundant in complexes **1** and **5** with same salen ligands. Belokon[6] has isolated a trinuclear titanium(salen) complex, in which each Ti ion is coordinated by a salen ligand and linked by oxo groups. It is proposed that the nature of the backbone may play an important role in the unique ionization pathway. The binaphthyl backbone is more rigid and sterically demanding than the cyclohexyl backbone. The Ti-coordinate salen ligands have to adjust their conformation/structure, in order to facilitate the formation of such polymeric species. The metal precursor may have little effect on the ionization, since no difference is found between **1**, **2** (using $TiCl_4$ as precursor) and **5** and **6** (using $Ti(O^iPr)_4$ as precursor). Furthermore, the π-π* stacking effect from the sidearms may influence the population of each species, such as di-Ti(salen) species is the least abundant in complex **6**, but the quasi-Ti(salen) one is the least abundant in complex **5**.
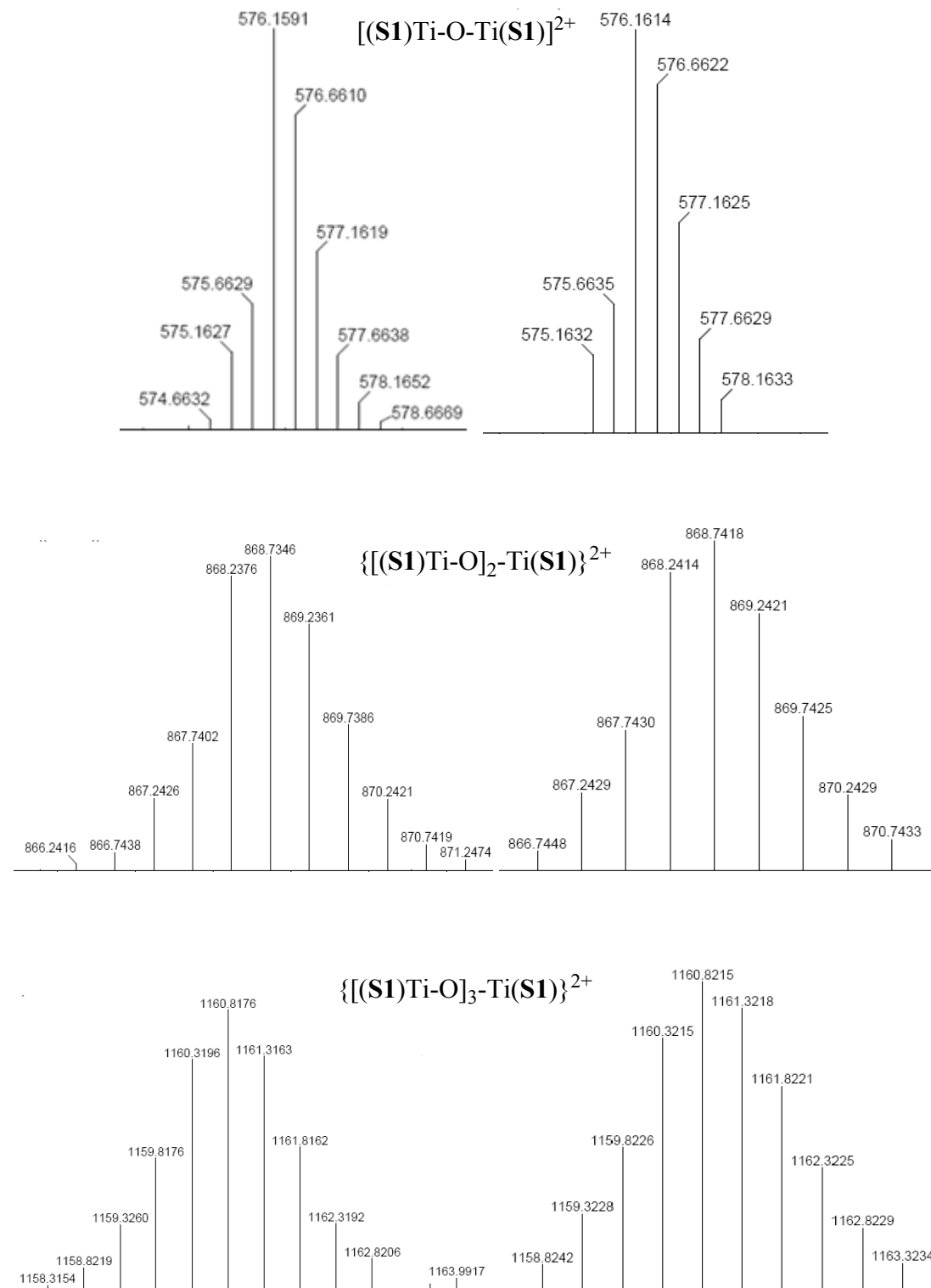
Figure 2.7 Experimental (left) and simulated (right) isotopic patterns of polymeric species of complex 5 obtained from HR-MS in MeOH solution.

Table 2.5 Doubly charged species from complexes 1, 2, 5 and 6 by HR-ESI-MS.

Complex	m/z of observed ion clusters $\{[Ti(salen)-O-]_n-Ti(Salen)\}^{2+}$
1 [Ti(**S1**)Cl$_2$]	n=1, 576.1591, calc. 576.1605, 2.4 ppm (27%) n=2, 868.2376, calc. 868.2395, 2.1 ppm (64%) n=3, 1160.3196, calc. 1160.3184, 1.0 ppm (9%)
2 [Ti(**S2**)Cl$_2$]	n=2, 1018.7870, calc. 1018.7903 3.2 ppm (100%)
5 [Ti(**S1**)(O^{i}Pr)$_2$]	n=1, 576.1613 ,calc. 576.1605, 1.4 ppm (30%) n=2, 868.2381, calc. 868.2395, 1.5 ppm (47%) n=3, 1160.8184, calc. 1160.3184, 3.4 ppm, (23%)
6 [Ti(**S2**)(O^{i}Pr)$_2$]	n=1, 676.1913, cacl. 676.1918, 0.7 ppm (23%) n=2, 1018.7809, cacl. 1018. 7903, 3.6 ppm (52%) n=3, 1360.8773, calc. 1360.3810, 2.7 ppm (25%)

The numbers in the bracket indicates the abudances.

2.5 Proton NMR studies

Tetradentate salen ligands can afford three pseudo-octahedral-coordinated isomers, namely *trans*, *cis*-α and *cis*-β (Figure 2.8). The three isomers have distinct symmetric elements (C_2 for *trans* and *cis*-α, C_1 for *cis*-β), which will lead to the distinct ^{1}H NMR patterns.[11,12]
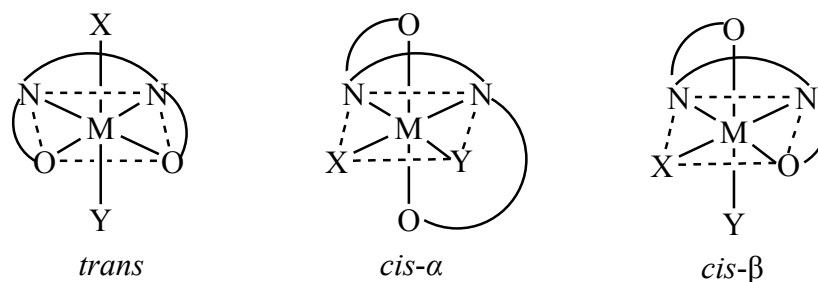
Figure 2.8 Three isomers of octahedral metallosalen complexes.

The complexes (**1-8**) are characterized by ^{1}H NMR in CDCl$_3$. The chemical shift of phenol protons in ligands are all above 12 ppm, while the signals in complexes disappear due to

deprotonation. Both the imine protons and bay protons are shifted downfield/upfield according to the individual case due to deshielding/shielding effects after metallation, indicating the coordination of the phenol oxygen and imino nitrogen atoms to the metal(s).

The ^{1}H NMR spectrum of complex **1** in CDCl$_3$ (Figure 2.9) shows only one major set of resonances, which indicates only one species present. The number of resonances is half the number of possible resonances, indicating the presence of a C_2 symmetric, *trans* or *cis*-α molecule (Figure 2.10).[12] In the crystal analysis each Ti(salen)Cl unit also shows as *trans*-isomer, even though the whole molecule is an oxo-bridged dititanium salen complex (see Section 2.6.1.).
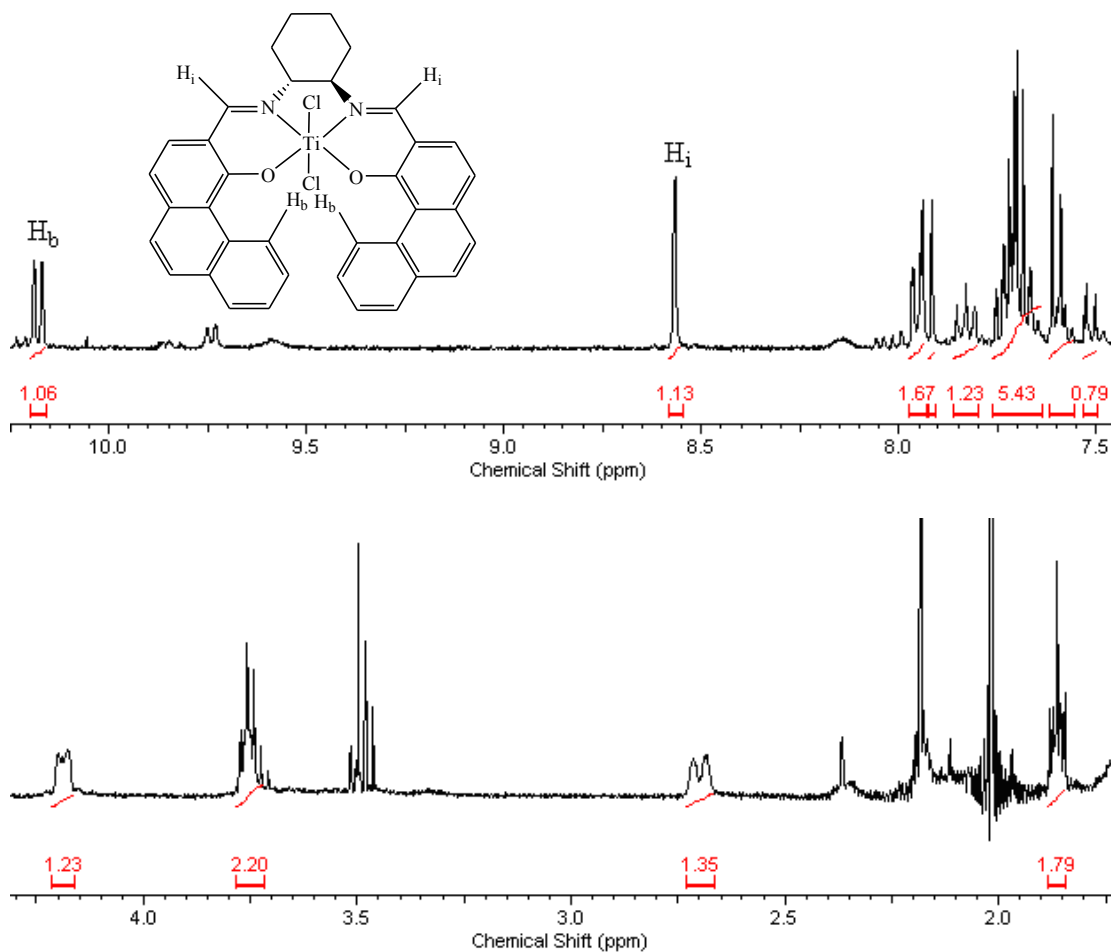
Figure 2.9 ^{1}H NMR spectrum of complex 1 in CDCl$_3$: upper, aromatic; lower, aliphatic regions.

48

It is presumed that partial hydrolysis of such C_2 symmetric isomers in solution may happen during crystallization. After complexation, the resonance for phenol protons disappears. The doublet signal for bay protons appears at 10.18 ppm, a 0.5 ppm upfield shift compared to free ligand. The imine protons show one broad singlet signal at 8.57 ppm that may be due to through space coupling with neighboring protons (Table 2.6). The protons in the cyclohexyl backbone show multiplet signals between 4.3 to 1.8 ppm.

Table 2.6 Chemical shifts of imine and bay protons of ligand S1 and complex 1.

	δ(imine prontons)/ppm	δ(bay protons)/ppm
H₂S1	8.61(2H)	10.61(2H)
1 [Ti(**S1**)Cl₂]	8.57(2H)	10.18(2H)
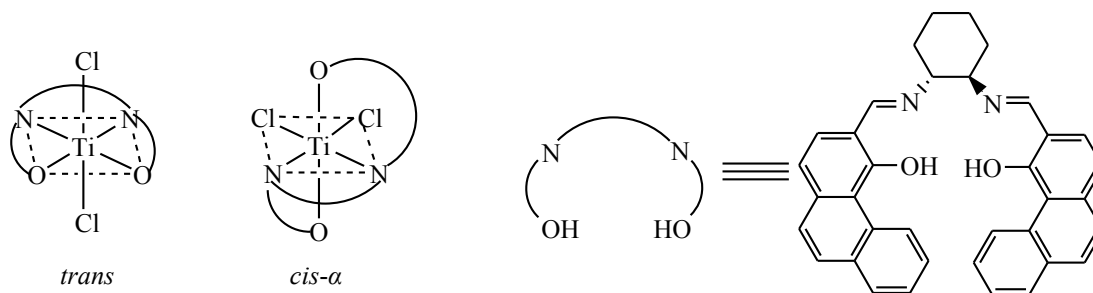
Figure 2.10 Possible structure of complex 1 in solution.

The NMR spectra of complexes **2**, **3**, **4**, **5** and **6** show the selective formation of only one isomer in solution. These isomers all exhibit a lower C_1-symmetric structure based on ^{1}H NMR as compared to the C_2-symmetric free ligands, thus indicating a *cis*-β complex geometry.[5,12,13]

The ^{1}H NMR spectrum of complex **2** (Figure 2.11) shows the signals of 32 protons, 22 in aromatic and 10 in aliphatic regions. This is consistent with a C_1-symmetric monomer or a C_2-dimer with two *cis*-β moieties (Figure 2.12).

49
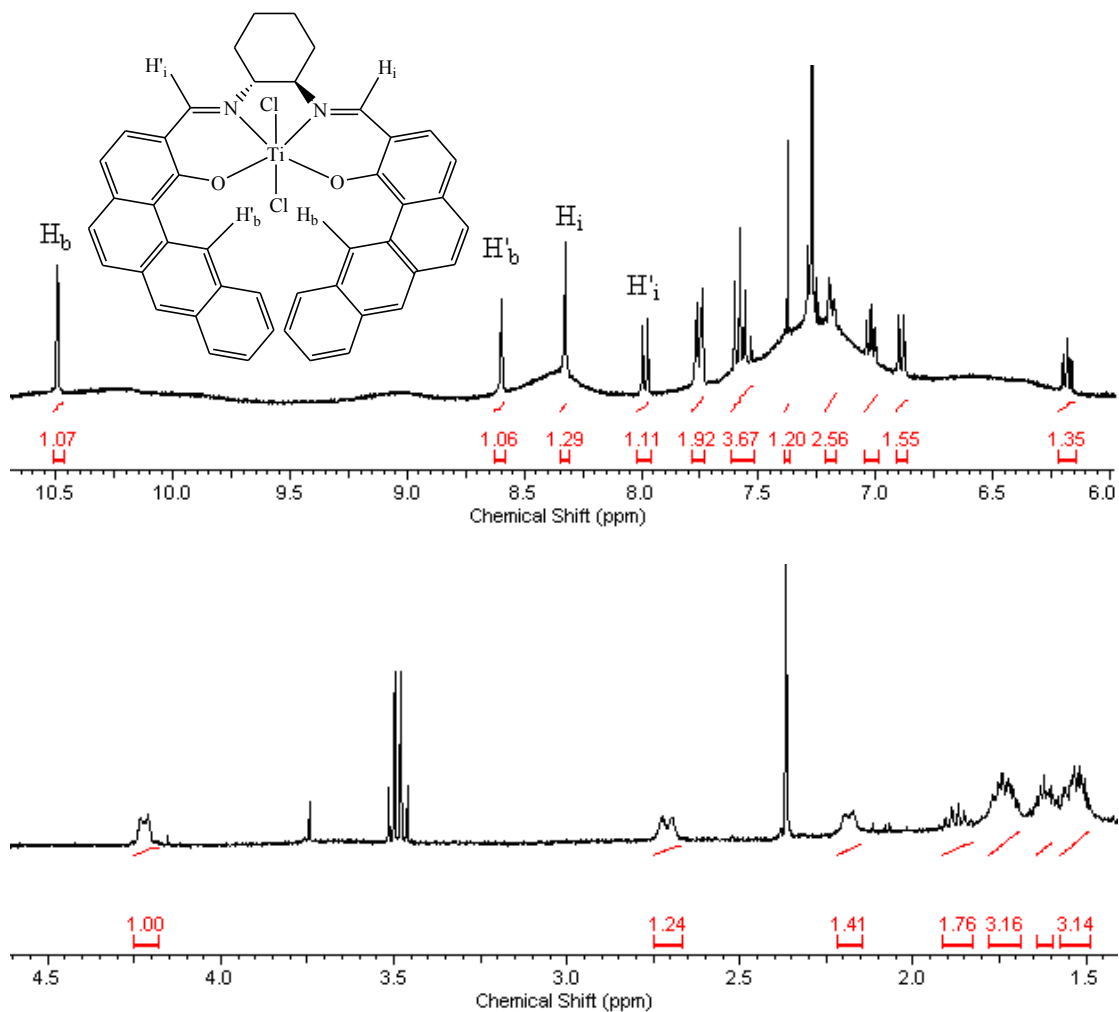
Figure 2.11 ^{1}H NMR spectrum of complex 2 in CDCl$_3$: upper, aromatic; lower, aliphatic regions.

The protons from the cylcohexyl backbone appear as broadened multiplets peaks in the aliphatic region due to the fluctuation of the ring. The methine protons can be found at 4.20 and 2.70 ppm, separated by 1.5 ppm. The methylene protons are partly separated in the area of 2.22-1.49 ppm. In the aromatic region, three singlet signals (10.49, 8.60, 8.33 ppm) are clearly found, which may be assigned to the 2 bay protons and 1 imine proton. The doublet resonance at 7.99 ppm may be assigned to the other imine proton, due to coupling to the adjacent aromatic proton after coordination (Table 2.7). This is supported by the triplet signal around 6.18 ppm, which is a

doublet at 7.11 ppm in free ligand. The upfield shift may be caused by the increased deshielding effect after metallation.

Table 2.7 Chemical shifts of imine and bay protons of ligand S2 and complex 2.

	δ(imine prontons)/ppm	δ(bay protons)/ppm
H₂S2	8.62(2H)	11.21(2H)
2 [Ti(S2)Cl₂]	8.33(1H), 7.99(d/1H)	10.49(1H), 8.60(1H)

cis-β monomer   *C₂* symmetric dimer
combined with *cis*-β monomers
B: (-2) charged bridging group
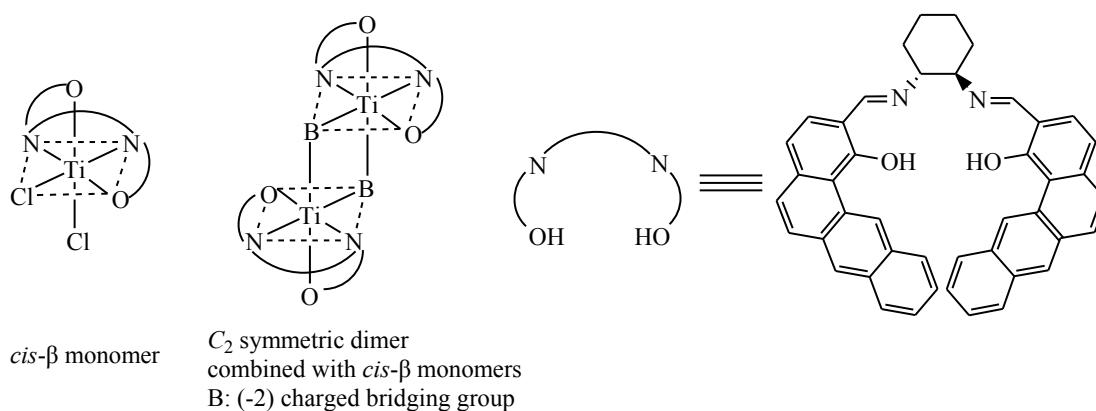
Figure 2.12 Possible structures of complex 2 in solution.

The ^{1}H NMR spectrum of complex **3** (Figure 2.13) indicates the presence of a *cis*-β monomer or a C_2 symmetric dimer with two *cis*-β halves like complex **2**. The formation of a *cis*-β structure is confirmed by the X-ray crystal structure analysis of complex **3** (see Section 2.6.2). Two resonances for the bay protons (10.13 and 10.25 ppm) are observed as doublets, which are separated by 0.12 ppm and correspond to one proton each. Accordingly, the imine protons (8.40 and 8.66 ppm) also appear as separated singlet signals (Table 2.8). The other aromatic signals (8.2-6.90 ppm) are too complicated and overlapped to completely assign, and both upfield and downfield shifts are observe in this area relative to the free ligand.
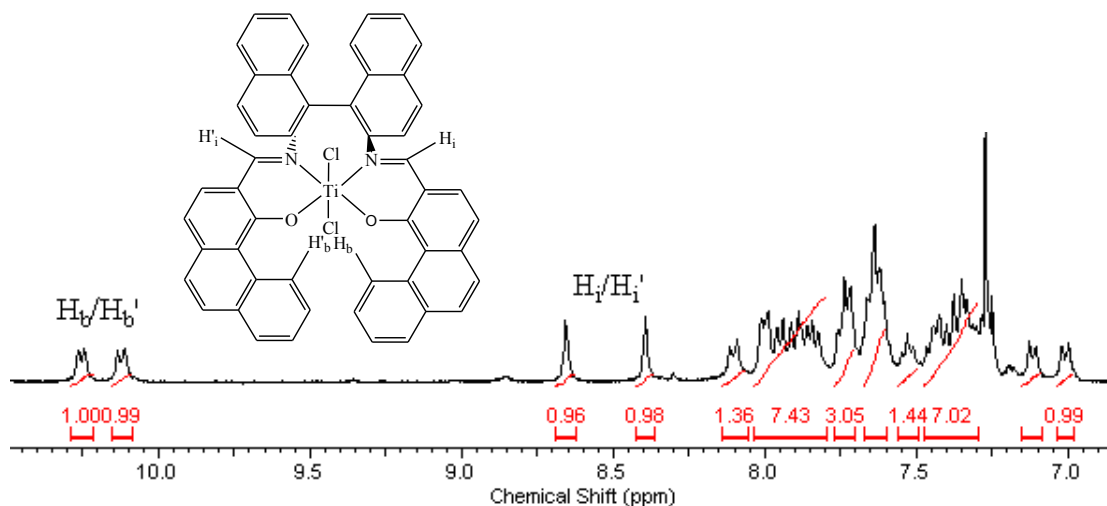
Figure 2.13 ^{1}H NMR spectrum of complex 3 in CDCl$_3$.

Table 2.8 Chemical shifts of imine and bay protons of ligand S3 and complex 3.

	δ(imine prontons)/ppm	δ(bay protons)/ppm
H$_2$S3	8.80(2H)	9.44(2H)
3 [Ti(**S3**)Cl$_2$]	8.40(1H), 8.66(1H)	10.13(1H), 10.25(1H)

The ^{1}H NMR spectum of complex **4** (Figure 2.14) exhibits a new set signal for a C_1 symmetric molecule, besides the set seen for C_2 symmetric ligand, indicating that both the ligand and the Ti complex are present. Two bay protons are observed at 10.85 and 10.59 ppm, downfield shifted compared to the free ligand. The singlet signals at 8.66 and 8.36 ppm are assigned to the imine protons (Table 2.9). Two aromatic multiplet peaks upfield shift to 6.96 and 6.31 ppm, due to the chelating to the highly positively charged metal center.

52
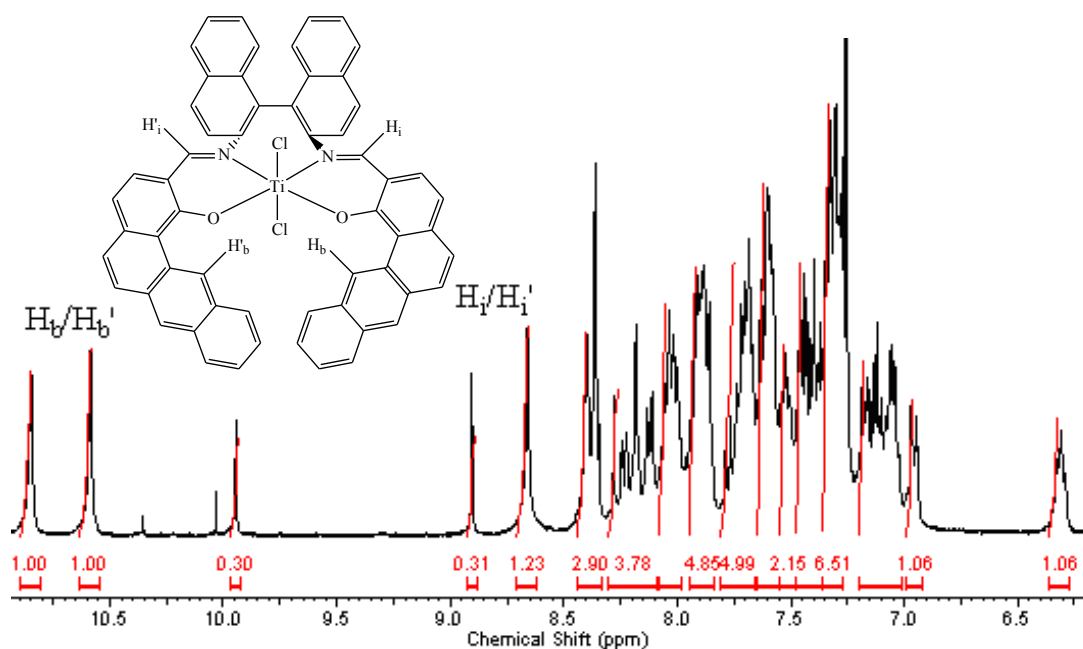
Figure 2.14 ^{1}H NMR spectrum of complex 4 in CDCl$_3$.

Table 2.9 Chemical shifts of imine and bay protons of ligand S4 and complex 4.

	δ(imine prontons)/ppm	δ(bay protons)/ppm
H$_2$S4	8.93(2H)	9.96(2H)
4 [Ti(**S3**)Cl$_2$]	8.66(1H), 8.36(1H)	10.85(1H), 10.59(1H)

In the proton spectrum of complex **5** (Figure 2.15), there are two doublet peaks observed at 10.06 and 10.62 ppm, may be assigned to the two bay protons in addition to two singlet signals (8.49 and 8.41 ppm) for imine protons, due to the loss of the symmetry. For the peaks in aromatic region (7.00-8.00 ppm), some overlap occurs, making the assignment difficult.

Two sets of resonance for the two Ti-bound isopropoxy ligands can be clearly observed in the aliphatic region of complex **5** (Table 2.10): 2 septet signals, which are typical for the CH of isopropoxy groups, and two pairs of doublet signals between 0.6 to 1.2 ppm, which can be assigned to the methyl groups of isopropoxy ligand. These suggest the coordination of two

different isopropoxy ligands to Ti center. Therefore, the structure of complex **5** can be tentatively proposed as (*R,R*)-*cis*-β-[Ti(salen)(O*i*Pr)$_2$] as show in Figure 2.16.

Figure 2.15 ^{1}H NMR spectrum of complex 5 in CDCl$_3$: upper, aromatic; lower, aliphatic regions.

Table 2.10 Proton NMR Chemical shifts of ligand H₂S1 and complex 5.

	δ(imine H)/ppm	δ(bay H)/ppm	δ(isopropoxy H)/ppm
H₂S1	8.61(2H)	10.61(2H)	
5	8.49(1H)	10.06(1H)	4.62, 4.82 (overlap) for 2CH;
[Ti(**S1**)(O^{i}Pr)₂]	8.41(1H)	10.62(1H)	0.80, 0.85, 1.13, 1.18 for 4CH₃

Figure 2.16 Proposed structure of complex 5 in CDCl₃ solution.

The NMR spectrum of complex **6** in figure 2.17 exhibits 22 proton signals in the aromatic region and 24 protons in aliphatic region, which is consistent with a C_1 symmetric structure. The two imine signals are clearly visible as singlets at 8.53 and 8.45 ppm. Two singlet resonances for bay protons are separately observed at 10.97 and 10.58 ppm. Two ArCH signals of complex **6** shift upfield below 7 ppm.

Similarly, two sets of typical signals for two isopropoxy groups apprear (Table 2.11). The signal for one α proton in the cyclohexylene backbone shifts downfield to 4.87 ppm, which overlaps with the methine proton from one isopropoxy group. This may be caused by the inefficient shielding effect after metal complexation. The structure of complex **6** is proposed to be quite similar to that of complex **5**, due to the similar ¹H NMR characteristics, while the structure analysis by single crystal XRD is partially supported this proposal.
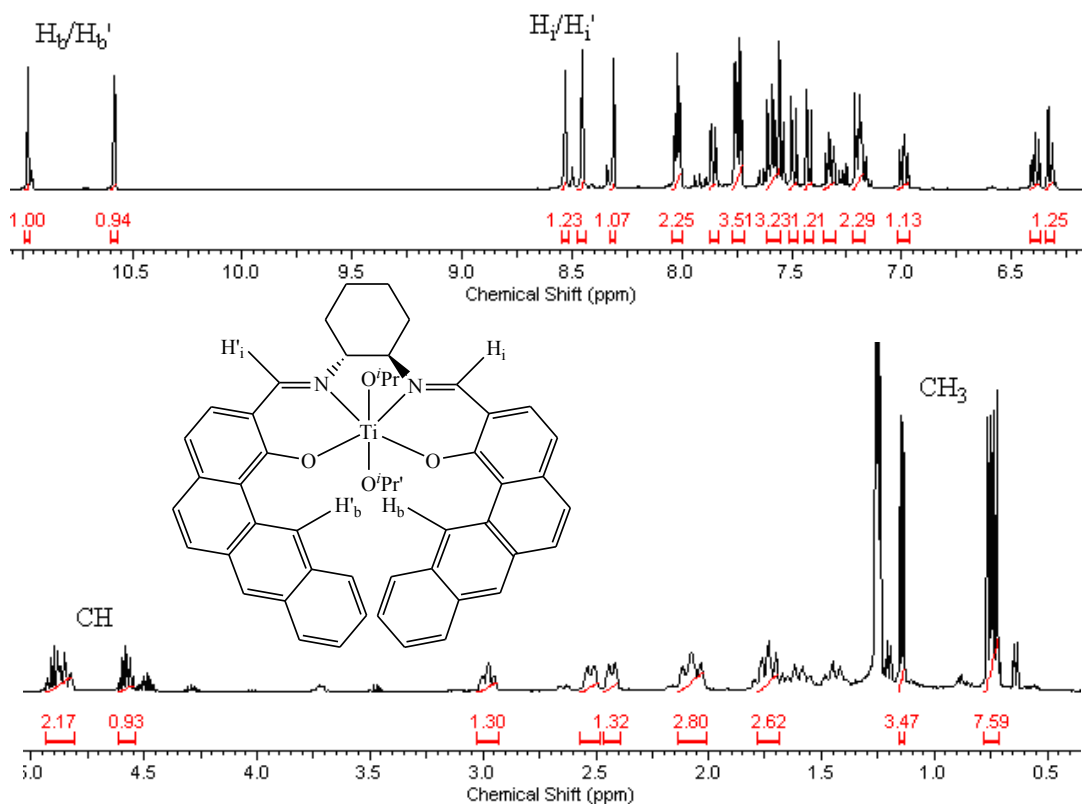
Figure 2.17 ^{1}H NMR spectrum of complex 6 in CDCl$_3$. upper, aromatic; lower, aliphatic regions.

Table 2.11 Proton NMR Chemical shifts of ligand H$_2$S2 and complex 6.

	δ(imine H)/ppm	δ(bay H)/ppm	δ(isopropoxy H)/ppm
H$_2$S2	8.62(2H)	11.21(2H)	-----
6	8.53(1H)	10.97(1H)	4.58, 4.87 (overlap) for 2CH
[Ti(**S2**)(O^{i}Pr)$_2$]	8.45(1H)	10.58(1H)	1.14 (3H), 0.74 (9H)

The NMR analysis of complexes **7** and **8** reveal the formation of more than one species in the NMR solution.

Figure 2.18 shows the ^{1}H NMR spectra of complex **7** in CDCl$_3$. There are two sets of peaks, one set corresponding to a C_1-symmetric structure and the other for a C_2-symmetric compound

56

with a ratio of 1:1, according to the peak integrals of the spectra. No signals in the characteristic phenol proton region can be observed in either set. In the C_1 symmetric set, the characteristic resonances for two isopropoxy groups appear in the aliphatic region (doublets at -0.22, 0.32, overlapping around 0.92, and 0.98 ppm for CH_3; 4.73 and 4.83 ppm for CH), and one doublet signal for methyl proton is greatly shifted upfield to the negative area, due to complexation to the positively charged Ti(IV) center (Table 2.12.). The doublet resonance for one bay proton can be clearly observed at 10.78 ppm, significantly downfield by 1.34 ppm from the free ligand. Additionally, the singlet for one imine proton appears at 8.38 ppm, which is upfield shifted from 8.80 ppm in the free ligand. The spectrum shows a broad multiplet at 10.58 ppm, which corresponds to 3 protons. This may be caused by the overlapping of one bay proton in C_1 species and two bay protons from C_2 species. The C_2 set of signals shows one septet (4.55 ppm) corresponding for 2H and overlapped multiplet (around 0.90 ppm) for 12H, indicating the presence of two chemically equivalent isopropoxy groups. The other signals for both species are quite difficult to assign, due to overlapping.
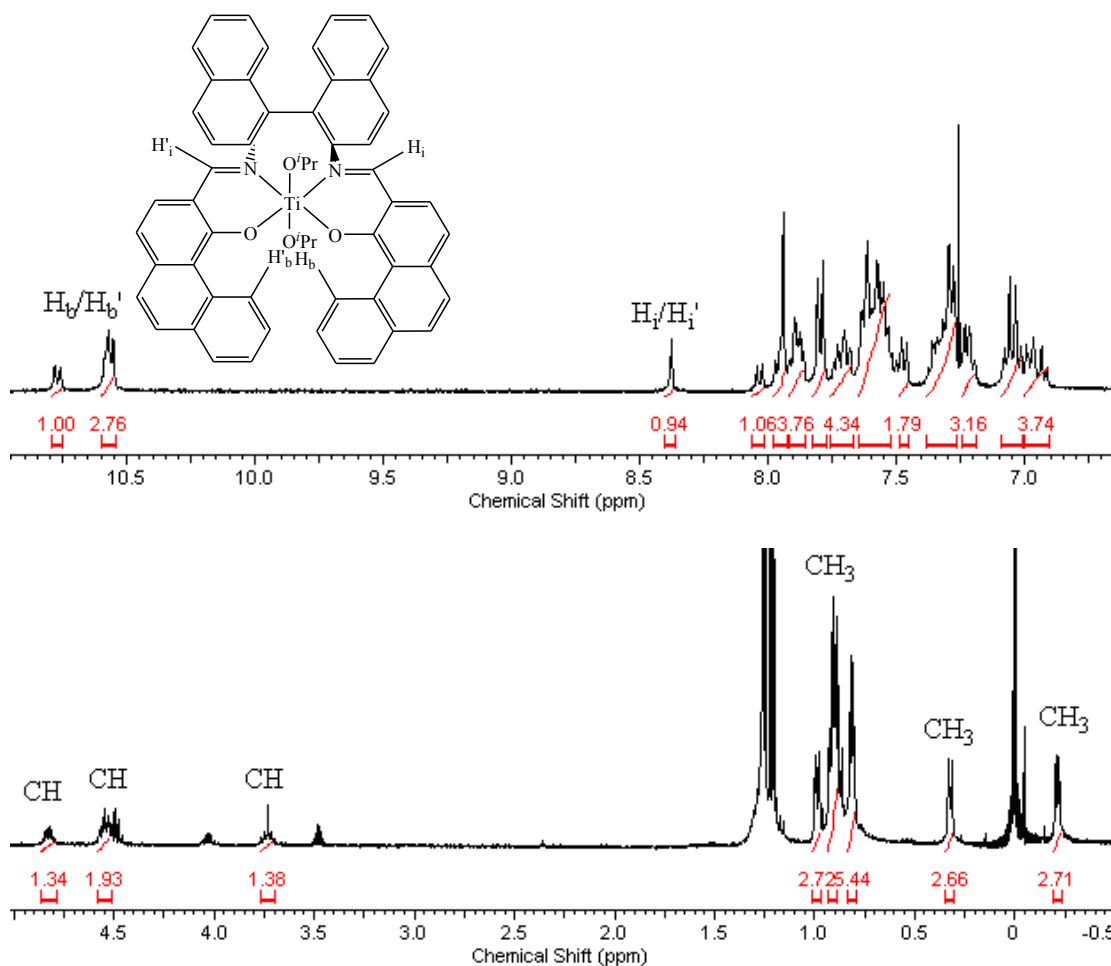
Figure 2.18 ^{1}H NMR spectrum for complex 7 in CDCl$_3$: upper, aromatic; lower, aliphatic regions

Table 2.12 Proton NMR Chemical shifts of ligand H$_2$S3 and complex 7.

	δ(imine H)/ppm	δ(bay H)/ppm	δ(isopropoxy H)/ppm
H$_2$S3	8.80(2H)	9.44(2H)	------
7 [Ti(**S3**)(O^{i}Pr)$_2$]	8.38(1H) Can't tell	10.78(1H) 10.58 (3H)	4.55(2CH), 0.92 (4CH$_3$); -0.22, 0.32, 0.86 and 0.92 for 4CH$_3$; 4.73, 4.83 for 2CH

All the above analysis suggests that the formation of a mixture of C_1 symmetric *cis*-β isomer and C_2 symmetric *trans*/*cis*-α isomer of monomeric Ti(salen)(O^{i}Pr)$_2$ complexes. The latter two can not be distinguished by NMR analysis. All attempts to separate the mixed products so that a single component is observed in solution have failed.

This indicates that there may be a solution equilibrium between the two species (Figure 2.19). However, the crystal structure shows somehow a different arrangement. There is no isopropoxy group at all. And the dimeric structure shows an overall C_2 symmetry, while each (salen)Ti half shows a C_1 symmtric element.
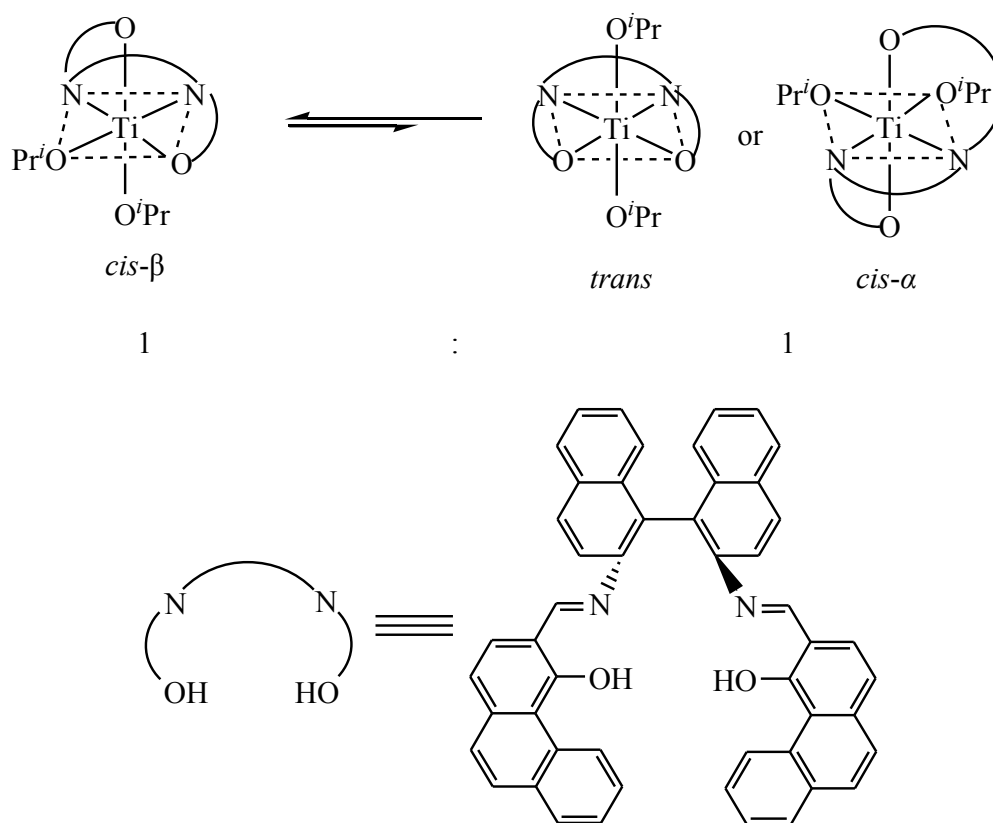
Figure 2.19 Possible equilibrium in the solution of complex 7.

The spectrum of complex **8** (Figure 2.20) shows one and a half times as many aromatic peaks as expected, based on C_1-symmetry. Two sharp singlet resonances are apparent for the bay protons (11.43 for 1H and 11.05 ppm for 2H). Three singlet peaks may be tentatively assigned to imine protons (8.46, 8.33 and 8.24 ppm) (Table 2.13). A possible interpretation of this spectral pattern is that both a *cis*-β isomer and a C_2-symmetric isomer form in the solution with the ratio of 2:1. In the aliphatic region, three septet signals for CH can be clearly observed between 5 and 3.6 ppm. The five doublet resonances for CH_3 are found below 1 ppm.
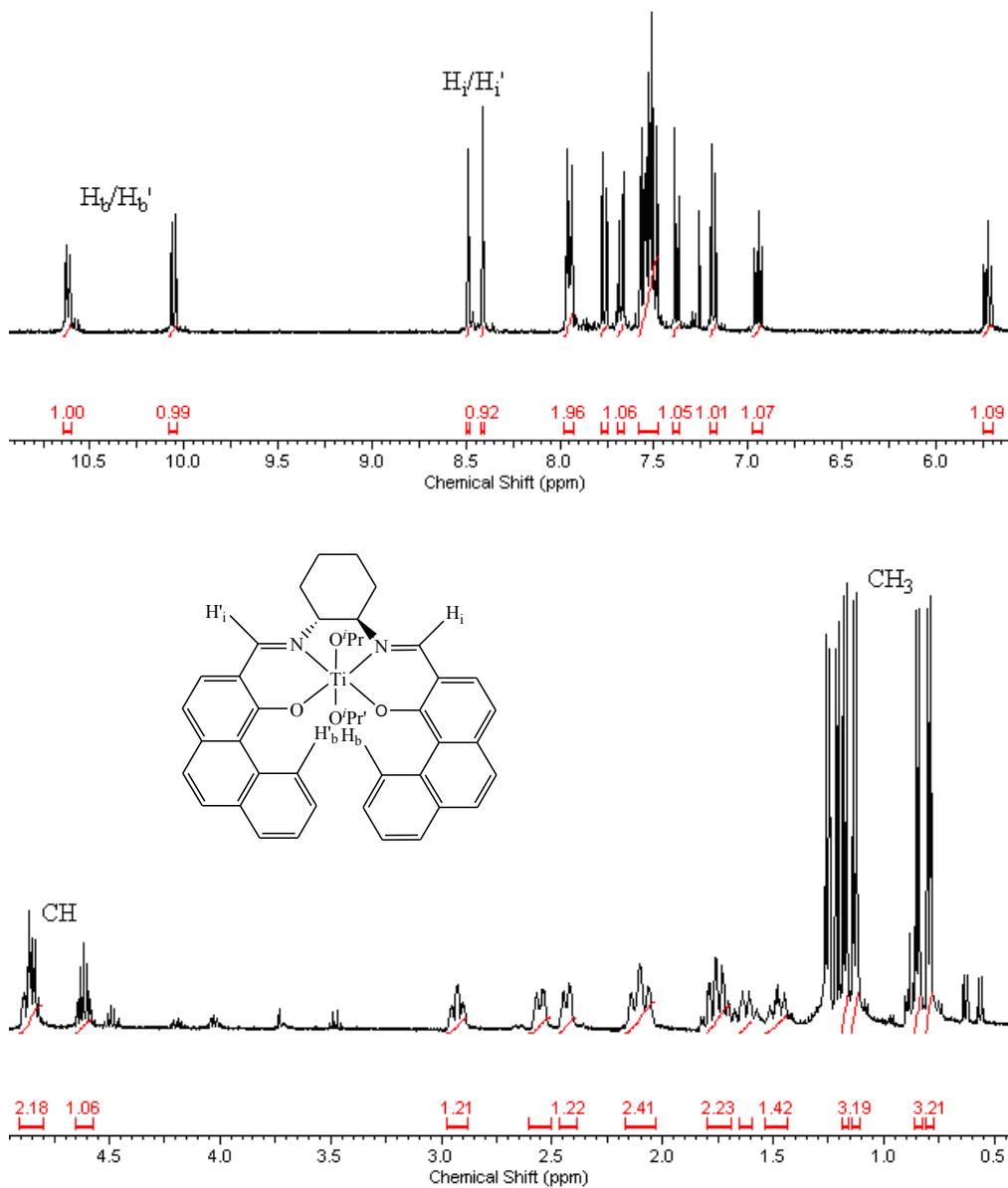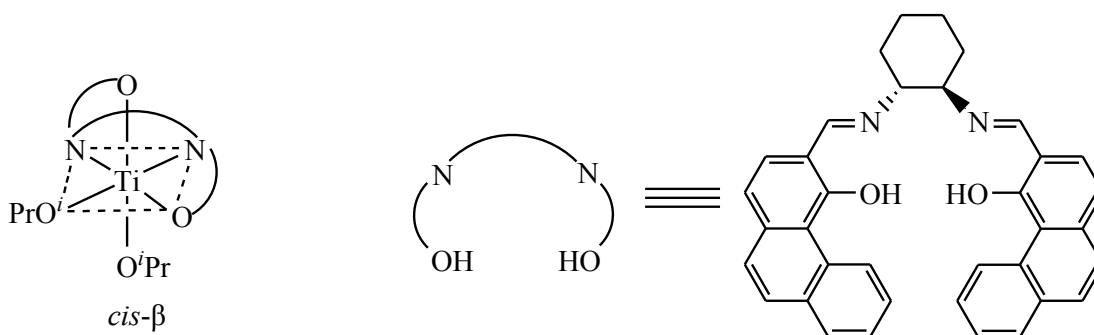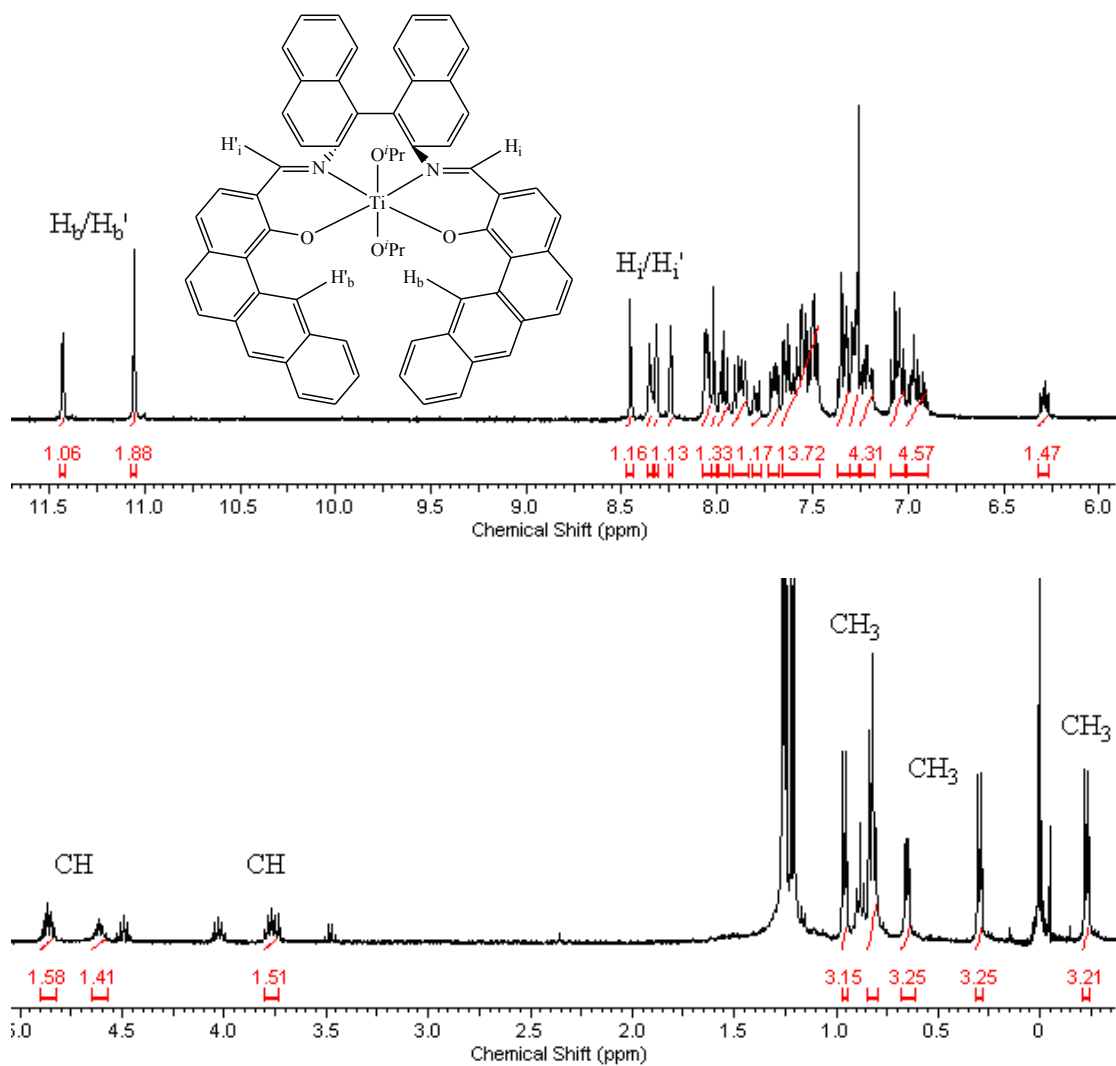

Figure 2.20 ^{1}H NMR spectrum of complex 8 in CDCl$_3$: upper, aromatic; lower, aliphatic regions.

Table 2.13 Proton NMR Chemical shifts of ligand H$_2$S4 and complex 8.

	δ(imine H)/ppm	δ(bay H)/ppm	δ(isopropoxy H)/ppm
H$_2$S4	8.93 (2H)	9.96 (2H)	----
8 [Ti(**S4**)(O^{i}Pr)$_2$]	8.46 (1H) 8.33 (1H) 8.24 (1H)	11.43 (1H) 11.05 (3H)	4.62 (CH), 0.79-0.84 (2CH$_3$); -0.23, 0.30, 0.65 and 0.96 for 4CH$_3$; 3.77, 4.87 for 2CH

In addition, the integration of these peaks indicates that there are three isopropoxyl groups: one assignable to two equivalent isopropoxyl groups of a C_2-symmetric isomer, and the other two, with the same intensity, assignable to *cis*-β isomer. The ratio between *cis*-β and symmetric isomer is about 2:1 (Figure 2.21).
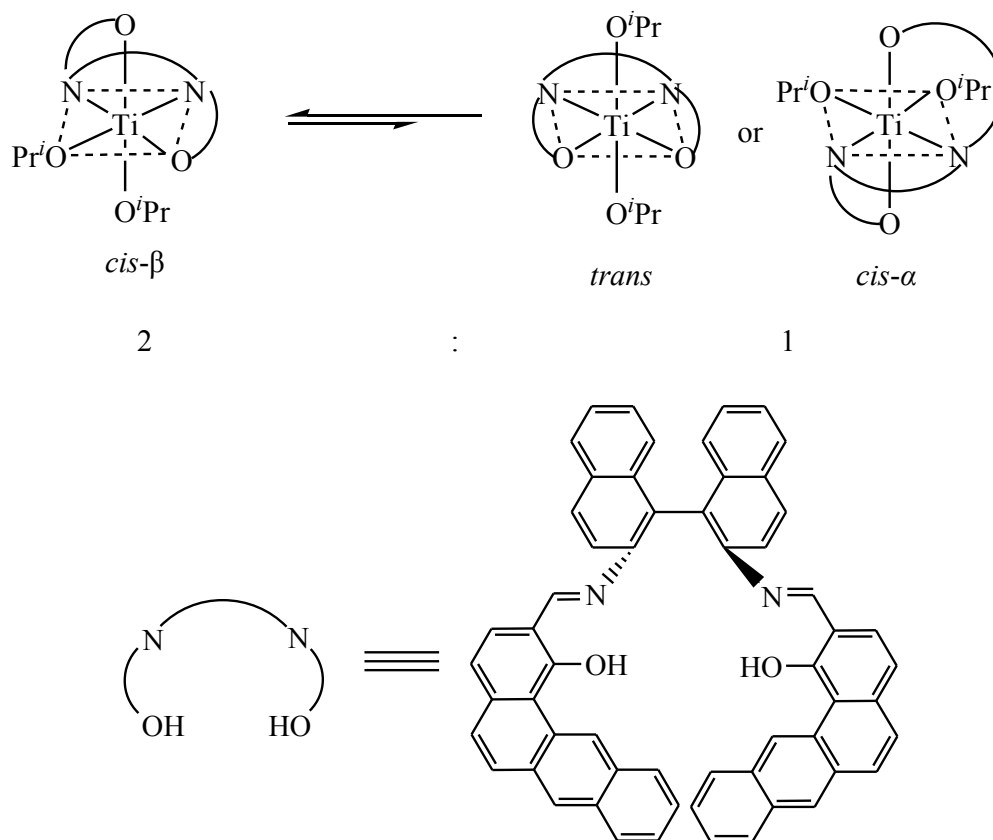
Figure 2.21 Possible equilibrium in the solution of complex 8.

All results are consistent with the analysis of the aromatic region. One triplet signal is visible at 6.22 ppm, different from the doublet observed in the free ligand, maybe due to the space coupling after complexation. An attempt to assign the peaks in aromatic region has failed, however, because of overlapping resonances.

The difference in the solution structure may be induced by both the salen and non-salen ligands in the complexes. In all 8 complexes, a *cis*-β isomer is the preferred/dominant structure. The rigidity of the cyclohexyl backbone of the salen ligand results in the selective formation of only the *cis*-β isomer, even though the structure of complex **1** is found to be a *trans*-[Ti(salen)Cl$_2$]. Compared to the cyclohexyl backbone, the binaphthyl is conformationally constrained, thus it is expected to show more selectivity in the structure formation. A mixture of both C_1- and C_2-symmetric molecules is produced in complexes **7** and **8** when Ti(O^{i}Pr)$_4$ is applied as metal precursor. The possible reason may be due to the bulkiness of isopropoxy groups bound to Ti metal center. The steric repulsion between isopropoxy groups and the aromatic rings of backbone/sidearm drives the switch from C_1 to C_2 symmetry. The overlapping of the extended sidearm of salen ligand helps to lock the conformer/structure in the solution, which may explain the different isomer ratios between complexes **7** (*trans*: *cis*-β = 1:1) and **8** (*trans*: *cis*-β = 2:1).

2.6. Solid-state structural studies of titanium(IV) salen complexes

The coordination of the tetradentate salen ligands to the titanium(IV) center can result in the formation of three octahedral coordination isomers, namely *trans*, *cis*-α, and *cis*-β. In monometallic complexes, the planar *trans*-isomer of salen ligands is usually preferred by energetics.[3] However, in *bis*-bridged bimetallic complexes, two bridging groups must occupy

positions *cis* to each other, which results in a *cis*-α or *cis*-β configuration. The two *cis*-isomers contain a chiral Ti metal center, which can result in two diasteroisomers (Δ and Λ) for each isomer.[5,12,14] The *cis*-β isomer is the most preferentially formed in all cases examined so far.[1,2,4,5] For bimetallic complexes bearing two identical *cis*-β salen ligands, there are four possible diastereomeric coordination isomers,[15] which are depicted in Figure 2.22.
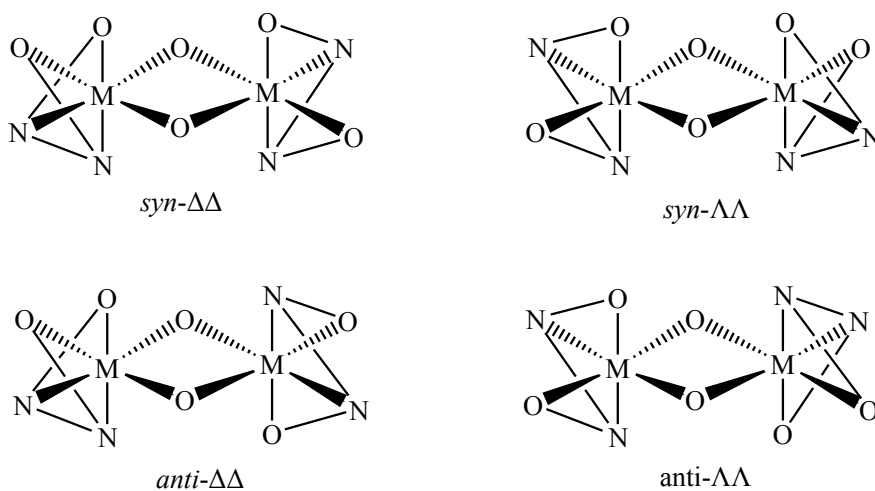
Figure 2.22 Four possible stereoisomers of a (μ-O)₂-[M(salen)]₂.
salen ligand adopts a *cis*-β configuration.

2.6.1 Mono oxo bridged structure of complex 1

Dark orange-red crystals of complex **1** Ti(IV)-S1 suitable for X-ray diffraction studies is grown under N_2 by the heating-cooling method in CH_2Cl_2. The crystal structure for the single molecule is shown in Figure 2.23 and the selected bond distances and angles are summerized in Table 2.14.

Figure 2.23 Structure of complex 1: top, thermal ellipsoid plot (50% probability, H omitted for clarity); bottom, space filling model.

The coordination environment around each titanium metal is a distorted octahedron. The titanium center is lying in the plane of the N_2O_2 core of the salen ligand with shorter Ti-O bond and longer Ti-N bond. The Cl ligand is *trans* to the bridged oxygen atom, indicating that the *trans* isomer is selectively obtained, which is consistent with the NMR analysis in solution. It is generally prosposed that in octahedral monometallosalen complexes, the planar, *trans* configuration is preferred in the view of energy.[3]

The axial Cl-Ti bond is not quite orthogonal to the TiN_2O_2 plane and slightly bent toward the imine nitrogen. Each salen ligand adopts a (*R,R*) configuration and *P* conformer. The aromatic sidearm is canted above and below the TiN_2O_2 plane and the torsion angles between phenanthryl sidearms are 22.3° and 24.5°, respectively. The Ti-μ-O-Ti bond is bent (156.4°) with similar Ti-O lengths (1.82 and 1.80 Å). Attractive π-π stacking between phenanthryl planes of two ligands is observed with carbon to centroid distance of 3.6 Å, which is within the expected range of 3.4-3.6 Å.[13,14,15] The metrical parameters for the two Ti(salen)Cl moieties are comparable.

Table 2.14 Selected bond distance (Å) and angles (°) for complex 1.

$Ti_1-O_{12\_1}$	1.848(2)	$Ti_2-O_{12\_3}$	1.898(2)
$Ti_1-O_{12\_2}$	1.885(2)	$Ti_2-O_{12\_4}$	1.870(2)
$Ti_1-N_{25\_1}$	2.128(2)	$Ti_2-N_{25\_3}$	2.129(2)
$Ti_1-N_{25\_2}$	2.124(2)	$Ti_2-N_{25\_4}$	2.133(2)
Ti_1-Cl_1	2.4173(9)	Ti_2-Cl_1	2.4401(9)
Ti_1-O_1	1.823(2)	Ti_2-O_1	1.797(2)
$Cl_1-Ti_1-O_1$	172.44(7)	$Cl_1-Ti_2-O_1$	174.74(7)
$Ti_1-O_1-Ti_2$	156.4(1)		

It is proposed that the monobridged crystal is a partially hydrolysis product from *trans*-[Ti(S1)Cl$_2$], due to the highly moisture-sensitive nature of Ti complex. In the presence of moisture, two Cl ligands each from one mononuclear Ti(salen)Cl$_2$ are cleaved as HCl, and the two units are bridged by one oxygen atom from water molecule (Figure 2.24). This hydrolysis may well have occurred during the crystallization process, rather than in the original synthesis.

$$2[Ti(\textbf{S1})Cl_2] \quad + \quad H_2O \longrightarrow \mu\text{-O-}[Ti(\textbf{S1})Cl]_2 \quad + \quad 2HCl$$
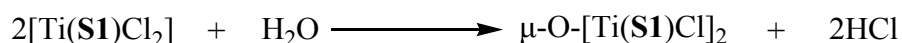
Figure 2.24 Proposed partial hydrolysis of complex 1.

2.6.2. Crystal structure of complex 3

Single crystals suitable for X-ray analysis were grown by slow-diffusion from dichloromethane to diethyl ether. The crystal structure of complex **3** is depicted in Figure 2.25, and contains two *M* helices with only minimal difference between them. The two molecules adopt a head to head arrangement. The molecular structure clearly reveals a six-coordinated monomeric Ti(IV) complex with two chloro ligands bonded in a *cis* arrangement for both helices. The salen ligand adopts a *cis*-β configuration and the complex shows Δ enantiomeric structure. The axial Cl is almost perpendicular to the TiN$_2$OCl plane, and it is bent to the downwardly pointed naphthal moiety of the backbone, to minimize unfavorable steric interactions. The dihedral angles arising between the naphthyl planes of backbone are 70.10˚ (Ti$_1$ centered) and 67.22˚ (Ti$_2$ centered), respectively, which are within the ~60-130˚ range. [5,9,12] The angles between the phenanthryl planes are 46.7˚ (Ti$_1$ centered) and 44.9˚ (Ti$_2$ centered), respectively. As expected, the bond lengths of Ti-O are shorter than those of Ti-N. The selected bond length and angles are listed in Table 2.15.

Figure 2.25 Structure of complex 3: top, thermal ellipsoid plot (50% probability, H omitted for clarity); bottom, space filling model. (both molecules: *M***).**

Table 2.15 selected bond length (Å) and bond angles (°) for complex 3.

Molecule 1		Molecule 2	
Ti_1-Cl_1	2.285(2)	Ti_2-Cl_3	2.299(2)
Ti_1-Cl_2	2.304(3)	Ti_2-Cl_4	2.300(3)
Ti_1-N_{25_1}	2.173(6)	Ti_2-N_{25_3}	2.209(6)
Ti_1-N_{25_2}	2.175(7)	Ti_2-N_{25_4}	2.160(6)
Ti_1-O_{12_1}	1.864(5)	Ti_2-O_{12_3}	1.835(5)
Ti_1-O_{12_2}	1.868(5)	Ti_2-O_{12_4}	1.832(5)
Cl_1-Ti_1-Cl_2	90.81(9)	Cl_3-Ti_2-Cl_4	89.71(9)
Cl_1-Ti_1-O_{12_2}	87.6(6)	Cl_3-Ti_2-O_{12_4}	89.1(2)
Cl_2-Ti_1-O_{12_2}	171.0(2)	Cl_4-Ti_2-O_{12_4}	171.7(2)
O_{12_1}-Ti_1-O_{12_2}	96.30(2)	O_{12_3}-Ti_2-O_{12_4}	95.1(2)
N_{25_1}-Ti_1-N_{25_2}	81.2(2)	N_{25_3}-Ti_2-N_{25_4}	79.8(2)

2.6.3. Crystal structure of complex 6

Figure 2.26 shows the crystal structure of Ti-salen complex **6**. The selected structure data are summarized in Table 2.16. The maroon needle-shaped crystals are obtained from hexane/CH_2Cl_2 by slow diffusion. The dinuclear structure shows two Ti(salen) units bridged by two oxo groups. Both Ti(salen) moieties have the Δ–configuration at the central Ti ion, and possess the (*R*,*R*)-configuration in the backbone. Each titanium center exhibits a distorted octahedral geometry with two oxo bridges *cis* to each other. The two salen ligands show a *syn* arrangement to each other. Each salen ligand adopts *cis*-β configuration. Exclusively *M* helical conformer is observed in the solid state, and the terminal aryl rings in benz[a]anthryl sidearms are overlapped as expected. The overall configuration is *syn*-Δ-(*R*,*R*)- Δ-(*R*, *R*).
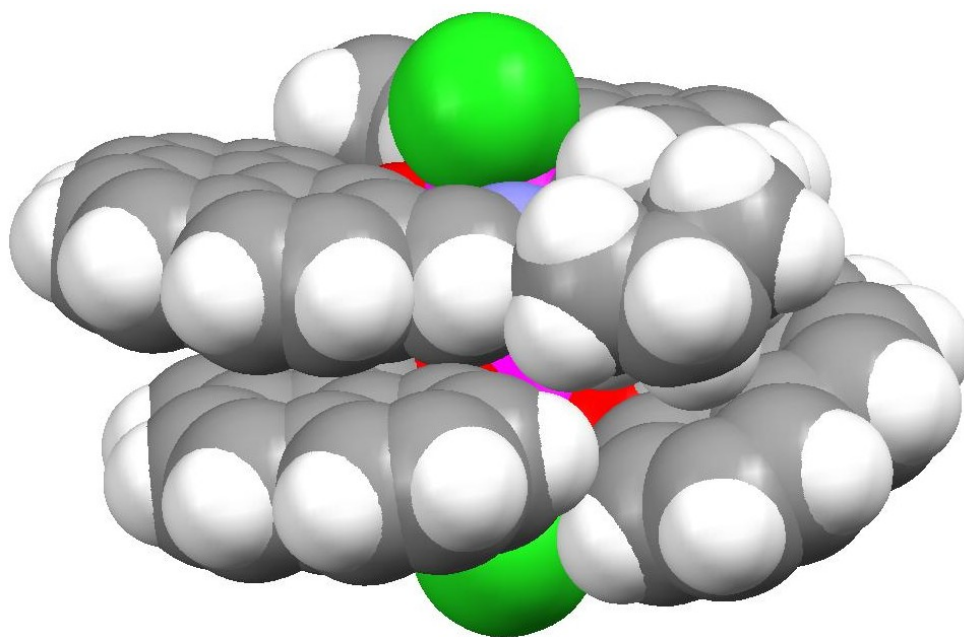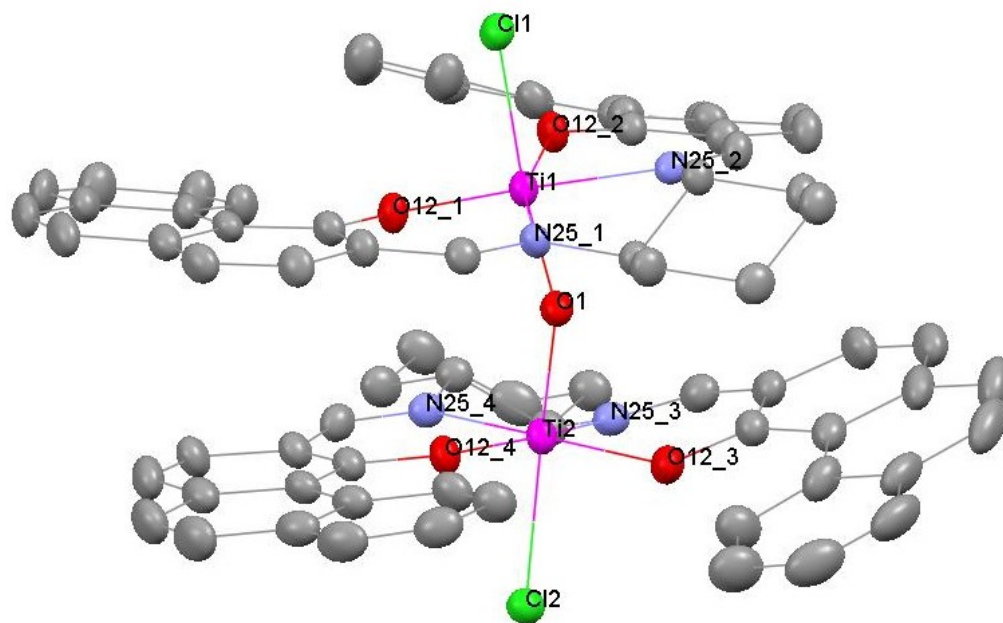
Figure 2.26 Structure of complex 6: top, thermal ellipsoid plot (50% probability, H omitted for clarity); bottom, space filling model.

The Ti$_2$O$_2$ core is near square, and four Ti-O$_{bridge}$ bonds have different lengths (1.82-1.97 Å). Moreover, the bridged Ti-O bonds are longer than the salen Ti-O bonds. The Ti-O bond lengths are shorter than the Ti-N ones as expected. There is evidence of π-π stacking between benz[a]anthryl from the two salen ligands. The carbon-centroid distance (3.6 Å) lies on the border of the favored 3.4-3.6 Å range. The metric parameters of two Ti(salen) moieties are comparable.

Table 2.16 Selected bond lengths (Å) and bond angles (°) for complex 6.

Ti$_1$-O$_1$	1.829(7)	Ti$_2$-O$_1$	1.866(7)
Ti$_1$-O$_2$	1.867(9)	Ti$_2$-O$_2$	1.838(8)
Ti$_1$-O$_{12\_1}$	1.905(9)	Ti$_2$-O$_{12\_3}$	1.963(9)
Ti$_1$-O$_{12\_2}$	1.965(9)	Ti$_2$-O$_{12\_4}$	1.851(9)
Ti$_1$-N$_{29\_1}$	2.234(9)	Ti$_2$-N$_{29\_3}$	2.139(9)
Ti$_1$-N$_{29\_2}$	2.130(9)	Ti$_2$-N$_{29\_4}$	2.25(1)
O$_1$-Ti$_1$-O$_2$	82.8(3)	O$_1$-Ti$_2$-O$_2$	82.6(3)
O$_{12\_1}$-Ti$_1$-O$_2$	103.1(4)	O$_{12\_3}$-Ti$_2$-O$_2$	90.6(4)
O$_{12\_1}$-Ti$_1$-O$_1$	110.5(4)	O$_{12\_3}$-Ti$_2$-O$_1$	166.7(3)
N$_{29\_1}$-Ti$_1$-O$_2$	86.8(3)	N$_{29\_3}$-Ti$_2$-O$_2$	100.7(4)
N$_{29\_1}$-Ti$_1$-O$_1$	165.8(3)	N$_{29\_3}$-Ti$_2$-O$_1$	90.4(3)

This dimeric structure may be generated by hydrolysis of a Ti(salen)(O^{i}Pr)$_2$ (Figure 2.27). The oxo bridges are formed after two (O^{i}Pr) groups from each monomer have been left as HO^{i}Pr in the presence of water.

$$2Ti(\mathbf{S2})(O^iPr)_2 \ + \ 2H_2O \longrightarrow (\mathbf{S2})Ti\underset{O}{\overset{O}{<>}}Ti(\mathbf{S2}) \ + \ 4HO^iPr$$
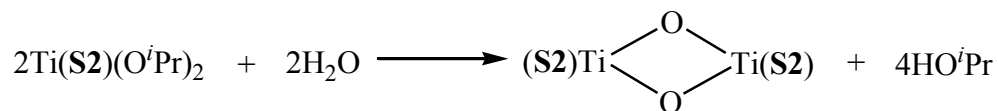
Figure 2.27 Possible hydrolysis reaction of complex 6.

2.6.4. Ti-dimer with di-oxo-bridges of complex 7

In order to gain further structural information of salen-Ti(O^{i}Pr)$_2$, numerous attempts have been made to obtain a crystal suitable for X-ray single crystal diffraction. Unfortunately, a partial hydrolysis product has been isolated.

The crystal structure of complex **7** (Figure 2.28) is characterized as a dimer containing a central four-membered Ti$_2$O$_2$ ring, which is structurally similar to complex **6**. The Ti$_2$O$_2$ core is a nearly planar, distorted square. The four Ti-O bonds within the ring are not of equal lengths, instead there are two equally short Ti-O (1.837 Å, *trans* to a N atom of salen ligand) and the other two equally long Ti-O bonds (1.868 Å, *trans* to an O atom of salen ligand).

The Ti(**S3**)-μ-O moieties are identical to each other. The titanium center is octahedrally coordinated, and the salen ligand adopts a *cis*-β configuration. Generally, in a *bis*-bridged dimeric complex as occurred in complex **7**, two bridging oxo groups have to occupy the positions *cis* to each other, which makes the planar, *trans* structure impossible. Each Ti(salen) unit exhibits *M*-helicity. The dihedral angles between the naphthyl units in the backbone decrease upon metallation, to 69.2° for the complex from 103.1° for the free ligand. Significant π-π stacking is observed between phenylthryl planes from two ligands. The C-centroid distance is approximate in 3.4 Å.

The crystallographic analysis shows that the two Ti(salen) units are homochiral, with both having an *R*-stereocenter and Δ–configuration. The two salen ligands are oriented *syn* to each other, giving selectively the syn-Δ-(*R*)-Δ-(*R*) stereoisomer. The Δ-configuration is derived from the presence of (*R*)-binaphthyl backbone within the salen ligand. The formation of the *syn*-conformation is the result of the different Ti-O$_{oxo}$ bond lengths in the central ring (1.837 and 1.868 Å). Each Ti-O-Ti bridge must contain one long and one short Ti-O bonds to form a least

distorted structure for the Ti_2O_2 core. If both salen ligands have the same configuration, only a *syn*-dimer can make the Ti-O-Ti bridge possible.[15] Selected bond distances and angles are shown in Table 2.17.
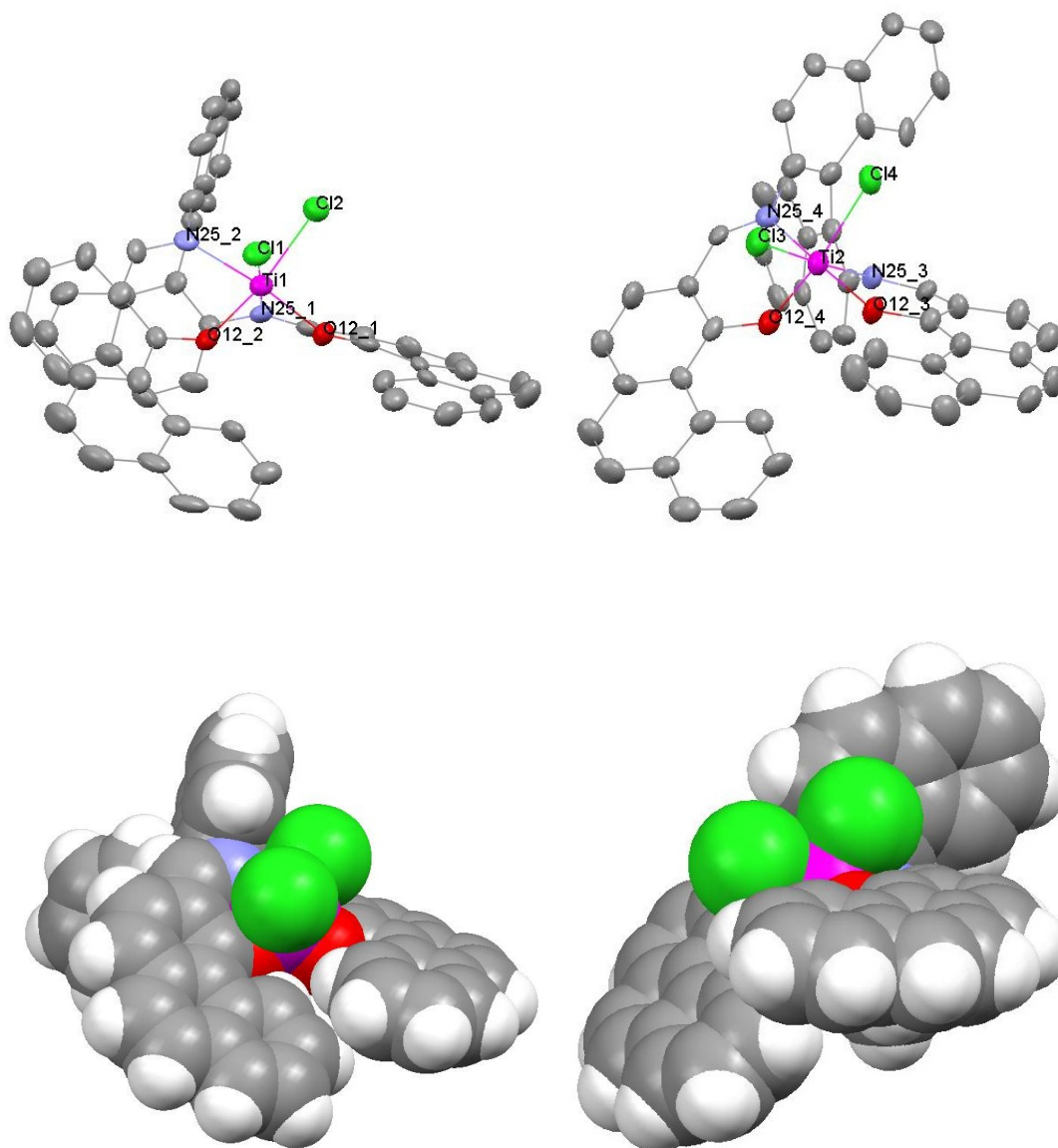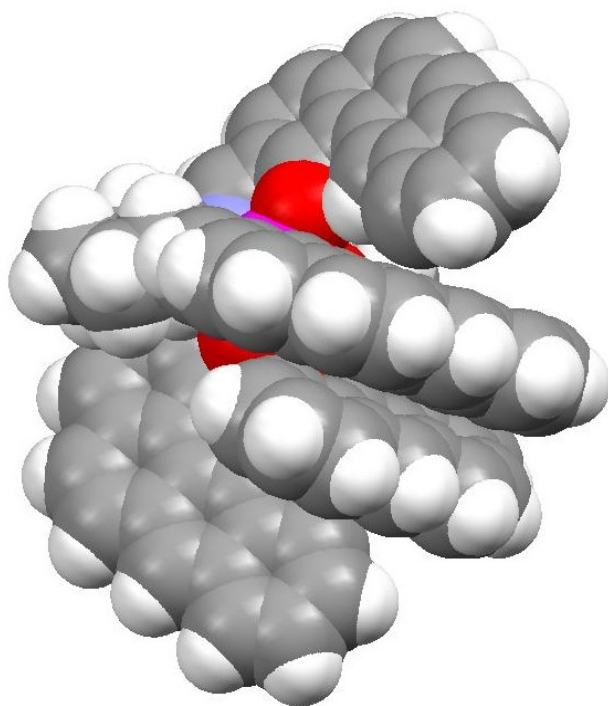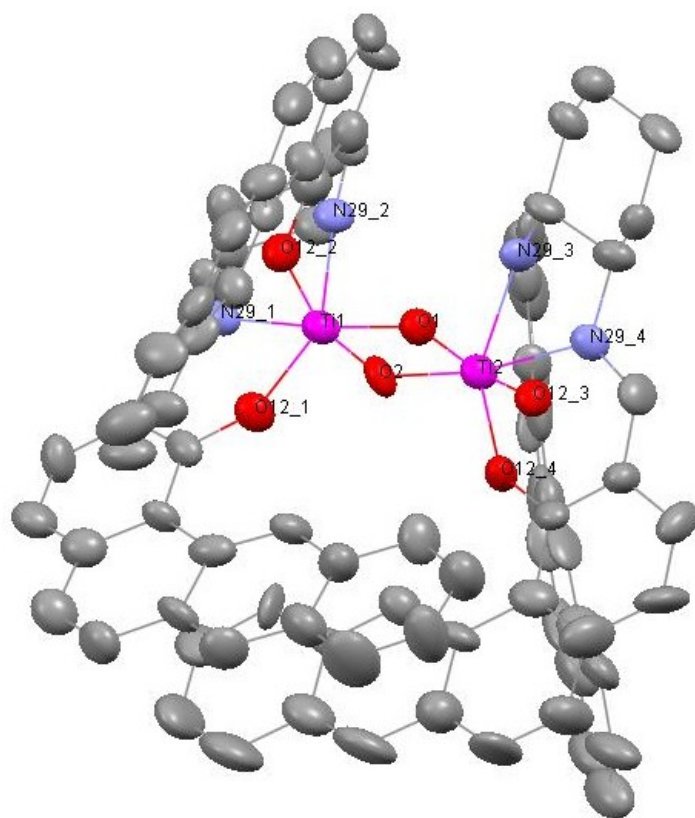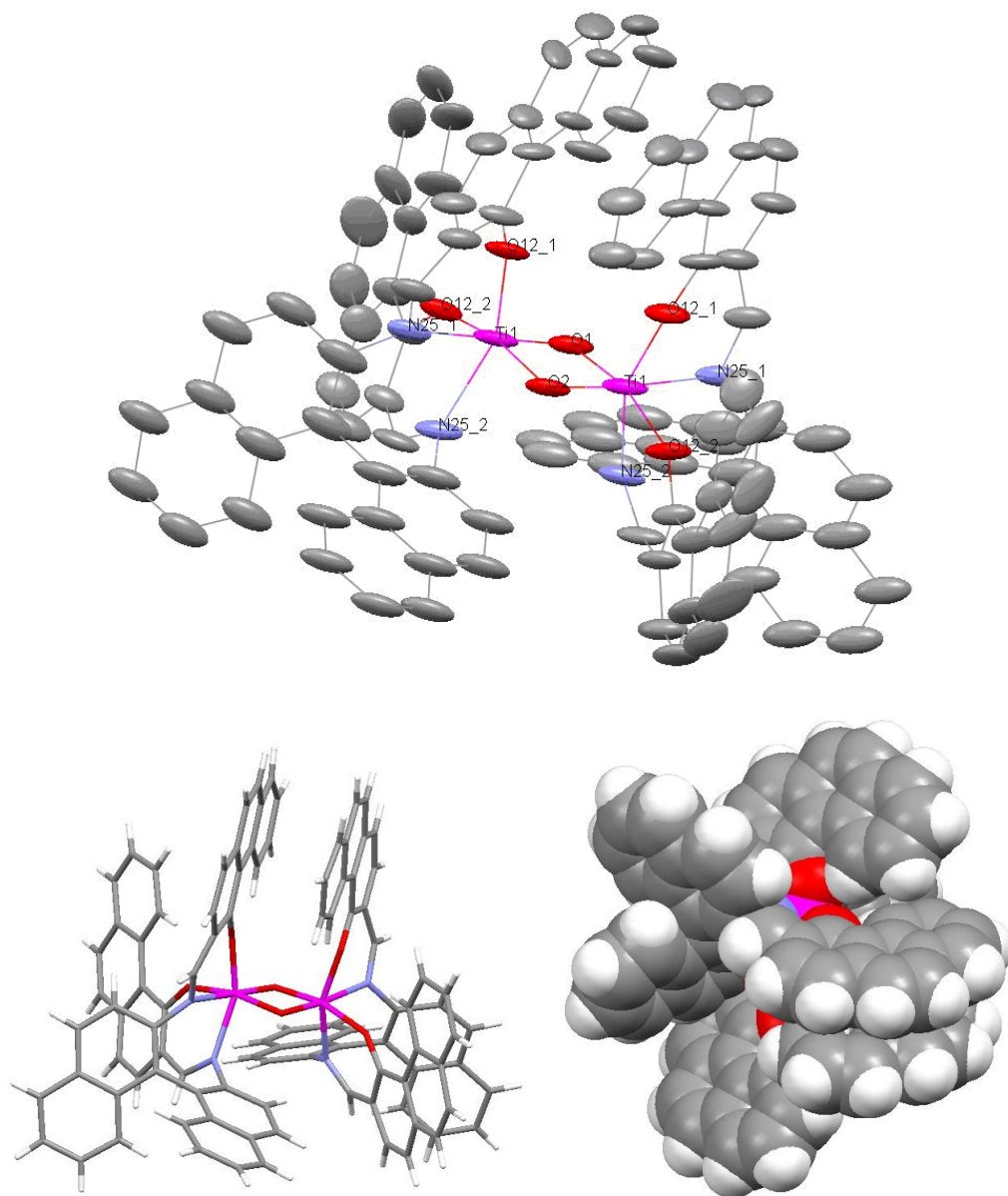

Figure 2.28 Structure of complex 7: top, thermal ellipsoid plot (50% probability, H omitted for clarity); bottom left and right are stick and space filling models.

Table 2.17 Selected bond lengths (Å) and bond angles (°) of complex 7.

Ti_1-O_1	1.837(5)	Ti_1-O_2	1.868(3)
$Ti_1-O_{12\_1}$	1.897(3)	$Ti_1-O_{12\_2}$	1.957(3)
$Ti_1-N_{25\_1}$	2.299(7)	$Ti_1-N_{25\_2}$	2.209(4)
$O_1-Ti_1-O_2$	82.0(2)	$O_{12\_1}-Ti_1-O_2$	102.3(2)
$O_{12\_1}-Ti_1-O_1$	99.0(2)	$O_{12\_2}-Ti_1-O_2$	164.9(2)
$O_{12\_2}-Ti_1-O_1$	93.4(2)	$N_{25\_1}-Ti_1-O_2$	93.1(2)
$N_{25\_1}-Ti_1-O_1$	174.2(2)	$N_{25\_2}-Ti_1-O_2$	87.5(2)
$N_{25\_2}-Ti_1-O_1$	106.0(2)		

The dimeric structures may be generated by hydrolytic cleavage of the (O^{i}Pr) groups of the Ti(salen) (O^{i}Pr)$_2$. It is proposed by Belokon[15,16] that a bimetallic Ti complex bearing two identical chiral salens selectively give *syn-*Δ stereoisomer, if the backbone of chiral salen has an absolute *R* configuration. The stereochemistry of complexes **6** and **7** is as expected on the basis of the proposal.

2.7. Asymmetric epoxidation

No epoxides have been detected by ^{1}H NMR in the products of asymmetric epoxidation of olefins when complexes **1**-**8** have been used as catalysts (Figure 2.29).
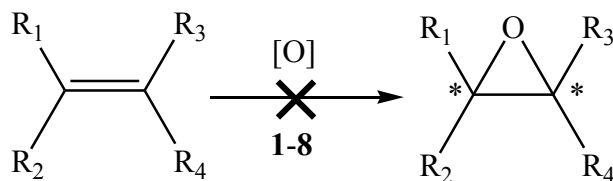
Figure 2.29 Unseccessful asymmetric epoxidation catalyzed by complexes 1-8.

Trans-β-methyl styrene, styrene and indene are used as substrates. Though different reaction conditions have been applied, such as reaction solvents (CH_2Cl_2 and CH_3CN), buffer solutions (pH 7.4 and 8.3), heating, complex loading (0.2 and 0.5 %mol) and oxidants (iodosylbenzene and aqueous H_2O_2), no epoxide is produced. It was found by Katsuki[10,17] that Ti(salen) complexes can not catalyze olefin epoxidation, while Ti(salan)/Ti(salalen) (salan and salalen are fully and half reduced salen analogous) can serve as an efficient catalyst in asymmetric epoxidation of unfunctionalized olefin. In addition, a μ-oxo-μ-$η^2$:$η^2$-peroxo bis-Ti(salan) complex (Figure 2.30, left)[17] is formed when treated with H_2O_2 in the absence of olefin, which is believed as a reservoir of active species in AE.

hydrogen-bonded peroxo-active with Ti(salalen) or Ti(salan)

peroxo-inactive with Ti(salen)
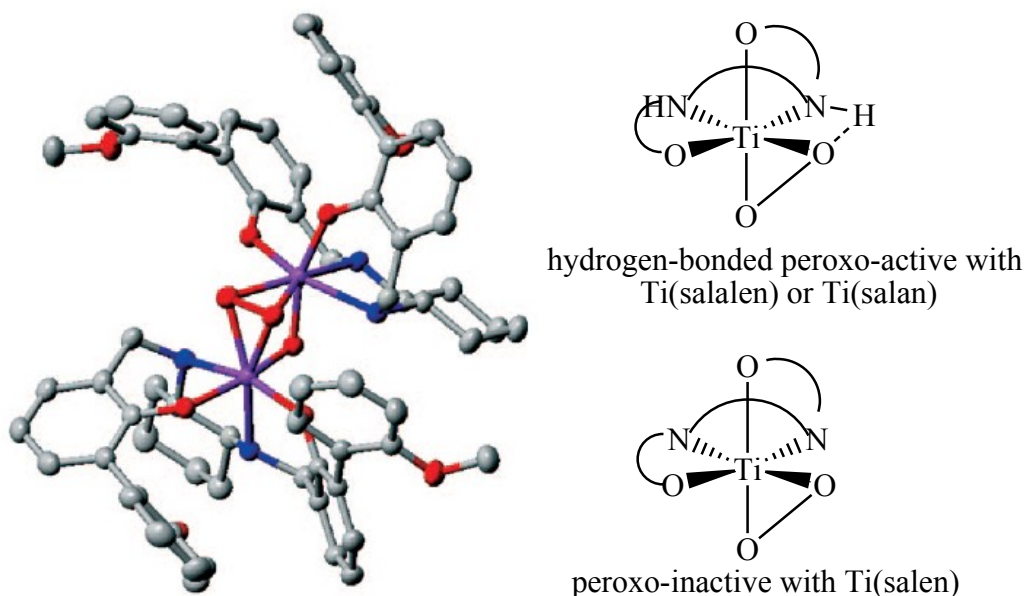
Figure 2.30 Putative explanation of unsuccessful AE catalyzed by complexes 1-8.[18]

They propose that during oxidation, the peroxotitanium species activated is by intramolecular hydrogen bonding with the amino proton, which is proposed to be the active species (Figure 2.30, top right). In the case of salen that contains two imine groups, no hydrogen

can be provided to form such bonding, which may be the main reason for the inert catalytic ability in AE (figure 2.30, bottom right).

2.3 Conclusion and future work

A series of helical Ti(IV)-salen complexes with chiral salen ligands have been synthesized and characterized. ESI-MS reveals that both mononuclear and dinuclear species are present, depending on the ionization methods. ^{1}H NMR studies show that in most cases (complexes **1-6**), one major species exists in the solution with *cis*-β octahedral geometry except complex **1**. While two species found in the solution of complexes **7** and **8**, indicating both the salen and non-salen lingands chelating to the Ti center would affect the solution behavior. And some crystallographic analyses further confirm some of the NMR results. Some dimeric structures (complex **3** with mono μ–oxo bridge, and complexes **6** and **7** with di-μ-oxo bridges) are consistent with previous studies. All the titanium(salen) complexes **1-8** failed in the dimerization and show no catalytic ability in the AE of olefin, and the absence of hydrogen bond in the peroxo species is proposed as the reason.

New reactions will be tried using complexes **1-8** as catalysts, such as sulfoxidation, and aldehyde addition. Meanwhile, titanium(salan) and titanium(salalen) complexes will be synthesized based on the current salens, and will be applied in catalytic AE and other reactions as well.

2.4 References

1. Zhou, Z., Li, Z., Wang, Q., Liu, B., Li, K., Zhao, G., Zhou, Q., Tang, C. (salen)Ti(IV)

complex catalyzed asymmetric ring-opening of epoxides using dithiophosphorus acid as the nucleophile. *J. Organometa. Chem.* **2006**, 691, 5790-5797.

2. Belokon, Y. N., Hunt, J., North, M. Asymmetric catalysis of carbon-carbon bond forming reactions using amino acid-derived C_1-symmetrical salen ligands. *Tetrahedron: Asymm.* **2008**, 19, 2804-2815.

3. Matsumoto, K., Saito, B., Katsuki, T. Asymmetric catalysis of metal complexes with non-planar ONNO ligands: salen, salalen and salan. *Chem. Comm.* **2007**, 3619-3627.

4. Achard, T. R. J., Clutterbuck, L. A., North, M. Asymmetric catalysis of carbon-carbon bond-forming reactions using metal(salen) complexes. *Synlett.* **2005**, 12, 1828-1847.

5. Niemeyer, J., Cloppenburg, J., Frohlich, R., Kehr, G., Erker, G. Salen-ligands based on a planar-chiral hydroxyferrocene moiety: synthesis, coordination chemistry and use in asymmetric silylcyanation. *J. Organometa. Chem.* **2010**, 695, 1801-1812.

6. Belokon, Y. N., Clegg, W., Harrington, R. W., North, M., Yong, C. *In situ* formation of heterobimetallic salen complexes containing titanium and/or vanadium ions. *Inorg. Chem.* **2008**, 47, 3801-3814.

7. Banerjee, P., Pandey, O. P., Sengupta, S. K. Microwave assisted synthesis, spectroscopic and antibacterial studies of titanocene chelates of Schiff bases derived from 3-substituted-4-amino-5-hydrazino-1,2,4-triazoles. *Transition Meta. Chem.* **2008**, 33, 1047-1052.

8. Belokon, Y. N., Green, B., Ikonnikov, N., Larichev, V. S., Lokshin, B. V., Moscalenko, M. A., North, M., Orizu, C., Peregudov, A. S., Timofeeva, G. I. Mechanistic investigation of the asymmetric addition of trimethylsilyl cyanide to aldehydes catalyzed by dinuclear chiral (salen)titanium complexes. *Eur. J. Org. Chem.*, **2000**, 2655-2661.

9. Belokon, Y. N., Chusov, D., Peregudov, A. S., Yashkina, L. V., Timofeeva, G. I., Maleev, V.

I., North, M., Kagan, H. B. Asymmetric *meso*-epoxide ring-opening with trimethylsilyl cyanide promoted by chiral binuclear complexes of titanium. Dichotomy of C-C versus C-N bond formation. *Adv. Synth. Catal.* **2009**, 351, 3157-3167.

10. Saito, B., Katsuki, T. Mechanistic consideration of Ti(salen)-catalyzed asymmetric sulfoxidation. *Tetadedron Lett.* **2001**, 42, 8333-8336.

11. Belokon, Y. N., Blacker, A. J., Carta, P., Clutterbuck, L. A., North, M. Synthetic and mechanistic studies on asymmetric cyanohydrin synthesis using a titanium(salen) bimetallic catalyst. *Tetrahedron* **2004**, 60, 10433-10447.

12. Soriente, A., De Rosa, M., Lamberti, M., Tedesco, C., Scettri, A., Pellecchia, C. Synthesis, crystal structure and application in regio- and stereoselective epoxidation of allylic alcohols of a titanium binapthyl-bridged Schiff base complex. *J. Mol. Cata. A: Chem.* **2005**, 235, 253-259.

13. Chen, H., White, P. S., Gagne, M. R. Synthesis and reactivity of titanium(IV)-salen complexes containing oxygen and chloride ligands. *Organometallics* **1998**, 17, 5358-5366.

14. Niemeyer, J., Kehr, G., Frohlich, R., Erker, G. Salen ligands revisited: synthesis and application of a planar chiral "Ferro-salen" ligand. *Eur. J. Inorg. Chem.* **2010**, 680-684.

15. Belokon, Y. N., Clegg, W., Harrington, R. W., Young, C., North, M. Aymmetric cyanohydrin synthesis using heterobimetallic catalysts obtained from titanium and vanadium complexes of chiral and achiral salen ligands. *Tetrahedron* **2007**, 63, 5287-5299.

16. Belokon, Y. N., Caveda-Cepas, S., Green, B., Ikonnikov, N., Khrustalev, V. N., Larichev, V. S., Moscalenko, M. A., North, M., Orizu, C., Tararov, V. I., Tasinazzo, M., Timofeeva, G. I., Yashkina, L. V. The asymmetric addition of trimethylsilyl cyanide to aldehydes catalyzed by chiral (salen)titanium complexes. *J. Am. Chem. Soc.* **1999**, 121, 3968-3973.

17. Kondo, S., Saruhashi, K., Seki, K., Matsubara, K., Miyaji, K., Kubo, T., Matsumoto, K., Katsuki, T. A μ–oxo-μ-η^2:η^2-peroxo titanium complex as a reservoir of active species in asymmetric epoxidation using hydrogen peroxide. *Angew. Chem. Int. Ed.* **2008**, 47, 10195-10198.

Chapter 3 - Synthesis, characterization and study of manganese(salen) complexes

3.1. Introduction

The chemistry of manganese in various oxidation states is currently attracting much attention owing to its importance in many enzymatic systems such as superoxide dismutase, catalase and photosystem II (PSII).[1] The oxygen evolving complex (OEC) of PSII (Figure 3.1), which is found in the thylakoid membrane of plants and algae, is critical to life, since almost all dioxygen on earth is generated by OEC-catalyzed water oxidation reaction. The active site of OEC is believed to be a cubane-like Mn_3CaO_4 cluster, coordinated with a fourth Mn ion by a mono-μ-oxo bridge.[1]
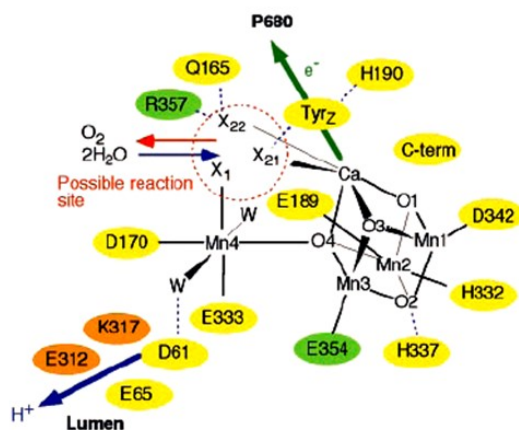
Figure 3.1 Scheme of theOEC mechanism in photosystem II.[1]
Residues in D1, D2 and CP43 subunits are shown in yellow, orange and green, respectively. X_1, X_{21} and X_{22} are possible substrate water binding positions to Mn and Ca. Possible water is indicated as W. Possible hydrogen bonds are shown as light-blue dotted lines.

The short Mn-Mn distance (2.7 Å, quite similar to manganese dimers with Mn_2O_2 cores) and relatively high oxidation states during catalytic cycle lead to increasing interests in high-valent oxo-bridged polynuclear manganese complexes, which can be regarded as the structural model to mimic the OEC and as candidates for water oxidation catalysts.[1]

Epoxides are versatile building blocks in organic synthesis, since a wide range of regio- and stereo-selective ring opening reactions are available to convert the epoxides to useful intermediates. Asymmetric epoxidation is the most straightforward method to prepare chiral epoxides. Since the discovery of Mn(salen) complexes as effective catalysts in epoxidation of olefins by Kochi,[2] a variety of chiral Mn(salen) complexes have been developed and investigated.[3,4,5] The best known Mn(salen) complex is the Jacobsen-Katsuki catalyst, which can enantioselectively transform unfunctionalized olefins to chiral epoxides (Figure 3.2). The selectivity is up to 98% *ee* for *cis* substrates. However, enantioselective epoxidation of *trans* olefins is not satisfactory in the same system (25% *ee* for *trans*-β-methylstyrene).[3, 4]
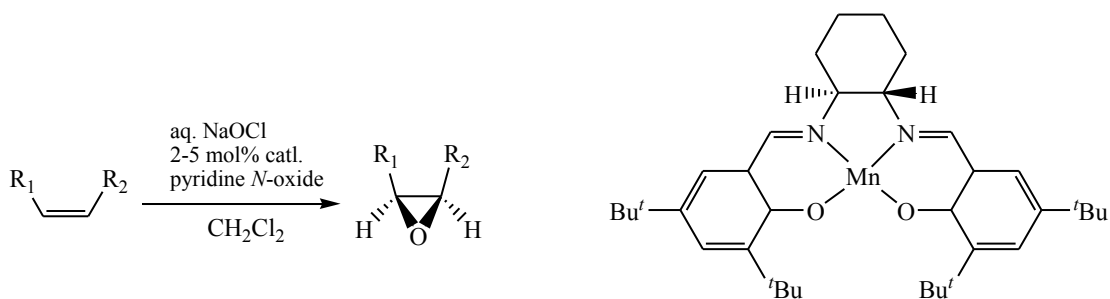
Figure 3.2 Jacobsen's (*S,S*)-Mn(salen) catalyst in asymmetric epoxidation of *cis*-olefins.

It is generally assumed that the enatioselectivity is dominated by the steric interaction between the chial O=Mn(salen) and the olefin. When the olefin substrate is approaching the Mn=O bond at 90° to allow favorable orbital overlap, however one substituent (R_1) from the

trans olefin is directed downwards into the salen ligand, resulting in an unfavorable interaction (Figure 3.3). Higher *ee* values are achieved for *trans*-olefins when the salen is deeply stepped, since the steric repulsion with R_1 is minimized.[5] Mechanistic studies of Mn(salen) complexes indicate that dimeric μ-oxo-bridged species act as reservoir species.[6]
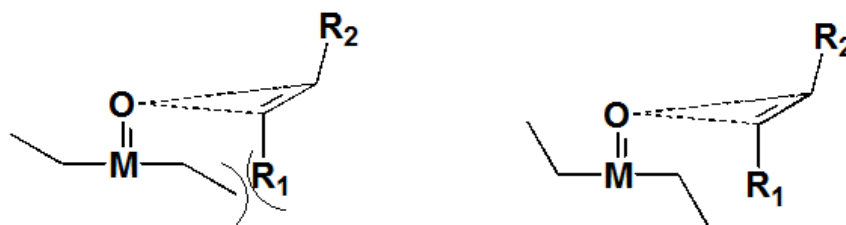
Figure 3.3 *trans*-olefin approach to slightly (left) and deeply (right) stepped Mn(salen).

In this chapter, results of the complexation of helix-directing salen ligands (**H₂S1**, **H₂S2, or H₂S3**) with manganese are presented, and the catalytic activity of complexes for asymmetric epoxidation is tested with *trans*-β-methylstyrene, as well as other unfunctionalized olefins.

3.2. Synthesis of Mn(salen) complexes

Dinuclear paramagnetic Mn(IV)-Mn(IV) (**9-11, 15**) or Mn(III)-Mn(III) (**12-13**) complexes are synthesized by reacting Mn(II) salts (MnCl₂, Mn(CH₃COO)₂ or Mn(NO₃)₂) with equimolar chiral salen ligands **H₂S1**, **H₂S2, or H₂S3**. The reactions were stirred for 18 h in a 2:1 mixture of dichloromethane/ethanol. Complexes were oxidized, without isolation by introducing oxygen gas (Figure 3.4).

$$\text{Mn}^{2+} \text{ salt} + \text{salen ligand (}\mathbf{H_2S}\text{)} \xrightarrow[\substack{\text{CH}_2\text{Cl}_2/\text{EtOH (2:1)} \\ \text{18 h}}]{\substack{\text{1. NaOMe}}} \xrightarrow[\text{2 h}]{\substack{\text{2. O}_2 \text{ gas}}} \text{Mn(salen) complex}$$

H₂S1

H₂S2

H₂S3
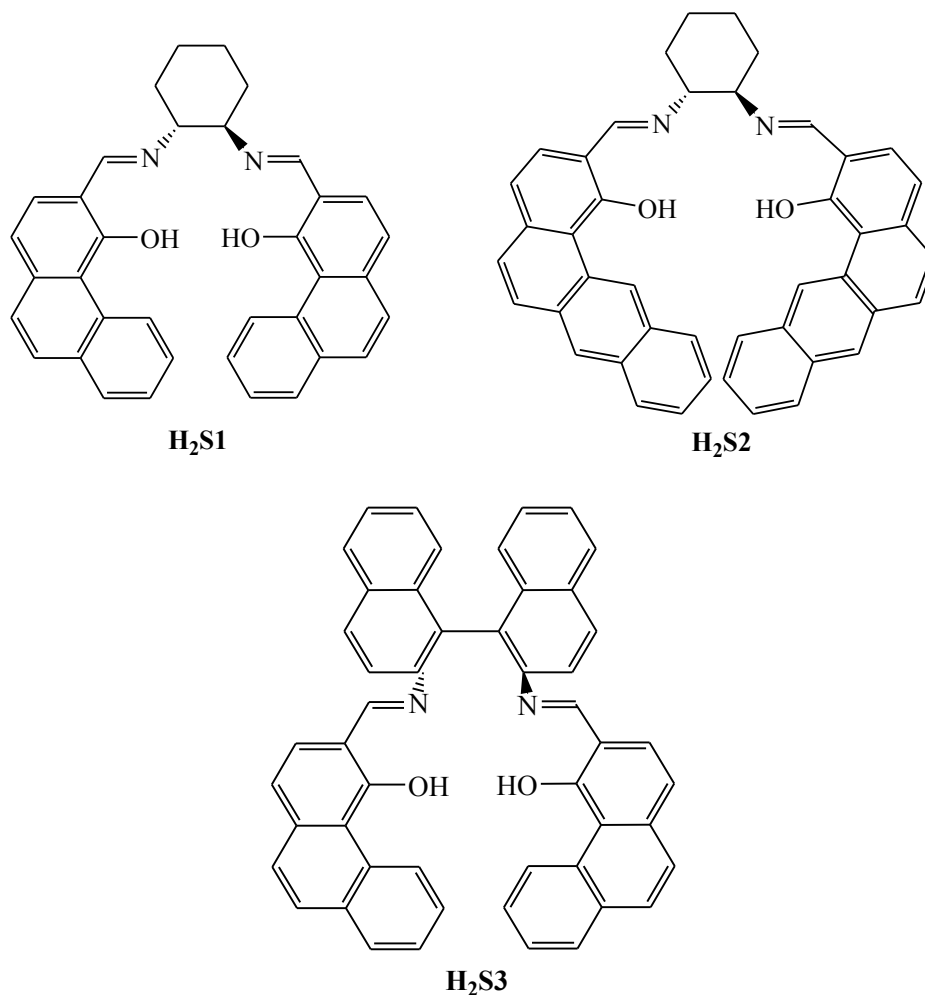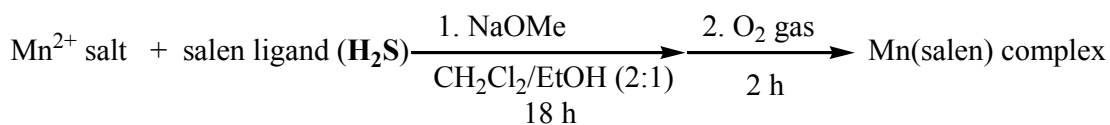
Figure 3.4 Synthesis scheme of Mn(salen) complexes 9-15.

Four equivalents sodium methoxide were added into the reaction mixture. The role of NaOMe is to deprotonate the two phenolic oxygens from the salen ligand to facilitate the metallation. The by-product, methanol, can be easily removed by vacuum drying. The dioxygen gas was bubbled through the pale brown suspension for 2 h to oxidize Mn(II) to higher oxidation states. Blackish brown solids are obtained upon Soxhlet extraction in CH₂Cl₂ in moderate yields

(ca. 40%) with high purity. All complexes (**9-15** in Table 3.1) are paramagnetic, characterized by broad ^{1}H NMR spectra (Figure 3.5).

Table 3.1 Synthetic compositions of Mn(salen) complexes 9-15.

Complex	Mn^{2+} salt	Salen ligand
9	$MnCl_2$	H_2S1
10	$Mn(OAc)_2$	H_2S1
11	$Mn(NO_3)_2$	H_2S1
12	$MnCl_2$	H_2S3
13	$Mn(OAc)_2$	H_2S3
14	$Mn(NO3)_2$	H_2S3
15	$MnCl_2$	H_2S2
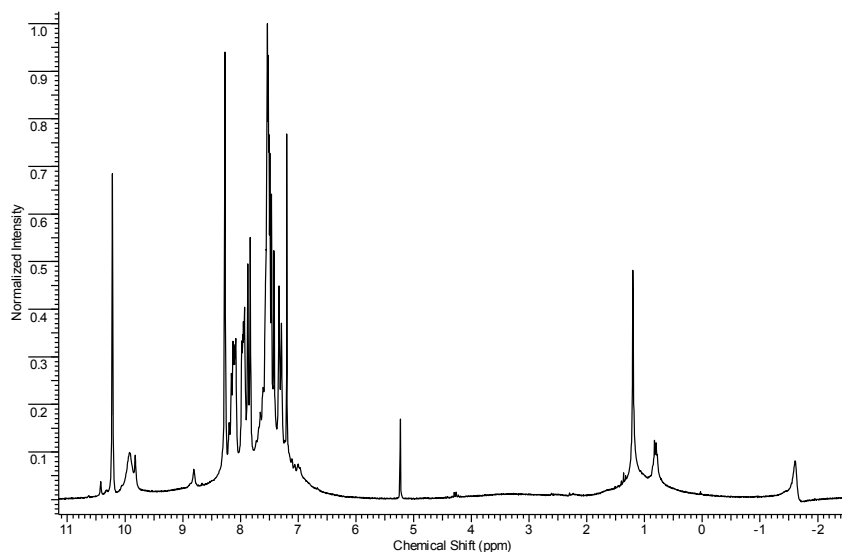
Figure 3.5 ^{1}H NMR spectrum of paramagnetic complex 12 in CDCl$_3$.

All complexes are very soluble in CH_2Cl_2 and dichloroethane, moderately soluble in toluene, THF, ethanol and acetonitrile, but only sparingly soluble in hexane and water. The complexes are also air and moisture-stable.

3.3. Infrared spectra

For dinuclear complexes with the Mn_2O_2 core, characteristic $\upsilon(Mn-O_{oxo})$ absorption bands are observed in the region 630-650 cm^{-1}.[7] This IR band is sensitive to the symmetry around central Mn ions and can be used to distinguish between bridging and chelating Schiff base ligands.[8,9] A sharp unsplit $Mn-O_{oxo}$ absorption band indicates the bridging Schiff base ligands. Such complexes have higher symmetry than the chelating dimer type (Figure 3.6), which have a split Mn-O band.[9]
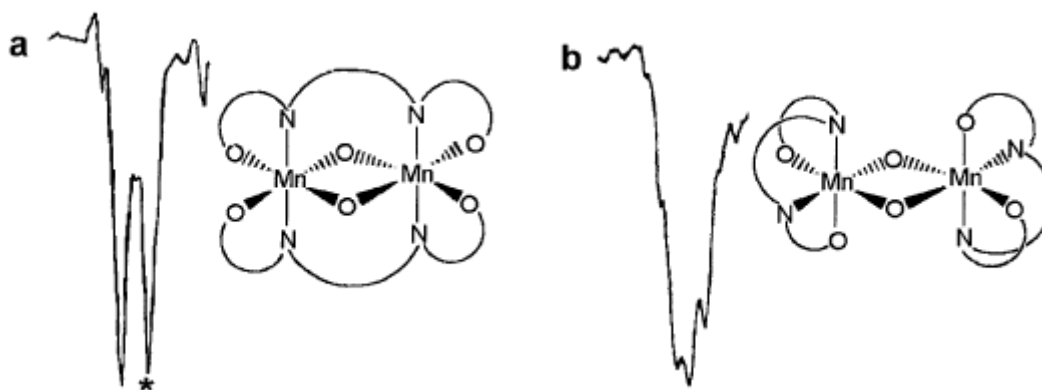
Figure 3.6 IR absorption band for Mn_2O_2 core.[9] (a) sharp unsplit $Mn-O_{oxo}$ band corresponding to bridging ligand; (b) split $Mn-O_{oxo}$ band for chelating Schiff base lignd. The lignad band is marked with an asterisk.

In the IR spectra of complexes **9-11** (Figure 3.7) the $\upsilon(C-O_{phenolate})$ and $\upsilon(C=N_{imine})$ bands shift to lower frequency, 28-30 cm^{-1} and 11-14 cm^{-1}, respectively, compared to the free ligand **H$_2$S1**.
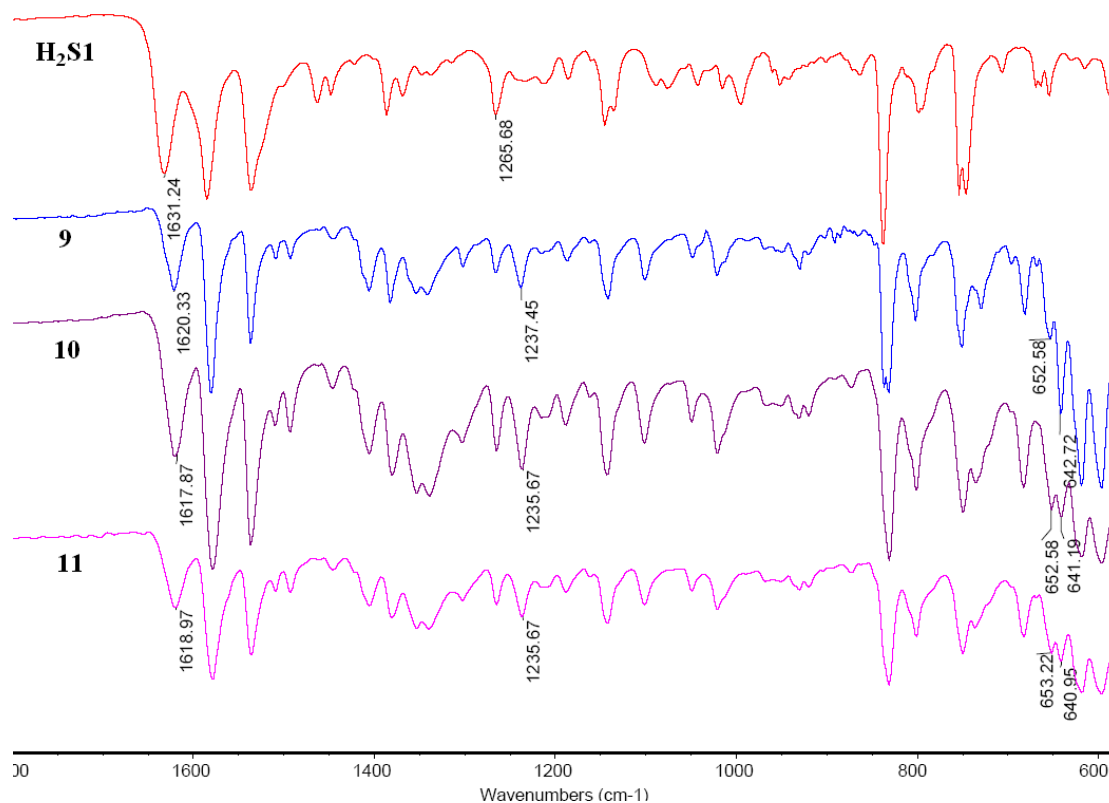
Figure 3.7 IR spectra of free ligand H₂S1 and complexes 9, 10 and 11.

Table 3.2 Characteristic IR absorption bands for free ligand and complexes 9-11.

Compound	$\upsilon(C=N)/cm^{-1}$	$\upsilon(C-O_{phenolate})/cm^{-1}$	$\upsilon(Mn-O_{oxo})/cm^{-1}$
H₂S1	1631	1265	---
9	1620	1237	652, 642
10	1617	1235	652, 641
11	1618	1235	653, 640

These shifts suggest the coordination of the salen ligand in its dianionic form to the metal through the phenol oxygen and the imine N atoms. In addition, the IR spectra exhibit sharp absorption bands with splitting pattern in the region 640-660 cm^{-1}, which can be assigned to $\upsilon(Mn-O_{oxo})$. [7,8,9] All these information indicates the possible existence of dimeric chelating Mn salen complex in the solution, which is in agreement with the solid study in Section 3.6.1.

As compared to **9-11**, the IR spectra of **12-14** (Figure 3.8) display no absorption bands characteristic for a Mn_2O_2 core in the region 600-700 cm^{-1}. The small shifts are observed both in the absorption of C=N and C-O bonds compared to free ligand, indicating the chelation of Mn to the ONNO unit. Furthermore, the spectra exhibit more than one set of bands for the stretches of C=N and C-O bonds (Table 3.3). It is indicated that phenolate oxygen atoms as well as imine nitrogen atoms are located in delicately different chemical environment. The result is consistent with the crystal structural analysis in section 3.6.2, which shows one set of ONNO unit coordinates to Mn(IV) center, one set of ONNO unit to Mn(III)center, and the third set of ONNO unit bridges between Mn(IV) and Mn(III).
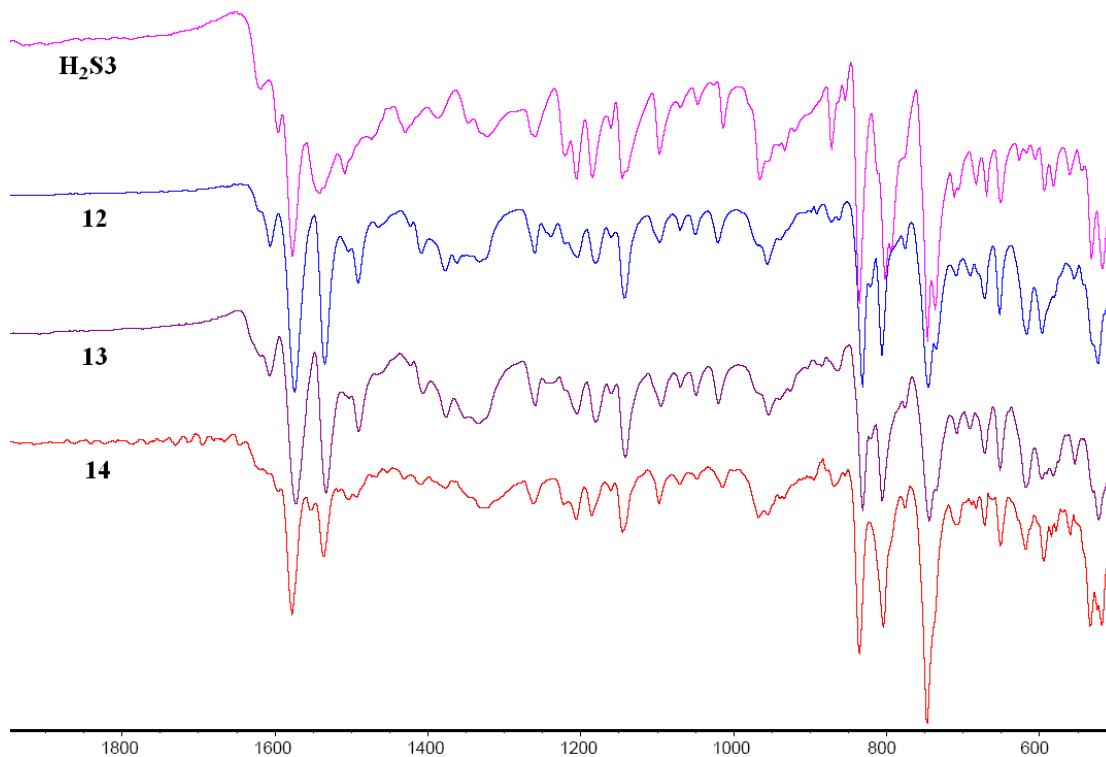
Figure 3.8 IR spectra of free ligand H_2S3 and complexes 12, 13 and 14.

Table 3.3 Characteristic IR absorption bands for complexes 12-14.

Compound	$\upsilon(C=N)/cm^{-1}$	$\upsilon(C-O_{phenolate})/cm^{-1}$
H$_2$S3	1576	1259
12	1605, 1573	1258, 1236
13	1605, 1572	1258, 1237
14	1597, 1576	1258

3.4 Electronic spectra

UV-Vis and circular dichroism (CD) spectra of complexes **9-14** are measured in acetonitrile. For complex **9**, the absorption bands at 440 nm with moderate intensity can be tentatively assigned to the ligand-to-metal charge-transfer transitions from the bridges to the Mn center.[8] The bands at 260 and 330 nm mainly arise from π-π* transitions in the ligand. By comparison the free ligand **H$_2$S1** shows corresponding absorption at 250 and 280 nm (Figure 3.9, left).
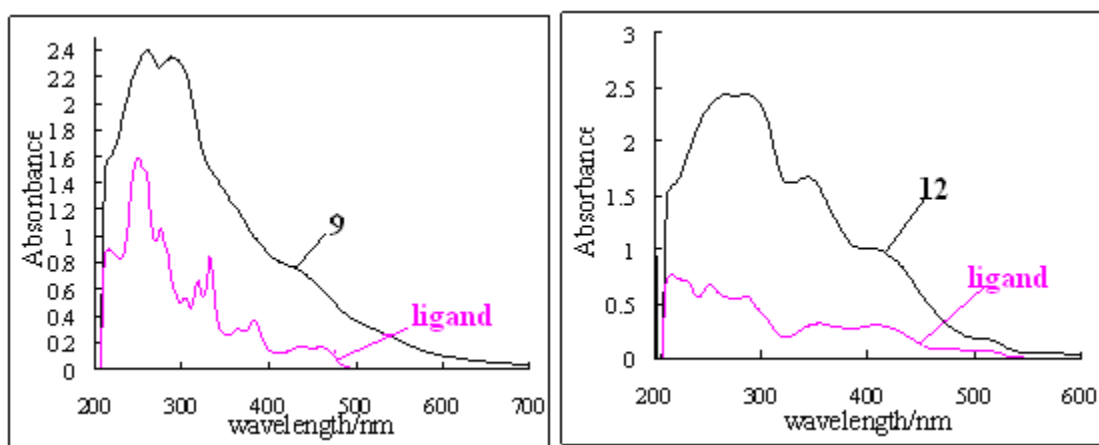
Figure 3.9 UV-vis spectra of complexes and corresponding ligands in acetonitrile. Left, 9 and H$_2$S1; right, 12 and H$_2$S3.

The UV-vis spectrum of **12** (Figure 3.9, right) features a broad absorption centered at 272 nm, along with other absorptions at 340 and 408 nm, which is very similar to that of free **H₂S3** ligand. The absorptions around 272 and 340 nm are tentatively assigned to π-π* transitions of the phenanthrene and imine groups in the ligand, and the bands around 408 to ligands to metal charge-transfer transitions.[8]

The room temperature CD spectra of **9**, **10** and **11** (Figure 3.10) in CH₃CN show similar characteristics: intense positive CD bands at 245-275 nm (π-π* transition of phenolate),[10] medium intensity negative bands at 310 nm (π-π* transition of azomethine),[10] broad bands at 400-410 nm and 450 nm, respectively. The latter two bands (longer than 400 nm) may arise from the charge-transfer transition from metal to ligand (MLCT).[10] Experimental and simulated CD spectra of Zn(**S1**) complex were previously reported from our group (Figure 3.11).[11] The CD patterns of **9-11** match well with the Zn(**S1**) complex in *M* conformation. The similarity of CD bands suggests the salen ligand might be twisted in an *M*-helical manner in **9**, **10** and **11**.
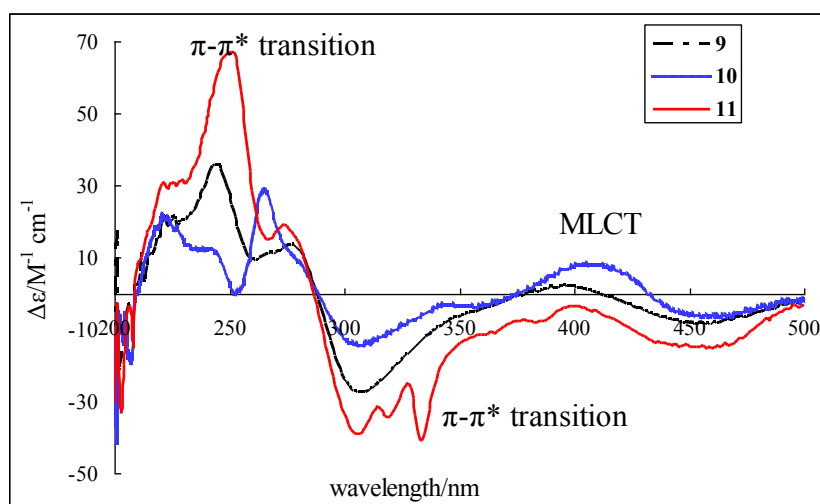
Figure 3.10 Circular dichroism (CD) spectra of complexes 9 (dashed), 10 (wavy), 11 (solid) in acetonitrile.
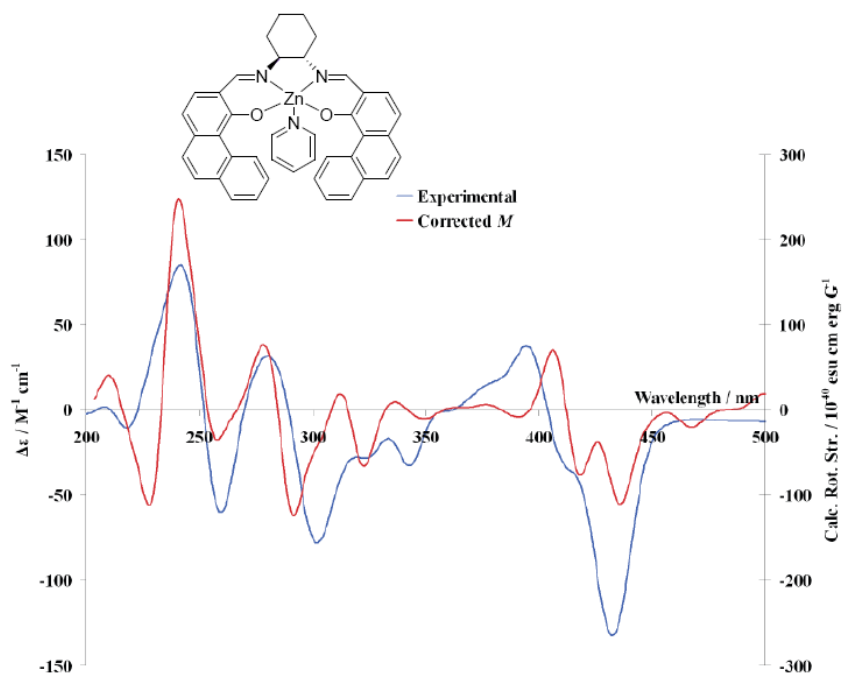
Figure 3.11 Experimental and simulated CD spectra of Zn(S1) complex.[11]

Complexes **12**, **13** and **14** show similar CD spectra (Figure 3.12). According to the previous study of CD of chiral salen complexes,[12] the bands below 300 nm (210, 230, 255 nm) may be assigned to π-π* transition of the phenolate, while the bands around 300-380 nm are due to π-π* transiton of the azomethine group. The bands longer than 400 nm can be assigned to the metal-to-ligand charge-transfer transition (MLCT). Their CD patterns show some similarity to zinc complex with same binaphthayl salen ligand, which has dominant *M* conformer in solution (Figure 3.13).[13] In the solid state study, **12** exit in the *M* helical conformation (section 3.6.2.). DFT simulation of CD spectra needs to be carried out to better understand the helical conformations of the information for manganese salen complexes in solution.
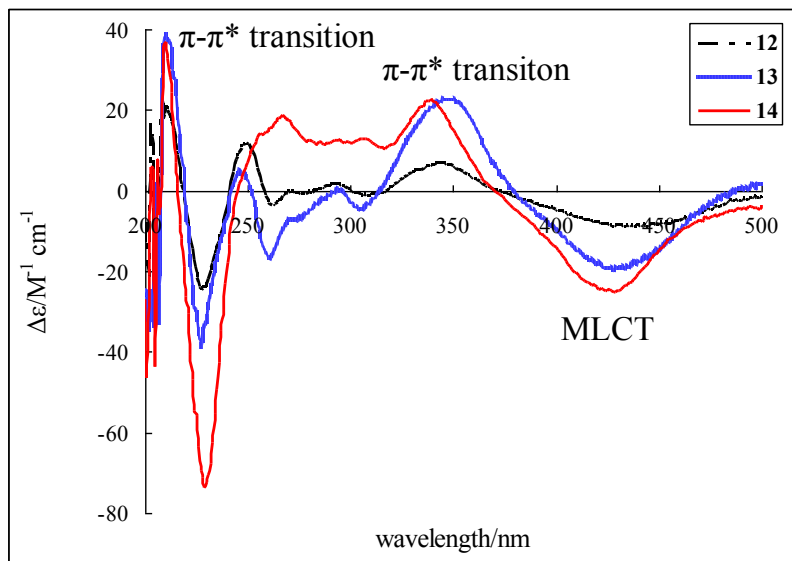
Figure 3.12 Circular dichroism (CD) spectra of complexes 12 (dashed), 13 (wavy) and 14 (solid) in acetonitrile.
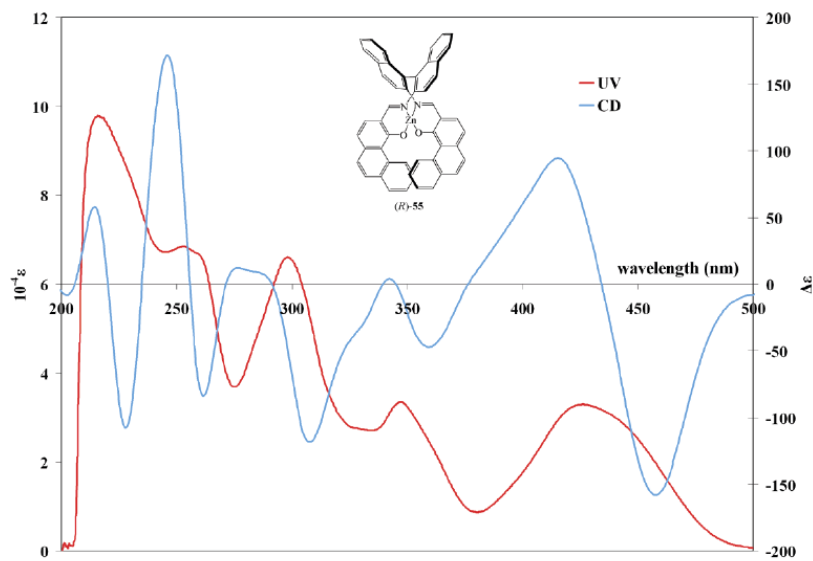
Figure 3.13 UV-CD spectrum of Zn(S3) complex.[13]

3.5. Mass spectrometric studies

Mass spectroscopy can directly measure the molecular weight of a molecular ion/fragment derived from a complex. In addition, the isotopic pattern may be quite distinct which can help to identify the compositions of species in solution.

The mass data of **9-11** were collected in acetonitrile by HR-ESI-MS and all the spectra are very similar to each other (Figure 3.14). In **10**, the spectra indicate the formation of a mixture of predominant $[CH_3CN-Mn^{III}(\mathbf{S1})]^+$ (*m/z* 616.1809, 1.9 ppm), $[Mn^{III}(\mathbf{S1})]^+$ (*m/z* 575.1537, 1.0 ppm) monomeric species. In addition, the dimeric species $\{[Mn^{IV}_2(\mathbf{S1})_2O_2]+H\}^+$ (*m/z* 1183.2992, 4.0 ppm) also has moderate intensity in the mass spectrum, consistent with the X-ray structural analysis (section 3.6.1).

Figure 3.14 Entire mass spectrum (left), experimental (middle) and simulated (right) isotopic patterns of major species (top, [Mn^{III}(S1)]⁺; bottom, [CH₃CN-Mn^{III}(S1)]⁺ of 10.

This observation suggests that the mononuclear Mn(III) complex ions are the major species in solution, and the formation of dinuclear Mn(IV) species is less favored in solution. It is reported that the Mn(IV) derivative is not stable and decomposes to the corresponding Mn(III) complex.[14] In addition, pairs of Mn ions can facilitate the formation and dissociation of O-O bonds, which will leads to dimerization.[14] A proposed equilibrium process is shown in Figure 3.15. It can be concluded that in the presence of **H₂S1** ligand, both Mn(III) and Mn(IV) complex ions form and the cationic species with similar characteristic are observed no matter what kind of metal salts are used in the synthesis.

$$(nelas)Mn^{IV} \underset{O}{\overset{O}{\diamondsuit}} Mn^{IV}(salen) \rightleftharpoons Mn^{III}(salen) \; + \; Mn^{V}(salen)(O)_2$$
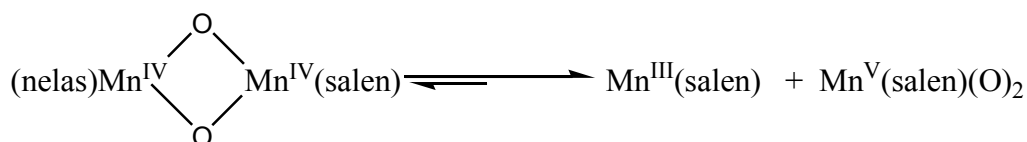
Figure 3.15 Proposed equilibrium between Mn(III) and Mn(IV) species.

The ESI-MS spectra of **12-14** in CH₃CN solution show both salen and half-salen coordinated Mn(III) cations (Figure 3.16). In **13**, [Mn^{III}(**S3**)]$^+$ (*m/z* 745.1660, 3.8 ppm) monomer is the predominant species, and the solvated monomer [CH₃CN-Mn^{III}(**S3**)]$^+$ (*m/z* 786.1938, 1.9 ppm) is also present with medium intensity. In addition, the complex ion {[Mn^{III}(**S3**)(H**S3**)]-H}$^+$ (*m/z* 1437.4133, 1.3 ppm) is also observed. The peak at *m/z* 1233.3553 (1.9 ppm) corresponds to {[Mn^{III}(**S3**)(**S3'**)]-H}$^+$, in which **HS3'** indicates the 1:1 sidearm to backbone condensation product. The peak for half-salen **S3'** appears at *m/z* 489.1945 (4.5 ppm) with high intensity, and the [H₂**S3**-H]$^+$ ion at *m/z* 693.2557 (2.2 ppm) is seen with low intensity. In **12** and **14**, all these species mentioned above are observed. The most obvious difference is the relative intensity of these peaks (Table 3.4).
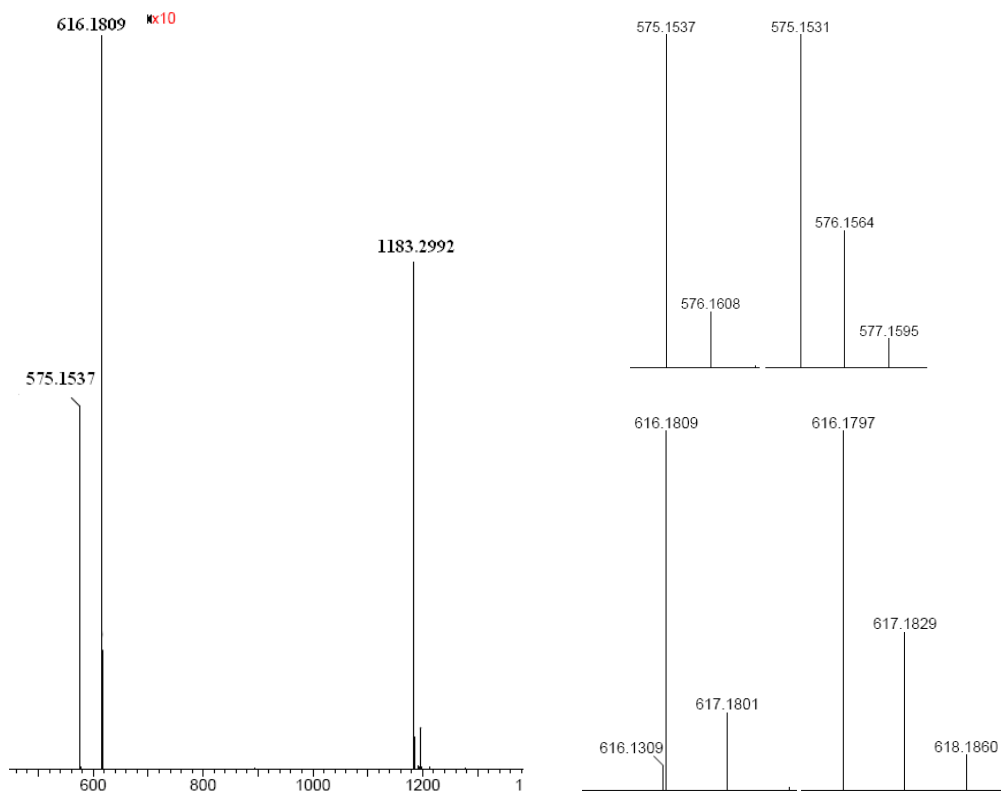
Figure 3.16 Entire mass spectrum (left), experimental (middle) and simulated (right) isotopic patterns of major species (top, $[Mn^{III}(S3)]^+$; bottom, $\{[Mn^{III}(S3)(HS3)]-H\}^+$) of 13.

Table 3.4 %Abundance of major species in complexes 12, 13 and 14.

Observed ions	m/z	% abundance		
		12	**13**	**14**
Half-salen **S3'**	489.1862	32	33	32
Salen **S3**	693.2536	1	<1	36
$[Mn^{III}(S3)]^+$	745.1630	35	23	11
$[CH_3CN-Mn^{III}(S3)]^+$	786.1929	17	7	<1
$\{[Mn^{III}(S3)(S3')]-H\}^+$	1233.3507	8	22	<1
$\{[Mn^{III}(S3)(HS3)]-H\}^+$	1437.4106	6	15	20

In **13** and **14**, the salen **S3** and half-salen **S3'** ions are the most dominant species, respectively. Besides, one peak at *m/z* 285.1370 (2.2 mmu), which can be assigned to the backbone fragment ion from the salen ligand, is present only in **13**. It can be concluded that only Mn(III) complexes form when chelated with the **H₂S3** ligand, and the metal sources seems to

93

influence the degree of ligand **S3** degradation observed, which leads to the difference in the ion distribution.

The HR-ESI-MS of **15** (Figure 3.17) shows the predominant ion peaks corresponding to $[Mn^{III}(S2)]^+$ species at *m/z* 716.2109 (0.1 ppm), and two additional peaks clearly indicate the presence of an acetonitrile adduct $CH_3CN-[Mn^{III}(S2)]^+$ (*m/z* 675.1800, 6.5 ppm) and the dimeric $\{[Mn^{IV}_2(S2)_2O_2]+H\}^+$ (*m/z* 1383.3687, 1.6 ppm) cation with moderate intensity. No evidence for doubly charged ions is found in the mass spectra. No ions derived from the ligand are observed.
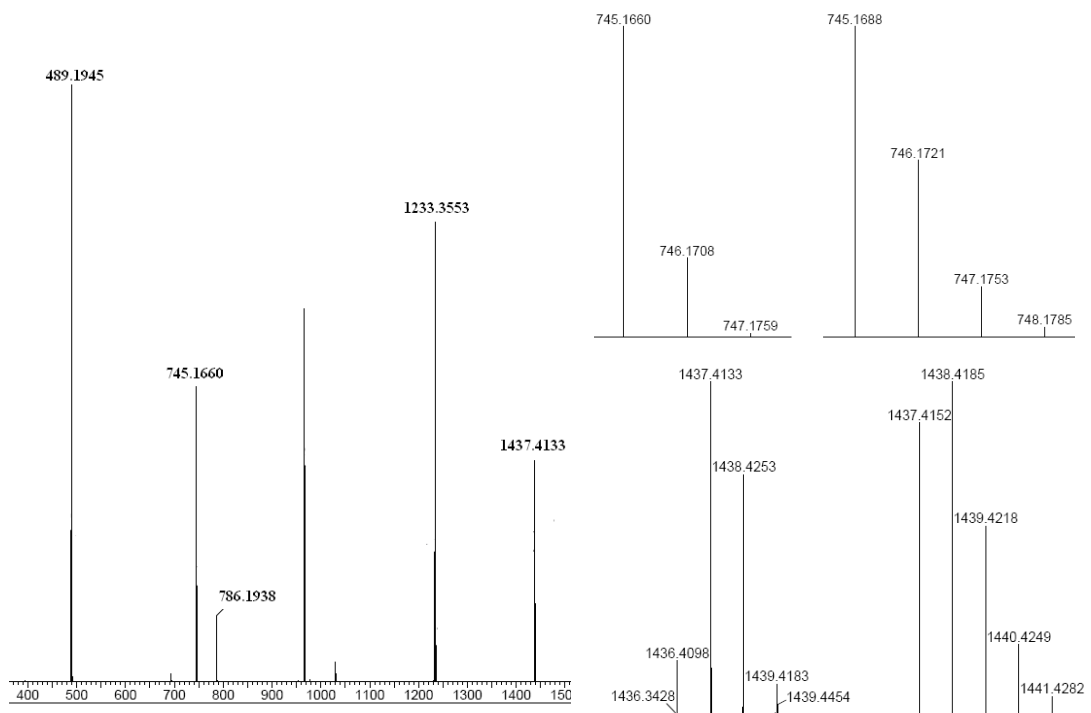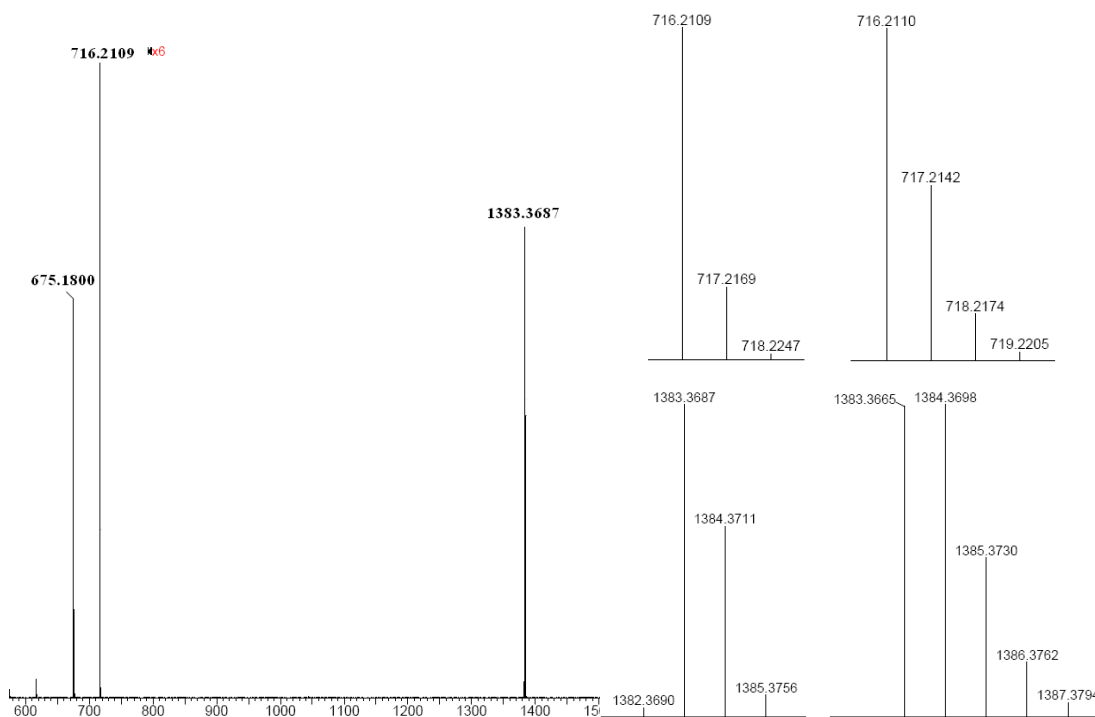

Figure 3.17 Entire mass spectrum (left), experimental (middle) and similated (right) isotope patterns of major species (top, CH$_3$CN-[Mn^{III}(S2)]$^+$; bottom, {[Mn^{IV}$_2$(S2)$_2$O$_2$]+H}$^+$) of 15.

3.6 Crystal structures of Mn(salen) complexes

3.6.1 Solid structure of complex 10

Dark brown X-ray quality crystals of **10** were obtained by slow diffusion of ether into a dichloroethane solution. The structure is shown in Figure 3.18, and selected bond lengths and angles are listed in Table 3.5.

Based on the oxidation number of anions around the metal center, the oxidation state of the two Mn centers was determined to be IV. The Mn(IV) center are d^3 ions and are expected to be spherically symmetric, indicating no significant axial elongation as compared to Mn(III) centers.

Two Mn(IV) centers are bridged by two μ-O groups to yield a planar Mn_2O_2 core. The local coordination environment around each Mn center can be described as a distorted octahedron. Each Mn center is chelated by one ONNO salen ligand, and two μ-O atoms. One phenolate O atom and one imine N atom (O_{12-2} and N_{25_1}, O_{12-3} and N_{25_4}, respectively) and two bridging oxo groups occupy the equatorial plane of the distorted octahedron, while the rest O and N donors in salens occupy the positions *trans* to the bridging oxygens. Both salen ligands wrap around the metal center in *cis*-β conformation and *M* helicity. The distance between two metal centers is 2.759(1) Å, which is in accordance to the reported Mn···Mn distances (2.60-2.78 Å).[15] The bridging Mn-O-Mn angles of (98.18(6)° and 98.03(6)°) are in the range of reported dimanganese(IV) complexes data (95.1-99.5°).[15] A Small variation is observed in Mn-O bridging distances (1.821(1) and 1.823(1) Å to Mn_1, and 1.820(1) and 1.818(1) Å to Mn_2), while both are in the range of reported Mn(IV)/Mn(IV) complexes (1.774-1.826 Å for Mn-O_{oxo} bond).[15] In addition, the Mn-μ-O distances are longer than those of Mn-$O_{phenolate}$ (mean 1.821 Å vs. mean 1.929 Å). The mean Mn-N distances of 2.000 Å and Mn-O distances of 1.850 Å are unexceptional and typical of similar Mn(IV) systems.[15]
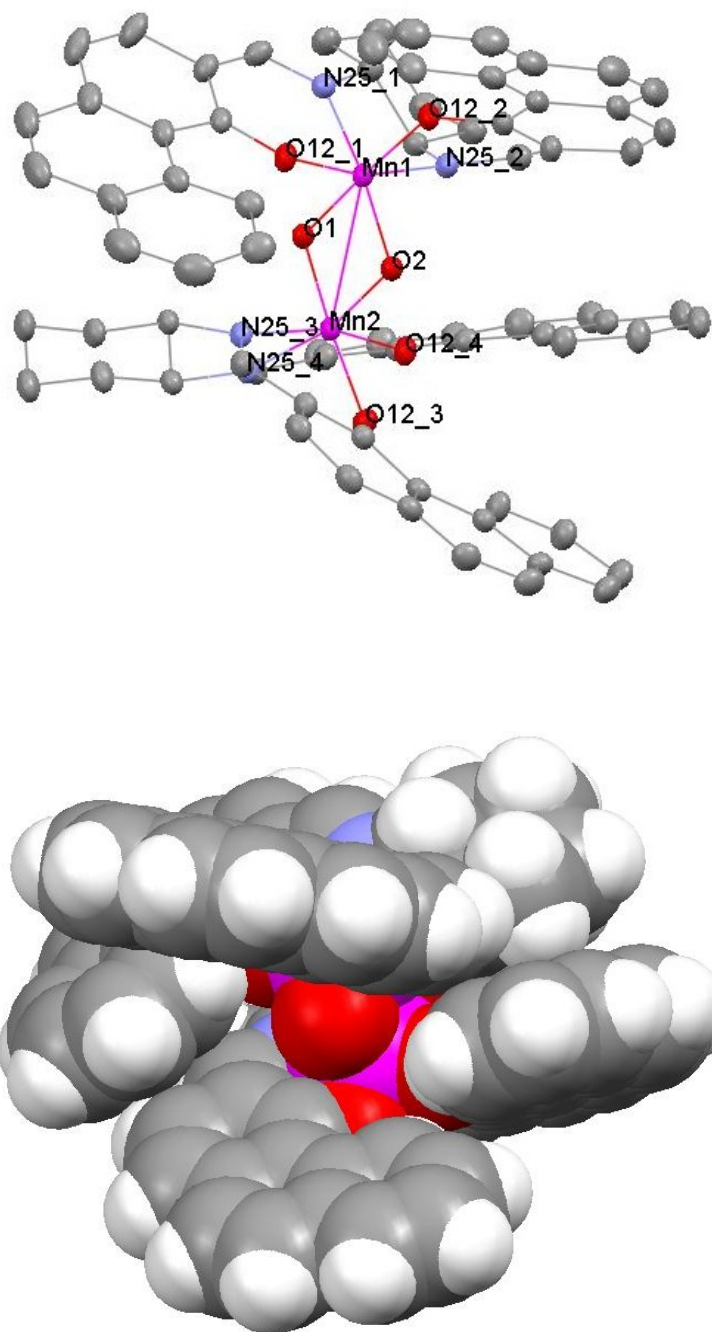
Figure 3.18 Structure of complex 10: top, thermal ellipsoid plot (50% probability, H and noncoordinated solvent omitted for clarity); bottom, space filling model.

Table 3.5 Selected bond lengths (Å) and bond angles (°) of complex 10 grown in N_2.

Mn_1-O_{12_1}	1.902(1)	Mn_2-O_{12_3}	1.936(1)
Mn_1-O_{12_2}	1.927(1)	Mn_2-O_{12_4}	1.917(1)
Mn_1-N_{25_1}	2.032(2)	Mn_2-N_{25_3}	1.985(1)
Mn_1-N_{25_2}	1.978(2)	Mn_2-N_{25_4}	2.048(2)
Mn_1-O_1	1.821(1)	Mn_2-O_1	1.818(1)
Mn_1-O_2	1.823(1)	Mn_2-O_2	1.820(1)
Mn_1-O_1-Mn_2	98.18(6)	Mn_1-O_2-Mn_2	98.03(6)
O_{12_1}-Mn_1-N_{25_2}	165.24(6)	O_{12_4}-Mn_2-N_{25_3}	163.69(6)

It is also found that the crystal of **10** grown under inert atmosphere shows similar characteristic to that grown in the air (Figure 3.19) and the crystal structure of **11** (Figure 3.20) is quite comparable to two crystals of **10**.
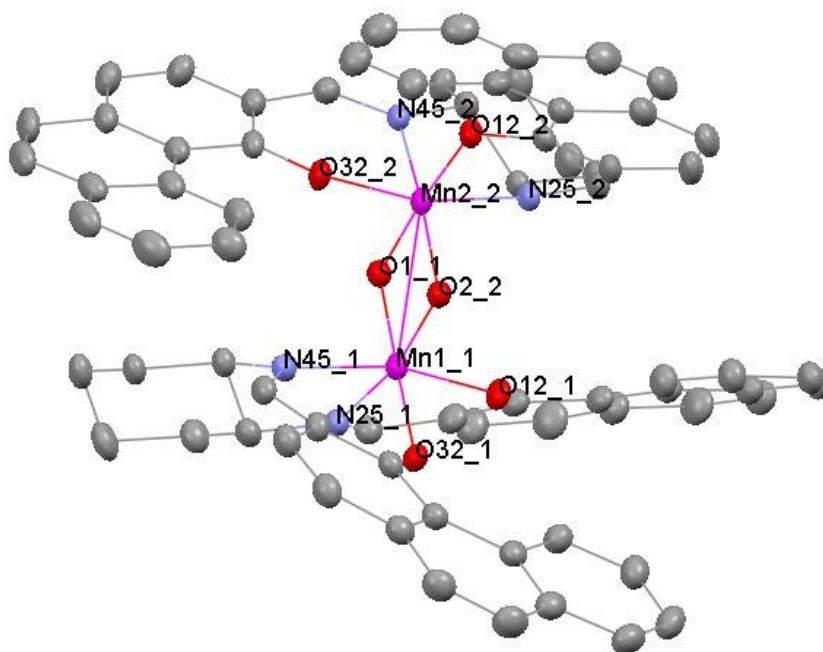
Figure 3.19 Thermal ellipsoid plot of complex 10 grown in air. (50% probability, H and noncoordinated solvent omitted for clarity).
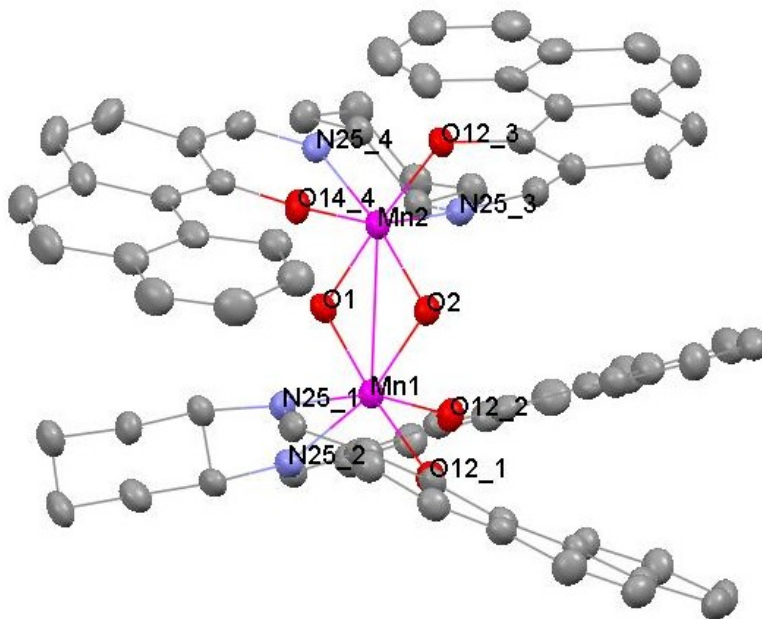
Figure 3.20 Thermal ellipsoid plot of complex 11. (50% probability, H and noncoordinated solvent omitted for clarity).

3.6.2 Crystal structure of complex 12

The dark brown crystal plate was grown by heating a dichloroethane solution of **12** followed by cooling to the room temperature. The structure of complex **12** is quite distinct, since the metal centers are only linked by bridging ligand, rather than other bridging groups (such as oxo, carboxylato) in most dimeric Mn(III) complexes reported previously.[15,16] An ORTEP view of complex **12** is shown in Figure 3.21, and selected bond lengths and angles are listed in Table 3.6. Two units of [Mn**S3**] are connetcted through a third **S3** ligand. All three **S3** ligands show M-helicity in the crystal.

One Mn(III) center (Mn_1) is six coordinated in a distorted octahedral fashion by N_2O_2 atoms (N_{25_5} and N_{25_6}, and O_{12_5} and O_{12_6}) of local **S3** ligand, and one imine nitrogen (N_{25_4}) and one phenolate oxygen (O_{12_4}) from the bridging **S3**. Among them, O_{12_6}, N_{25_6}, O_{12_4} and O_{12_5} define the basal plane, and Mn_1 almost lie in this plane. The axial sites are occupied by N_{25_5} of local **S3**

and N_{25_4} of bridging **S3**. The conformation of its local salen displays as *cis*-β with *M* helicity. As expected for an octahedral Mn(III) center, the Jahn-Teller distortion leads to enlogated axial bond lengths of Mn_1-N_{25_5} and Mn_1-N_{25_4} (2.270(3) Å and 2.263(3) Å, respectively). The dihedral angle between the naphthyl units in the backbone increases to 125.8˚ upon metallation from 103.1˚ for the free ligand.
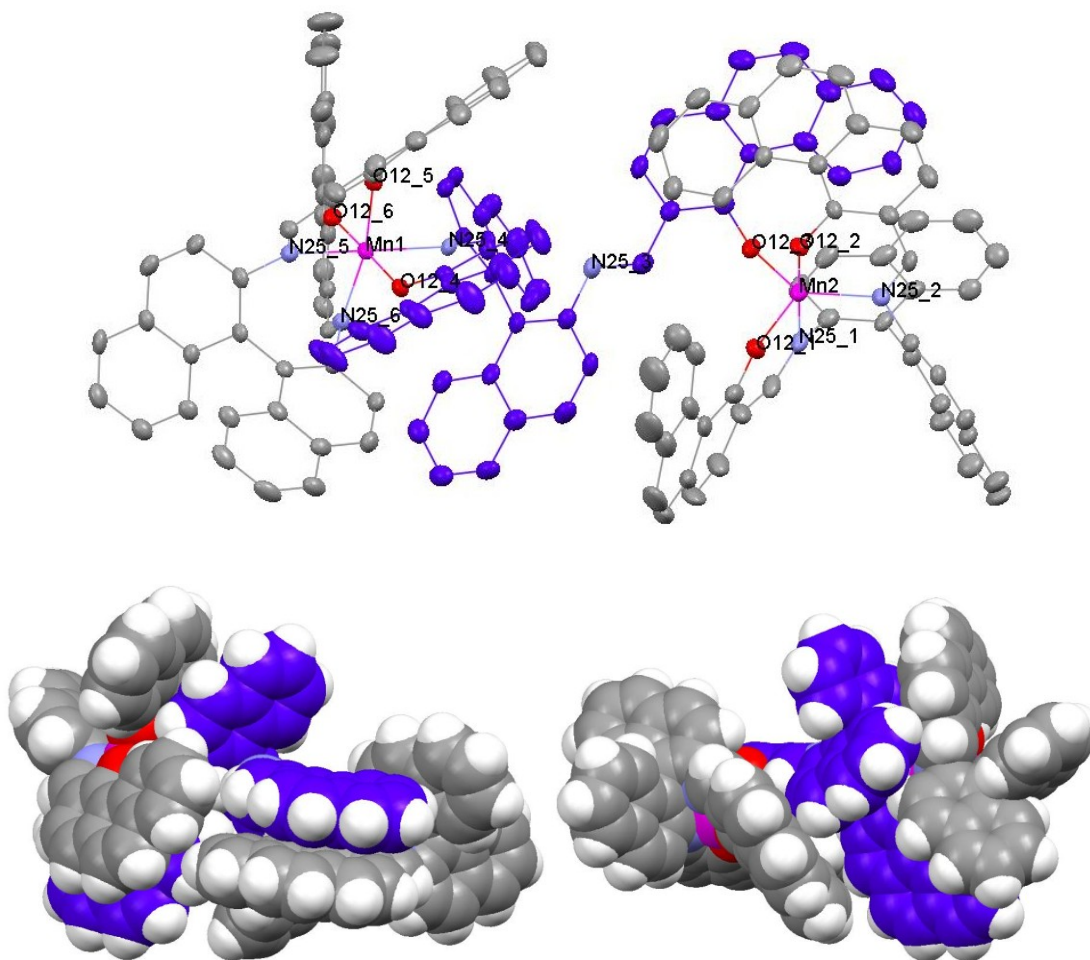

Figure 3.21 Crystal structure of complex 12: top, thermal ellipsoid plot (50% probability, H and noncoordinated solvent omitted for clarity); bottom, space filling model: left, front view; right, back veiw. (blue indicates the carbon in bridging S2 **ligand).**

The other Mn(III) center (Mn_2) is penta-coordinated in a trigonal bipyrimidal fashion by N_2O_2 atoms (O_{12_1}, O_{12_2}, N_{25_1} and N_{25_2}) of local **S3** ligand, and only one phenolate oxygen (O_{12_3}) from the **S3** bridge. Mn_2 lies on the basal plane composed by N_{25_1}, O_{12_1} and O_{12_2}. The apical positions are occupied by O_{12_1} and N_{25_2}. The difference of the Mn-O and Mn-N bond distances between apical (1.992(3) and 2.053(4) Å) and equatorial positions (1.867(2)/1.910(3) and 2.001(3) Å) is observed. The dihedral angle in the binaphtyl backone is 123.1˚.

In the bridging salen ligand, one nigrogen atom (N_{25_3}) is non-coordinated, while the other three atoms are coordinated (N_{24_4} and O_{12_4} to Mn_1, O_{12_3} to Mn_2). The dihedral angle between the two naphthyl units is comparable to that of free ligand (109.4˚ vs. 103.1˚). Due to coordinating to two distinct metal centers, two phenylthryl sidearms flip outside, instead of hug-in as the free ligand. Significant π-π stacking is observed between phenylthryl planes from local salens and bridging **S3** ligands, with a separation between overlapping rings of 3.4 and 3.6 Å. The Mn-Mn separation is 10.910 Å, due to the high rigidity and big size of the bridging ligand.

Table 3.6 Selected bond lengths (Å) and bond angles (˚) of complex 12.

Mn_1-O_{12_4}	1.902(3)	Mn_2-O_{12_1}	1.992(3)
Mn_1-O_{12_5}	1.911(2)	Mn_2-O_{12_2}	1.867(2)
Mn_1-O_{12_6}	1.912(3)	Mn_2-O_{12_3}	1.910(3)
Mn_1-N_{25_4}	2.263(3)	Mn_2-N_{25_1}	2.001(3)
Mn_1-N_{25_5}	2.270(3)	Mn_2-N_{25_2}	2.053(4)
Mn_1-N_{25_6}	2.209(3)		
O_{12_4}-Mn_1-O_{12_6}	176.2(1)	O_{12_2}-Mn_2-N_{25_1}	179.0(1)
O_{12_4}-Mn_1-N_{25_4}	84.7(1)	O_{12_2}-Mn_2-N_{25_2}	88.5(1)
N_{25_5}-Mn_1-N_{25_4}	170.4(1)	O_{12_1}-Mn_2-N_{25_2}	117.7(1)
O_{12_5}-Mn_1-N_{25_6}	168.4(1)	O_{12_3}-Mn_2-N_{25_2}	133.6(1)

3.6.3 Crystal structure of complex 15

The crystals of **15** were obtained by slow-diffusion of dichloroethane/ether. The molecular structure of **15** is shown in Figure 3.22. Selected bond lengths and angles of complex **15** are listed in Table 3.7. In this bis(μ-oxo)-bridged dimanganese(IV) compound, the Mn_2O_2 core is pseudo-square planar with the Mn-Mn distance of 2.747 Å. Besides two oxo bridges, two phenolate O atoms and two imine N atoms of **S2** ligand are chelated to each Mn ion, which make the roughly octahedral coordination environment around each metal center. Both salen ligands show as *M*-helix and adopt a *cis*-β configuration so as to leave two *cis* sites for two oxo bridges. The axial ligation is provided by nitrogen and oxygen atoms from salen units. The Mn-μ-O bond is slightly shorter that the Mn-$O_{phenolate}$ (mean 1.812 vs. 1.940 Å). The bond distance *trans* to oxo bridge are longer that those *cis* ones (Mn_1-$O_{phenolate}$ 1.910 vs. 1.930 Å; Mn_2-N_{imine} 1.962 vs. 2.042 Å). This may be due to the *trans* influence of oxo bridging groups.

A π-π stacking interaction between the two benz[a]anthryl rings of ligands, with an approximate separation between overlapping planes of 3.4 Å. The terminal aryl rings in benz[a]anthryl sidearms are overlapped as expected. The angles between two sidearm planes are 41.95° (Mn_1 centerd) and 48.08° (Mn_2 centered), respectively. All structural parameters of **15** fall within the ranges of other similar Mn(salen) complex containing Mn_2O_2 core.[15]
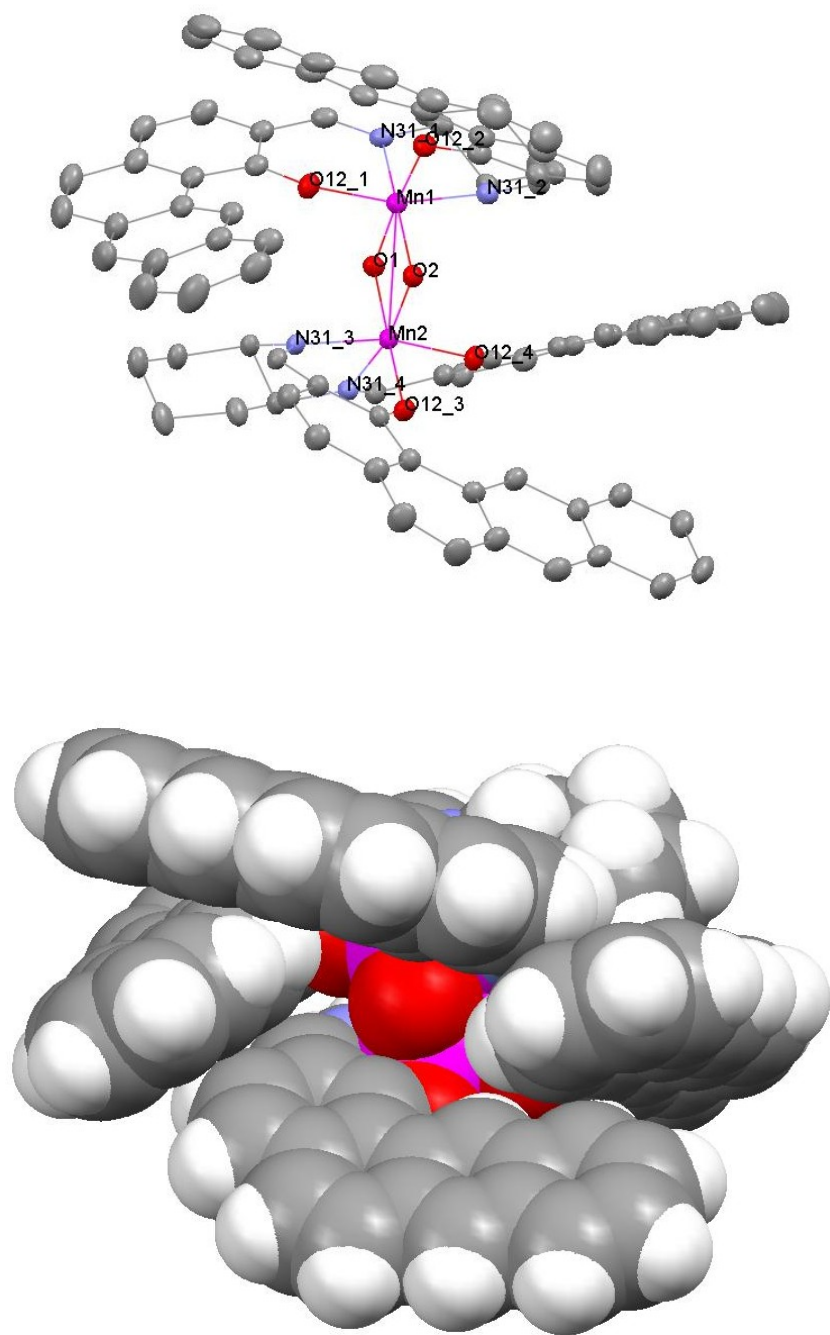
Figure 3.22 Structure of complex 15: top, thermal ellipsoid plot (50% probability, H and noncoordinated solvent omitted for clarity); bottom, space filling model.

Table 3.7 Selected bond lengths (Å) and bond angles (°) of complex 15.

$Mn_1\text{-}O_{12\_1}$	1.902(1)	$Mn_2\text{-}O_{12\_3}$	1.939(1)
$Mn_1\text{-}O_{12\_2}$	1.922(1)	$Mn_2\text{-}O_{12\_4}$	1.918(1)
$Mn_1\text{-}N_{31\_1}$	2.042(2)	$Mn_2\text{-}N_{31\_3}$	1.960(2)
$Mn_1\text{-}N_{31\_2}$	1.965(2)	$Mn_2\text{-}N_{31\_4}$	2.040(2)
$Mn_1\text{-}O_1$	1.818(1)	$Mn_2\text{-}O_1$	1.810(1)
$Mn_1\text{-}O_2$	1.812(1)	$Mn_2\text{-}O_2$	1.809(1)
$Mn_1\text{-}O_1\text{-}Mn_2$	98.43(6)	$Mn_1\text{-}O_2\text{-}Mn_2$	98.66(6)
$O_{12\_1}\text{-}Mn_1\text{-}N_{31\_2}$	163.84(6)	$O_{12\_4}\text{-}Mn_2\text{-}N_{31\_3}$	164.16(6)

A view of the packing diagram of **15** down the *a* axis and on the *ac* plane is present in Figure 3.23. This reveals a 2D double-layered column structure. In each layer all di-Mn(IV) molecule is identical and stacked. The Mn(IV) dimeric units in the neighboring columns are reversely oriented, in order to fully occupy the space. In addition, the dimers are stabilized by π-π stacking between the aromatic ring of sidearm and cyclohexyl backbone of adjacent molecule. The distance between layers is about 10.60 Å. The shortest Mn···Mn distance is around 10.87 Å.
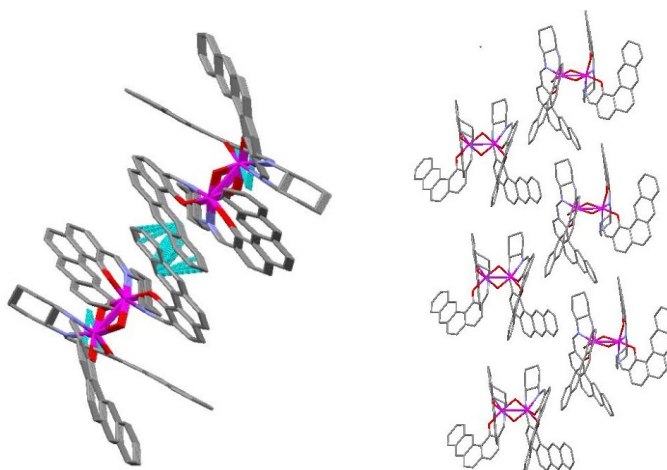
Figure 3.23 Packing diagram of complex 15. (left, view along the *a* axis; right, on the *ab* plane).

3.7 Asymmetric expoxidation of olefin catalyzed by manganese(salen) complexes

The catalytic potential of manganese complexes as enantioselective catalysts was tested in the asymmetric epoxidation of several simple model compounds, *trans* -β-methyl styrene, styrene and indene, which are representative *trans*, terminal, and *cis* olefins respectively.

3.7.1. The effect of co-catalyst on the catalytic acitivity of asymmetric epoxidation of *trans* -β-methyl styrene by 9

The beneficial effects of co-catalysts have been observed in many epoxidations.[17] Both pyridine-*N*-oxide (PNO) and 4-methylmorpholine-*N*-oxide (MNO) have been tested as co-catalysts when the catalytic reactions performed with iodosylbenzene (PhIO) as oxidant in dry CH$_3$CN. The results are presented in Table 3.8.

Table 3.8 Epoxidation of alkenes catalyzed by complex 9 in dry CH$_3$CN.

substrate	Conversion/%		
	Without co-catalyst	With PNO	With MNO
trans -β-methyl stryene	0	43.8	trace
indene	0	25.6	trace
stryrene	0	89.3	none

Conditions: 2-10 mol% catalyst, 0.1-0.4 mmol iodosylbezene, 0.1 mL substrate, 5 mL dry acetonitrile, room temperature, yield is determined by ^{1}H NMR.
PNO: pyridine-*N*-oxide; MNO: 4-methylmorpholine-*N*-oxide.

No epoxide products have been detected in the absence of any co-catalyst even when increasing the catalyst loading and prolonging the reaction time. However, upon addition of PNO, the conversion of *trans* -β-methyl stryene oxide is detected as 43.8% under the same

conditions. In the presence of MNO, the catalytic activity is very low, only traces of epoxides are found. The role of the co-catalyst is not very clear. It may serve as an axial ligand to activate the Mn=O species.[10,17,18]

3.7.2. Asymmetric epoxidation of *trans*-β-methyl styrene by 9 and 12

Asymmetric epoxidation of *trans*-β-methyl styrene is carried out in dry acetontrile in the presence of pyridine-*N*-oxide (PNO) as co-catalyst at room temperature. Both **9** and **12** have been tested to catalyze this reaction (Figure 3.24).
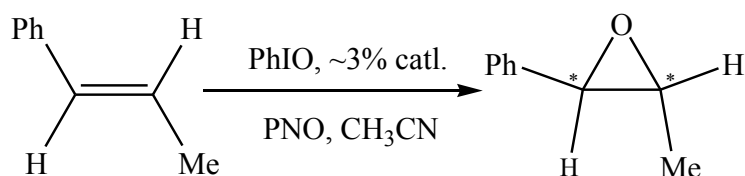

Figure 3.24 Scheme of asymmetric epoxidation of *trans*-β-methyl styrene catalyzed by 9/12.

After 20 h, the epoxide conversion is found to be 74.5% by **9** with 73.6% enantiomeric excesses (*ee*). Meanwhile, the conversion by **12** is 22.6% with 84.9% *ee*. No significant rate decrease is observed in the epoxidation catalyzed by **9** after 6 h. The epoxide production over this period exhibits a linear concentration increase (Figure 3.25, solid line). When catalyzed by **12** under the same conditions, the epoxidation proceeds with moderately lower conversion as compared to **9** (19.9% vs. 24.6%) in the initial reaction period. There is no significant increase in reaction rate after that (Figure 3.25, dashed line). The *ee* in both **9** and **12** reaches the maxima after 40 mins, then the *ee* values level off. The enantioselectivity is slightly higher with **12** than **9** (Figure 3.26). The results indicate that both **9** and **12** display catalytic potential in the

asymmetric epoxidation of *trans* alkenes. Catalyst **9** shows better reactivity, while catalyst **12** shows better selectivity.
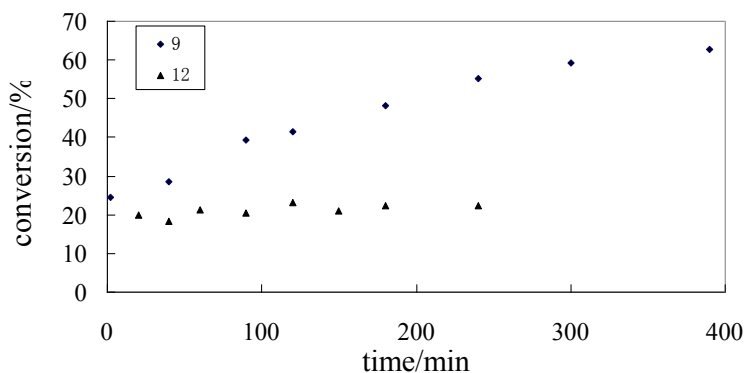

Figure 3.25 Percent yield versus time plot of *trans*-β-methyl styrene epoxidation with PhIO in acetonitrile at room temperature catalyzed by 9 (■, solid line) and 12 (▲, dashed line).
Conditions: 3.0 mol % catalyst, 1.05 mmol iodosobenzene, 0.1 mL substrate, 0.17 mmol pyridine N-oxide, 10 mL dry acetonitrile, room temperature. Both converson and ee are determined by GC analysis on a chiral column.
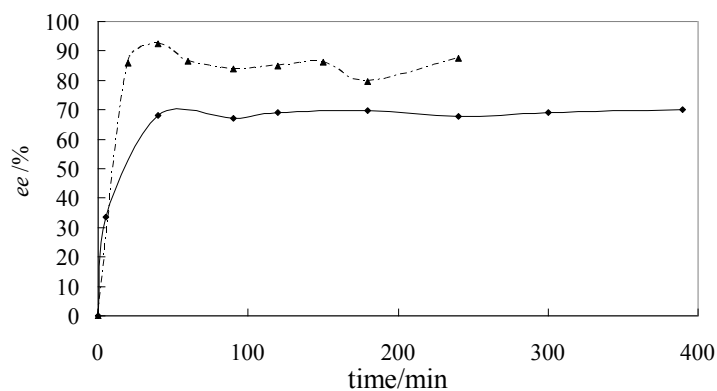
Figure 3.26 *ee* value versus time plot of *trans*-β-methyl styrene epoxidation with PhIO in acetonitrile at room temperature catalyzed by 9 (■, solid line) and 12 (▲, dashed line).
Reaction condition is the same to Figure 3.24.

It is believed that catalytic epoxidation involves a reactive O=Mn^V species.[2,3,,6,18] The X-ray crystallographic studies of **10** and **12** show a deep-stepped conformation. The rigidity of chiral backbone as well as the bulkiness of phenylthryl ring sidearm can help to lock such a deeply

106

twisted geometry even in the O=Mn^V active species. As expected, such deeply twisted conformation of manganese complexes minimizes the steric hindrance when *trans* substrate is approaching the active center, hence high selectivity is observed (Figure 3.27).

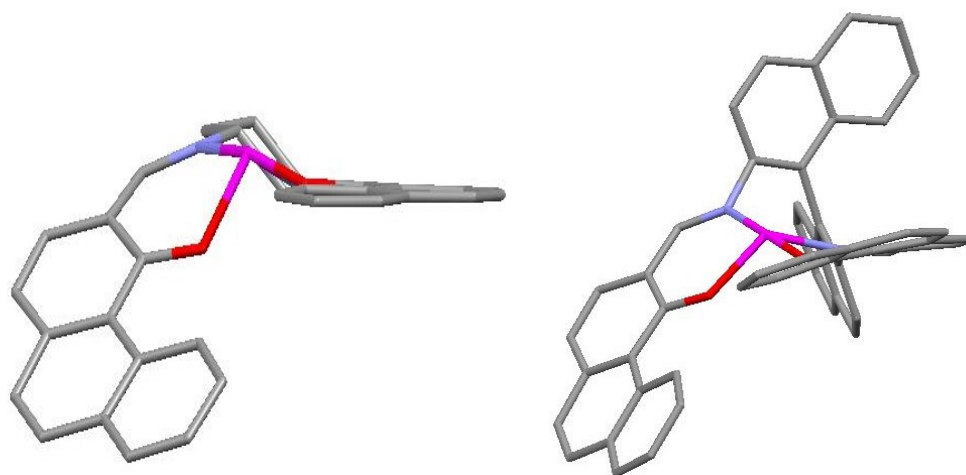

Figure 3.27 Deeply stepped conformation models of Mn(salen) [10 (left) and 12 (right)], created using crystal data.

Both the solution and solid studies of **9** and **12** suggest only Mn(III) and Mn(IV) centers exist, while no Mn(V) species is observed. Oxidation need to carry out in **9** and **12** during the reaction, in order to form high oxidation state oxene manganese salen complexes. This step is the possible rate-determining step, since significant difference is observed in the reaction rates catalyzed by **9** and **12**. Furthermore, the better selectivity by **12** may arise from the higher bulkiness of binaphthyl backbone as compared to the cyclohexyl in **9**. The reactive O=Mn^V(salen) species generated from **12** adopts more restricted reactive site for the substrate and leads to higher selectivity (Figure 3.28).
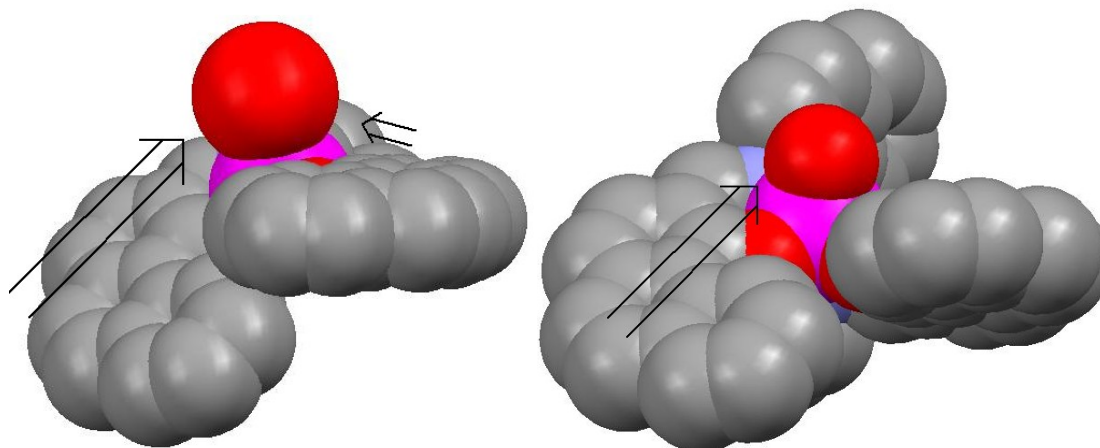
Figure 3.28 Reaction sites for the substrate to approach O=Mn(salen) species [10 (left) and 12 (right)], created using crystal data.

3.7.3. The effects of counterion and oxidant on the catalytic acitivity of asymmetric epoxidation of *trans* -β-methyl styrene by 12, 13 and 14

It is reported that the ligand counterions play a role in the epoxidation.[18,19] Complexes **12**, **13** and **14** were synthesized from different metal precursors while with the same salen ligand. Though they show very similar characteristics in spectroscopy and the counterion is absent from crystal structure of **12**, the relative abundances of species found in mass spectrometry are quite different (Section 3.5).

The results for the asymmetric epoxidation of *trans*-β-methyl styrene catalyzed by **12**, **13** and **14** using different oxidants (PhIO, aqueous H_2O_2, and bleach/sodium hypochlorite) are presented in Table 3.9. In all cases, the epoxides are formed with moderate enantioselectivity (60-70%) and the *R* isomer is the dominant product. All yields obtained are fairly low (10-23%). No significant difference is observed for **12**, **13** and **14** in terms of percent conversion and *ee*. PhIO and bleach are slightly better oxidants than H_2O_2. The best catalytic performance is obtained using **12** as catalyst, with PhIO or bleach as the oxidant. Complex **13** gives the highest

yield (11.1%) with 80.3% *ee* when using H_2O_2 as the oxidant. It seems that the counterion plays a very limited role in the asymmetric epoxidation in this study. During the catalysis, the couterion will dissociate to generate reactive species, even if the couterions chelate to the metal center. The similar dissocation pathways of Cl^-, OAc^-, and NO_3^- lead to the identical $O=Mn^{IV}$(salen) complex. Manganese complexes are reported to decompose in the presence of H_2O_2, which may cause the low conversion with this oxidant.[18]

Table 3.9 Comparative acticity study of 12, 13 and 14 in the epoxidation of *trans*-β-methyl styrene.

oxidant	catalyst	% conversion	% *ee*
PhIO	**12**	22.6	69.8
	13	21.3	64.5
	14	21.8	69.1
H_2O_2	**12**	10.3	67.1
	13	11.1	80.3
	14	10	84.4
Chlorox	**12**	36.6	61.9
	13	23.5	61.1
	14	20.7	61.4

Conditions: ~3.0 mol % catalyst, 1.05 mmol oxidant, 0.1 mL substrate, 0.17 mmol pyridine-*N*-oxide, 5 mL dry acetonitrile for PhIO or 5 mL mixture of oxidant and dichloromethane for H_2O_2 and bleach, room temperature, 20 h. The conversion is determined by ^{1}H NMR and *ee* is determind by GC.

The terminal oxidants, *tert*-butyl hydroperoxide (*t*-BuOOH) and di-*tert*-butyl peroxide (*t*-BuOOBu-*t*) have been employed for the catalytic epoxidation by **9** in CH_2Cl_2 (in addition to PhIO, aqueous H_2O_2, and bleach). *Trans* -β-methyl styrene, styrene, indene, cyclooctene and cyclohexene were used as model substrates. Some of the results are summarized in Table 3.10.

Table 3.10 Epoxidation of some alkenes with different oxidants using 9 as catalyst.

oxidant	% conversion		
	trans-β-methyl styrene	styrene	indene
PhIO	43.8 (73.6)	89.3 (11.3)	--
Aqueous H$_2$O$_2$	50 (>90)	27.8	28.6
Clorox	36.4 (83.7)	76.9	66.7
t-BuOOH	33.5	trace	trace
t-BuOOBu	trace	trace	trace

Conditions: 1.5-2.5 mol% catalyst, 1.0 mmol oxidant, 0.1 mL substrate, 0.15-0.2 mmol pyridine-N-oxide, ~ 6 mL dichloromethane at room tempature, 18 h. % Conversion is determined by 1H NMR. The numbers in brackets indicate %*ee*.

Of the organic terminal oxidants, PhIO is superior to the others. It can oxidize all three olefins to corresponding epoxides, with moderate to acceptable conversion and selectivity. *t*-BuOOH can only catalytically oxidize *trans*-β-methyl styrene to its epoxide with moderate conversion. *t*-BuOOBu-*t* has also been tried in this system, but no epoxides are detected in all substrates. It is reported that polymerization of alkene could be initialized in the presence of *t*-BuOOBu-*t*.[20]

Epoxidation in aqueous medium is attractive due to its green feature, but it is usually confronted by such challenges as limited solubility, catalyst degradation, and/or relatively low product yield/selectivity. The catalyst **9** is sparingly soluble in water, but readily soluble in dichloromethane. This leads to a two-phase reaction media when using aqueous H$_2$O$_2$ and bleach as oxidants: substrate/product, catalyst and co-catalyst are in organic phase; oxidant in water phase. The highest activity with aqueous H$_2$O$_2$ is observed in *trans*-β-methyl styrene oxidation with 50% conversion and 90% *ee*. The conversions are only modest in both styrene and indene. It should be mentioned that at the end of reaction, the decomposition of catalyst is evidenced by the fading color of reaction medium from dark brown to light/grayish brown. In the presence of

bleach, low conversion and moderate *ee* are observed in the oxidation of *trans*-β-methyl styrene, while moderate conversion is seen for the oxidation of styrene and indene.

The catalytic epoxidation of cyclohexene and cyclooctene are also carried out with both inorganic and organic terminal oxidants. The analysis of the reaction mixture shows that the major products are other oxidation products (alcohol, ketone), rather than epoxide.
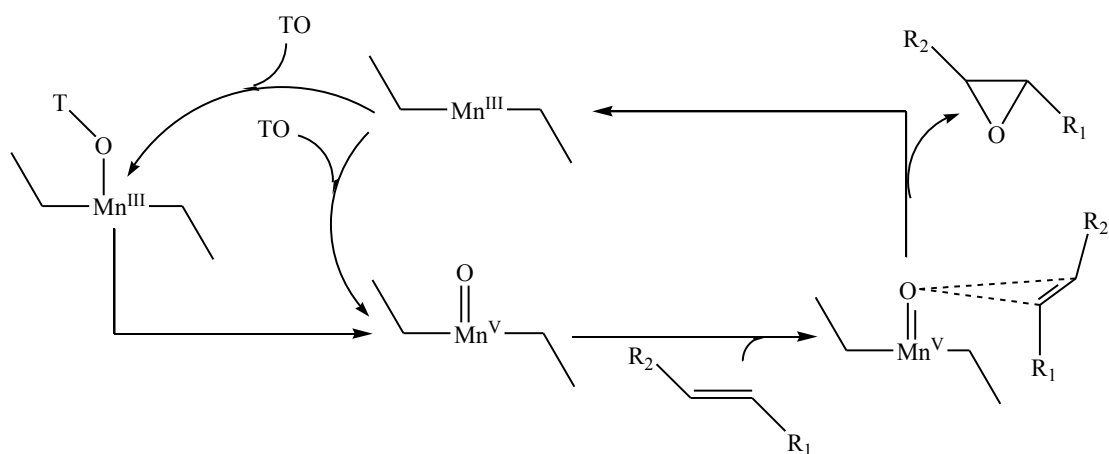

Figure 3.29 Proposed mechanism for Mn(salen) catalyzed asymmetric epoxidation of *trans* olefin. TO: terminal oxidant, stepped shape indicates the helix-directing H$_2$S1 and H$_2$S3 salen ligands.

The prosposed reaction pathways for asymmetric epoxidation with **9/12** in the presence of terminal oxidant (TO) are shown in Figure 3.29. When O=Mn^V(**S**) is believed to be the active species, there are two possible ways to generate it: directly from Mn^{III}(**S**) by oxidation, or first ligation of TO to Mn^{III}(**S**), then conversion to O=Mn^V(**S**).[18,19] This step is believed to be the rate-determining step, since different epoxidation rate is observed with **9** and **12** (Figure 3.24 and 3.35). Different oxidants may have different abilities to generate and stabilize this species, since different reactivity and selectivity are observed (Table 3.10). Next, the olefin approaches and the oxygen atom transfers, leading to the regeneration of Mn^{III}(**S**). The deeply stepped conformation

of O=Mn^V(**S**) greatly reduces the steric repulsion when the *trans* substrate approaches. Other olefins such as terminal and *cis* may also approach in the similar way.

3.8. Conclusion and future work

Novel Mn(IV) and Mn(III) complexes containing helix-directing salen ligands have been synthesized and characterized. In the solution, these complexes are believed to be the mixture of dimer and monomer, according to MS, IR and UV-vis. In the solid state, only binuclear molecules are seen by XRD. One kind of dimeric structure is bridged by two oxo groups, and the other kind bridged by the third salen ligand. The difference may be derived from the distinct steric and electronic features of backbone and sidearm of the ligands. These complexes show catalytic activity in the epoxidation of olefins, especially *trans*-β-methyl styrene with moderate selectivity.

New helix-directing ligands are currently being investigated in our group, in order to synthesize transition metal complexes that would act as catalysts for asymmetric reactions. Magnetic characterization (EPR, magnetic susceptibility) of these Mn(salen) complexes is a good tool to understand specific spin and oxidation states of manganese as well as other *d*-electron properties. Computational studies are also necessary to further determine the conformation in solution and explore the catalytic process.

The catalytic epoxidation systems in this work will be explored in the following aspects.

1. optimize the reaction conditions, especially when using aqueous H_2O_2 as oxidant;

2. examine the substrate scope;

3. investigate the underlying mechanism.

3.9 References

1. Ferreira, K. N.; Iverson, T. M.; Maghlaoui, K.; Barber, J.; Iwata, S. Architecture of the photosynthetic oxygen-evolving center. *Science* **2004** 303, 1831-1838. and related references.

2. Sheldon, R. A., Kochi, J. K. *Metal-catalyzed oxidations of organic compounds*, **1981**, Academic Press, London.

3. Bachvall, J. E. (Ed.) *Modern oxidation methods*, **2005**, Wiley-VCH, Weinheim.

4. Katsuki, T. Unique asymmetric catalysis of *cis*-β metal complexes of salen and its related Schiff-base ligands. *Chem. Soc. Rev.* **2004**, 33, 437-444.

5. O'Mahony, C. P.; McGarrigle, E. M.; Renehan, M. F.; Ryan, K. M.; Bousque, C.; Gilheany, D. G. Asymmetric alkene epoxidation with chromium oxo salen complexes. A systematic study of salen ligand substituents. *Org. Lett.* **2001**, 3, 3435-3438.

6. Fichtinger, D.; Plattner, D. A. Oxygen transfer to manganese-salen complexes: an electrospray tandem mass spectrometric study. *J. Chem. Soc., Perkin Trans.* **2000**, 2, 1023-1208.

7. Punniyamurthy, T., Velusamy, S., Iqbal, J. Recent advances in transition metal catalyzed oxidation of organic substrates with molecular oxygen. *Chem. Rev*. **2005**, 105, 2329-2363.

8. Torayama, H., Nishide, T., Asada, H., Fujiwara, M., Matsushita, T. Preparation and characterization of two different types of di-μ-oxo dimanganese(IV) complexes with tetradentate Schiff bases. *Polyhedron* **1998** 17, 105-118.

9. Maneiro, M., Bermerjo, M. R., Fondo, M., Gonzalez, A. M., Sanmartin, J., Garcia-Monteagudo, J. C., Pritchard, R. G., Tyryshkin, A. M. Structural and photolytic studies on new mononuclear and binuclear manganese complexes containing Schiff base ligands. The crystal structure of [Mn(μ-3,5-Brsalpn)(μ-O)]$_2$·2DMF. *Polyhedron* **2001**, 20, 711-719.

10. Kurahashi, T., Fujii, H. Chiral distortion in a Mn^{IV}(salen)$(N_3)_2$ derived from Jacobsen's catalyst as a possible conformation model for its enantioselective reactions. *Inorg. Chem.* **2008**, 47, 7556-7567. and related references.

11. Wiznycia, A. V., Desper, J., Levy, C. J. Monohelical iron(II) and zinc(II) complexes of a (1*R*,2*R*)-cyclohexyl salen ligand with benz[a]anthryl sidearms. *Inorg. Chem*. **2006**, 45, 10034-10036.

12. Hirotsu, M.; Nakajima, K.; Kojima, M.; Yoshikawa, Y. Manganese(III) complexes containing optically active tetradentate Schiff base ligands. effects of phenyl substituents. *Inorg. Chem.* **1995**, 34, 6173-6178.

13. Wiznycia, A. The preparation and studyof bis(pyridyl-imine) and monohelical salen-type complexes of iron and zinc. PhD thesis. **2006**

14. Yin, G., McCormick, J. M., Buchalova, M., Danby, A. M., Rodgers, K., Day, V. W., Smith, K., Perkins, C. M., Carter, J. D., Scheper, W. M., Busch, D. H. Synthesis, characterization, and solution properties of a novel cross-bridged cyclam manganese(IV) complex having two terminal hydroxo ligand. *Inorg. Chem.* **2006**, 45, 8052-8061.

15. Ruiz-Garcia, R., Pardo, E., Munoz, M. C., Cano, J. High-valent bis(oxo)-bridged dinuclear manganese oxamates: synthesis, crystal structure, magnetic properties, and electronic structure calculations of bis(μ-oxo)dimanganese(IV) complexes with a binucleating *o*–phenylenedioxamate ligand. *Inorg. Chim. Acta.* **2007**, 1, 221-232.

16. Mikata, Y., So, H., Yamashita, A., Kawamura, A., Mikuriya, M., Fukui, K., Ichimura, A., Yano, S. Quinoline-based tetradendate nitrogen ligands stabilized the bis(μ-oxo) dinuclear manganese(III,III) core. *Dalton Trans.* **2007**, 3330-3334.

17. Rasmussen, K. G., Thomsen, D. S., Jorgensen, K. A. Oxidation of imines to oxaziridines catalyzed by transition metal complexes using molecular oxygen as the terminal oxidant. *J. Chem. Soc. Perkin Trans.* **1995**, 699-704.

18. Oyama, S. T. (Ed.) *Mechanisms in Homogeneous and Heterogeneous Epoxidation catalysis*, **2008**, Elsevier, Oxford, UK.

19. Adam, W., Roschmann, K. J., Saha-Moller, C. R., Seebach, D. *cis*–stilbene and (1α,2β,3α)-(2-ethenyl-3-methoxycyclopropyl)benzene as mechanistic probes in the Mn^{III}(salen)-catalyzed epoxidation: influence of the oxygen source and the counterion on the diastereoselectivity of the competitive concerted and radical-type oxygen transfer. *J. Am. Chem. Soc.* **2002**, 124, 5068-5073.

20. Romakh, V. B., Therrien, B., Suss-Fink, G., Shul'pin G. B. Synthesis, molecular structure, and catalytic potential of the tetrairon complexes$[Fe_4(N_3O_2-L)_4(\mu-O)_2]^{4+}$ (L=1-carboxymethyl-4,7-dimethyl-1,4,7-triazacyclononane). *Inorg. Chem.* **2007**, 46, 3166-3175.

21. Wang, S. H. Mandimutsira, B. S., Todd, R., Ramdhanie, B., Fox, J. P., Goldberg, D. P. Catalytic sulfoxidation and epoxidation with a Mn(III) triazacorrole: Evidence for a "third oxidant" in high-valent porphyrinoid oxidations. *J. Am. Chem. Soc.* **2004**, 18-19.

Experimental Section

General methods

All reactions were run under inert atmospheres unless otherwise noted. All organic solvents (CH$_2$Cl$_2$, hexane and diethyl ether) used in metallation reaction were purchased from Fisher Scientific, stored over sodium benzophenone ketyl or calcium hydride, and degassed prior to transfer via high-vacuum line technique. Other organic solvents (methanol, CH$_3$CN and spectroscopic grade THF) used in characterization was purchased from Fisher Scientific and used as received. Argon gases (LINWELD INC, Lincoln NE) and oxygen gases (Metheson tri-gas INC, Basking ridge NJ) were purifed by passing through 4 Å molecular sieves and an Engelhard Q5 catalyst bed.

IR spectra were collected on Nicolet 380 FT-IR (Thermo Scientific, Madison MN) at room temperature. UV-Vis spectra were obtained on a Varian Cary 500 scan UV-Vis-NIR spectrophotometer (Agilent Technologies) in acetonitrile, and CD spectra on a JASCO J-815 spectropolarimeter (Jasco, Tokyo Japan) in spectroscopic grade tetrahydrofuran (THF). The solution samples for UV-Vis and CD were prepared at room temperature, with the concentrations ranged between 1.5 and 2.5 $\times$ 10^{-5} M. A 1.00 cm path length quartz cell was employed for both analyses. HR-ESI-Mass spectra were collected by Quattro Ultima (Micromass Ltd, Manchester UK) in methanol (for Ti(salen) complexes **1-8**) and CH$_3$CN (for Mn(salen) complexes **9-15**). LR-ESI-Mass Spectra were acquired on Bruker Esquire 3000 Plus ion trap mass spectrometer (Bruker Daltonics Inc, Milford MA) in CH$_2$Cl$_2$. ^{1}H NMR spectra were obtained at ambient temperature on a Varian Unity 400 MHz spectrometer employing residual solvent protons as an internal standard. Crystallographic data were collected using either either a Bruker SMART 1000

CCD or a Bruker-AXS SMART APEX CCD. Gas chromatography was carried out using a Varian 3900 fitted with an FDI detector ans using hydrogen gas as the carrier gas. The enantiometric excess was determined by GC using a chiral Supelco β-Dex 120 column (30 m × 0.25 mm). With an initial temperature of 100 ℃ for 20 min, followed by a ramp rate of 20 ℃/min to a final temperature of 180 ℃ for 15.5 min. (S)-trans-β-methyl styrene oxide has a retention time of 22.3 min, and (R)-trans-β-methyl styrene oxide has a retention time of 24.1 min.

Manganese(II) chloride anhydrous 97% was purchased from Strem Chemicals. Manganese(II) acetate anhydrous 98% was purchased from Aldrich Chemicals. Manganese(II) nitrate hydrate (98%, Aldrich) was dried under vacuum for one week with heating before using. Titanium(IV) tetrachloride (97%) and titanium(IV) tetra(isopropoxide) (99.9%) was purchased from Aldrich Chemicals. CDCl$_3$ is purchased from Cambridge Isotope Labotories, INC and dried over 4Å molecular sieves before using. 30% aqueous H$_2$O$_2$ is purchased from Fisher Scientific. Iodosylbenzene (PhIO) was prepared according to the reported proceducre.[1] Pyridine N-oxide (98%) and sodium methoxide were purchased from Acros Chemicals. tert-butyl hydroperoxide (t-BuOOH) (70% solution in water) and di-tert-butyl peroxide (t-BuOOBu-t) were purchased from Acros Organics. trans-β-methyl styrene (stabilized 97%), styrene from (stabilized 99%), and indene (stabilized 90%) were all purchase from Acros Chemicals.

Ligands: the salen ligands (**H$_2$S1**, **H$_2$S2**, **H$_2$S3**, **H$_2$S4**) used for this study were prepared according to the reported procedures.[2]

General synthetic procedure for titanium-salen complexes A solution of titanium(IV) tetrachloride (0.11 mmol) [or titanium(IV) tetraisopropoxide (0.11 mmol)] in CH$_2$Cl$_2$ was added to the salen ligand (0.10 mmol) solution in 3 mL CH$_2$Cl$_2$ in a drop wise manner. After stirring 3

hrs the reaction mixture was concentrated. The solid was decanted by hexane (5 mL×2) to obtain a powder.

Ti(IV)-S1 complex (1). Dark reddish brown powder. (0.061 g, 85%). ^{1}H NMR (CDCl$_3$, 400 MHz): δ 1.68-1.84 (m, 2H, CH), 2.67-2.73 (m, 2H, CH), 3.72-3.78 (m, 4H, CH), 4.16-4.21 (m, 2H, CH), 7.50-7.53 (m, 2H, CH), 7.57-7.62 (m, 4H, CH), 7.65-7.76 (m, 10H, CH), 7.80-7.86 (m, 2H, CH), 7.92 (s, 2H, CH), 7.93-7.98 (m, 4H, CH), 8.57 (s, 2H, CH), 10.18 (d, 2H, CH). X-ray quality crystals of the partially hydrolyzed product were obtained by heating-cooling method of CH$_2$Cl$_2$ solution of complex **1**. ESI-MS (MeOH) *m/z*: [Ti(**S1**)(OMe)]$^+$, calcd for C$_{37}$H$_{31}$N$_2$O$_3$Ti$^+$, 599.1814; found 599.1810 (0.7 ppm).

Ti(IV)-S1 complex (2). Dark reddish brown powder. (0.067 g, 74%). ^{1}H NMR (CDCl$_3$, 400 MHz): δ 1.49-1.57 (m, 1H, CH), 1.59-1.64 (m, 2H, CH), 1.69-1.78 (m, 3H, CH), 1.82-1.92 (m, 2H, CH), 2.15-2.22 (m, 1H, CH), 2.67-2.75 (m, 1H, CH), 4.18-4.25 (m, 1H, CH), 6.15-6.21 (t, 1H, CH), 6.89 (d, 2H, CH), 6.99-7.05 (m, 2H, CH), 7.17-7.21 (m, 3H, CH), 7.37 (s, 1H, CH), 7.52-7.62 (m, 4H, CH), 7.76 (m, 2H, CH), 7.99 (d, 1H, CH), 8.33 (s, 1H, CH), 8.60 (s, 1H, CH), 10.49 (s, 1H, CH). ESI-MS (MeOH) *m/z*: [Ti(**S2**)(OMe)]$^+$, calcd for C$_{45}$H$_{35}$N$_2$O$_3$Ti$^+$, 699.2127; found 699.2112 (2.1 ppm).

Ti(IV)-S1 complex (3). Dark reddish brown powder. (0.069 g, 79%). ^{1}H NMR (CDCl$_3$, 400 MHz): δ 6.98-7.04 (d/m, 1H, CH), 7.08-7.15 (d/m, 1H, CH), 7.29-7.48 (m, 7H, CH), 7.49-7.56 (m, 1H, CH), 7.60-7.67 (m, 5H, CH), 7.71-7.77 (m, 3H, CH), 7.80-8.03 (m, 7H, CH), 8.07-8.14 (m, 1H, CH), 8.40 (s, 1H, CH), 8.66 (s, 1H, CH), 10.13 (d, 1H, CH), 10.25 (d, 1H, CH). Crystals suitable for X-ray analysis were grown from dichloromethane over which was layered diethyl

ether. ESI-MS (MeOH) *m/z*: [Ti(**S3**)(OMe)]$^+$, calcd for C$_{51}$H$_{33}$N$_2$O$_3$Ti$^+$, 769.1917; found 769.1985 (1.8 ppm).

Ti(IV)-S1 complex (4). Dark reddish brown powder. (0.063 g, 65%). ^{1}H NMR (CDCl$_3$, 400 MHz): δ 6.27-6.37 (m, 1H, CH), 6.96 (d, 1H, CH), 7.03-7.14 (m, 3H, CH), 7.30-7.34 (m, 4H, CH), 7.37-7.41 (m, 2H, CH), 7.41-7.44 (m, 1H, CH), 7.50-7.54 (m, 2H, CH), 7.56-7.64 (m, 4H, CH), 7.66-7.72 (m, 3H, CH), 7.87-7.92 (m, 3H, CH), 7.99-8.07 (m, 3H, CH), 8.10-8.15 (m, 1H, CH), 8.16-8.20 (m, 1H, CH), 8.21-8.26 (m, 1H, CH), 8.36 (s, 1H, CH), 8.66 (s, 1H, CH), 10.59 (s, 1H, CH), 10.85 (s, 1H, CH). ESI-MS (MeOH) *m/z*: [Ti(**S4**)(OMe)]$^+$, calcd for C$_{59}$H$_{37}$N$_2$O$_3$Ti$^+$, 869.2284; found 869.2278 (0.7 ppm).

Ti(IV)-S1 complex (5). Greenish yellow powder. (0.062 g, 77%). ^{1}H NMR (CDCl$_3$, 400 MHz): δ 0.80 (d, 3H, CH$_3$), 0.85 (d, 3H, CH$_3$), 1.13 (d, 3H, CH$_3$), 1.18 (d, 3H, CH$_3$), 1.43-1.53 (m, 1H, CH), 1.59-1.66 (m, H, CH), 1.70-1.80 (m, 2H, CH), 2.03-2.16 (m, 2H, CH), 2.40-2.48 (m, 1H, CH), 2.51-2.59 (m, 1H, CH), 2.89-2.97 (m, 1H, CH), 4.62 (sep, 1H, CH), 4.81-4.90 (m, 2H, CH), 5.72 (t, 1H, CH), 6.95 (t, 1H, CH), 7.17-7.20 (m, 1H, CH), 7.36-7.40 (m, 1H, CH), 7.47-7.58 (m, 6H, CH), 7.65-7.69 (m, 1H, CH), 7.75-7.79 (m, 1H, CH), 7.93-7.97 (m, 2H, CH), 8.41 (s, 1H, CH), 8.49 (s, 1H, CH), 10.06 (d, 1H, CH), 10.62 (d, 1H, CH). ESI-MS (MeOH) *m/z*: [Ti(**S1**)(OMe)]$^+$, calcd for C$_{37}$H$_{31}$N$_2$O$_3$Ti$^+$, 599.1814; found 599.1804 (1.7 ppm).

Ti(IV)-S1 complex (6). Greenish yellow powder. (0.057 g, 63%). ^{1}H NMR (CDCl$_3$, 400 MHz): δ 0.71-0.78 (m, 9H, CH3), 1.14 (d, 3H, CH3), 1.69-1.78 (m, 3H, CH), 2.02-2.14 (m, 3H, CH), 2.40-2.47 (m, 1H, CH), 2.49-2.56 (m, 1H, CH), 2.94-3.02 (m, 1H, CH), 4.58 (sep, 1H, CH),

4.81-4.94 (m, 2H, CH), 6.30-6.34, 6.36-6.42, 6.99 (t, 1H, CH), 7.17-7.22, 7.33 (t, 1H, CH), 7.42 (d, 1H, CH), 7.49 (d, 1H, CH), 7.52-7.62 (m, 4H, CH), 7.72-7.77 (m, 1H, CH), 7.86 (d, 1H, CH), 8.00-8.05 (m, 2H, CH), 8.31 (s, 1H, CH), 8.45 (s, 1H, CH), 8.53 (s, 1H, CH), 10.58 (s, 1H, CH), 10.97 (s, 1H, CH). Crystals suitable for X-ray analysis were grown from dichloromethane over which was layered hexane. ESI-MS (MeOH) m/z: [Ti($S2$)(OMe)]$^+$, calcd for $C_{45}H_{35}N_2O_3Ti^+$, 699.2127; found 699.2104 (3.3 ppm).

Ti(IV)-S1 complex (7). Greenish yellow powder. (0.064 g, 65%). ^{1}H NMR (CDCl$_3$, 400 MHz): δ -0.22 (d, 3H, CH3), 0.32 (d, 3H, CH3), 0.79-0.84 (m, 6H, CH3), 0.89-0.94 (m, 9H, 3CH3), 0.98 (d, 3H, CH3), 3.73 (sep, 1H, CH), 4.55 (sep, 2H, CH), 4.83 (sep, 1H, CH), 6.91-7.00 (m, 4H, CH), 7.01-7.09 (m, 5H, CH), 7.19-7.24 (m, 3H, CH), 7.27-7.38 (m, 10H, CH), 7.45-7.49 (m, 2H, CH), 7.53-7.64 (m, 14H, CH), 7.67-7.76 (m, 4H, CH), 7.78-7.82 (m, 4H, CH), 7.86-7.92 (m, 4H, CH), 7.93-7.98 (m, 4H, CH), 8.01-8.07 (d, 1H, CH), 8.38 (s, 1H, CH), 10.54-10.60 (m, 3H, CH), 10.77 (d, 1H, CH). Partially hydrolyzed crystals suitable for X-ray analysis were grown from dichloromethane over which was layered diethyl ether. ESI-MS (MeOH) m/z: [Ti($S3$)(OMe)]$^+$, calcd for $C_{51}H_{33}N_2O_3Ti^+$, 769.1917; found 769.1917 (0.0 ppm).

Ti(IV)-S1 complex (8). Greenish yellow powder. (0.057 g, 54%). ^{1}H NMR (CDCl$_3$, 400 MHz): δ -0.23 (d, 3H, CH$_3$), 0.30 (d, 3H, CH$_3$), 0.65 (d, 3H, CH$_3$), 0.79-0.84 (m, 6H, CH$_3$), 0.96 (d, 3H, CH$_3$), 3.77 (sep, H, CH), 4.61 (sep, H, CH) 4.87 (sep, H, CH), 6.89-7.01 (m, 5H, CH), 7.02-7.10 (m, 5H, CH), 7.18-7.25 (m, 4H, CH), 7.26-7.30 (m, 4H, CH), 7.31-7.38 (m, 5H, CH), 7.46-7.66 (m, 14H, CH), 7.68-7.73 (m, 2H, CH), 7.77-7.82 (m, 1H, CH) 7.84-7.92 (m, 4H, CH), 7.94-8.00 (m, 3H, CH), 8.02 (s, 1H, CH), 8.03-8.08 (m, 3H, CH), 8.24 (s, 1H, CH), 8.33 (s, 1H, CH), 8.33-

8.37 (m, 2H, CH), 8.46 (s, 1H, CH), 11.05 (s, 2H, CH), 11.43 (s, 1H, CH). ESI-MS (MeOH) m/z: $[Ti(\mathbf{S4})(OMe)]^+$, calcd for $C_{59}H_{37}N_2O_3Ti^+$, 869.2284; found 869.2292 (0.9 ppm).

Mn(IV)-S1 complex (9). Manganese(II) chloride (0.12 g, 0.96 mmol), sodium methoxide (0.10 g, 1.9 mmol) and **H₂S1** (0.26 g, 0.502 mmol) were suspended into a 2:1 mixture of dichloromethane/ethanol (15 mL) and stirred overnight. The reaction mixture was oxidized by oxygen gas for 2 hours followed by soxhletation in dichloromethane (100 mL). The filtrate was concentrated to yield a blackish brown powder (0.16 g, 42 %). ESI-MS (CH₃CN) m/z: $[Mn(\mathbf{S1})(CH_3CN)]^+$, calcd for $C_{38}H_{31}N_3O_2Mn^+$, 616.1797; found 616.1754.

Mn(IV)-S1 complex (10) and Mn(IV)-S1 complex (11). These compounds were prepared as above, starting with manganese(II) acetate, manganese(II) nitrate in the place of manganese(II) chloride. The yields were 38% and 24%, respectively. Single crystals suitable for X-ray analysis were grown by slow diffusion of ether into a solution of **10/11** in dichloroethane. ESI-MS of **10** (CH₃CN) m/z: $[Mn(\mathbf{S1})(CH_3CN)]^+$, calcd for $C_{38}H_{31}N_3O_2Mn^+$, 616.1797; found 616.1760 (1.9 ppm). ESI-MS of **11** (CH₃CN) m/z: $[Mn(\mathbf{S1})(CH_3CN)]^+$, calcd for $C_{38}H_{31}N_3O_2Mn^+$, 616.1797; found 616.1718.

Mn(III)-S3 complex (12). Manganese(II) chloride (0.10 g, 0.81 mmol), sodium methoxide (0.11 g, 2.1 mmol) and **H₂S3** (0.30 g, 0.43 mmol) were suspended into a 2:1 mixture of dichloromethane/ethanol (15 mL) and stirred overnight. The reaction mixture was oxidized by oxygen gas for 2 hours followed by soxhletation in dichloromethane (100 mL). The filtrate was concentrated to yield a blackish brown powder (0.10 g, 25 %). Single crystals suitable for X-ray

analysis were grown by heating-cooling in a solution of **12** in dichloroethane. ESI-MS (CH_3CN) m/z: [Mn(**S3**)]$^+$, calcd for $C_{50}H_{30}N_2O_2Mn^+$, 745.1688; found 745.1630.

Mn(III)-S3 complex (13) and Mn(III)-S3 complex (14). These compounds were prepared as above, starting with manganese(II) acetate, manganese(II) nitrate in the place of manganese(II) chloride. The yields were 60% and 18%, respectively. ESI-MS of **13** (CH_3CN) m/z: [Mn(**S3**)]$^+$, calcd for $C_{50}H_{30}N_2O_2Mn^+$, 745.1688; found 745.1574 (3.8 ppm). ESI-MS of **14** (CH_3CN) m/z: [Mn(**S3**)]$^+$, calcd for $C_{50}H_{30}N_2O_2Mn^+$, 745.1588; found 745.1630.

Mn(III)-S2 complex (15). Manganese(II) chloride (0.08 g, 0.64 mmol), sodium methoxide (0.11 g, 2.1 mmol) and **H₂S2** (0.36 g, 0.59 mmol) were suspended into a 2:1 mixture of dichloromethane/ethanol (15 mL) and stirred overnight. The reaction mixture was oxidized by oxygen gas for 2 hours followed by soxhletation in dichloromethane (100 mL). The filtrate was concentrated to yield a blackish brown powder (0.14 g, 32%). Single crystals suitable for X-ray analysis were grown by slow diffusion of ether into a solution of **15** in dichloroethane. ESI-MS (CH_3CN) m/z: [Mn(**S3**)]$^+$, calcd for $C_{50}H_{30}N_2O_2Mn^+$, 716.2110; found 716.2059 (0.1 ppm).

Epoxidation with different co-catalysts. Mn complex **9** (2-10 mol%), co-catalyst (0.16-0.23 mmol) and olefin substrate (1.0 mmol) were dissolved in acetonitrile (5 mL). The resultant mixture was stirred at room temperature after PhIO (0.16-0.31 mmol) had been added. The reaction medium was extracted with hexane (5 mL×2), and the hexane layer was concentrated after dried over $MgSO_4$. The oily residue was analyzed by ^{1}H NMR in $CDCl_3$.

Kinetic studies: To a 25 mL round-bottom flask was added **9/12** (~3 mol%), pyridine *N*-oxide (0.17 mmol), and *trans*-β-methyl styrene (0.10 mL) in 10 mL acetonitrile. After PhIO (1.1 mmol) was added, the aliquot of 0.2 mL was taken at indicated interval when the reaction was briefly stopped to allow phase separation. The sample was washed by 10-15 drops of hexane, quenched by Na_2SO_3, dried over anhydrous $MgSO_4$ for 15 min. The *ee* value and yield were determined by GC analysis on a chiral column. GC conditions: Supelco β-Dex 120 0.25 mm×30 m column, 100 ℃ for 20 min followed by a ramp of 20 ℃/min to 180 ℃ which is kept for 15.50 min. The temperatures of FID and injector are 200 ℃ and 135 ℃, respectively.

Epoxidation with different oxidants: To the solution of **9** (1.5-2.5 mol%), pyridine *N*-oxide (0.15-0.20 mmol), alkene substrate (0.1 mL) in 6 ml CH_2Cl_2 was added oxidant (aqueous H_2O_2, PhIO, *t*-BuOOH or *t*-BuOOBu, 1.0 mmol). After 18 hours, the reaction medium was diluted with dichloromethane and the organic phase was washed by water (5 mL×2) and brine (5 mL) before dried over $MgSO_4$. The filtrate was concentrated and analyzed by ^{1}H NMR in $CDCl_3$.

In the case of Clorox[®], 1.0 mL 0.5 M $Na_2B_4O_7$ •10 H_2O buffer solution was applied and the pH was adjusted to 10 by adding a few drops of 10 M NaOH. The CH_2Cl_2 solution of substrate and co-catalyst is added into the bleach drop by drop.

References

1. Blackmond, D. G., Hodnett, N. S., Lloyd-Jones, G. C. Mechanistic implication of zero-order kinetic resolution. *J. Am. Chem. Soc.* **2006**, 7450-7451.

2. Wiznycia, A. V., Desper, J., Levy, C. J. Iron(II) and zinc(II) monohelical binaphthyl salen complexes. *Chem. Comm.* **2005**, 37, 4693

Appendix A - [^1]H NMR spectra

Complex 1

Complex 2

Complex 3

Complex 4

125

Complex 5

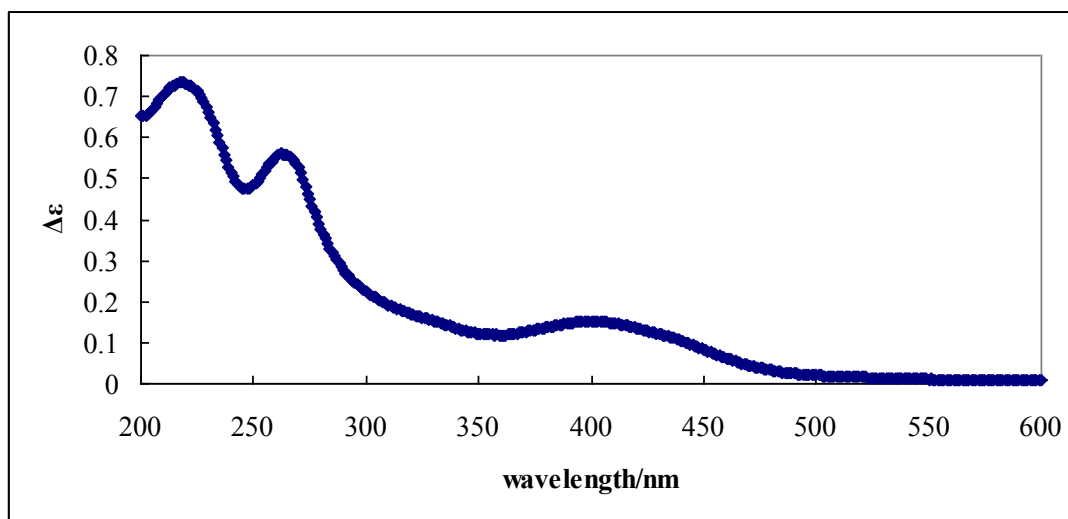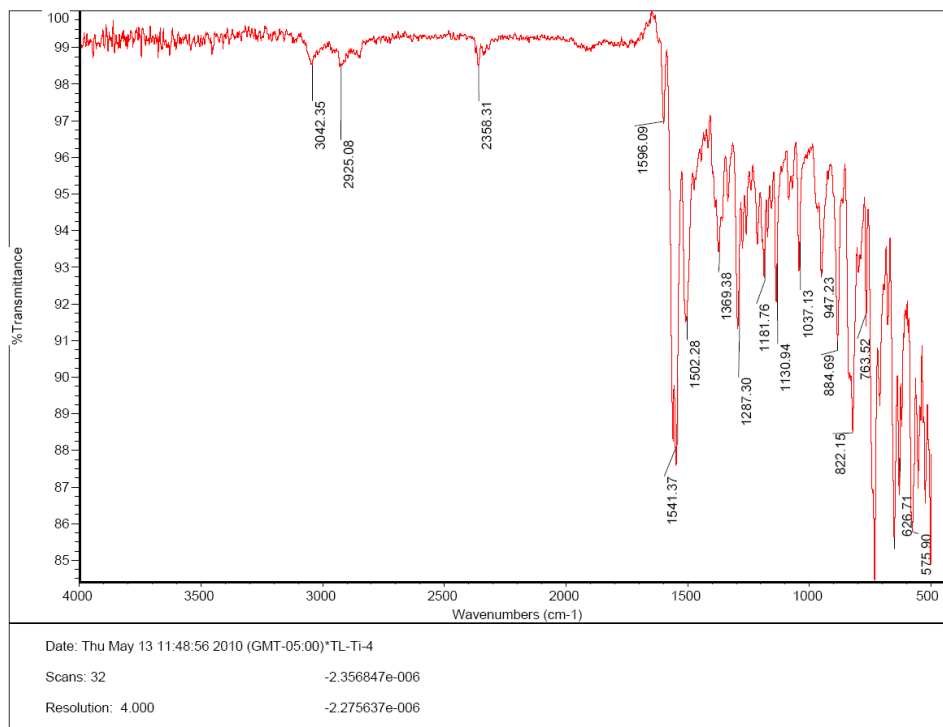**Complex 6**

126

Complex 7

Complex 8

Appendix B - IR, UV and ECD spectra

Date: Thu May 13 11:36:24 2010 (GMT-05:00)*TL-Ti-1

Scans: 32   -2.073565e-006

Resolution: 4.000   -2.190471e-006
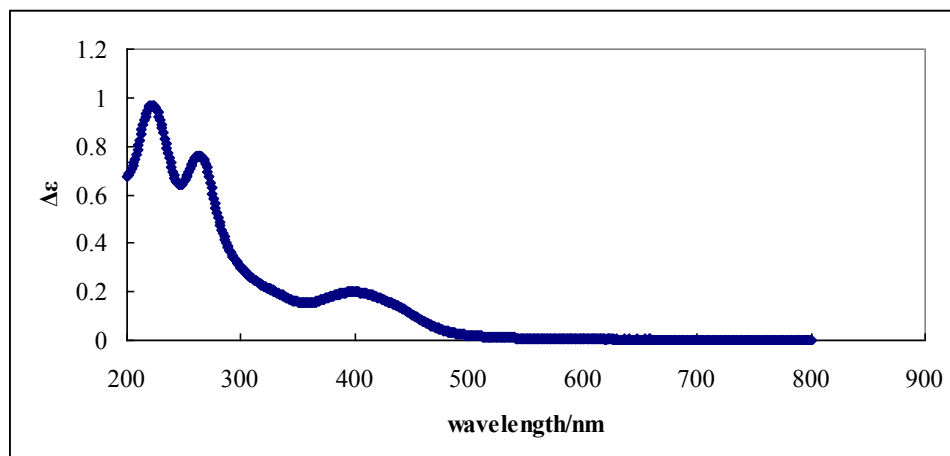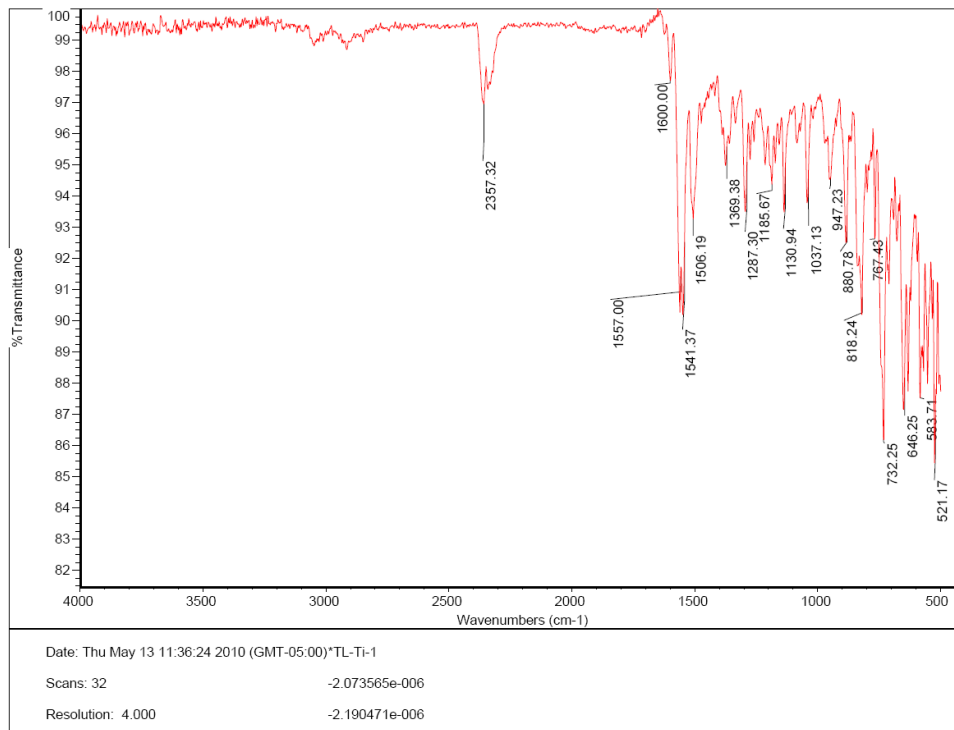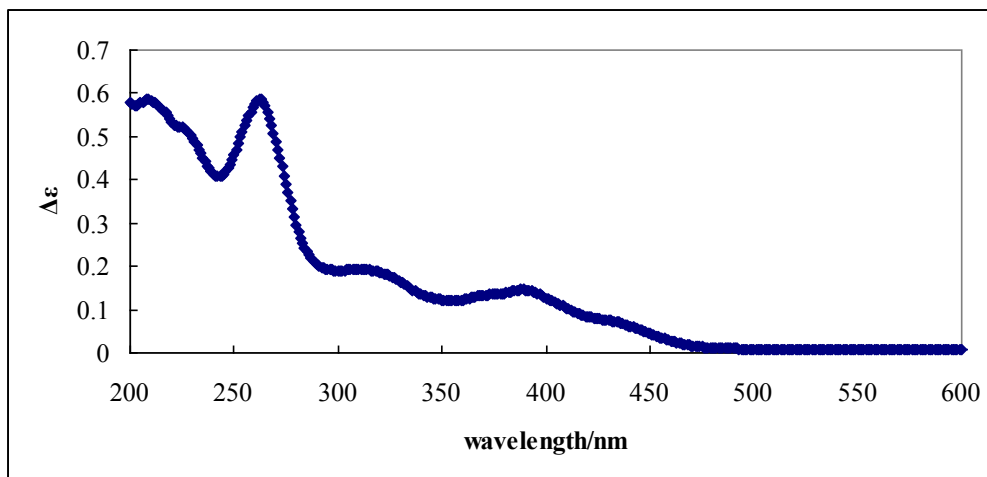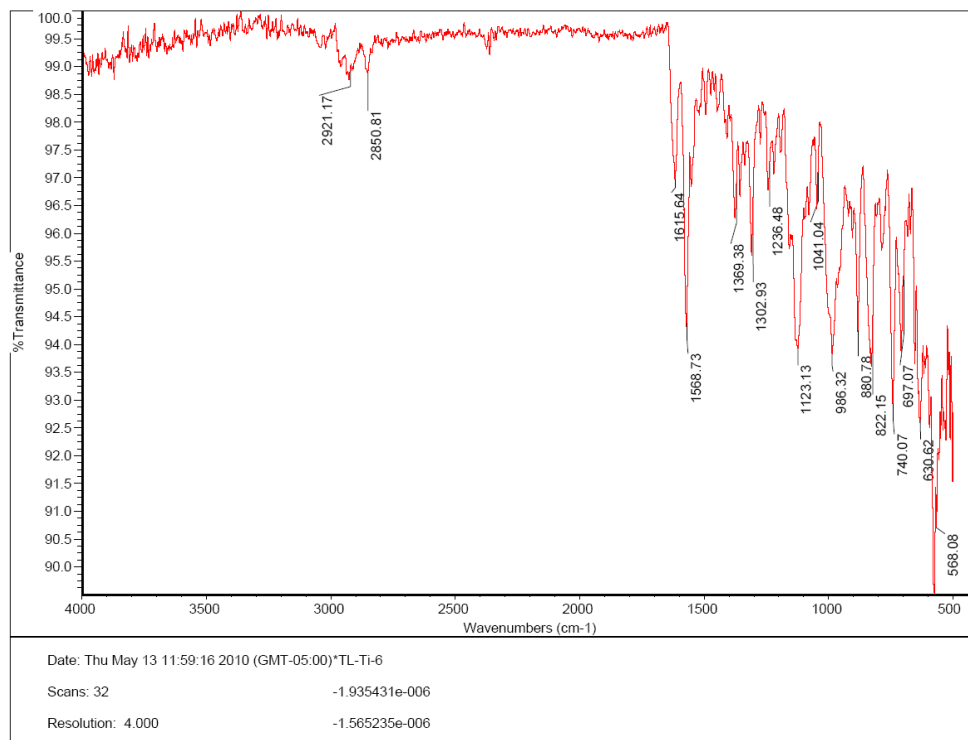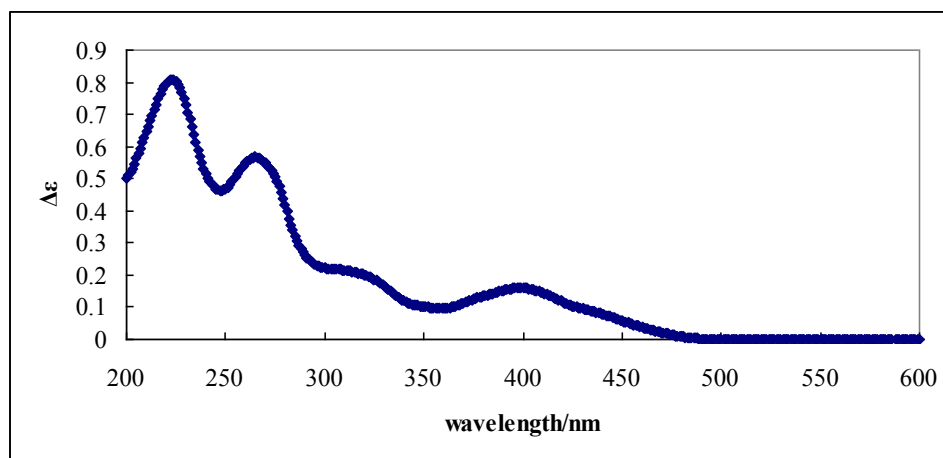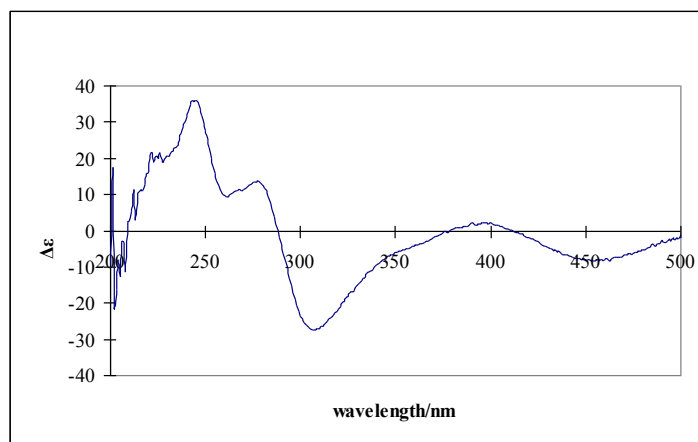

IR and UV-Vis of complex 1
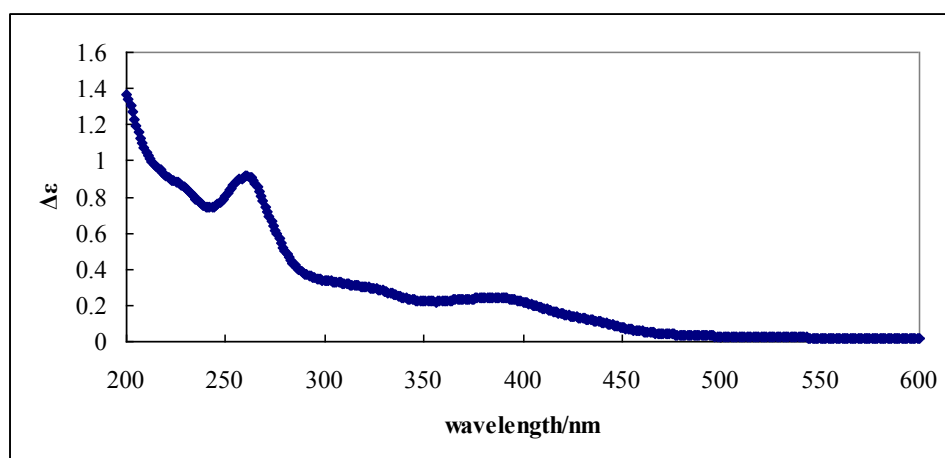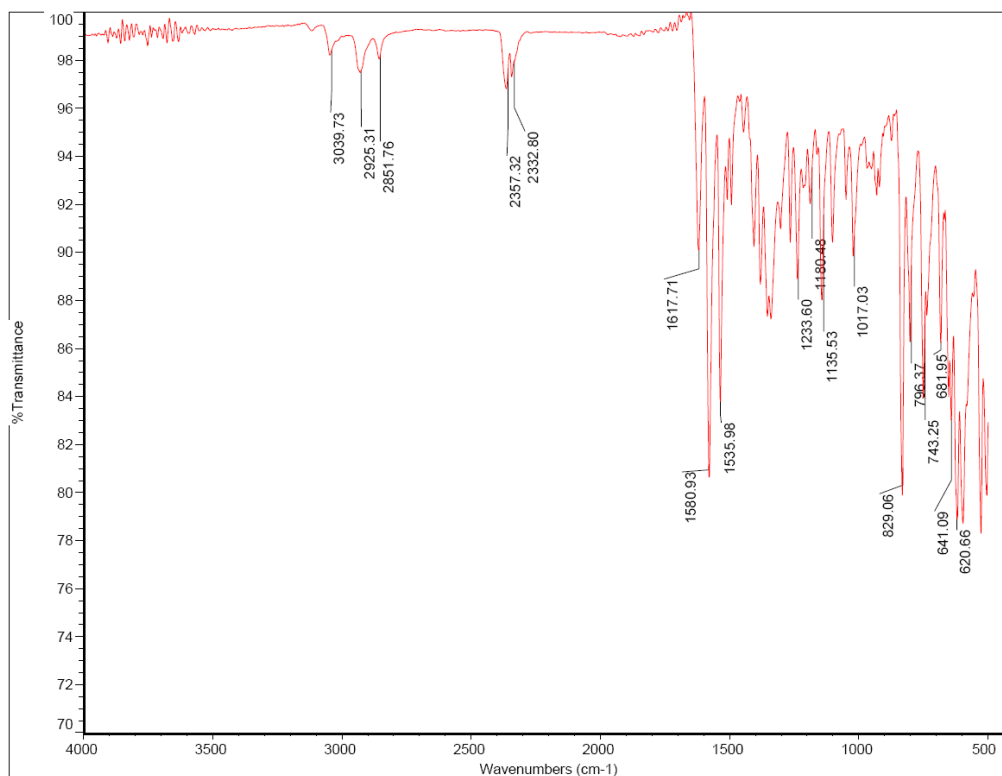
IR and UV-Vis of complex 2
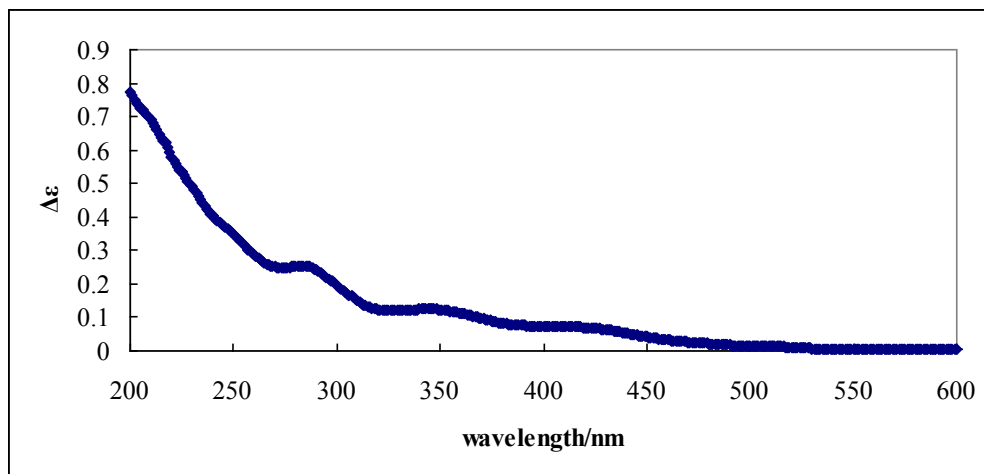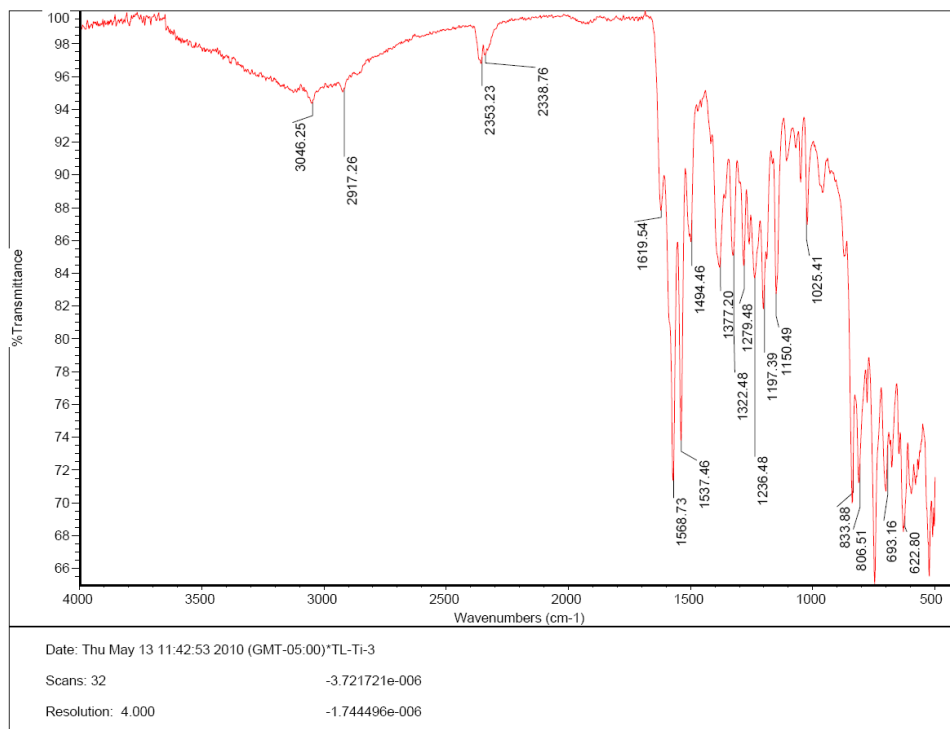
IR and UV-Vis of complex 3
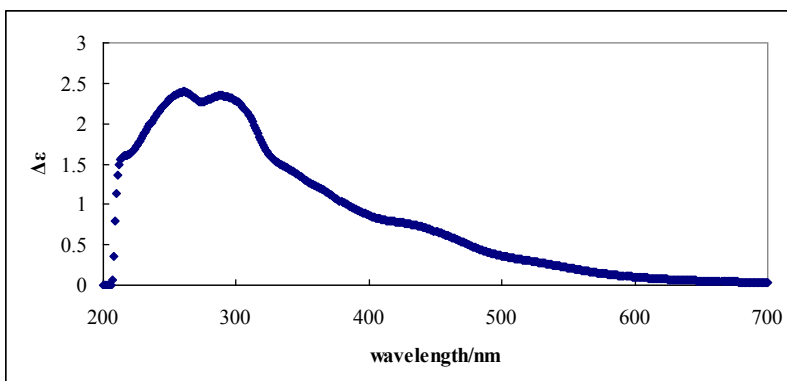
IR and UV-Vis of complex 4
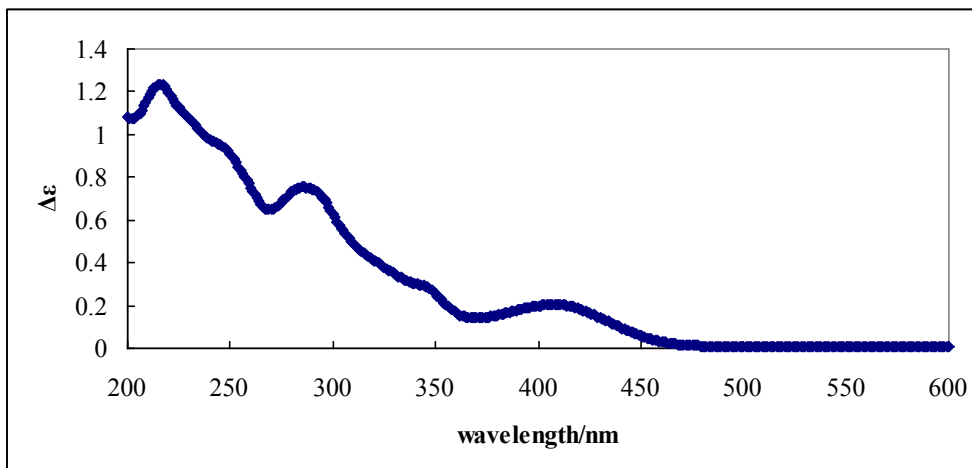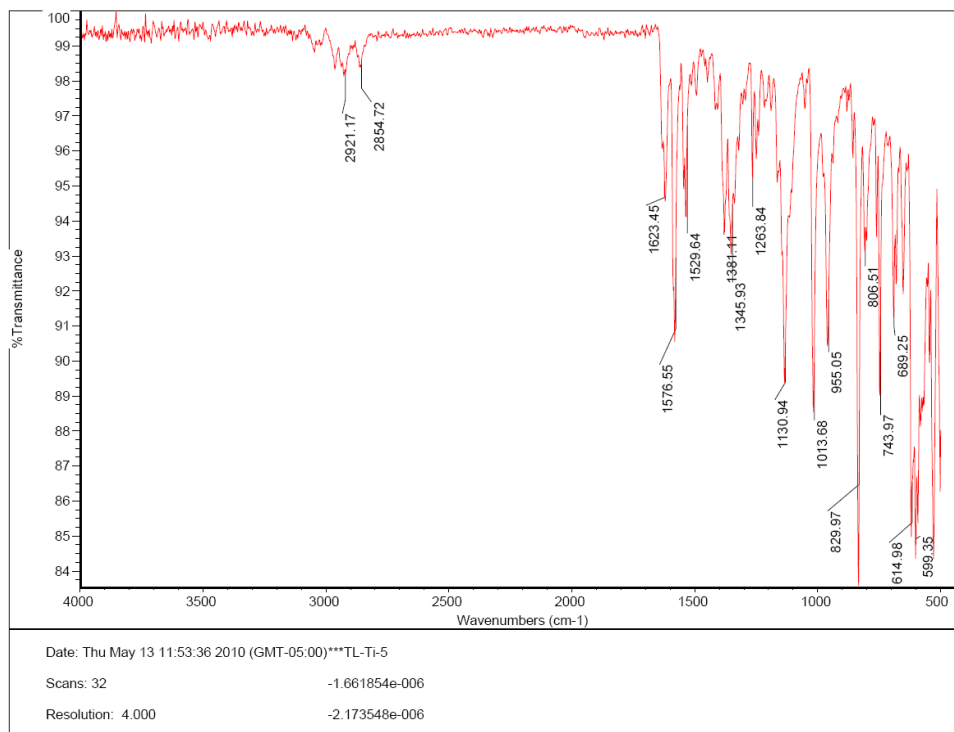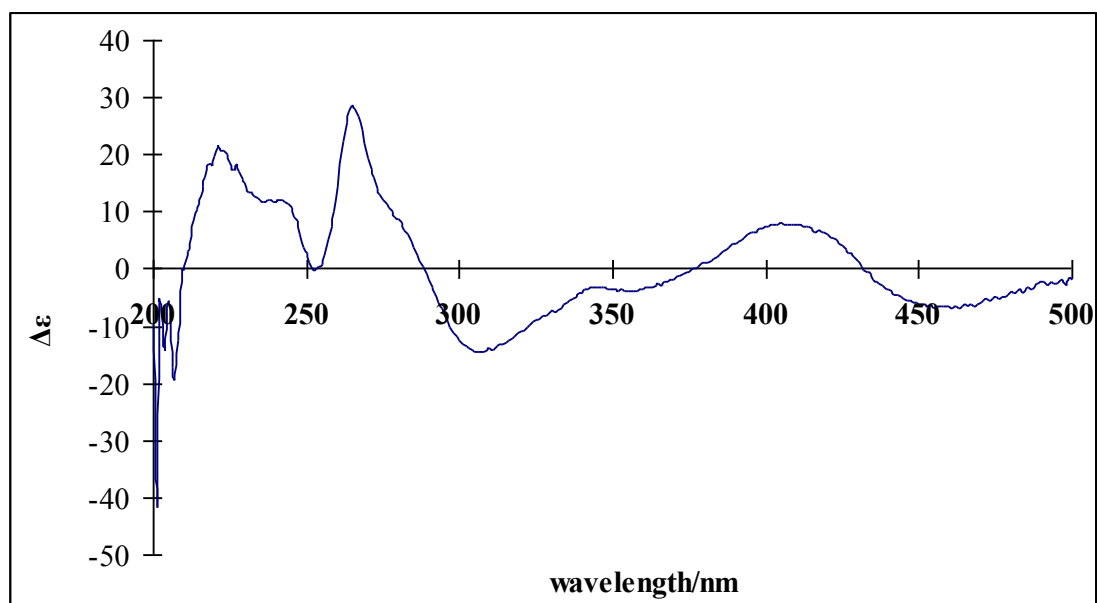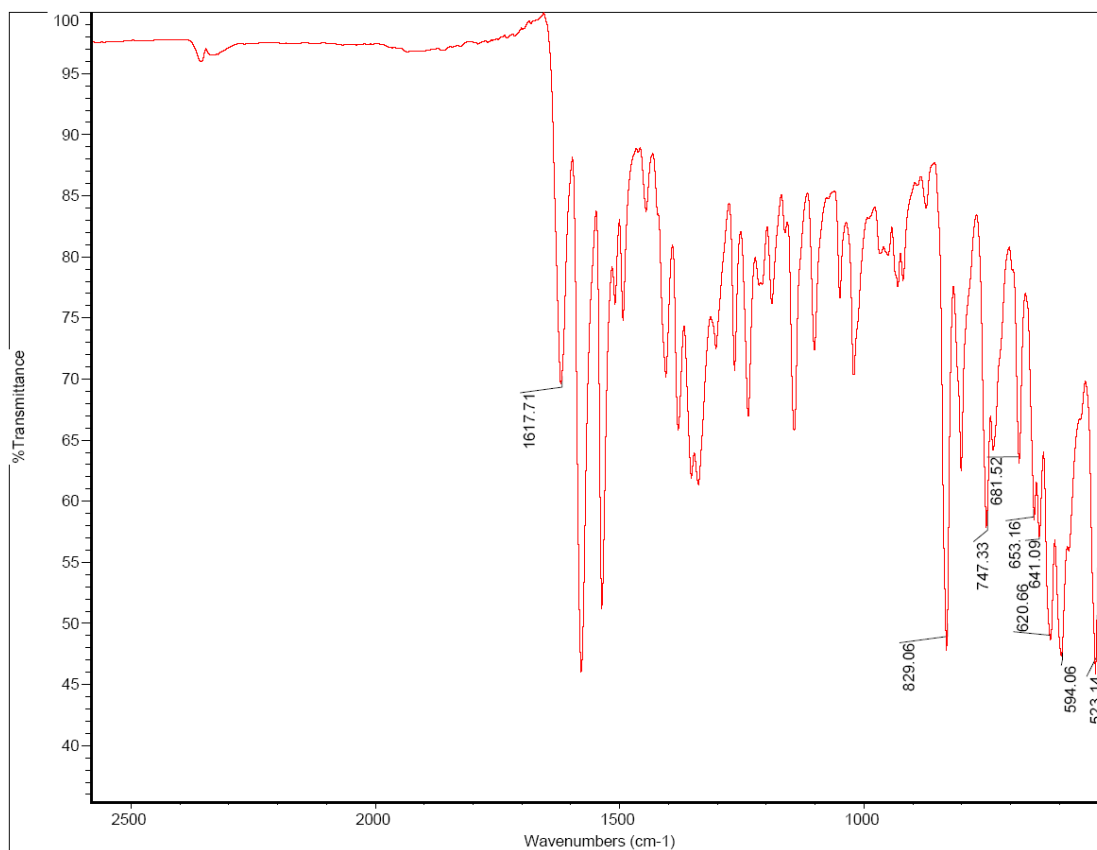
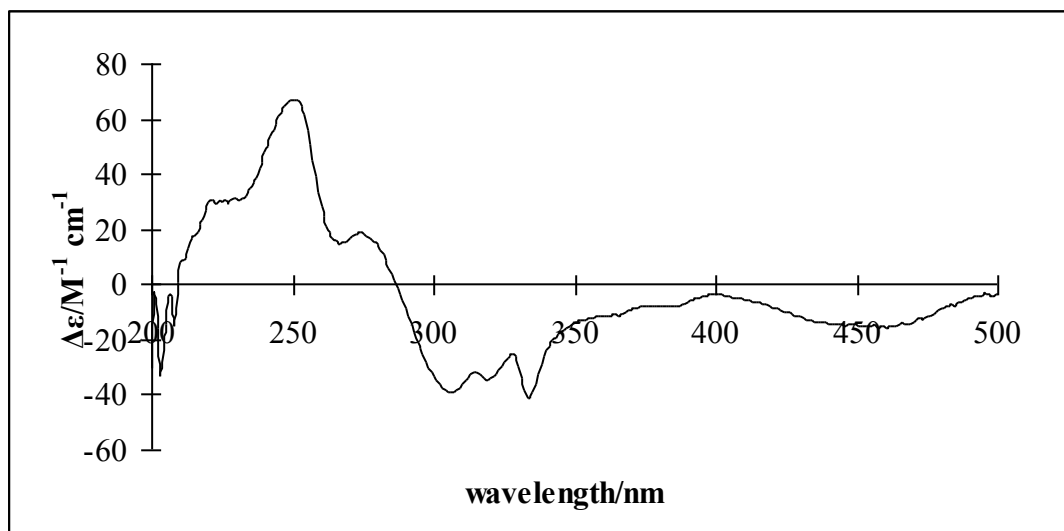**IR and UV-Vis of complex 5**

IR and UV-Vis of complex 6
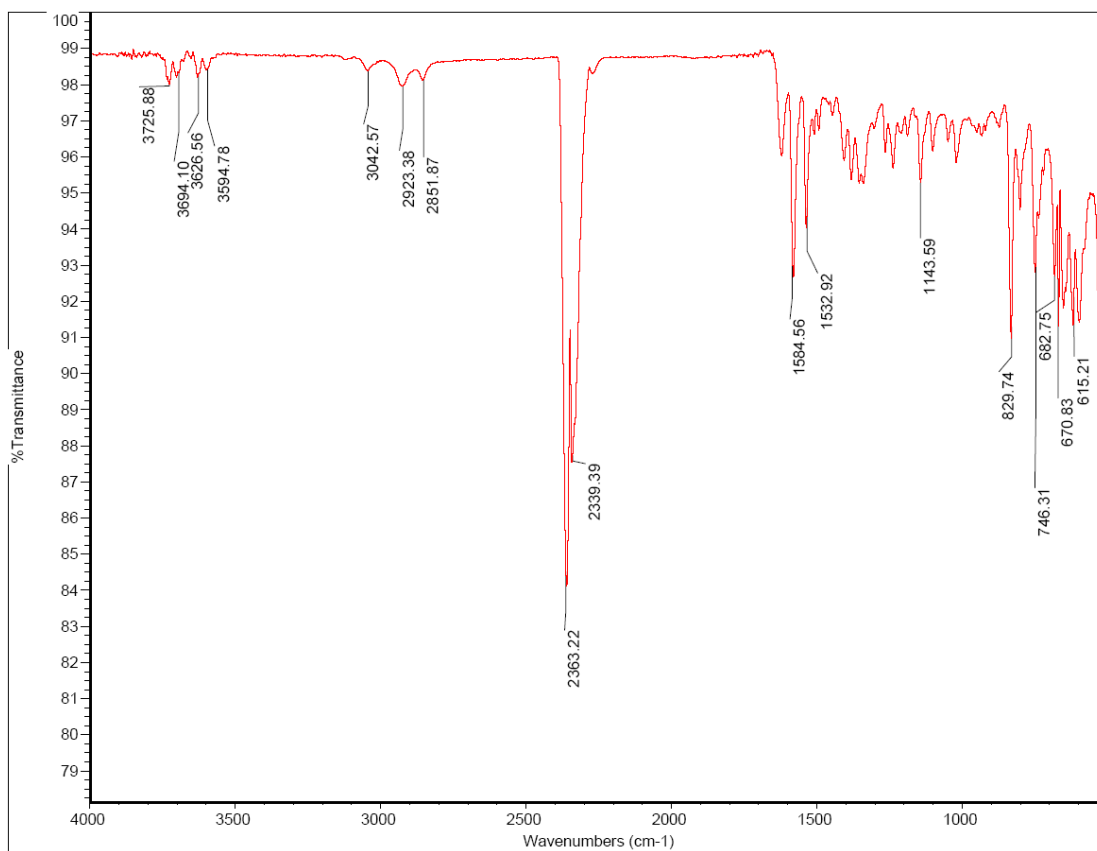
133
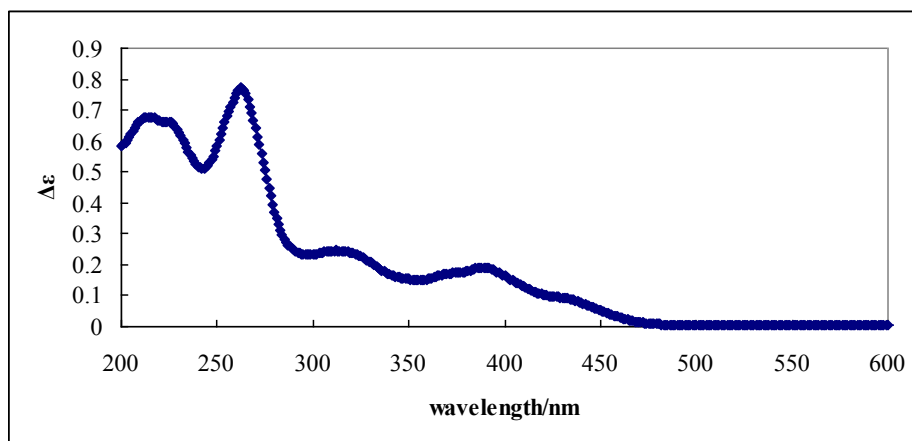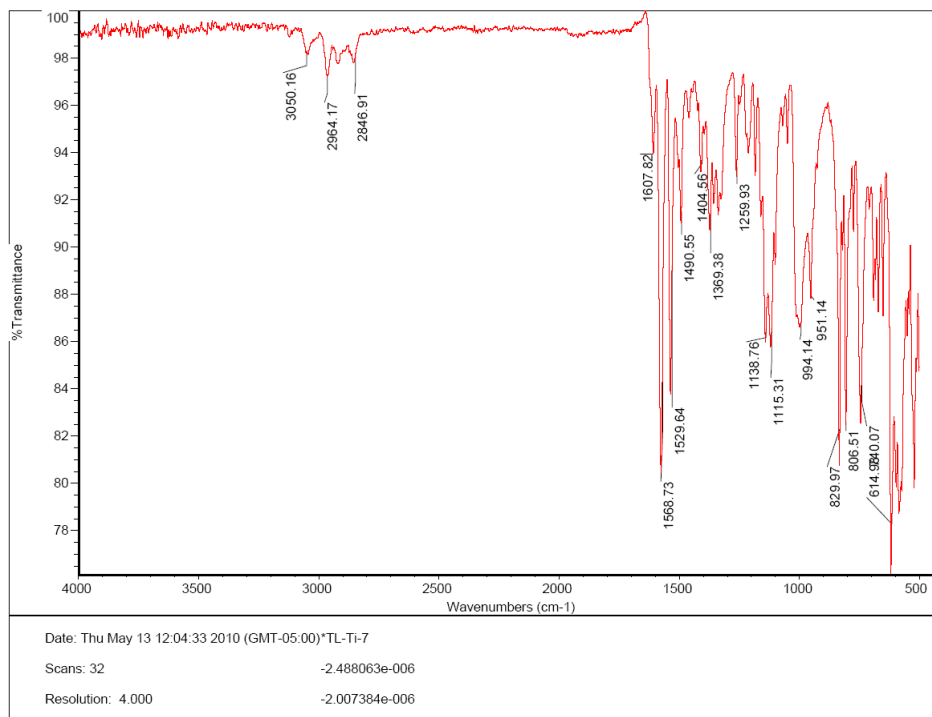
IR and UV-Vis of complex 7
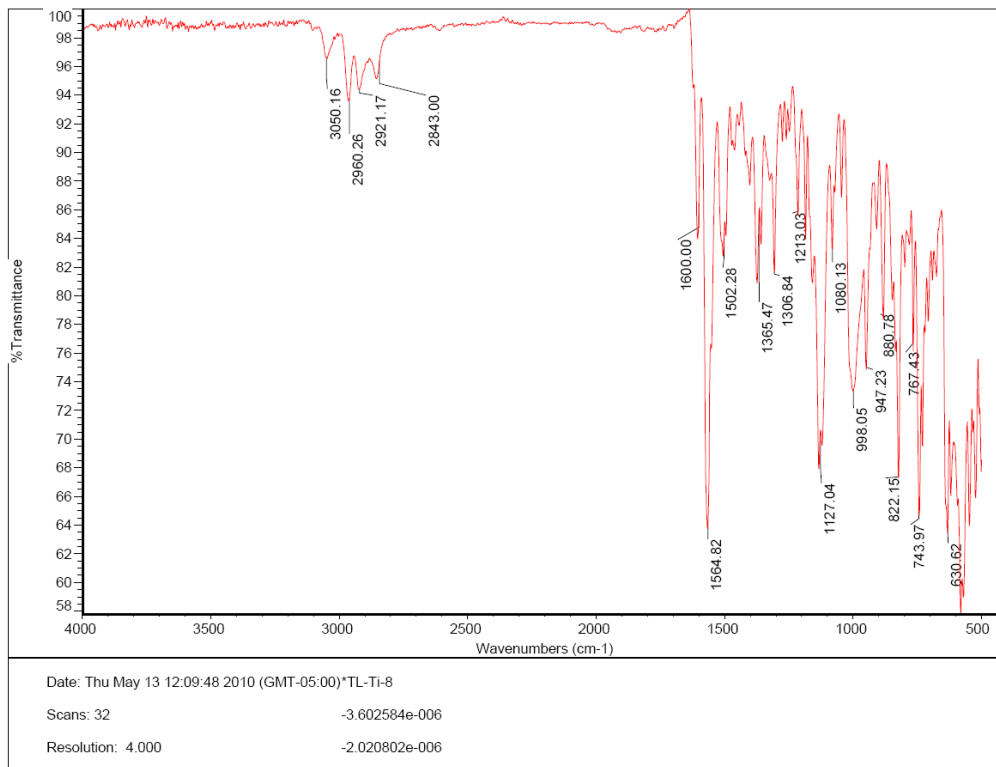
IR and UV-Vis of complex 8
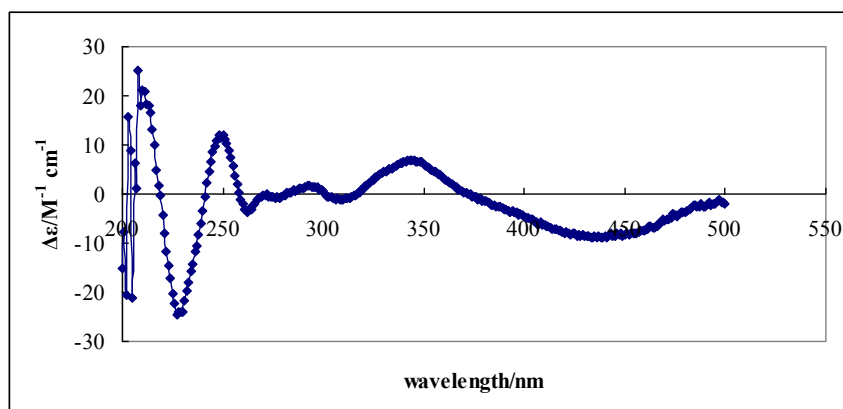
135
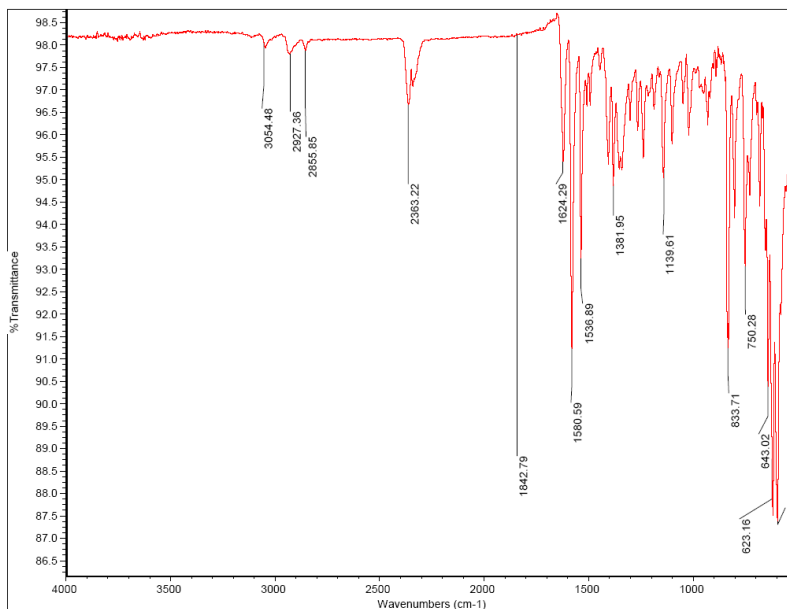
IR, UV-Vis and CD of complex 9

IR and CD of complex 10

IR and CD of complex 11
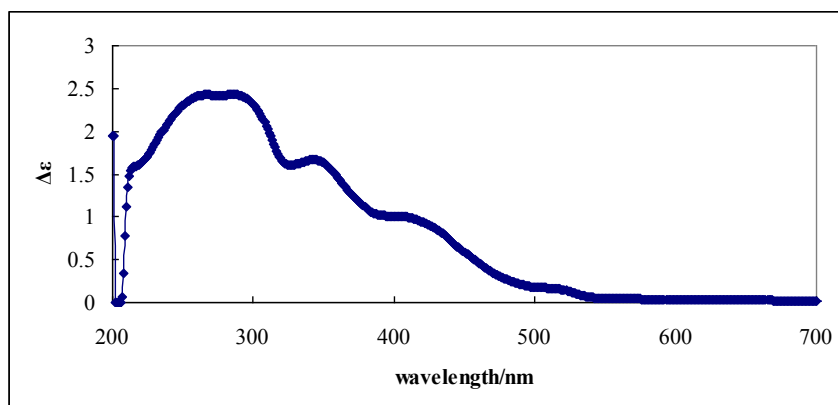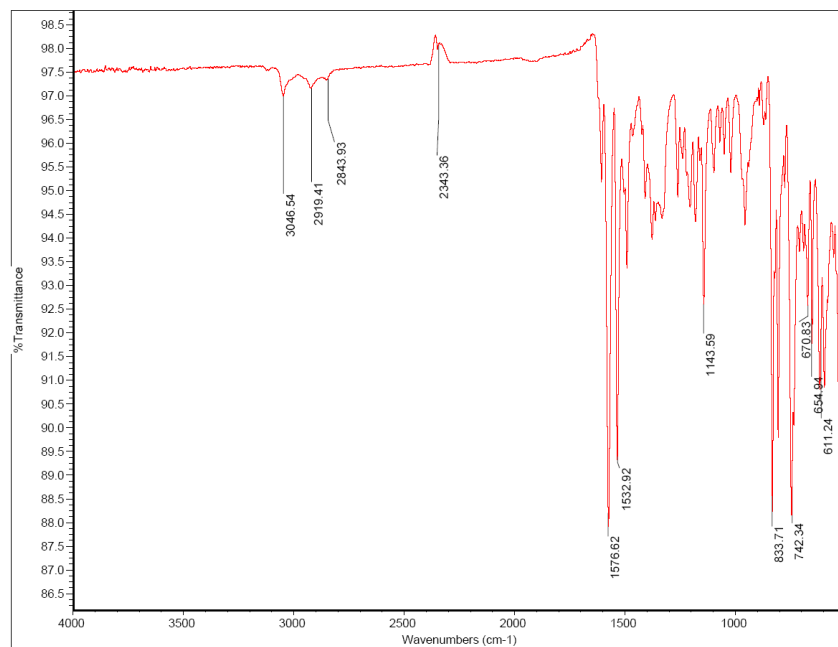
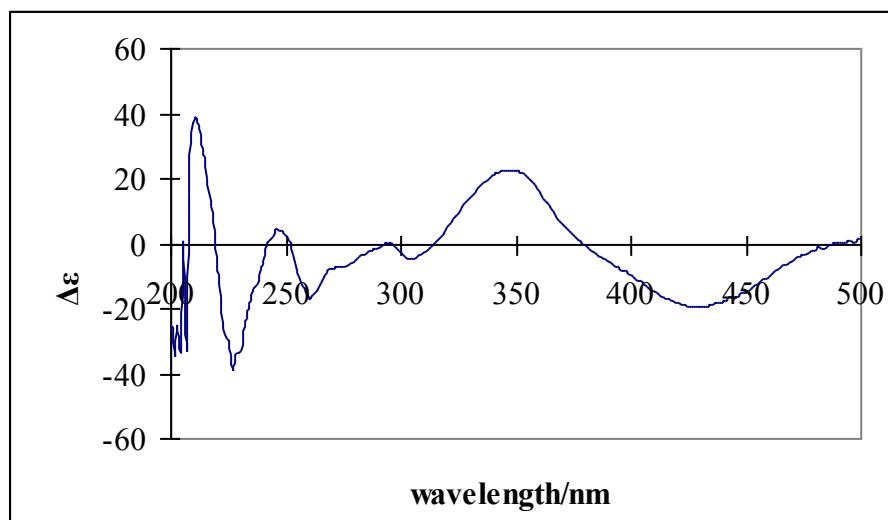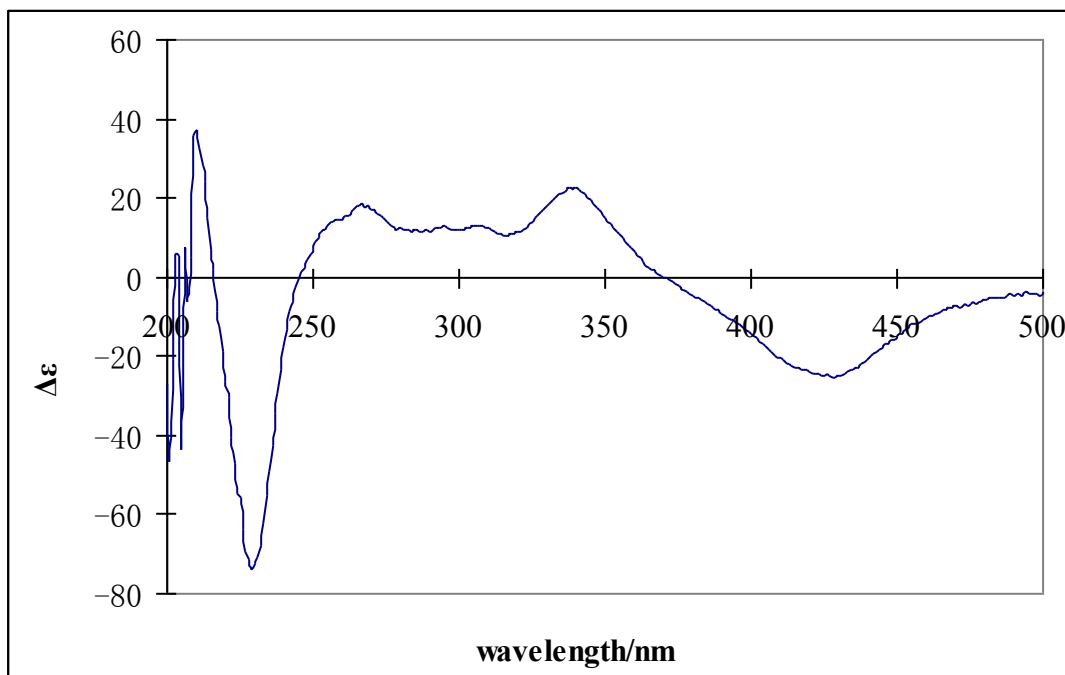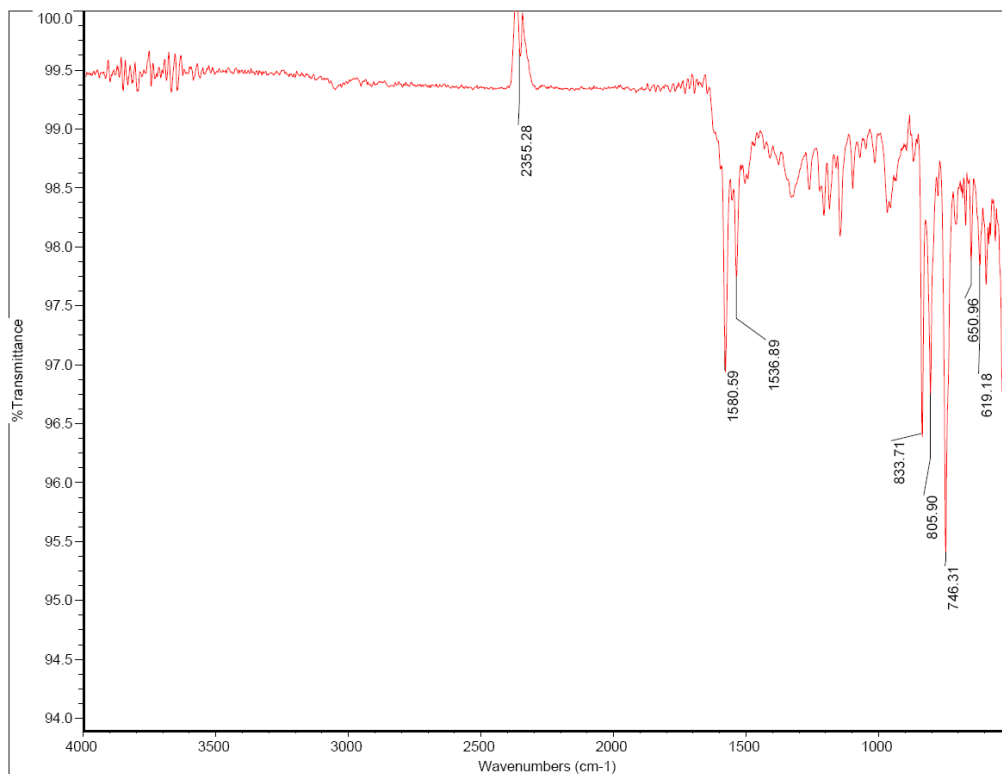**IR, UV-Vis and CD of complex 12**
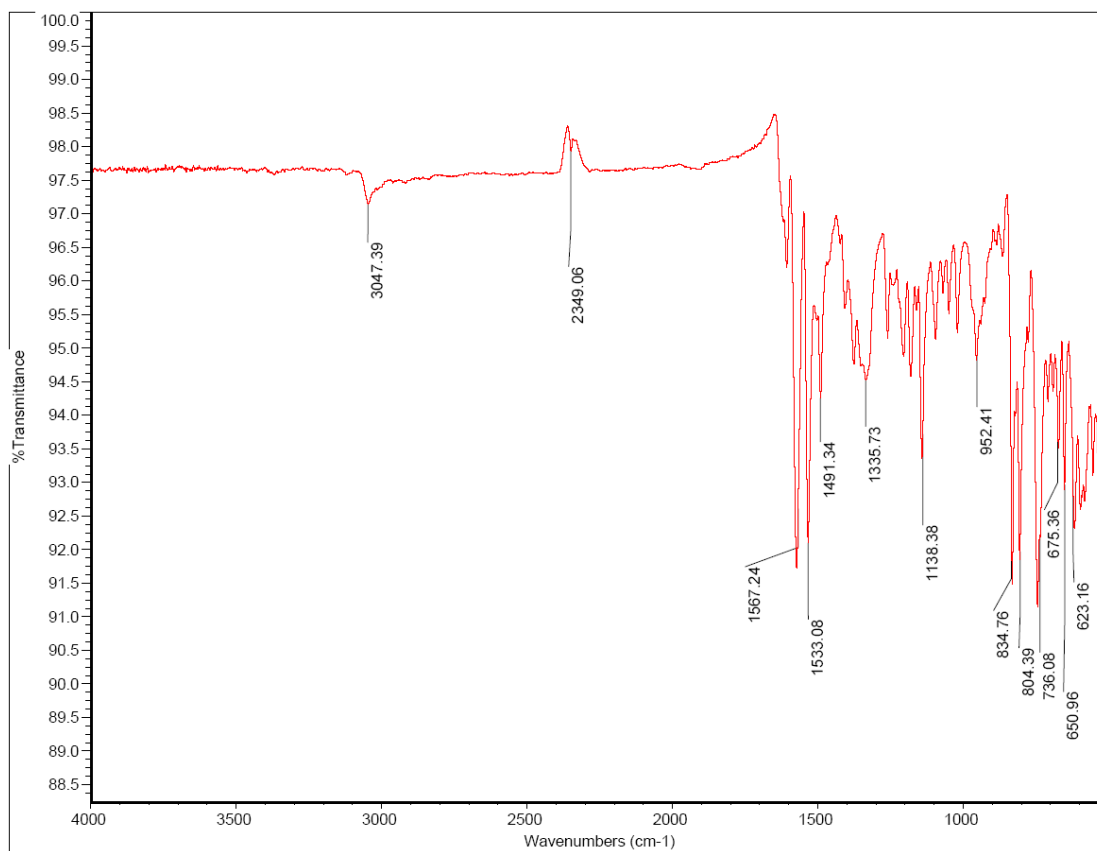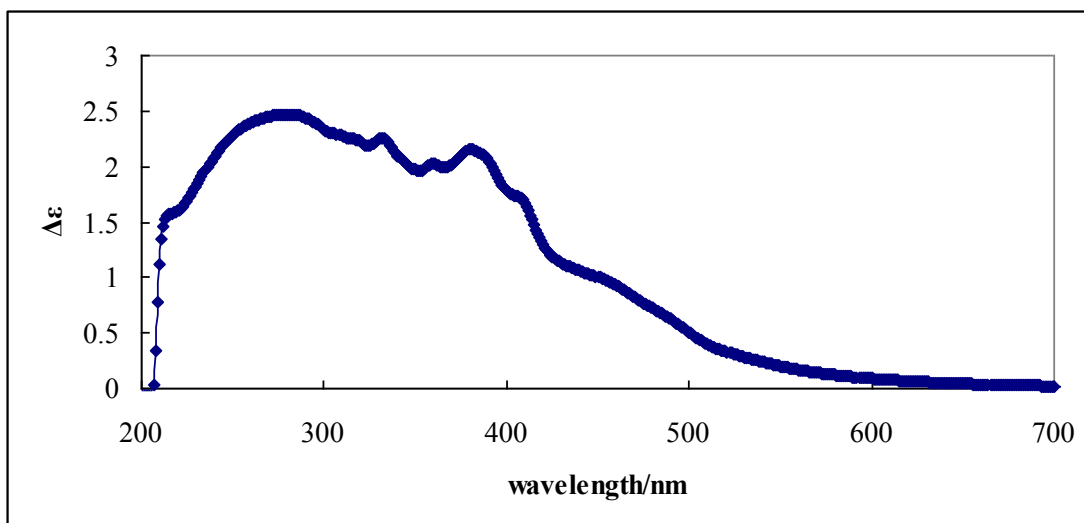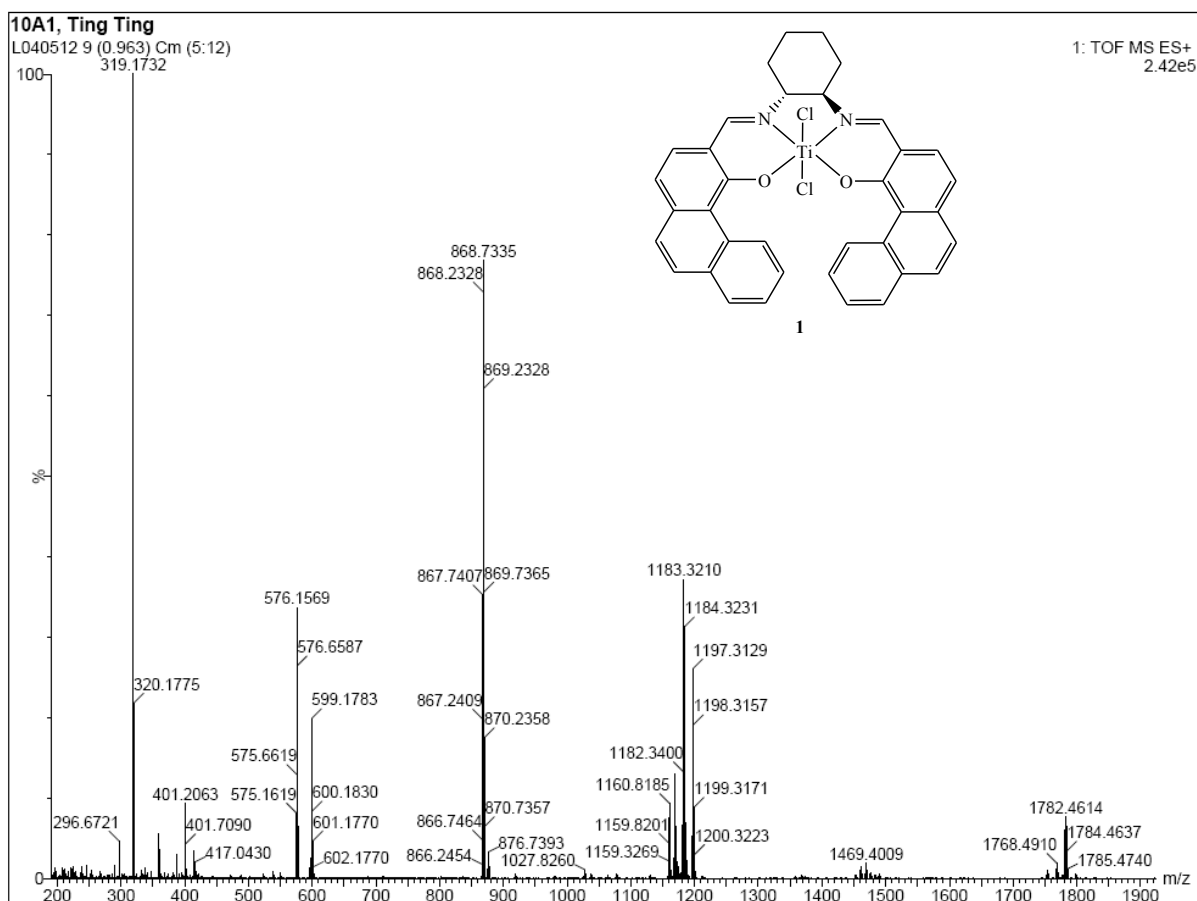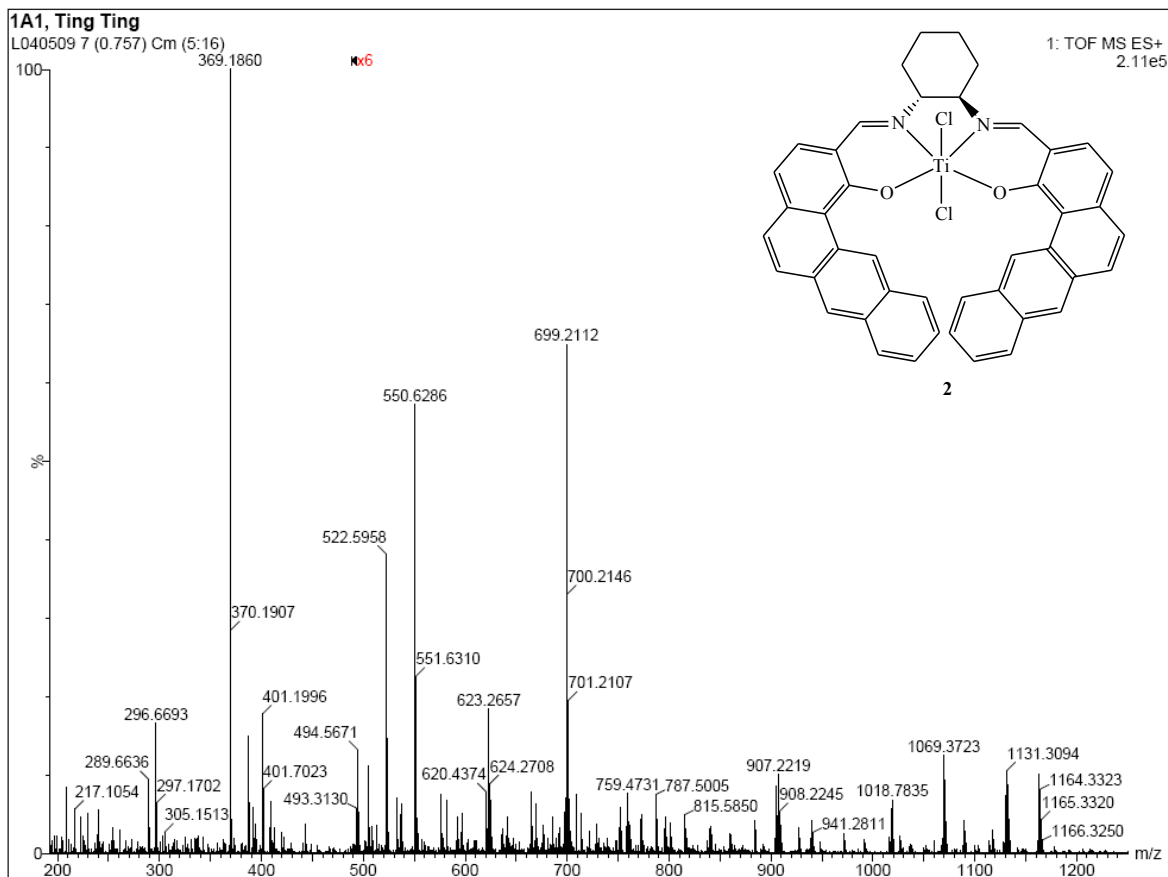
IR and CD of complex 13

IR and CD of complex 14

UV-Vis of complex 15

Appendix C - HR-ESI-MS

Complex 1

Complex 2
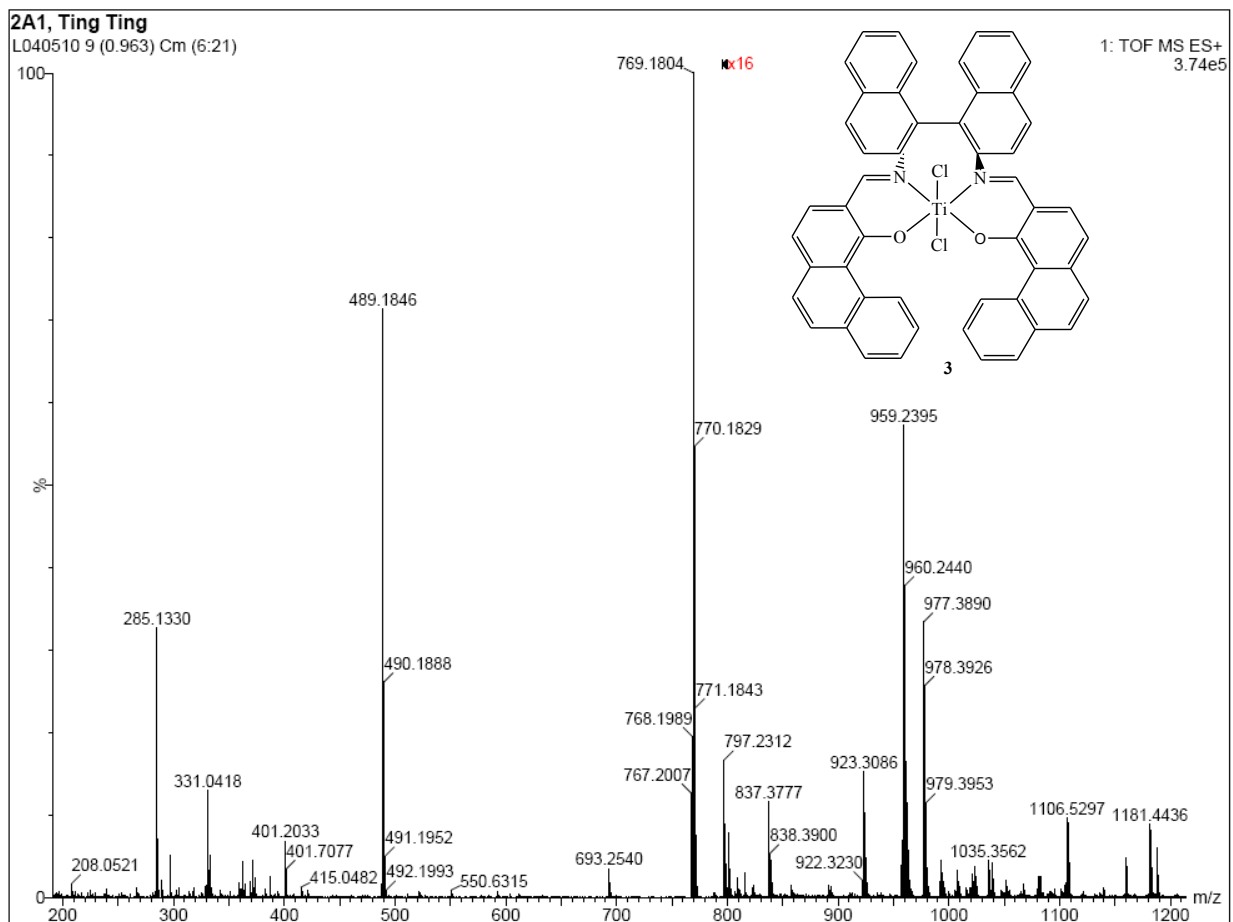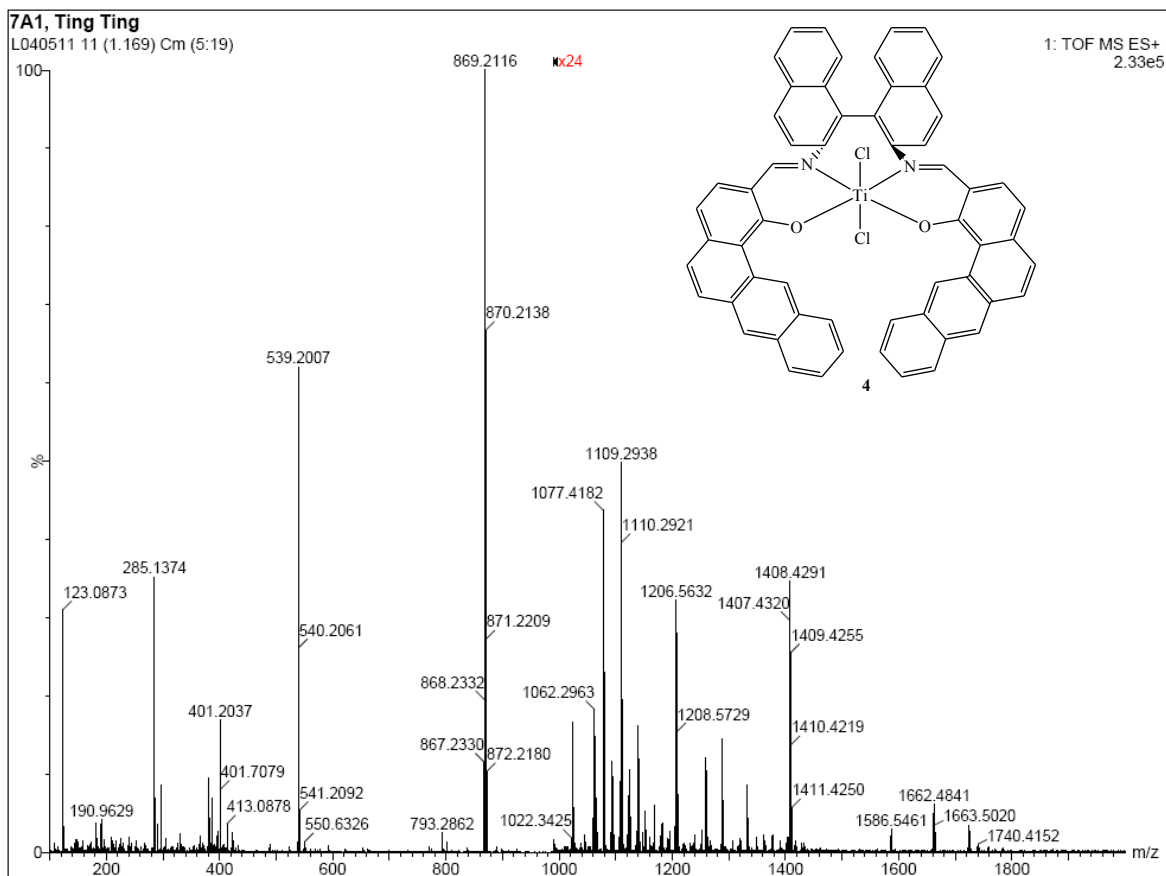
Complex 3
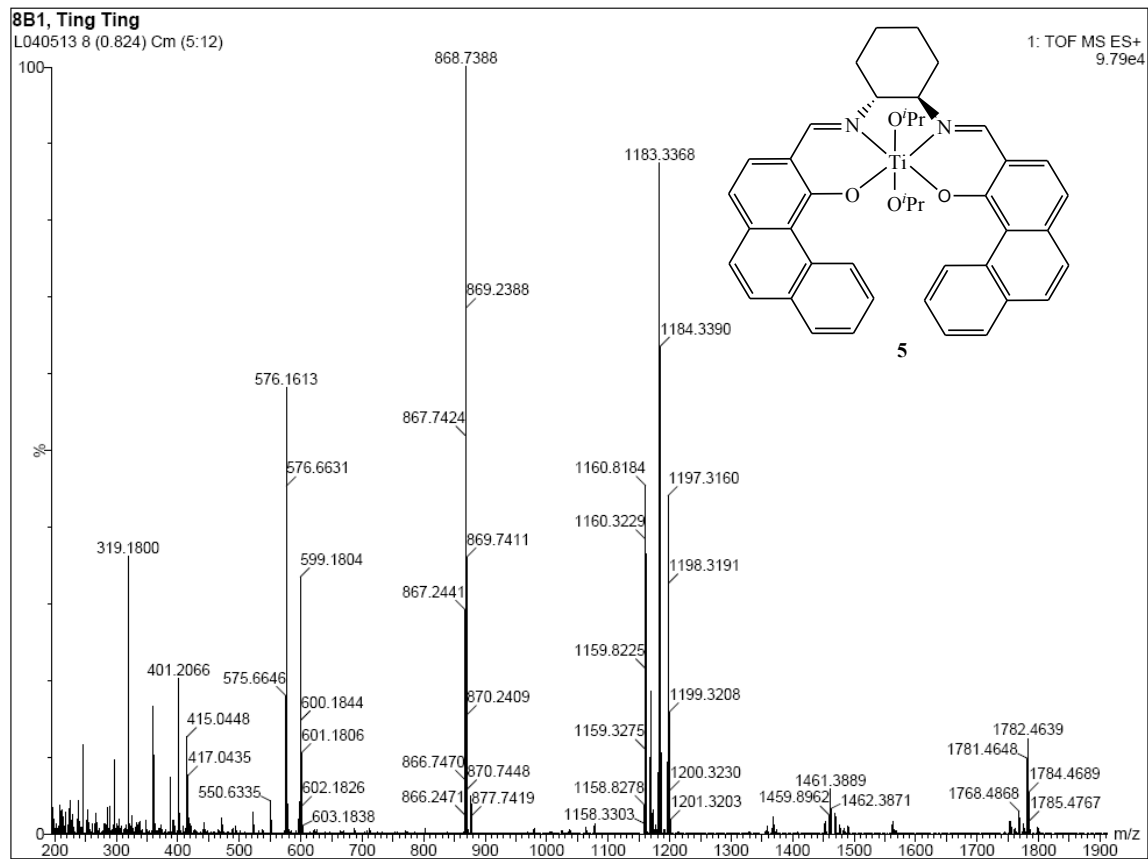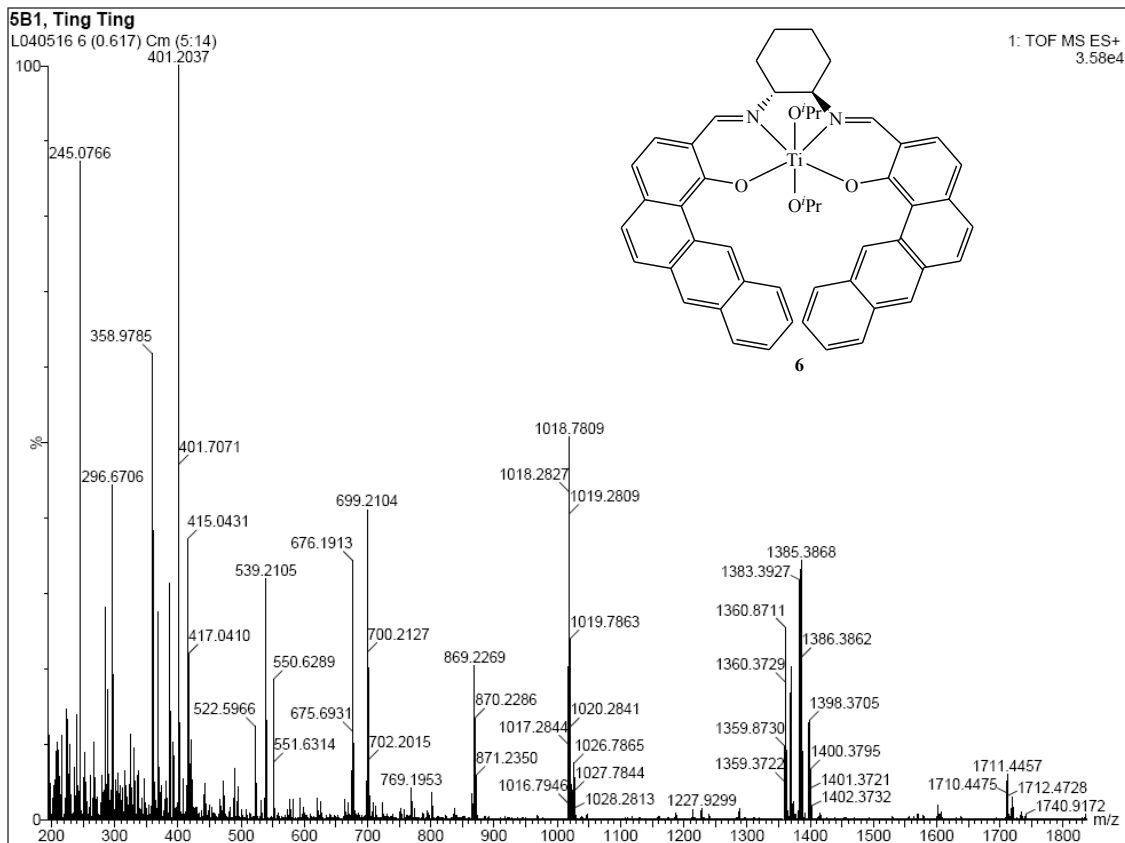
Complex 4

Complex 5
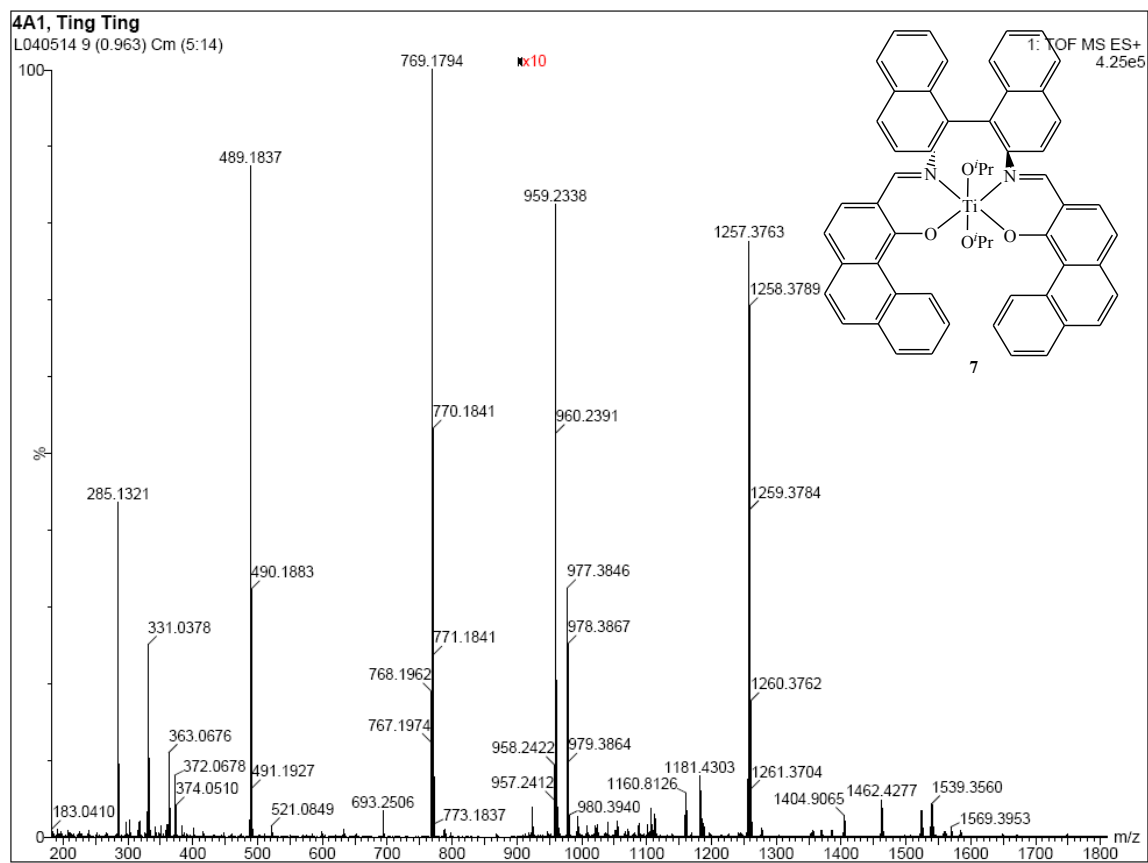
Complex 6

Complex 7
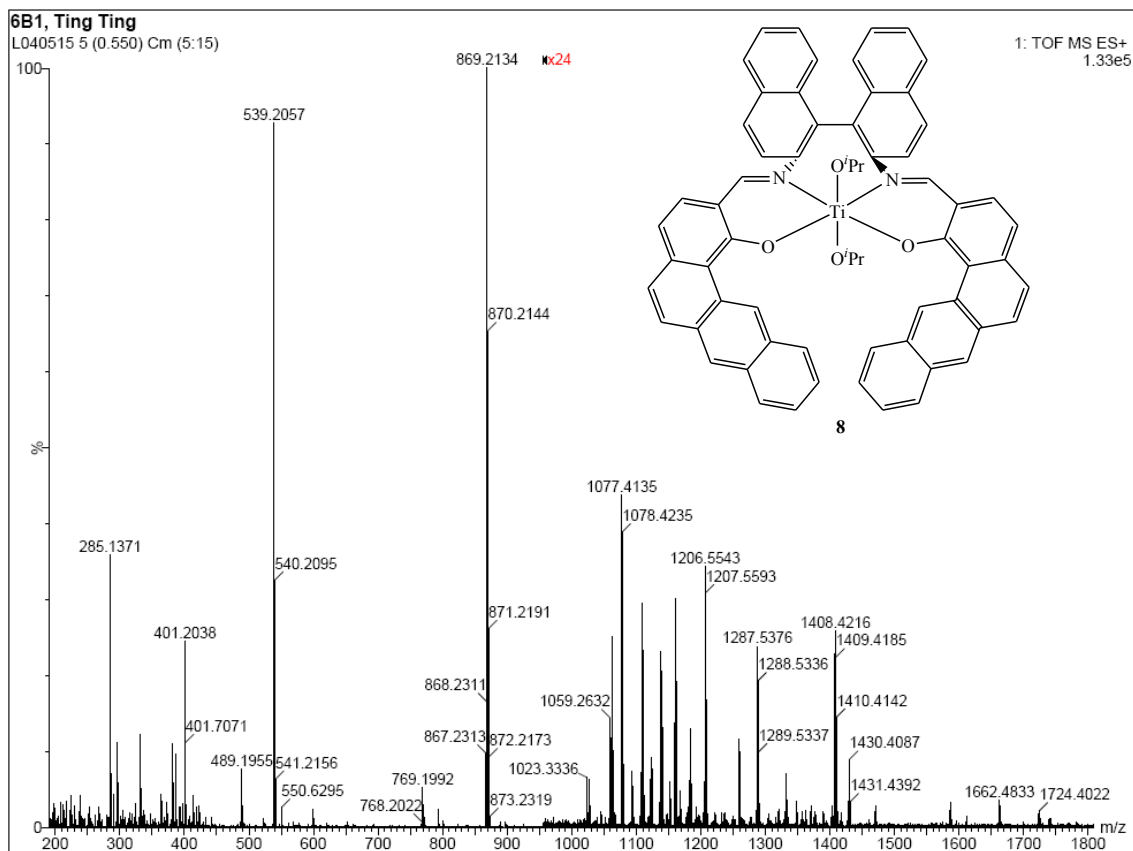
Complex 8
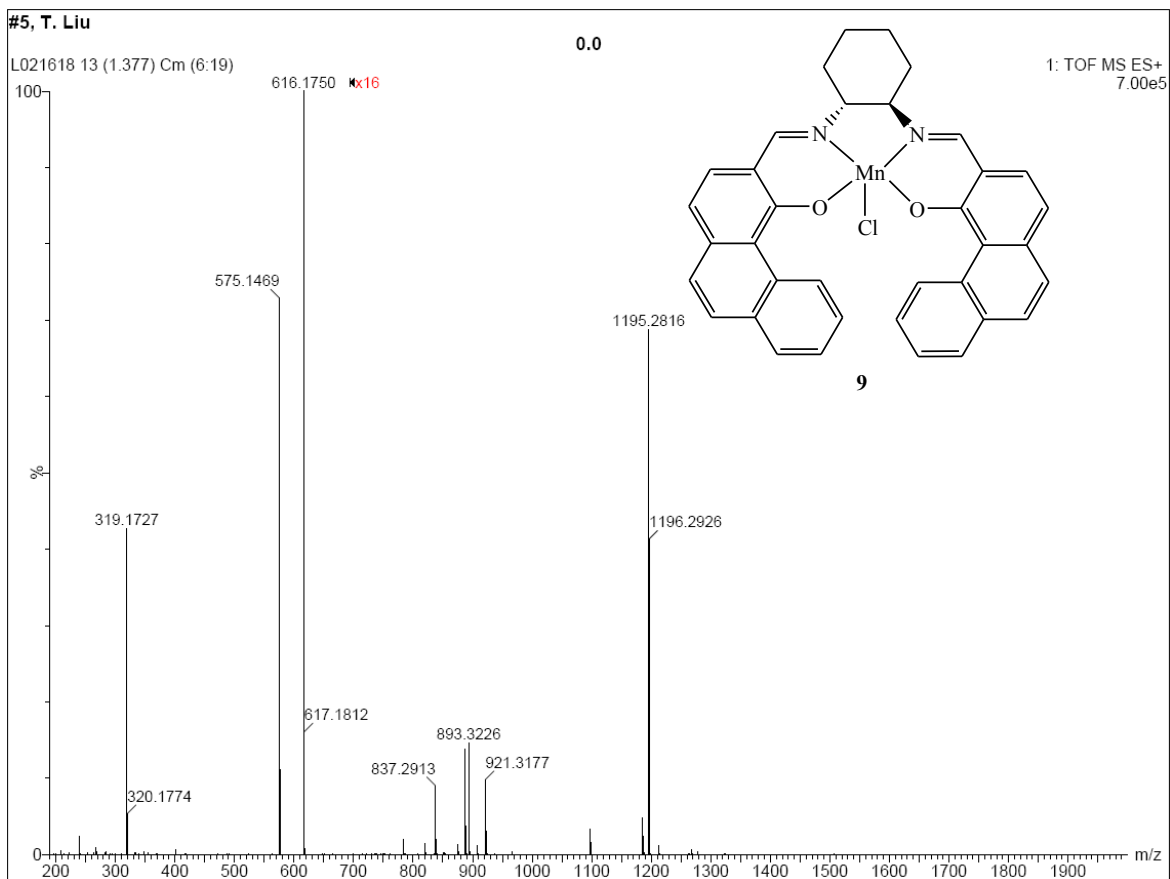
Complex 9
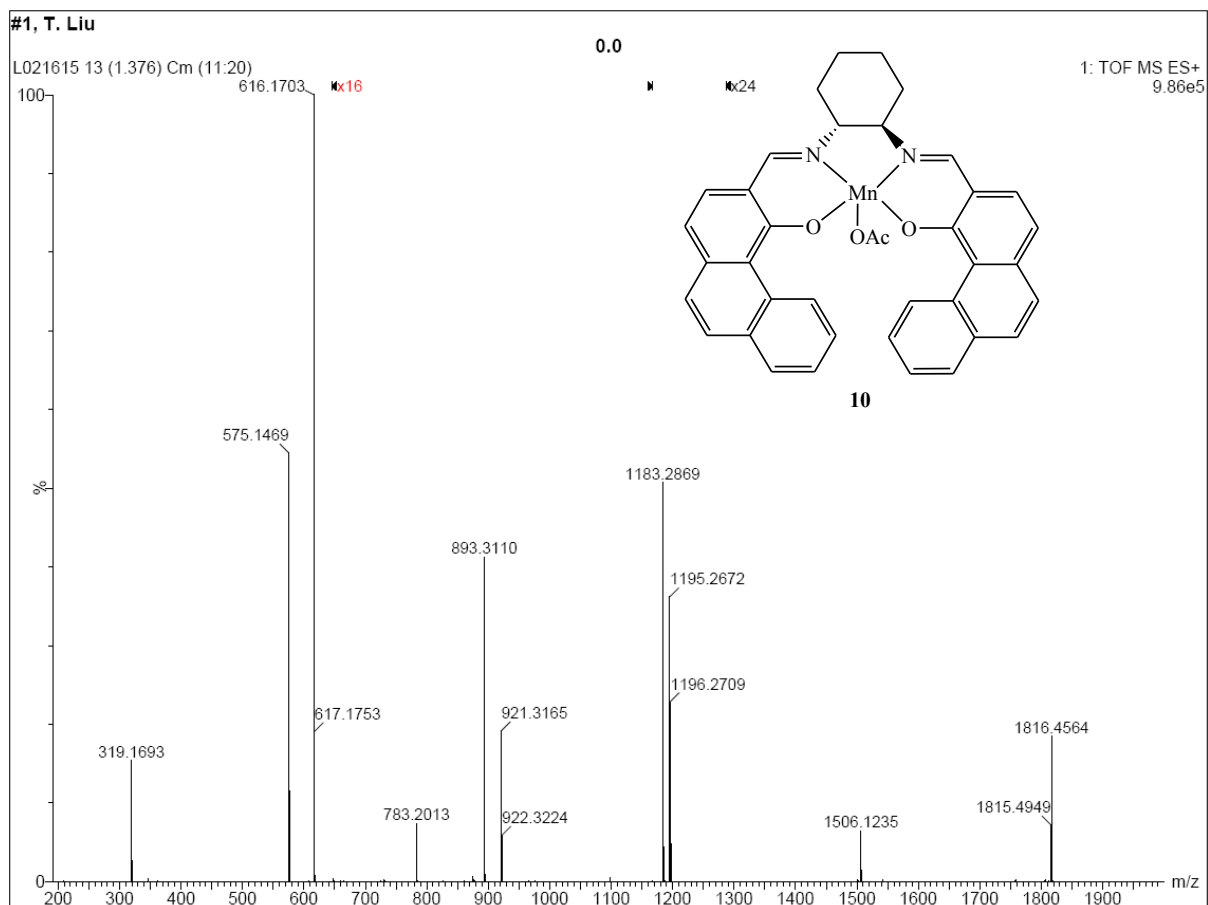
Complex 10
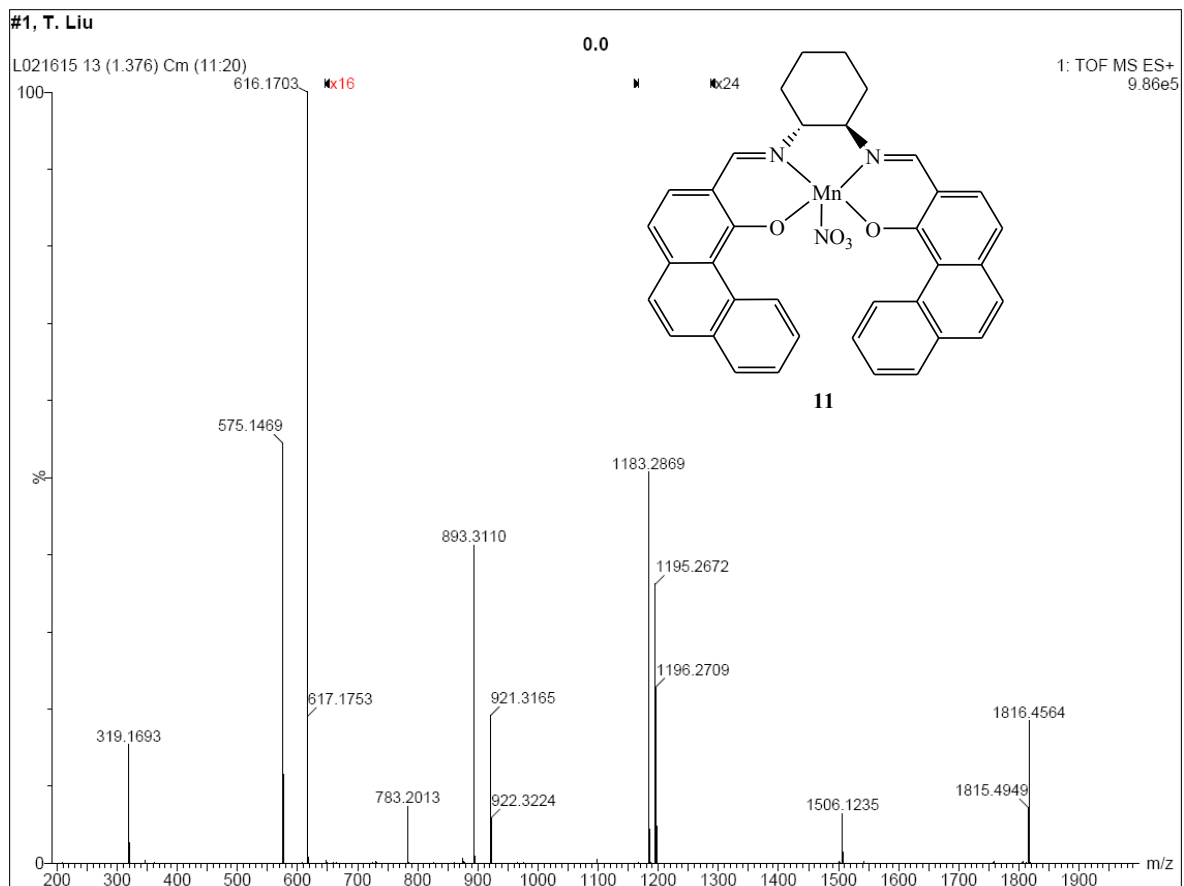
Complex 11
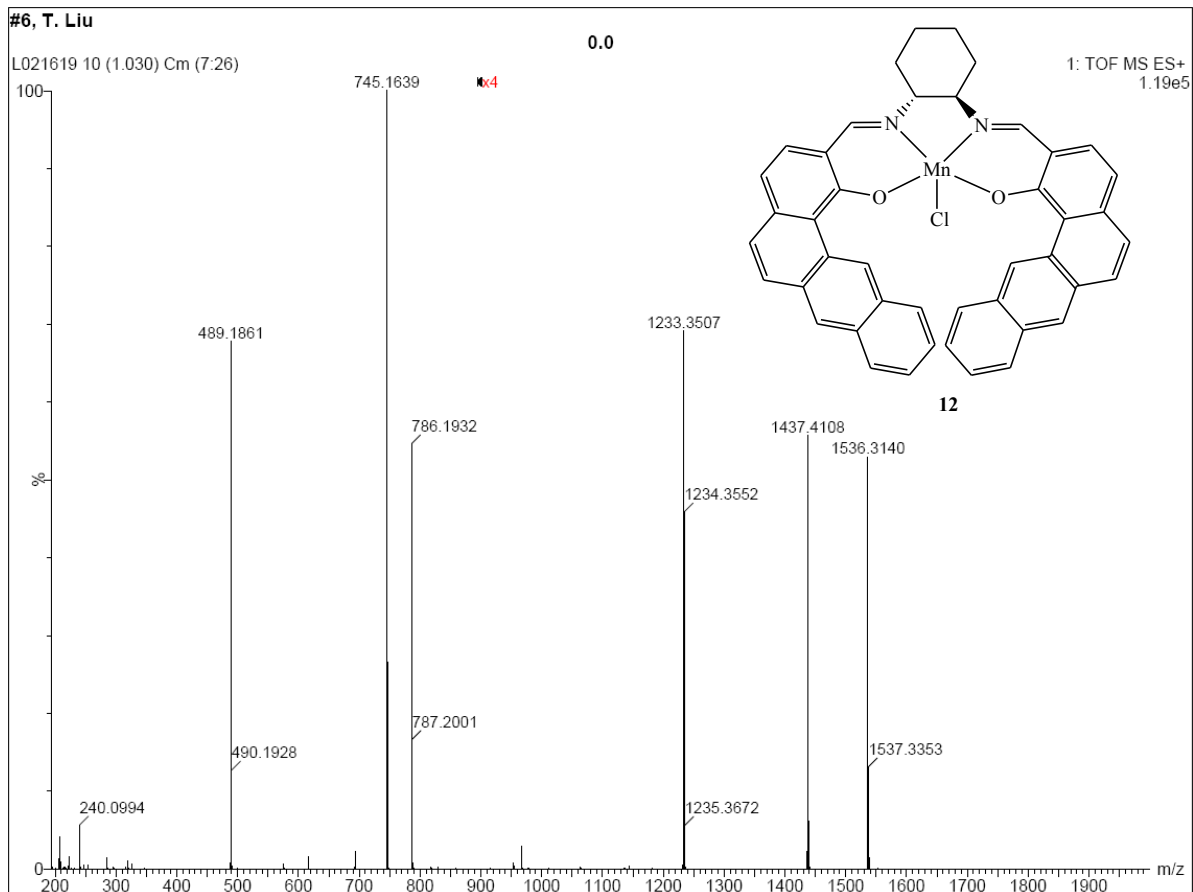
Complex 12
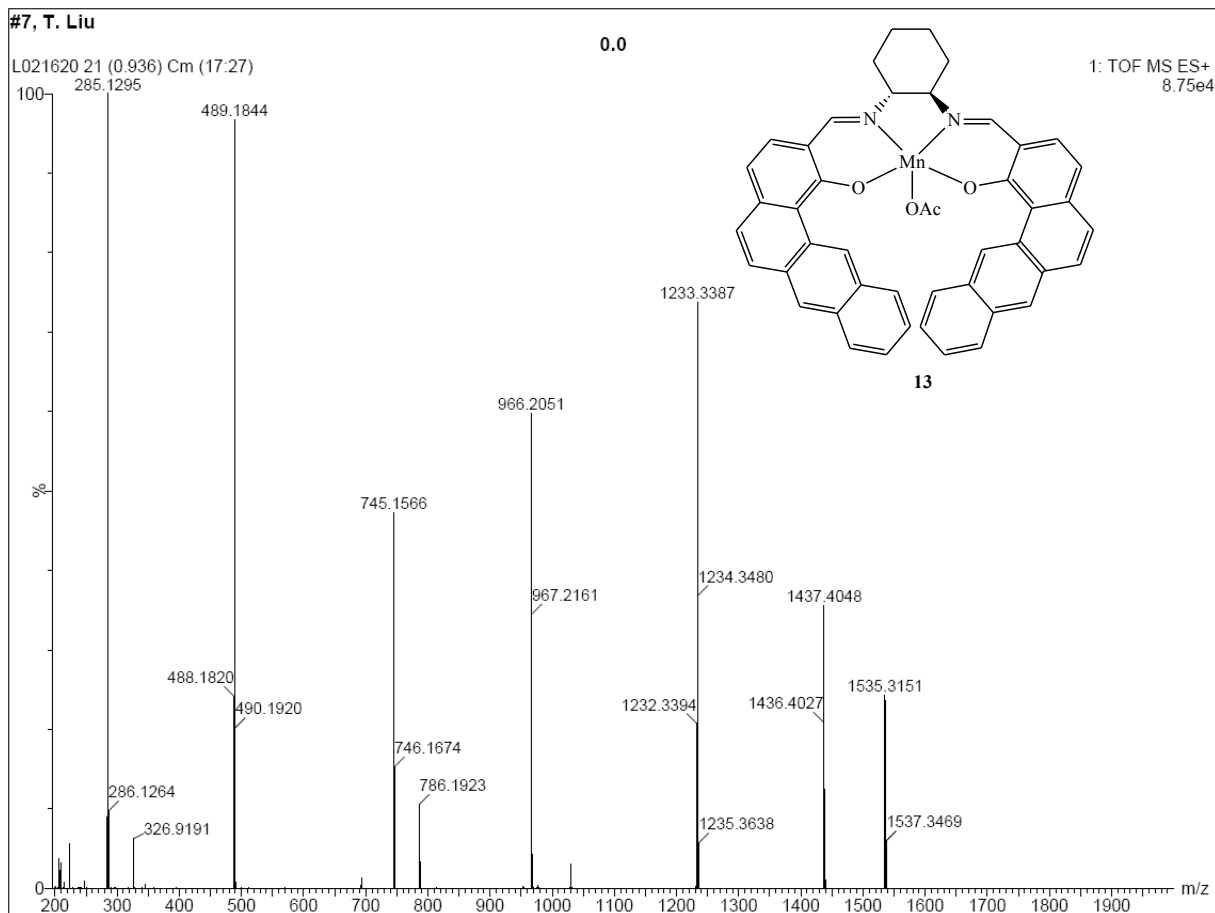
Complex 13
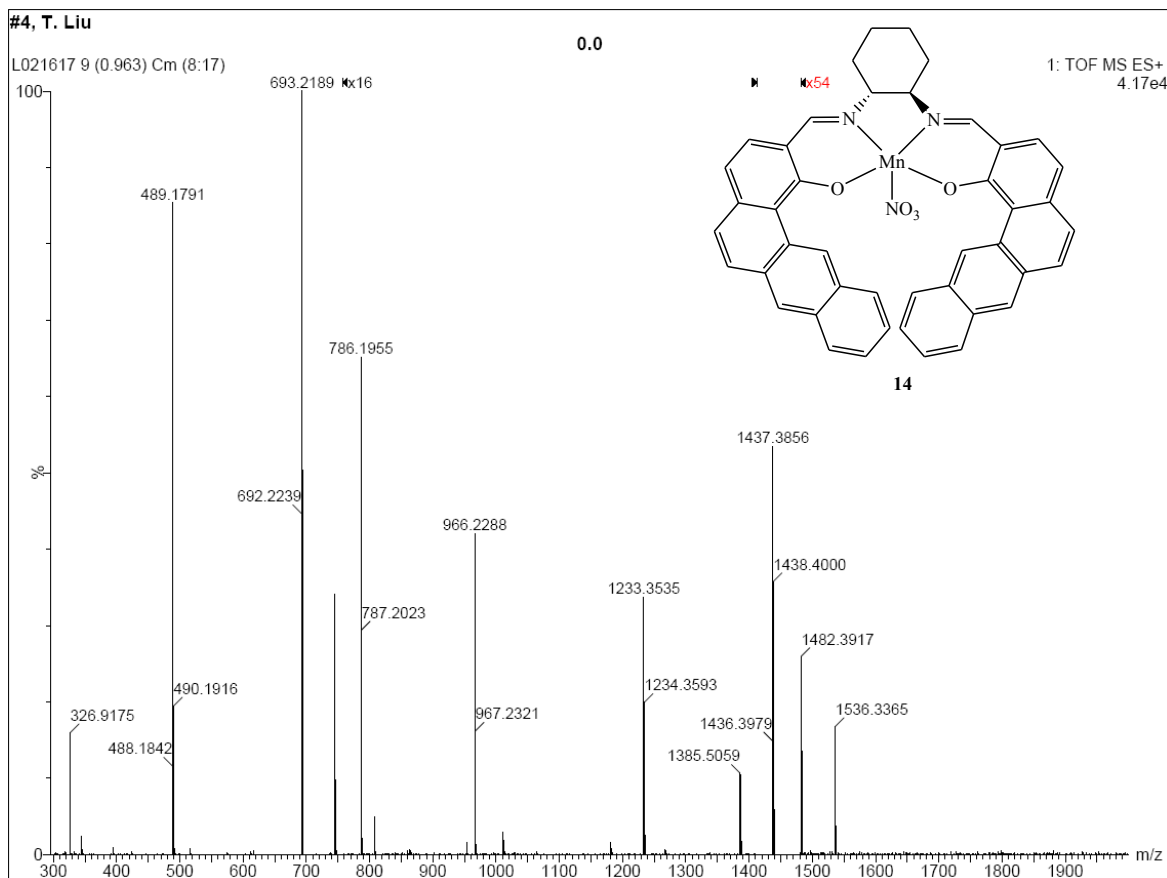
Complex 14
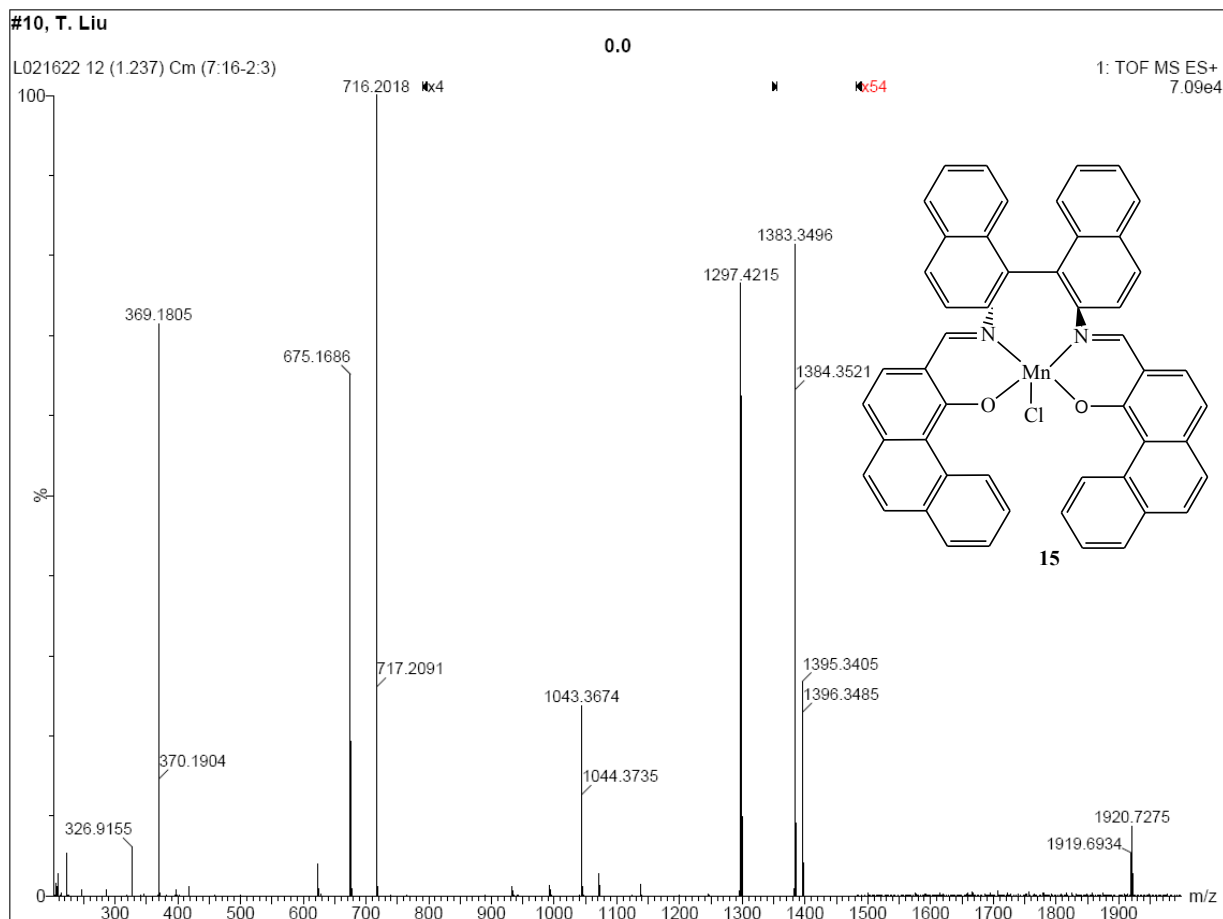
Complex 15

Appendix D - Crystal data

Table 1. Crystal data and structure refinement for complex 1 (tl0903m).

Identification code	tl0903m
Empirical formula	C75 H62 Cl8 N4 O5 Ti2
Formula weight	1478.69
Temperature	120(2) K
Wavelength	0.71073 Å
Crystal system	Orthorhombic
Space group	P2(1)2(1)2(1)

Unit cell dimensions	a = 14.5966(7) Å	$\alpha = 90°$.
	b = 14.6674(8) Å	$\beta = 90°$.
	c = 30.3466(15) Å	$\gamma = 90°$.

Volume	6497.0(6) $Å^3$
Z	4
Density (calculated)	1.512 g/cm^3
Absorption coefficient	0.633 mm^{-1}
F(000)	3040
Crystal size	0.30 x 0.24 x 0.14 mm^3
Theta range for data collection	1.55 to 32.03°.
Index ranges	-10<=h<=21, -16<=k<=21, -45<=l<=32
Reflections collected	45898
Independent reflections	19548 [R(int) = 0.0360]
Completeness to theta = 32.03°	99.2 %
Absorption correction	Semi-empirical from equivalents
Max. and min. transmission	0.9166 and 0.8327
Refinement method	Full-matrix least-squares on F^2
Data / restraints / parameters	19548 / 45 / 869
Goodness-of-fit on F^2	1.046
Final R indices [I>2sigma(I)]	R1 = 0.0555, wR2 = 0.1320
R indices (all data)	R1 = 0.0777, wR2 = 0.1472
Absolute structure parameter	0.05(2)
Largest diff. peak and hole	0.976 and -0.837 e.$Å^{-3}$

Table 2. Crystal data and structure refinement for complex 3 (tl1001m).

Identification code	tl1001m
Empirical formula	C54 H40 Cl2 N2 O3 Ti
Formula weight	883.68
Temperature	120(2) K
Wavelength	0.71073 Å
Crystal system	Monoclinic
Space group	P2(1)
Unit cell dimensions	a = 13.5996(9) Å $\quad$ α= 90°.
	b = 22.3064(16) Å $\quad$ β= 98.469(4)°.
	c = 14.2640(10) Å $\quad$ γ = 90°.
Volume	4279.9(5) Å^3
Z	4
Density (calculated)	1.371 Mg/m^3
Absorption coefficient	0.374 mm^{-1}
F(000)	1832
Crystal size	0.22 x 0.14 x 0.08 mm^3
Theta range for data collection	1.51 to 29.57°.
Index ranges	-18<=h<=11, -30<=k<=28, -19<=l<=19
Reflections collected	42735
Independent reflections	18624 [R(int) = 0.1142]
Completeness to theta = 29.57°	97.9 %
Absorption correction	Semi-empirical from equivalents
Max. and min. transmission	0.9707 and 0.9223
Refinement method	Full-matrix least-squares on F^2
Data / restraints / parameters	18624 / 1 / 1117
Goodness-of-fit on F^2	0.956
Final R indices [I>2sigma(I)]	R1 = 0.0841, wR2 = 0.1738
R indices (all data)	R1 = 0.2031, wR2 = 0.2313
Absolute structure parameter	0.02(4)
Largest diff. peak and hole	0.594 and -0.681 e.Å^{-3}

Table 3. Crystal data and structure refinement for complex 6 (tl1004m).

Identification code	tl1004m
Empirical formula	C90 H64 Cl4 N4 O6 Ti2
Formula weight	1535.05
Temperature	120(2) K
Wavelength	0.71073 Å
Crystal system	Orthorhombic
Space group	P2(1)2(1)2(1)
Unit cell dimensions	a = 11.602(3) Å α= 90°.
	b = 22.055(5) Å β= 90°.
	c = 28.245(8) Å γ = 90°.
Volume	7227(3) Å^3
Z	4
Density (calculated)	1.411 g/cm^3
Absorption coefficient	0.431 mm^{-1}
F(000)	3168
Crystal size	0.28 x 0.14 x 0.06 mm^3
Theta range for data collection	1.90 to 27.88°.
Index ranges	-7<=h<=15, -29<=k<=22, -35<=l<=37
Reflections collected	41031
Independent reflections	9342 [R(int) = 0.2707]
Completeness to theta = 27.88°	99.2 %
Absorption correction	Semi-empirical from equivalents
Max. and min. transmission	0.9746 and 0.8889
Refinement method	Full-matrix least-squares on F^2
Data / restraints / parameters	9342 / 369 / 936
Goodness-of-fit on F^2	1.140
Final R indices [I>2sigma(I)]	R1 = 0.1194, wR2 = 0.2278
R indices (all data)	R1 = 0.2792, wR2 = 0.2867
Absolute structure parameter	0.44(7)
Largest diff. peak and hole	0.937 and -0.800 e.Å^{-3}

Table 4. Crystal data and structure refinement for complex 7 (tl1002m).

Identification code	tl1002m
Empirical formula	C51 H32 Cl2 N2 O3 Ti
Formula weight	839.59
Temperature	120(2) K
Wavelength	0.71073 Å
Crystal system	Orthorhombic
Space group	P2(1)2(1)2
Unit cell dimensions	a = 17.1580(16) Å α= 90°.
	b = 17.5684(17) Å β= 90°.
	c = 13.2935(11) Å γ = 90°.
Volume	4007.2(6) Å^3
Z	4
Density (calculated)	1.392 g/cm^3
Absorption coefficient	0.395 mm^{-1}
F(000)	1728
Crystal size	0.26 x 0.20 x 0.14 mm^3
Theta range for data collection	1.53 to 30.03°.
Index ranges	-14<=h<=24, -24<=k<=19, -18<=l<=18
Reflections collected	25151
Independent reflections	11131 [R(int) = 0.0688]
Completeness to theta = 30.03°	99.8 %
Absorption correction	Semi-empirical from equivalents
Max. and min. transmission	0.9467 and 0.9042
Refinement method	Full-matrix least-squares on F^2
Data / restraints / parameters	11131 / 0 / 424
Goodness-of-fit on F^2	1.554
Final R indices [I>2sigma(I)]	R1 = 0.1055, wR2 = 0.2678
R indices (all data)	R1 = 0.1459, wR2 = 0.2820
Absolute structure parameter	0.18(5)
Largest diff. peak and hole	1.103 and -0.952 e.Å^{-3}

Table 5. Crystal data and structure refinement for complex 10 grown in N_2 (tl0802).

Identification code	tl0802m
Empirical formula	C80 H74 Cl4 Mn2 N4 O7
Formula weight	1455.11
Temperature	120(2) K
Wavelength	0.71073 Å
Crystal system	Orthorhombic
Space group	P2(1)2(1)2(1)
Unit cell dimensions	a = 15.9291(6) Å α= 90°.
	b = 19.5228(7) Å β= 90°.
	c = 21.8734(9) Å γ = 90°.
Volume	6802.2(5) Å^3
Z	4
Density (calculated)	1.421 g/cm^3
Absorption coefficient	0.589 mm^{-1}
F(000)	3024
Crystal size	0.30 x 0.25 x 0.15 mm^3
Theta range for data collection	1.86 to 34.97°.
Index ranges	-21<=h<=25, -26<=k<=30, -33<=l<=35
Reflections collected	81345
Independent reflections	28405 [R(int) = 0.0298]
Completeness to theta = 34.97°	99.2 %
Absorption correction	None
Max. and min. transmission	0.9168 and 0.8430
Refinement method	Full-matrix least-squares on F^2
Data / restraints / parameters	28405 / 0 / 849
Goodness-of-fit on F^2	1.054
Final R indices [I>2sigma(I)]	R1 = 0.0486, wR2 = 0.1274
R indices (all data)	R1 = 0.0672, wR2 = 0.1384
Absolute structure parameter	-0.006(9)
Largest diff. peak and hole	1.024 and -0.953 e.Å^{-3}

Table 6. Crystal data and structure refinement for complex 10 grown in air (tl0805m).

Identification code	tl0805m
Empirical formula	C88 H88 Mn2 N4 O10
Formula weight	1471.50
Temperature	120(2) K
Wavelength	0.71073 Å
Crystal system	Orthorhombic
Space group	P2(1)2(1)2(1)

Unit cell dimensions
$a = 16.2832(9)$ Å $\qquad \alpha = 90°.$
$b = 19.4044(11)$ Å $\qquad \beta = 90°.$
$c = 22.4359(12)$ Å $\qquad \gamma = 90°.$

Volume	7089.0(7) Å^3
Z	4
Density (calculated)	1.379 g/cm^3
Absorption coefficient	0.424 mm^{-1}
F(000)	3096
Crystal size	0.25 x 0.25 x 0.10 mm^3
Theta range for data collection	1.39 to 32.03°.
Index ranges	-24<=h<=23, -28<=k<=28, -33<=l<=28
Reflections collected	75149
Independent reflections	22355 [R(int) = 0.0473]
Completeness to theta = 25.00°	99.9 %
Absorption correction	None
Max. and min. transmission	0.9588 and 0.9015
Refinement method	Full-matrix least-squares on F^2
Data / restraints / parameters	22355 / 57 / 940
Goodness-of-fit on F^2	1.038
Final R indices [I>2sigma(I)]	R1 = 0.0455, wR2 = 0.0977
R indices (all data)	R1 = 0.0788, wR2 = 0.1101
Absolute structure parameter	-0.008(9)
Largest diff. peak and hole	0.614 and -0.532 e.Å^{-3}

Table 7. Crystal data and structure refinement for complex 11 (tl0902m).

Identification code	tl0902m
Empirical formula	C76 H64 Cl8 Mn2 N4 O6
Formula weight	1522.79
Temperature	120(2) K
Wavelength	0.71073 Å
Crystal system	Orthorhombic
Space group	P2(1)2(1)2(1)
Unit cell dimensions	a = 15.6830(13) Å α= 90°.
	b = 19.5846(16) Å β= 90°.
	c = 21.8586(19) Å γ = 90°.
Volume	6713.8(10) Å^3
Z	4
Density (calculated)	1.507 g/cm^3
Absorption coefficient	0.754 mm^{-1}
F(000)	3128
Crystal size	0.24 x 0.12 x 0.06 mm^3
Theta range for data collection	1.86 to 32.03°.
Index ranges	-23<=h<=22, -20<=k<=29, -16<=l<=32
Reflections collected	55121
Independent reflections	21993 [R(int) = 0.0687]
Completeness to theta = 32.03°	98.2 %
Absorption correction	None
Max. and min. transmission	0.9562 and 0.8398
Refinement method	Full-matrix least-squares on F^2
Data / restraints / parameters	21993 / 45 / 880
Goodness-of-fit on F^2	1.007
Final R indices [I>2sigma(I)]	R1 = 0.0642, wR2 = 0.1541
R indices (all data)	R1 = 0.1118, wR2 = 0.1794
Absolute structure parameter	-0.001(16)
Largest diff. peak and hole	1.174 and -0.861 e.Å^{-3}

Table 8. Crystal data and structure refinement for complex 12 (tl0804m).

Identification code	tl0804m
Empirical formula	C162 H114 Cl12 Mn2 N6 O6
Formula weight	2775.87
Temperature	120(2) K
Wavelength	0.71073 Å
Crystal system	Monoclinic
Space group	P2(1)
Unit cell dimensions	a = 13.4517(6) Å $\qquad$ α= 90°.
	b = 26.4318(11) Å $\qquad$ β= 98.245(3)°.
	c = 18.7382(9) Å $\qquad$ γ = 90°.
Volume	6593.6(5) Å^3
Z	2
Density (calculated)	1.398 g/cm^3
Absorption coefficient	0.498 mm^{-1}
F(000)	2860
Crystal size	0.20 x 0.15 x 0.10 mm^3
Theta range for data collection	2.90 to 31.50°.
Index ranges	-19<=h<=19, -37<=k<=38, -26<=l<=15
Reflections collected	59770
Independent reflections	33165 [R(int) = 0.0649]
Completeness to theta = 25.00°	94.2 %
Absorption correction	None
Max. and min. transmission	0.9519 and 0.9069
Refinement method	Full-matrix least-squares on F^2
Data / restraints / parameters	33165 / 46 / 1723
Goodness-of-fit on F^2	0.999
Final R indices [I>2sigma(I)]	R1 = 0.0696, wR2 = 0.1460
R indices (all data)	R1 = 0.1319, wR2 = 0.1744
Absolute structure parameter	-0.009(14)
Largest diff. peak and hole	1.317 and -0.701 e.Å^{-3}

Table 9. Crystal data and structure refinement for complex 15 (tl0901m).

Identification code	tl0901m
Empirical formula	C118 H94 Mn2 N4 O6
Formula weight	1773.85
Temperature	120(2) K
Wavelength	0.71073 Å
Crystal system	Orthorhombic
Space group	P2(1)2(1)2(1)
Unit cell dimensions	a = 15.0530(7) Å α= 90°.
	b = 16.0863(7) Å β= 90°.
	c = 36.6821(16) Å γ = 90°.
Volume	8882.5(7) Å^3
Z	4
Density (calculated)	1.326 Mg/m^3
Absorption coefficient	0.348 mm^{-1}
F(000)	3712
Crystal size	0.25 x 0.20 x 0.15 mm^3
Theta range for data collection	1.38 to 31.51°.
Index ranges	-20<=h<=19, -22<=k<=23, -53<=l<=52
Reflections collected	82634
Independent reflections	27947 [R(int) = 0.0528]
Completeness to theta = 31.51°	96.1 %
Absorption correction	None
Max. and min. transmission	0.9496 and 0.9180
Refinement method	Full-matrix least-squares on F^2
Data / restraints / parameters	27947 / 0 / 1132
Goodness-of-fit on F^2	1.052
Final R indices [I>2sigma(I)]	R1 = 0.0479, wR2 = 0.1000
R indices (all data)	R1 = 0.0695, wR2 = 0.1094
Absolute structure parameter	-0.013(8)
Largest diff. peak and hole	0.410 and -0.369 e.Å^{-3}